



TECHNISCHE  
UNIVERSITÄT  
WIEN

# DISSERTATION

## Mathematical models for pulse wave analysis considering ventriculo-arterial coupling in systolic heart failure

Ausgeführt zum Zwecke der Erlangung des akademischen Grades einer  
Doktorin der technischen Wissenschaften  
unter der Leitung von

Ao.Univ.Prof. Dipl.-Ing. Dr.techn. Felix Breitenecker

E101

Institut für Analysis und Scientific Computing

eingereicht an der Technischen Universität Wien  
Fakultät für Mathematik und Geoinformation

von

Dipl.-Ing. Stephanie Parragh

0526658

Währinger Gürtel 166/2/4

1090 Wien

---

Ort, Datum

---

Unterschrift

# Zusammenfassung

Die Pulswellenanalyse (PWA) aortaler Druck- und Flussverläufe ermöglicht es Parameter zu bestimmen, die wichtige Informationen über den Status des kardiovaskulären Systems einer Person liefern. Für die Risikostratifizierung werden insbesondere immer öfter nichtinvasiv gemessene aortale Druckkurven und modellierte Flusskurven eingesetzt. In Patienten mit systolischer Herzinsuffizienz (SHI) ist die Interpretation der PWA Parameter allerdings schwierig und bekannte Risikofaktoren sind nicht anwendbar. Außerdem ist nur wenig über die Verwendbarkeit von bereits bestehenden Flussmodellen in diesen Patienten bekannt.

SHI wird durch eine Veränderung der ventrikulo-arteriellen Kopplung, d.h. dem Zusammenspiel von Herz und Arteriensystem, charakterisiert, die oft mit einem veränderten Auswurfmuster des linken Ventrikels einhergeht. Um diese Charakteristik richtig darstellen zu können wird in dieser Arbeit ein neues Flussmodell präsentiert. Dieses basiert auf einem Kompartimentmodell des arteriellen Systems, dem sogenannten 4-elementigen Windkessel, das verwendet wird um eine parametrische Darstellung der Transferfunktion zwischen Blutdruck und Blutfluss im Frequenzbereich zu erhalten. Ausgehend von einer aortalen Druckkurve, kann der Blutfluss mittels einer Parameteridentifikation somit direkt berechnet werden. Simulationsergebnisse zeigen, dass es mit diesem Modell tatsächlich möglich ist, sowohl physiologische als auch pathologische Flussverläufe darzustellen. Die Resultate einer Sensitivitätsanalyse weisen weiters darauf hin, dass die beschriebene Methode robust auf Änderungen der Eingangsgröße sowie der Modellparameter reagiert. Das verwendete Windkesselmodell berücksichtigt jedoch keine Wellenreflexionen, weshalb das Flussmodell für einen bestimmten Typ von Druckkurven, der vor allem in Patienten mit normaler systolischer Pumpleistung vorkommt, nicht geeignet ist. Deshalb wird eine Möglichkeit vorgestellt, den Windkesselfluss mit einem bereits bestehenden Flussmodell zu kombinieren. Als Entscheidungskriterium dient dabei ein Formfaktor der Druckkurve, der im Frequenzbereich bestimmt wird.

Um die Rolle der ventrikulo-arteriellen Kopplung für die arterielle Hämodynamik weiter zu untersuchen, wurde der Einfluss von SHI auf die PWA Parameter analysiert. Dafür wurden gemessene Fluss- und Druckverläufe von 61 Patienten mit SHI und einer Kontrollgruppe bestehend aus 122 Patienten mit normaler systolischer Pumpleistung verwendet. Das Ausmaß der Wellenreflexionen war in der SHI Gruppe scheinbar niedriger als in der Kontrollgruppe, was durch die Reduktion der Auswurfdauer, als Ausdruck der gestörten Kopplung zwischen Ventrikel und Arteriensystem,

erklärt werden konnte. PWA wird allgemein zur Quantifizierung der Gefäßeigenschaften verwendet. Die Ergebnisse dieser Arbeit zeigen jedoch, dass die PWA Parameter in SHI stark von der Herzfunktion beeinflusst werden, was für die Risikostratifizierung in diesen Patienten unbedingt berücksichtigt werden sollte.

Schließlich wurden verschiedene bereits bestehende Flussmodelle aus der Literatur, sowie der neu vorgestellte Ansatz in derselben Studienpopulation auf ihre Anwendbarkeit für PWA untersucht. Die Ergebnisse zeigen, dass ein Flussmodell eine gewisse Flexibilität in der Flussform sowie einen physiologischen Verlauf aufweisen sollte um akkurate Schätzer der PWA Parameter zu liefern, die dasselbe qualitative Verhalten aufweisen wie Parameter, die mittels gemessenem Fluss bestimmt wurden. Der kombinierte Windkesselfluss erfüllt diese Kriterien und war das einzige Modell, das sowohl in den beiden Patientengruppen separat als auch im Vergleich beider Gruppen eine akzeptable Übereinstimmung mit gemessenem Fluss erreichte. Diese Resultate stellen allerdings nur einen Machbarkeitsnachweis dar, da dieselben Daten zur Modellentwicklung und -evaluierung verwendet wurden.

Zusammenfassend unterstreichen die Resultate die Wichtigkeit der Herzfunktion für die Interpretation druckbasierter Parameter und zeigen, dass nur mit einem akkuraten Flussmodell auch akkurate Schätzer der PWA Parameter erreicht werden können. Mit dem vorgestellten Ansatz konnten erste, sehr vielversprechende Ergebnisse erzielt werden, die eine vergleichbare Präzision für Patienten mit normaler und eingeschränkter systolischer Funktion aufzeigen.

# Abstract

Parameters gained from pulse wave analysis (PWA) of the pressure and flow waveforms in the human aorta yield important information about the status of the cardiovascular system. In particular, non-invasively measured aortic blood pressure together with modelled flow are more and more used for the stratification of cardiovascular risk. However, in patients with systolic heart failure (SHF), the interpretation of PWA parameters is puzzling and general risk indicators are not applicable. Moreover, little is known about the feasibility of using existing flow models for PWA in these patients.

SHF is characterized by an alteration in the ventriculo-arterial coupling (i.e. the interplay of the heart and the arterial system), which often results in a modified ejection pattern. To properly describe these characteristics, a new flow model is presented in this thesis. In brief, the proposed approach is based on a one compartment model of the arterial system, the so-called 4-element Windkessel, from which a parametric equation for the transfer function between pressure and flow in the frequency domain is derived. Using non-invasively assessed aortic pressure as input, a parameter identification then allows for a direct computation of blood flow. Simulation runs and the results of a sensitivity analysis indicate that the presented model is able to reproduce physiological and pathological ejection patterns and is robust against changes in the input values and model parameters. However, the Windkessel model does not account for the effects of wave reflections, making the flow model unsuitable for a specific type of pressure waves found mainly in subjects with normal systolic function. Therefore, a combination of the Windkessel flow with an already established flow model is proposed based on a form factor of the pressure wave derived in the frequency domain.

To further investigate the role of ventriculo-arterial coupling for arterial hemodynamics, the impact of an impaired systolic function on the PWA parameters derived from measured pressure and flow was investigated in 61 patients with SHF and 122 controls. Most parameters quantifying wave reflections were reduced in SHF, which could be attributed to a shortening of the ejection duration as a manifestation of an impaired coupling between the ventricle and the arterial system. PWA is commonly used to quantify arterial function only. However, the results demonstrate that the derived parameters are susceptible to cardiac function in SHF, which has to be kept in mind for risk stratification in these patients.

Finally, the performance of different existing flow models as well as of the novel approach for PWA was examined in the same study population. The results indicate that for a flow model, both a physiological waveform as well as the capability to adapt in shape are necessary to yield accurate PWA parameters that show the same qualitative behaviour as parameters obtained with measured flow. The combined Windkessel flow fulfils these criteria and was the only flow model that achieved an acceptable agreement to measured flow in and across both groups of patients. However, it should be emphasised that these results represent a proof of concept only because the same study population was used for model development and evaluation.

In conclusion, the results underline the importance of cardiac function for the interpretation of pressure-derived parameters and stress that an accurate flow estimate is needed to derive accurate PWA parameters. First promising results could be achieved with the novel flow model, yielding parameter estimates with a comparable accuracy and precision in both, patients with normal and impaired systolic function.

# Acknowledgements

First of all, I want to thank Prof. Felix Breitenecker for offering me the opportunity and privilege to do a doctorate and for involving me in his research group, which meant a lot to me.

I would also like to express my gratitude to Sigi Wassertheurer, who enabled me to carry out my thesis at the Austrian Institute of Technology and guided me throughout this project.

Furthermore, my special thanks belong to Bernhard Hametner from the AIT for the many insightful discussions, for critically questioning (almost) everything, for the helpful advice and suggestions when I was stuck, and, last but not least, for proofreading this thesis.

The four years that I have spent at the AIT would not have been the same without my great colleagues Martin, Christopher, Brigitte, Stefan (x3), Andi, Evi and (again) Bernhard, who made the days in the office always pleasant and most often delightful. Thank you!

Moreover, I would like to extend my thanks to my collaborator Thomas Weber from the Klinikum Wels-Grieskirchen, who not only provided the data used in this thesis but also his scientific advice and medical expertise in several common projects.

I would also like to say thank you to my family and friends for supporting me all the way - I am more than lucky to have you! Especially, I wish to thank my parents, Rita and Laci for the love and care they have given me and for always believing in me, as well as my siblings Sophie and Nico plus families for being there for me no matter what.

Finally, finishing this thesis would have been all the more difficult were it not for my boyfriend Dominik, who endured all my moods and my ups and downs with an incredible patience and encouraged me over and over again. I don't know what I would have done without you, and I want to thank you from the bottom of my heart.

Many thanks to all of you,

Stephanie Parragh

# Contents

<b>List of Figures</b>	<b>ix</b>
<b>List of Tables</b>	<b>xii</b>
<b>1 Introduction</b>	<b>1</b>
1.1 Background and motivation . . . . .	1
1.2 Aim of the thesis . . . . .	3
1.3 Outline of the thesis . . . . .	3
1.4 Heart failure . . . . .	4
1.4.1 The heart failure epidemic . . . . .	4
1.4.2 Systolic heart failure . . . . .	5
<b>2 Parameters for the assessment of cardiovascular risk</b>	<b>7</b>
2.1 Pressure pulse wave analysis . . . . .	7
2.1.1 Timing information and pressure levels . . . . .	9
2.1.2 Parameters quantifying the propagation of the pressure pulse throughout the body . . . . .	10
2.1.3 Pressure time integrals and wasted energy . . . . .	13
2.2 Impedance analysis . . . . .	15
2.2.1 Fourier analysis and input impedance . . . . .	15
2.2.2 Wave separation analysis . . . . .	18
2.2.3 Estimating aortic characteristic impedance . . . . .	20
2.3 Windkessel models . . . . .	22
2.3.1 Two-element Windkessel . . . . .	22
2.3.2 Three- and four-element Windkessel . . . . .	24
2.3.3 Diastolic decay . . . . .	27
2.4 Wave intensity analysis . . . . .	28
2.4.1 Deriving a 1D model of blood flow and pressure in an elastic vessel . . . .	29
2.4.2 Solution using the method of characteristics . . . . .	33
2.4.3 Wave intensity . . . . .	36
2.4.4 Waterhammer equations and wave separation . . . . .	37

<b>3</b>	<b>Models of aortic blood flow based on pressure alone: existing methods and a novel approach</b>	<b>41</b>
3.1	Triangular flow . . . . .	41
3.2	Averaged flow . . . . .	42
3.3	ARCSolver flow . . . . .	43
3.4	Windkessel flow . . . . .	46
3.4.1	Concept . . . . .	46
3.4.2	Methods and implementation . . . . .	48
3.4.3	Sensitivity Analysis . . . . .	51
3.4.4	Simulation results . . . . .	61
3.4.5	Combination with ARCSolver flow . . . . .	64
<b>4</b>	<b>Non-invasive quantification of wave reflections in systolic heart failure: state of the art and data analysis</b>	<b>66</b>
4.1	State of the art . . . . .	66
4.2	Aim of the study . . . . .	69
4.3	Methods . . . . .	69
4.4	Results . . . . .	73
4.5	Discussion . . . . .	80
<b>5</b>	<b>Using flow models based on pressure alone in patients with systolic heart failure: state of the art and data analysis</b>	<b>85</b>
5.1	State of the Art . . . . .	85
5.2	Aim of the study . . . . .	87
5.3	Methods . . . . .	88
5.4	Results . . . . .	89
5.5	Discussion . . . . .	92
<b>6</b>	<b>Summary and conclusions</b>	<b>105</b>
<b>Appendix A Asymptotic pressure as an additional parameter in the Windkessel models</b>		<b>107</b>
A.1	Methods . . . . .	108
A.1.1	Simulation runs . . . . .	108
A.1.2	Fitting performance . . . . .	109
A.2	Results . . . . .	110
A.2.1	Simulation runs . . . . .	110
A.2.2	Fitting performance . . . . .	110
A.3	Discussion . . . . .	113
<b>Appendix B Remarks on the pulse wave velocity</b>		<b>115</b>
B.1	Moens-Korteweg and Bramwell-Hill . . . . .	115
B.2	Investigating the assumption of constant pulse wave velocity . . . . .	116
<b>Bibliography</b>		<b>119</b>



---

<b>Abbreviations</b>	<b>133</b>
<b>Nomenclature</b>	<b>134</b>
<b>List of Publications</b>	<b>136</b>
<b>Curriculum Vitæ</b>	<b>138</b>

# List of Figures

1.1	Hospitalisations due to heart failure in different European countries and the United States. . . . .	4
1.2	Schematic representation of a normal heart compared to systolic and diastolic dysfunction. . . . .	6
2.1	Examples of different measurement techniques to acquire arterial pressure. . . . .	8
2.2	Determination of timing information and pressure levels . . . . .	9
2.3	Computation of AIx. . . . .	11
2.4	Assessment of carotid-femoral PWV using sequential pressure measurements and a simultaneous electrocardiogram. . . . .	12
2.5	Computation of the time indices representing the areas under different portions of the pressure wave. . . . .	14
2.6	Fourier decomposition and approximation of aortic pressure and flow for the first 10 harmonics. . . . .	16
2.7	Modulus and phase of arterial input impedance. . . . .	17
2.8	Aortic pressure and flow separated in their forward and backward components using wave separation analysis. . . . .	19
2.9	Estimation of aortic characteristic impedance. . . . .	21
2.10	Representation of the two-element Windkessel model as an electrical circuit. . . . .	23
2.11	Representation of the three- and four-element Windkessel model as electrical circuits. . . . .	25
2.12	Comparison of the aortic pressure waves modelled by the three different Windkessel models. . . . .	26
2.13	$P_{RC}$ and $P_{LZ}$ . . . . .	27
2.14	Comparison of the modulus and phase of the arterial input impedances described by the three different Windkessel models. . . . .	28
2.15	A straight arterial segment with length $l$ , oriented along the $x$ -axis. . . . .	30
2.16	Schematic representation of the characteristic directions and the corresponding Riemann invariants. . . . .	35
2.17	Wave intensity obtained from measured pressure and flow velocity. . . . .	36
2.18	A single forward wave travelling in a uniform, lossless vessel along the characteristic direction $\hat{x}_+$ . . . . .	38
2.19	Aortic pressure and flow separated in their forward and backward components using wave intensity analysis. . . . .	39

2.20	Forward and backward wave intensity. . . . .	40
3.1	Triangular approximation and averaged waveform as estimates of aortic blood flow. . . . .	42
3.2	Estimation of initial values used for the computation of blood flow. . . . .	50
3.3	Exemplary data of a patient with normal EF and one with reduced EF used for sensitivity analysis. . . . .	52
3.4	Sensitivity analysis showing the effect of changes in the model parameters $C_a$ , $Z_c$ and $L$ . . . . .	53
3.5	Sensitivity analysis showing the effect of changes in the model parameters $P_\infty$ , $R_p$ and $\tilde{n}$ . . . . .	54
3.6	Boxplots showing the changes in the objective function relative to its baseline for varying $C_a$ (a), $Z_c$ (b) and $L$ (c) from 85% to 115% of their respective baseline values while keeping all other parameters constant. . . . .	55
3.7	Analysis of the effect of the grid-search approach for $\tilde{n}$ . . . . .	56
3.8	Analysis of the effect of the upper boundary of $P_\infty$ used in the optimisation. . . . .	57
3.9	Influence of the upper boundary (ub) of $P_\infty$ on an exemplary pressure wave from a patient with normal (a) and reduced EF (b). . . . .	58
3.10	Analysis of the influence of changes in DBP, SBP and MBP. . . . .	59
3.11	Sensitivity analysis showing the effect of changes in the magnitude of $\pm 5$ mmHg in the input pressure levels DBP, SBP and MBP. . . . .	60
3.12	Exemplary simulation results for patients with reduced EF. . . . .	62
3.13	Exemplary simulation results for patients with normal EF. . . . .	63
3.14	Phase angle of central pressure for patients with normal and reduced EF. . . . .	64
4.1	Examples of an angiographic and echocardiographic measurement of diastolic left ventricular volume. . . . .	70
4.2	Assessment of aortic blood pressure and flow. . . . .	72
4.3	Averaged flow and pressure waveform for patients with reduced and normal EF. . . . .	74
4.4	Difference of the mean values of wave reflection parameters between patients with reduced and normal EF adjusted for temporal characteristics. . . . .	79
4.5	Difference of the mean values of the S to D ratio between patients with reduced and normal EF adjusted for temporal characteristics. . . . .	79
5.1	Examples of Doppler flow waves and the corresponding model estimates for patients with reduced EF . . . . .	89
5.2	Examples of Doppler flow waves and the corresponding model estimates for controls. . . . .	90
5.3	Bland-Altman plots comparing $ P_f $ . . . . .	96
5.4	Bland-Altman plots comparing $ P_b $ . . . . .	96
5.5	Bland-Altman plots comparing RM. . . . .	97
5.6	Bland-Altman plots comparing the S wave energy. . . . .	97
5.7	Bland-Altman plots comparing the R wave energy. . . . .	98
5.8	Bland-Altman plots comparing the ratio of the R to S wave energy. . . . .	98
5.9	Bland-Altman plots comparing the D wave energy. . . . .	99
5.10	Bland-Altman plots comparing the ratio of the S to D wave energy. . . . .	99

A.1	Exemplary aortic pressure signal including a missing heart beat. . . . .	109
A.2	A: typical flow curve used as input to the models. B-D: simulated pressure waves for $P_\infty$ ranging from 0 to 75 mmHg obtained with the WK2 (B), WK3 (C) and the WK4p (D). . . . .	111
A.3	Difference between modulus and phase of modelled input impedance for $P_\infty = 0$ and $P_\infty = 75$ mmHg for the three different Windkessel models. . . . .	111
A.4	Exemplary result of fitting. . . . .	112
A.5	Mean RMSE between analytical function and regular and prolonged diastole when fitted to the regular and prolonged part respectively. . . . .	113
B.1	Distension of the cross-sectional area for a constant pulse wave velocity as a function of pressure. . . . .	118

# List of Tables

2.1	Nomenclature used for the dominating waves according to the sign of $dI$ and $dP$ .	37
3.1	Parameter values for the baseline parametrisation. . . . .	51
3.2	Results of the parameter identification. . . . .	61
4.1	Baseline characteristics of the study population. . . . .	74
4.2	Clinical measurements. . . . .	75
4.3	PWA parameters derived by the SphygmoCor system and pressure time indices.	76
4.4	WSA and WIA parameters. . . . .	77
4.5	Correlations between PWA, WSA and WIA parameters. . . . .	78
4.6	Correlations between measures of cardiac function and structure and haemodynamic parameters. . . . .	81
5.1	Comparison of the flow shape and the WSA parameters obtained by the different blood flow models. . . . .	93
5.2	Comparison of the WIA energies obtained by the different blood flow models. . .	94
5.3	Comparison of the WIA peaks obtained by the different blood flow models. . . .	95
A.1	The input impedances $Z_{in}$ described by the three different Windkessel models. .	108
A.2	Parameter values for the standard parametrisation. . . . .	109

# Chapter 1

## Introduction

### 1.1 Background and motivation

Arterial blood pressure has been used for the stratification of cardiovascular risk for literally thousands of years. For a long time, its assessment was restricted to palpation only [79]. The non-invasive measurement of both the systolic and diastolic blood pressure became feasible in 1905 and is still in use today in conventional blood pressure readings. Systolic blood pressure (SBP) describes the maximum and diastolic blood pressure (DBP) the minimum of the arterial pressure waveform. It is well accepted that this "usual blood pressure is strongly and directly related to vascular (and overall) mortality" [102, p. 1903], as demonstrated in a multitude of studies and meta-analyses [102]. However, besides the absolute values of brachial SBP and DBP, also an excessive pulsatility of arterial pressure, given by the pulse pressure  $PP=SBP-DBP$ , was found to be a strong indicator of cardiovascular risk [157] and has been included as an additional risk factor in the elderly by the current European guidelines for the treatment of hypertension [61]. Even though these relations were first reported for peripheral pressure levels only, first evidence exists that central or more precisely aortic pressure (measured or synthesised) might be even superior [1, 65, 110]. This is in line with the idea that central and not peripheral pressure is the one directly affecting the organs and determining the load the heart has to eject against.

Analysis of the central pressure and flow waveforms moreover helped to gain a deeper understanding of the mechanisms underlying physiological ageing or the pathogenesis of cardiovascular disease, showing the importance and contribution of arterial stiffness and wave reflections to pulsatile haemodynamics [54, 77]. For this purpose, various mathematical models have been developed, adapted or simplified to describe the relation between properties of the arterial system and the corresponding pressure and flow dynamics [28, 91, 148, 152]. Based on these models, different methodologies were subsequently introduced to derive information about the status of the cardiovascular system of a specific person from (non-invasively) measured pressure and/or flow, often summarised under the general term pulse wave analysis (PWA) [84]. Nowadays, PWA parameters are more and more finding their way into clinical research and increased arterial stiff-

ness and excessive wave reflections have been shown to be related to a worse prognosis in the general population [17, 133] as well as in different groups of high risk patients [111].

However, the situation changes when the contractility of the left ventricle is impaired and the ventriculo-arterial coupling, in other words the interplay of the heart and the arterial system, is therefore altered. The corresponding clinical syndrome, characterised by a left ventricular systolic dysfunction accompanied by typical symptoms and signs, is called systolic heart failure (SHF) or heart failure with reduced ejection fraction (EF). The latter refers to the imperfect emptying of the left ventricle due to the impaired contractility [5], whereby the EF is defined as the volume of blood that is ejected during one cardiac cycle relative to the left ventricular filling volume prior to ejection.

Even though high blood pressure [127], excessive wave reflections [17] and increased arterial stiffness [128] have been found to be important predictors for the new onset of heart failure, the behaviour of conventional pressure-based risk indicators changes as soon as systolic heart failure develops. The relation of peripheral pulse pressure to outcome was found to be reversed [4, 26, 42, 67, 107] or U-shaped [53] and a low systolic blood pressure was associated to a worse prognosis in a recent meta-analysis including more than 8000 heart failure patients [106]. Moreover, indices of wave reflections assessed by PWA were repeatedly reported to be lower in patients with systolic heart failure compared to controls [21, 137], complicating their interpretation and usability as risk indicators. Overall, as stated in the 2016 guidelines for the diagnosis and treatment of acute and chronic heart failure of the European Society of Cardiology (ESC), the "precise risk stratification in HF remains challenging" [101, p.10]. These observations underline the importance of ventriculo-arterial coupling for all haemodynamic parameters and the necessity to understand and ideally to quantify the impact of cardiac function on the derived PWA parameters in order to use them for risk assessment in these patients.

The umbrella term PWA comprises a large variety of models with varying complexities, ranging from the simple detection of an inflection point over linear transmission line theory to one-dimensional models describing the conservation of mass and balance of momentum in an arterial segment. The most simple approaches are thereby based on a single pressure measurement, which will be referred to as pressure pulse wave analysis, while the more advanced methods use both pressure and flow. Two prominent representatives of the latter class are wave separation analysis (WSA), introduced by Westerhof and coworkers in 1972 [148], and wave intensity analysis (WIA), proposed by Parker et al. in 1990 [91]. However, independent of their level of sophistication, all of these methods are intended to help in the stratification of cardiovascular risk and the early detection of cardiovascular disease. Therefore, they should ideally be easily applicable at a primary care level and should present no risk for the patients, i.e. non-invasive measurements are preferable. For blood pressure, validated transfer functions exist to synthesise central pressure from peripheral readings [47], which can be performed using a simple pressure cuff [134, 135]. The non-invasive acquisition of aortic blood flow, on the other hand, is more complicated. Doppler ultrasound can be used to non-invasively measure the blood flow velocity in the left ventricular

outflow tract [105], but this requires dedicated equipment and specially trained operators which limits its widespread use. To facilitate the acquisition of blood flow, different flow models based on pressure alone have therefore been introduced in literature [35, 49, 142].

Data regarding the applicability of these flow models for WSA is limited to patients with normal systolic function so far [35, 49, 142]. Even though one approach has already been used to compute WSA in SHF as well [122], these patients often show a modified ejection pattern compared to controls and the feasibility is therefore more than questionable. With regards to WIA, no systematic evaluation of any of the flow models exists to date, independent of the cardiac function. The use of a blood flow model facilitating the computation of WSA or WIA parameters from pressure alone is a key element in order to enable a widespread use of these techniques, including in patients with SHF. Therefore, further research is needed to evaluate the feasibility of the existing approaches. Moreover, because of the unique features found in SHF, a new flow model might be needed that is able to accurately reproduce also pathological flow patterns.

## 1.2 Aim of the thesis

The aim of this thesis can be separated into three individual, yet interrelated goals: 1) to analyse the differences in the PWA, WSA and WIA parameters in SHF compared to controls and to investigate how they can be attributed to alterations in ventriculo-arterial coupling, 2) to develop a new model of blood flow based on pressure alone that is capable to capture the pathological flow patterns found in patients with SHF and 3) to investigate and to compare the performance of different existing flow models as well as of the novel approach for WSA and WIA in SHF patients and controls.

## 1.3 Outline of the thesis

In chapter 1, the topic of the thesis is motivated and the specific objectives are formulated. Furthermore, a short introduction to heart failure is given including its medical definition, epidemiology and significance as socio-economic health burden. Chapter 2 provides an overview of the different methodologies to derive parameters for the stratification of cardiovascular risk from measured pressure and flow waves, with a main focus on their mathematical background and physiological interpretation. In chapter 3, three existing models of blood flow based on pressure alone are presented and a new approach for the computation of blood flow is introduced. Chapter 4 is dedicated to the analysis of the parameters derived by the different methods given in chapter 2 in patients with systolic heart failure compared to controls. For this purpose, clinical data of 183 patients is analysed. In chapter 5, the same study population is used to test and to evaluate the performance of the different blood flow models introduced in chapter 3. Finally, a short summary of the results and derived conclusions is given in chapter 6.



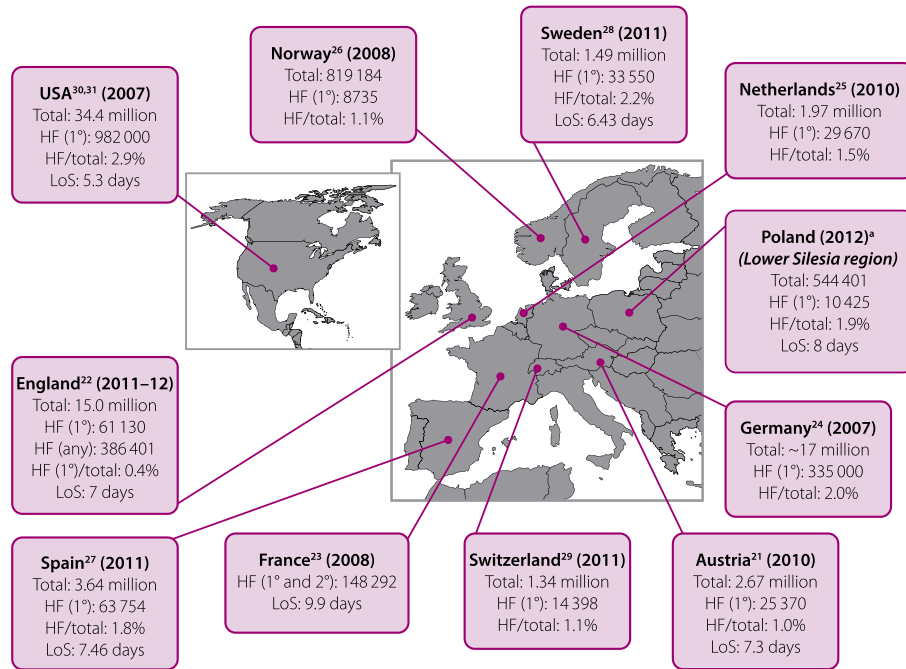


Figure 1.1: Hospitalisations due to heart failure in different European countries and the United States. (1°), (2°), (any) indicates HF being the primary, secondary or any diagnosis; total describes the total number of (all-cause) hospital admissions per year; LoS: average length of hospital stay in days. Reproduced from [18], licensed under CC BY-NC-ND 4.0. Please refer to the original work for the corresponding data sources which are indicated by numbers in the graphic.

## 1.4 Heart failure

Heart failure (HF) describes any abnormality of cardiac function or structure that results in a reduction of cardiac output or an elevation of the cardiac pressure levels and causes typical symptoms like breathlessness or fatigue [101]. In this section, a short overview over its epidemiology as well as the definition of systolic heart failure will be given.

### 1.4.1 The heart failure epidemic

”Heart failure, be it with preserved or reduced left ventricular function, is *the* cardiovascular epidemic of the 21st century”. -Thomas F. Lüscher, 2015 [57]

Worldwide, more than 23 million people are suffering from HF [109]. The total prevalence in the adult population equals 1-2% in western countries and increases with age, with a prevalence of more than 10% in persons aged 70 or older [101]. As a result of the ageing society, HF is expected to become even more frequent in the future, whereby projections in the U.S. show an increase in prevalence of up to 46% from 2012 to 2030 [71]. In the Rotterdam study, the lifetime risk for developing HF was found to be 30% for a person aged 55, whereby men showed a higher risk than women (33% vs. 28%) [8] and from data in the U.S., a lifetime risk of 20% at the age of 40 was determined [71]. The health related quality of life is significantly reduced for patients

living with HF, particularly with regards to physical activity and vitality [155], and mortality is high. Even though modern treatment could improve the mortality rates of HF within 5 years of the diagnosis, which were as high as 60-70% before 1990 [5], they still reach approximately 50% [71].

HF is furthermore "characterized by periodic exacerbations" [109, p.653], which mostly require hospitalisation. Therefore HF had become "the single most frequent cause of hospitalization in persons 65 years of age or older" [10, p. 1365] in 1997. In Austria, more than 25000 hospital admissions due to HF as primary cause were reported in 2010 based on data collected by the Statistik Österreich [18], representing 1% of all hospital admissions in this year, see figure 1.1. For patients with stable HF, i.e. patients without any changes for at least one month, the 12-month hospitalisation rate equals 32%, meaning that almost one third will be admitted to a hospital within the next year. For patients with acute HF, who are currently hospitalised, this rate increases to 44% [101] and the 1-month (all-cause) readmission rate reaches 25% in these patients [155]. Figure 1.1 gives an overview over total annual hospitalisations due to HF in Europe and the U.S.. The high amount of hospital admissions associated to HF of course represents a considerable economic burden. For example for the U.S., hospitalisation costs are in the range of 15\$ billion per year, which equals approximately half of the total costs caused by HF comprising healthcare, medication and lost productivity [155].

### 1.4.2 Systolic heart failure

Heart failure is very heterogenous in itself and various subtypes exist. The most prominent classification considers two different types, namely HF with reduced EF, normally defined as  $EF < 40\%$ , and HF with preserved EF, i.e.  $EF > 50\%$  [101]<sup>1</sup>. The first type is also referred to as systolic and the latter as diastolic heart failure, relating to the impairment in systolic ejection (systolic dysfunction) and diastolic filling (diastolic dysfunction) respectively. In systolic heart failure, the ventricle typically dilates and the contractility is decreased, while in diastolic heart failure, the thickness of the ventricular wall and therefore its stiffness increases and its filling capacity is decreased, compare figure 1.2. However, it should be noted that diastolic dysfunction may be present in systolic heart failure and subtle systolic dysfunction in diastolic heart failure, which is why the ESC recommends the use of heart failure with reduced and preserved EF instead [101]. Nevertheless, in this thesis, the terms heart failure with reduced EF and systolic heart failure will be used interchangeably. HF with reduced EF constitutes approximately one half of all HF cases and generally shows a worse prognosis than HF with preserved EF [101].

---

<sup>1</sup>Patients with HF and EF between 40% and 50% represent a borderline group, which should be treated as a third, separate group according to the latest ESC guidelines [101].

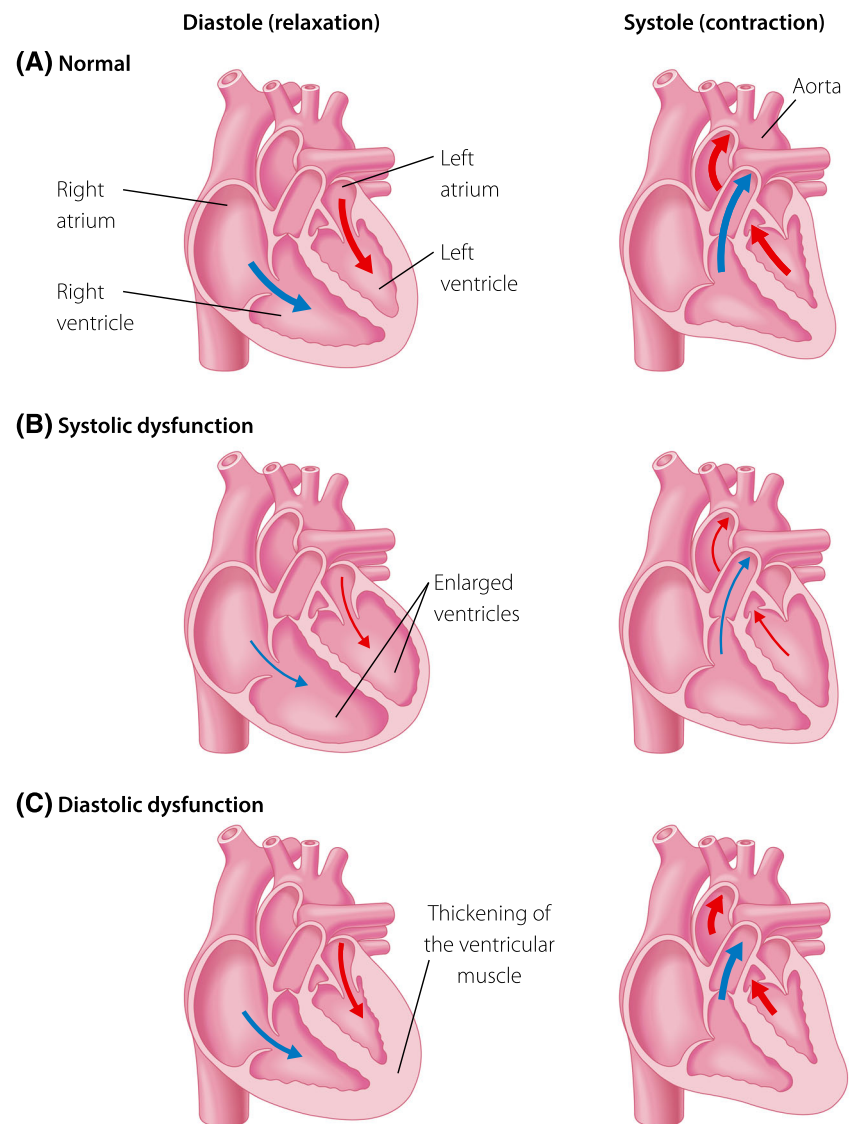


Figure 1.2: Schematic representation of a normal heart (A) compared to systolic (B) and diastolic dysfunction (C). Reproduced from [18], licensed under CC BY-NC-ND 4.0.

## Chapter 2

# Parameters for the assessment of cardiovascular risk

The haemodynamics in the arterial system result from a complex, dynamic interaction of the heart and the vasculature. Analysis of the corresponding pressure and flow waveforms can therefore provide important information about the cardiovascular health status of a specific person. Various methodological approaches exist to gain parameters from measured pressure and/or flow waves for the assessment of cardiovascular risk and some of the most widely used techniques and their mathematical background will be presented in this chapter.

### 2.1 Pressure pulse wave analysis

High blood pressure has been identified as a risk factor for stroke as early as 4000 years ago. Back then, the diagnosis was based on the 'hardness' of the pulse felt by palpation of superficial arteries. This diagnostic procedure did not change until the first sphygmographs were developed in the 19th century enabling the non-invasive measurement and recording of the arterial pressure pulse. [79]

Based on these sphygmographical measurements, Frederick Akbar Mahomed<sup>1</sup> was already able to describe the effects of ageing and hypertension on the shape of the radial pressure wave in the middle of the nineteenth century, thereby laying the foundation of modern pulse wave analysis. Moreover, he found that the pulse form changes during its propagation through the body, a phenomenon that was almost one hundred years later explained by McDonald<sup>2</sup> and Womersley<sup>3</sup> with the occurrence of wave reflections. [86, 87]

---

<sup>1</sup>Frederick Henry Horatio Akbar Mahomed (1849-1889), British physician

<sup>2</sup>Donald Arthur McDonald (1917-1973), British physician

<sup>3</sup>John Ronald Womersley (1907-1958), British mathematician

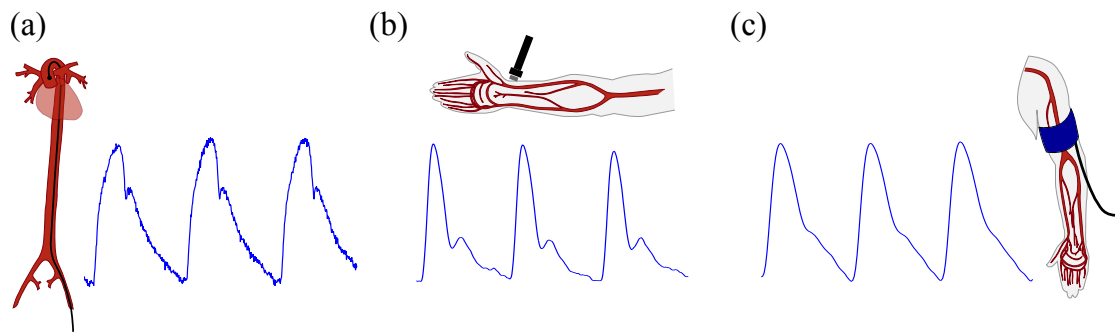


Figure 2.1: Examples of different measurement techniques to acquire arterial pressure. (a) invasive measurement of intra-aortic pressure during cardiac catheterisation, (b) non-invasive recording of radial pressure by applanation tonometry, (c) non-invasive brachial pressure reading using an oscillometric pressure cuff. Partly adapted from [59]

However, at the turn of the 20th century, the sphygmographs were replaced by cuff sphygmomanometers, which were easier to handle but provided the extreme values of pressure only. The method introduced by Riva-Rocci<sup>4</sup> in 1896 was based on the occlusion of the brachial artery by an inflatable cuff around the upper arm, a manometer to measure the pressure applied and palpation of the radial pulse to determine the inflation pressure needed for a total occlusion, which equals the maximum, systolic blood pressure. By replacing palpation by auscultation as proposed by Korotkov<sup>5</sup>, the measurement of both maximum and minimum (diastolic) blood pressure became feasible. This principle is still in use today, but also automatic devices based on oscillometric pressure cuffs evolved which determine systolic and diastolic blood pressure by measuring the oscillations in the cuff introduced by the semi-occluded artery. [79, 80]

During most parts of the 20th century, entire pressure waveforms were therefore primarily assessed invasively during cardiac catheterisation until, starting in the 1980ies, new sphygmographical techniques were developed. These include applanation tonometry, photo-plethysmography and methods based on oscillometric pressure cuffs to non-invasively record peripheral pressure waveforms [23, 79, 134], compare figure 2.1. Furthermore, the investigation of the relation of peripheral to central pressure in the frequency domain led to generalised transfer functions that enable the estimation of the central pressure wave from a peripheral reading [47, 135]. Thus, nowadays, peripheral and central pressure waves can be obtained non-invasively and be used for cardiovascular risk stratification, in line with the idea of Mahomed dating back to 1872 [86]:

”...the information which the pulse affords is of so great importance, and so often consulted, surely it must be to our advantage to appreciate fully all it tells us, and to draw from it every detail that it is capable of imparting.” [60, p. 62]

This section focuses on the computation and interpretation of parameters that can be directly derived from measurements of the arterial pressure waveform.

<sup>4</sup>Scipione Riva-Rocci (1863-1937), Italian internist

<sup>5</sup>Nikolai Sergeyewich Korotkov (1874-1920), Russian surgeon

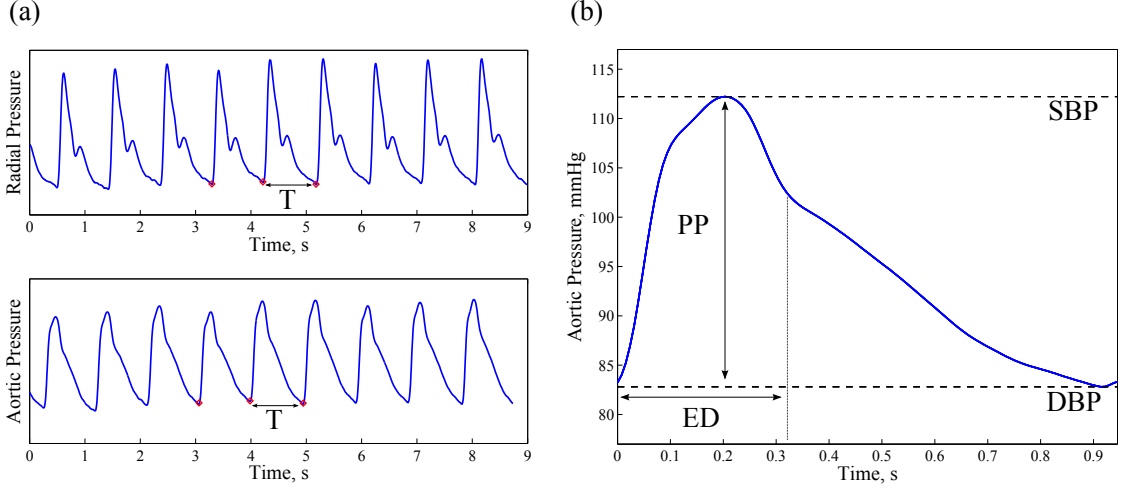


Figure 2.2: Determination of timing information and pressure levels. (a): Exemplary radial pressure signal (upper panel) assessed by applanation tonometry and the corresponding aortic pressure (lower panel) obtained by a generalised transfer function (SphygmoCor device, AtCor Medical, Sydney, Australia). The red dots indicate the feet of the pressure waves at the beginning of systolic upstroke which are used to identify single heartbeats and to compute the heartbeat duration  $T$ . (b): aortic pressure wave obtained from the measurement shown on the left by taking the average over several heartbeats (SphygmoCor). Systolic (SBP) and diastolic blood pressure (DBP) as well as the amplitude of the pressure wave, the pulse pressure (PP), are shown. By identifying the dicotic notch at the end of systole, the ejection duration (ED) can be derived.

### 2.1.1 Timing information and pressure levels

A typical pressure signal measured at the radial artery and the corresponding aortic pressure derived with a generalised transfer function are shown in figure 2.2 (a). Left ventricular ejection results in a fast increase in blood pressure and by identifying the beginning of upstroke, it is possible to discriminate single heartbeats in the signal. The heartbeat duration  $T$  is then given by the time distance between the feet of two successive pressure waves and the heart rate (HR) subsequently by  $HR = 60/T$ . The closure of the aortic valve at the end of systole is normally marked by an incisura in the pressure wave called the dicotic notch that can be used to determine the ejection duration (ED) as the time between the foot and the incisura.

The pressure wave  $P(t)$ ,  $t \in [0, T]$ , corresponding to one single heartbeat or, in order to reduce the influence of noise, the average over several heartbeats can be further analysed as shown in figure 2.2 (b). As mentioned before, the most famous measures are the maximum and minimum value. The maximum is always reached during ventricular ejection in systole and is therefore called systolic blood pressure (SBP). When ejection stops, pressure decreases until it reaches its minimum at the end of diastole, called the diastolic blood pressure (DBP). The difference between SBP and DBP equals the amplitude of the pressure wave and is termed pulse pressure (PP).

$$PP = SBP - DBP = \max_{t \in [0, T]} P(t) - \min_{t \in [0, T]} P(t) \quad (2.1)$$

PP represents the pulsatile component of pressure whereas the mean blood pressure (MBP)

corresponds to the steady part and can be computed as

$$\text{MBP} = \frac{1}{T} \int_0^T P(t) dt. \quad (2.2)$$

### 2.1.2 Parameters quantifying the propagation of the pressure pulse throughout the body

During systole, the ejecting heart generates pressure waves that propagate throughout the body and result in the characteristic pulse that is palpable at any superficial artery. The initial waves originating at the ventricle are travelling away from the heart in forward direction. At any bifurcation, any irregularity in the vessel wall or more generally discontinuity of the arterial tree, parts of these waves are reflected resulting in backward travelling waves. On the way back towards the heart, re-reflections occur, giving again rise to forward waves and so forth. The observable, measured waveforms at any arterial site are therefore composed of multiple forward and backward running waves. For this and all of the other concepts presented in this chapter, only one forward and one backward wave will be considered which represent the cumulation of all forward and backward waves respectively.

The morphology of the pressure wave thus depends on the magnitude and relative timing of both the forward and the reflected wave. To quantify the contribution of each, the so-called augmentation index (AIx) was introduced. From data obtained in invasive studies using catheters to measure pressure and flow in the ascending aorta, it was observed that peak flow corresponds to the first shoulder "defined as the first concavity on the upstroke" of the pressure wave [48, p.1654]. The first shoulder can either lay before or be equal to the maximum which implies that the corresponding pressure level  $P_1 \leq \text{SBP}$ .

Up to the first shoulder, pressure is mainly caused by blood flow and therefore directly by ventricular ejection. Due to the return of the reflected wave, this initial pressure is further increased, resulting in a second peak or shoulder  $P_2$ , where either  $P_1$  or  $P_2$  equals SBP. For  $\text{SBP} = P_2 > P_1$ , wave reflections cause an augmentation of total maximum pressure by  $P_2 - P_1$ , which is termed augmentation or augmented pressure (AP). Naturally, the magnitude of AP depends on the absolute pressure level and amplitude of a specific person and is therefore indexed to PP in order to obtain a relative and comparable measure, the augmentation index (AIx).

$$\text{AIx} = \frac{P_2 - P_1}{\text{PP}} = \frac{\text{AP}}{\text{PP}} \quad (2.3)$$

For  $\text{SBP} = P_1 > P_2$ , AIx is defined analogously, resulting in negative values of both AP and AIx without direct physiological interpretation. Depending on the value of AIx, an aortic pressure waveform can be classified as type A for  $\text{AIx} > 0.12$ , type B for  $0 < \text{AIx} \leq 0.12$  or type C for  $\text{AIx} \leq 0$  [72].

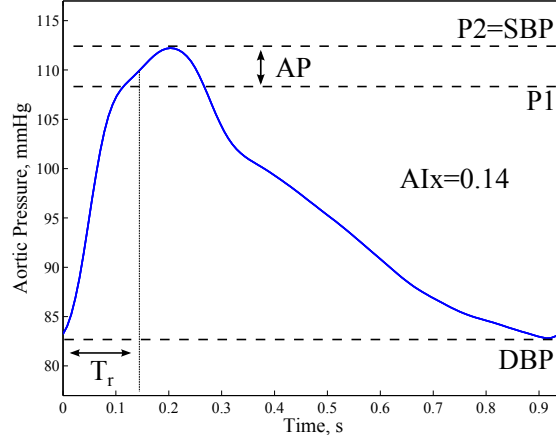


Figure 2.3: Computation of AIx. By identifying the two shoulders in the pressure signal, the corresponding pressure levels  $P_1$  and  $P_2$  can be obtained. In this case,  $P_1 < P_2$  and the returning reflected wave therefore causes an augmentation of total pressure by  $AP$ , resulting in an AIx of 0.14. The pressure wave can thus be classified as a type A waveform. The inflection point marks the return of the reflected wave, which is used to derive the round-trip travel time  $T_r$ .

The arrival of the backward wave corresponds to an inflection point in the pressure signal [83], which can be used to determine the time it takes for a wave to reach a reflection site and subsequently return to the heart, called round trip travel time  $T_r$ . Figure 2.3 shows an exemplary type A pressure wave and the corresponding pressure levels  $P_1$  and  $P_2$  as well as  $T_r$ .

For the computation of  $AP$  and  $AIx$ , commonly higher order derivatives of the pressure signal are employed. In particular, the zero-crossings of the fourth derivative can be used to detect the first or second shoulder depending on whether  $P_1$  or  $P_2$  equals SBP [20, 48, 124]. Another approach is to use the zero crossings of the second derivative to identify the inflection point and to compute  $AIx$  from the inflection pressure [114]<sup>6</sup>. Even though quantitative differences exist between these two approaches, the corresponding values of  $AIx$  were shown to be highly correlated [114]. For  $T_r$ , in contrast, differences resulting from applying the second or the fourth derivative to identify the inflection point are more pronounced [114, 143].

The round trip travel time  $T_r$  is affected by the distance to the reflection site as well as the propagation speed, the pulse wave velocity (PWV). PWV in turn depends on the properties of the vessel and the blood within as well as on the pressure level. Under some simplifying assumptions<sup>7</sup>, local PWV can be directly related to the stiffness of the arterial wall by the Moens-Korteweg equation [11].

$$PWV = \sqrt{\frac{Eh}{2\rho r_0}} \quad (2.4)$$

$E$  thereby denotes the elastic modulus of the vessel wall,  $\rho$  the blood density,  $h$  the stationary wall

<sup>6</sup>It should be noted that Segers et al. [114] did not use the mathematical definition of inflection point but defined it as the mid-point between two consecutive zero-crossings of the second derivative.

<sup>7</sup>The main assumptions include blood to be inviscous and the tube to be thin-walled. For a more detailed description of the derivation as well as the simplifications applied, see e.g. [11].



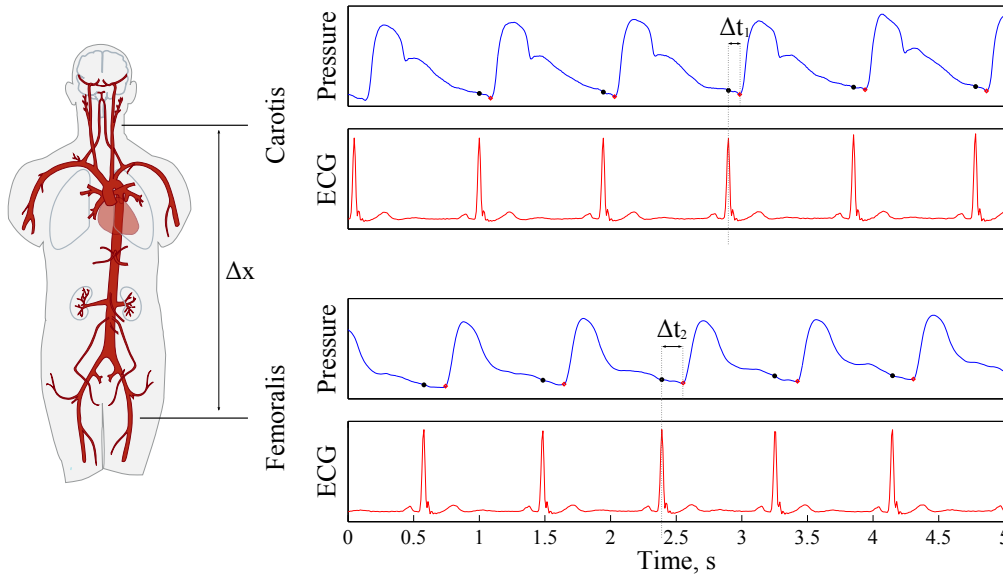


Figure 2.4: Assessment of carotid-femoral PWV using sequential pressure measurements and a simultaneous electrocardiogram (SphygmoCor). For both measurement sites, the time delay between the R-peak in the ECG (indicated by a black circle in the pressure signal) and the arrival of the foot of the pressure wave (red diamonds) are computed resulting in the total travel time  $\Delta t = \Delta t_2 - \Delta t_1$ . The corresponding travel distance  $\Delta x$  is obtained directly from the patient, either by approximating it by the total distance between the two sites as depicted in this figure, or by various other approaches accounting for the fact that the waves are actually travelling in different directions [136]. In either case, PWV is subsequently determined by  $PWV = \Delta x / \Delta t$ . Partly adapted from [59]

thickness and  $r_0$  the stationary lumen radius. According to the above relation, the propagation speed increases with arterial stiffening (increasing  $E$ ), leading to an earlier return of the reflected wave and a shift of its arrival from diastole to late systole. Consequentially, blood pressure augmentation and therefore also SBP and PP are increased. Arterial stiffening is a normal consequence of ageing, mainly affecting the large conduit arteries and in particular the aorta. Aortic PWV might be more than twice as high in old age compared to youth. However, also cardiovascular diseases can cause premature or exaggerated arterial stiffness making PWV an important indicator. [85, 86]

PWV is commonly assessed by the time delay or foot-to-foot method. For this approach, pressure is measured (simultaneously or sequentially with a simultaneous electrocardiographic recording) at two different sites and the distance between the sites is divided by the time delay between the arrival of the foot of the pressure wave at the respective sites [54], compare figure 2.4. In contrast to the Moens-Korteweg PWV, the so-obtained PWV represents the average velocity over the whole path from site A to site B.

The current gold standard in the assessment of aortic pulse wave velocity is its measurement during cardiac catheterisation. In this case, the time delay method is employed during catheter pullback with both measurement sites located in the aorta. A non-invasive alternative is given by

the carotid-femoral PWV, which uses tonometric or oscillatory pressure measurements at both the carotis and the femoralis to cover the aortic path except for the ascending aorta [138]. Even though this method is "generally accepted as the most simple, non-invasive, robust and reproducible method to determine arterial stiffness" [54, p.2591], special attention has to be laid on the estimation and measurement of the travel distance, which strongly influences the computed velocity [136, 138].

Recently, also a one-point estimate of aortic PWV based on a single oscillometric pressure reading, i.e. a reading performed at one site only, has been proposed and implemented as part of the ARCSolver method (AIT, Austrian Institute of Technology GmbH) [34]. The estimation procedure combines parameters of pulse wave analysis, age and model-based characteristic impedance, a parameter of impedance analysis which will be introduced in section 2.2. Estimated values showed acceptable agreement with invasively assessed PWV [34, 138].

The elasticity of the arterial wall characterised by the elastic modulus  $E$  in the Moens-Korteweg equation is a local property that varies throughout the body. The large conduit arteries close to the heart show the lowest values, whereas  $E$  increases in distal direction away from the heart [77]. Although radius and wall thickness are decreasing too, the term  $Eh/r_0$  was found to grow almost exponentially with decreasing  $r_0$  in the main arteries [81] resulting in a high increment of PWV according to the Moens-Korteweg equation (2.4). Exemplary values taken from a study by Wang et al. [132] predict a 1.6-fold increase in PWV from the ascending aorta to the femoral artery, if the blood density is taken to be constant  $\rho = 1060 \text{ kg/m}^3$  [143].

Invasive measurements show a similar boost in PWV towards the periphery [77]. Moreover, the length of the arteries decreases and the branching increases away from the heart leading to shorter distances to the reflection sites. As a result, reflected waves return much earlier during the cycle in the peripheral than in the central arteries, amplifying both systolic and pulse pressure [54]. This phenomenon can be quantified by the ratio of peripheral to central PP, the pulse pressure amplification (PPAmp).

$$\text{PPAmp} = \frac{\text{peripheral PP}}{\text{central PP}} \quad (2.5)$$

PPAmp is highest in young ages, when aortic PWV is low and the pressure augmentation mainly occurs during diastole. With age and stiffening of the central arteries, central PP increases and the amplification diminishes. [77, 85]

### 2.1.3 Pressure time integrals and wasted energy

Pressure time integrals or indices represent different areas under the pressure curve obtained by integration over a specific time interval. The systolic pressure time index (SPTI), as the name

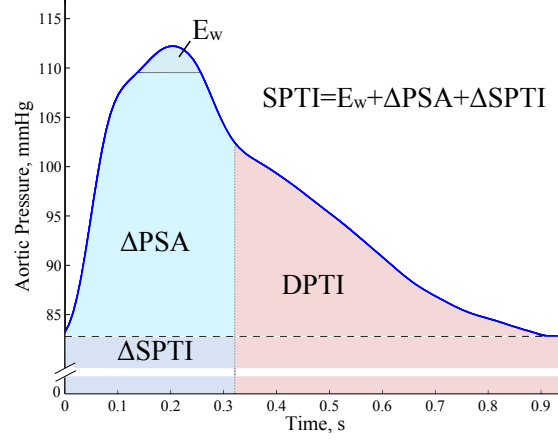


Figure 2.5: Computation of the time indices representing the areas under different portions of the pressure wave. The systolic index (SPTI) can furthermore be separated in the area below DBP ( $\Delta\text{SPTI}$ ) and, if the inflection point occurs before the maximum as depicted in this figure, the area below ( $\Delta\text{PSA}$ ) and above the inflection point ( $E_w$ ).

already suggests, represents the integral of  $P$  over systole

$$\text{SPTI} = \int_0^{t_s} P(t) dt, \quad (2.6)$$

where  $t_s$  denotes the time of the end of systole. SPTI is also called tension time index and is supposed to be directly related to the cardiac oxygen demand [29], since the pressure developed during cardiac ejection greatly affects the cardiac workload. Due to an early return of reflected waves during systole, as observed in type-A and type-B waveforms, the left ventricular afterload is augmented and additional energy is required for blood ejection. In line with the concepts introduced in the last section, this wasted effort  $E_w$  can be estimated by the portion of systolic pressure above the inflection point [39].

Hence, SPTI can be separated into the rectangular area below DBP denoted as  $\Delta\text{SPTI} = \text{DBP} \cdot \text{ED}$  and the area above DBP called pressure systolic area (PSA). If the inflection point occurs before the maximum, PSA can be further subdivided into the area below ( $\Delta\text{PSA}$ ) and above the inflection point ( $E_w$ ). [21]

The diastolic pressure time index (DPTI) denotes the corresponding area under the diastolic part of the pressure wave

$$\text{DPTI} = \int_{t_s}^T P(t) dt, \quad (2.7)$$

and is related to coronary blood flow. Coronary perfusion, particularly with regards to the left heart, mainly occurs during diastole when the heart is relaxed. Driven by a pressure gradient, the blood is pushed into the myocardium and DPTI provides an estimate of this perfusion gradient. The ratio of DPTI to SPTI finally represents an index of coronary perfusion termed myocardial

viability ratio, that indicates if the cardiac oxygen demand is met by the supply. [12]

## 2.2 Impedance analysis

Modern arterial haemodynamics started with the work of McDonald and Womersley describing the propagation of waves in the arterial system in the frequency domain. Based on the (non-linear) Navier-Stokes equations, Womersley formulated the mathematical conditions needed for linearisation<sup>8</sup> [156]. Thereby he showed that nonlinearities are negligible in larger arteries in a first approximation under most pathophysiological conditions. These theoretical considerations were later corroborated by experimental results [76], justifying the assumption of linearity. If the arterial system is furthermore assumed to be in steady state, i.e. a regularly beating heart with both pressure and flow being periodic functions, it can be completely characterised by the ratio of pressure to flow at the inlet of the system in the frequency domain using Fourier analysis [6]. Referring to electrical engineering, this transfer function is called arterial or input impedance  $Z_{in}$ .

Based on this concept, a method to separate measured aortic waveforms in their forward and backward travelling components, called wave separation analysis (WSA), was introduced by Westerhof and coworkers in 1972 [148] and will be presented in the following sections.

### 2.2.1 Fourier analysis and input impedance

The real-valued, periodic, time-varying functions of both pressure  $P(t)$  and flow  $Q(t)$  can be represented by their Fourier series<sup>9</sup>

$$P(t) = \bar{P} + \sum_{n=1}^{\infty} (a_n \cos(\omega_n t) + b_n \sin(\omega_n t)),$$

$$Q(t) = \bar{Q} + \sum_{n=1}^{\infty} (c_n \cos(\omega_n t) + d_n \sin(\omega_n t)),$$

with  $a_n, b_n, c_n, d_n \in \mathbb{R}$  denoting the real Fourier coefficients defined by

$$a_n := \frac{2}{T} \int_0^T P(t) \cos(\omega_n t) dt, \quad b_n := \frac{2}{T} \int_0^T P(t) \sin(\omega_n t) dt, \quad (2.8)$$

$$c_n := \frac{2}{T} \int_0^T Q(t) \cos(\omega_n t) dt, \quad d_n := \frac{2}{T} \int_0^T Q(t) \sin(\omega_n t) dt. \quad (2.9)$$

The angular frequency  $\omega_n$  is given by  $\omega_n = n \frac{2\pi}{T}$  and  $T$  denotes the period, i.e. the heartbeat duration.  $\bar{P}$  and  $\bar{Q}$  are the zero-frequency coefficients and represent the mean, steady components

<sup>8</sup>The main assumptions include (1) blood to be a homogenous, incompressible, Newtonian fluid with constant viscosity (2) the arteries to be circular and axisymmetric and (3) the wavelength of the considered pressure and flow waves to be much larger than the radius of the tube, as well as the mean flow velocity to be much smaller than the pulse wave velocity, see [156] for details.

<sup>9</sup>Natural signals are generally smooth functions, in other words it can be assumed that  $P$  and  $Q$  are at least continuously differentiable implying that the Fourier series converges uniformly.

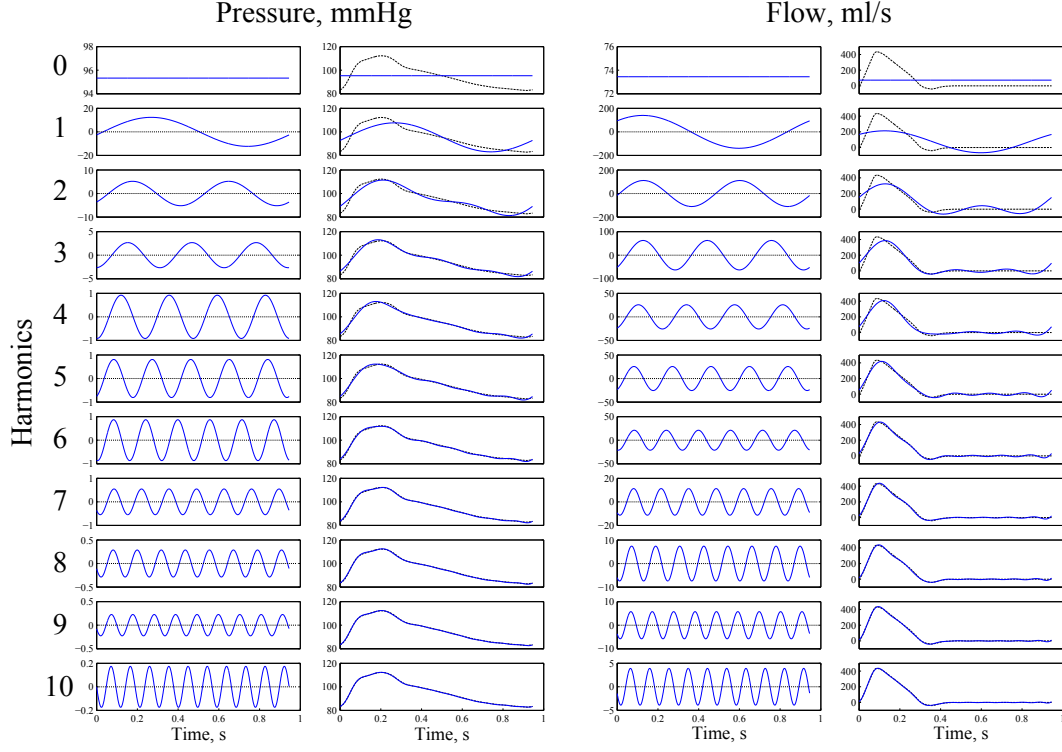


Figure 2.6: Fourier decomposition and approximation of aortic pressure and flow for the first 10 harmonics. The single sinusoids for harmonics 0-10 are shown in the respective left panel and the waveforms corresponding to the sum of all preceding harmonics (blue solid line) as well as the original measured ones (black, dashed line) in the respective right panel.

of pressure and flow respectively

$$\bar{P} := \frac{1}{T} \int_0^T P(t) dt, \quad (2.10)$$

$$\bar{Q} := \frac{1}{T} \int_0^T Q(t) dt. \quad (2.11)$$

Thus in particular it holds that  $\bar{P} = \text{MBP}$ . For each harmonic describing the oscillations with a frequency equal to an integer multiple of the fundamental frequency  $1/T$ , the corresponding real coefficients can be summarised in the following complex coefficients

$$\hat{P}_n := a_n - ib_n, \quad \hat{Q}_n := c_n - id_n, \quad (2.12)$$

which are also referred to as complex amplitude or phasor.

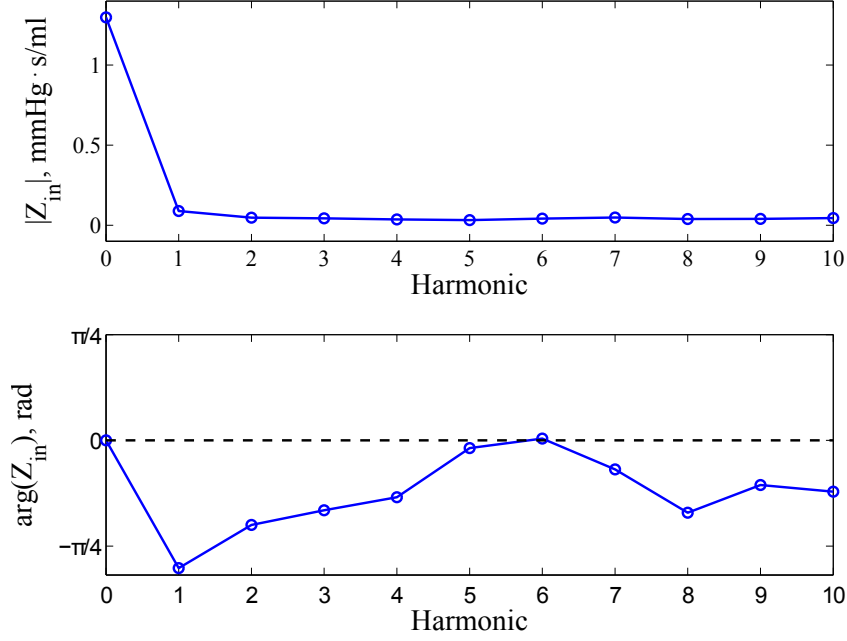


Figure 2.7: Modulus (upper panel) and phase (lower panel) of the arterial input impedance computed from the flow and pressure waves shown in figure 2.6 for the first 10 harmonics.

In this notation, the Fourier series representations are given by

$$P(t) = \bar{P} + \operatorname{Re} \left( \sum_{n=1}^{\infty} \hat{P}_n e^{i\omega_n t} \right) = \bar{P} + \sum_{n=1}^{\infty} |\hat{P}_n| \cos \left( \omega_n t + \arg(\hat{P}_n) \right), \quad (2.13)$$

$$Q(t) = \bar{Q} + \operatorname{Re} \left( \sum_{n=1}^{\infty} \hat{Q}_n e^{i\omega_n t} \right) = \bar{Q} + \sum_{n=1}^{\infty} |\hat{Q}_n| \cos \left( \omega_n t + \arg(\hat{Q}_n) \right), \quad (2.14)$$

where  $i$  denotes the imaginary unit,  $\operatorname{Re}(\cdot)$  the real part and  $\arg(\cdot)$  the argument of a complex number. For measured pressure and flow signals, where the continuous functions  $P(t)$  and  $Q(t)$  are represented by a discrete sequence of  $N$  equidistant data points per heartbeat depending on the sampling rate  $dt$ ,  $\hat{P}_n$  and  $\hat{Q}_n$  for the harmonics  $n = 1, \dots, \lfloor (N-1)/2 \rfloor$  can easily be obtained by applying the fast Fourier transform. To reconstruct the original signal, usually the first 10-15 harmonics are sufficient [90, 123], compare figure 2.6.

Introducing the notation  $\hat{P}_0 = \bar{P}$  and  $\hat{Q}_0 = \bar{Q}$ , the input impedance  $Z_{in}(\omega_n)$  is now defined by

$$Z_{in}(\omega_n) = \frac{\hat{P}_n}{\hat{Q}_n}, \quad n \geq 0. \quad (2.15)$$

Figure 2.7 shows an example of  $Z_{in}$  obtained from measured pressure and flow. The zeroth frequency component of  $Z_{in}$  equals the ratio of mean pressure to mean flow and represents the systemic vascular resistance (SVR) or, in other words, the total resistance the vasculature opposes to flow.

### 2.2.2 Wave separation analysis

For the approach of wave separation analysis, the arterial system is considered a network of elastic tubes transmitting the waves generated by the left ventricle to the periphery. The system is assumed to be linear, implying that "a single sinusoid of flow as input produces a sinusoid of pressure as output with identical frequency and with a phase shift" [6, p.150]. Therefore each harmonic of pressure and flow can be treated separately and concepts of linear transmission line theory can be applied. In this framework, pressure corresponds to voltage and flow to current. [148]

For the following analysis, only the oscillatory components and therefore the coefficients for  $n \geq 1$  will be considered while the mean parts are omitted. In the reflectionless case, e.g. for an infinitely long, uniform tube, the ratio of pressure to flow is the same at any instance and at any location along the tube and is given by the frequency-dependent characteristic impedance  $Z_0(\omega_n) = \frac{\hat{P}_n}{\hat{Q}_n}$ ,  $n \geq 1$ .  $Z_0(\omega_n)$  is determined by the (cross-sectional) geometry and material properties of the tube and the blood within and is independent of its actual length [113].

Generally,  $Z_0$  is a complex quantity, meaning that pressure and flow waves differ not only in their amplitude but are also shifted in phase, i.e. a time delay occurs. However, for lossless tubes (tubes without friction),  $Z_0(\omega_n)$  is a real, frequency-independent constant  $Z_c$ . In this case, pressure and flow are in phase, have the same overall shape and, because no reflections occur, equal the incident (superscript  $i$ ), forward (superscript  $f$ ) waves generated at the inlet.

$$\hat{P}_n = \hat{P}_n^f = \hat{P}_n^i, \quad \hat{Q}_n = \hat{Q}_n^f = \hat{Q}_n^i$$

In particular, this implies that  $Z_{in}(\omega_n) = Z_0(\omega_n) = Z_c$ .

When the uniform tube is finite in length and loaded with an impedance  $Z_L(\omega_n)$  at the end, parts of the forward running waves are reflected according to the pressure reflection coefficient  $\Gamma = \frac{Z_L - Z_0}{Z_L + Z_0}$ .  $\Gamma$  defines the ratio of backward to forward pressure with an absolute value between 0, no reflections, and 1, total reflection. The reflection coefficient of flow has the same magnitude but opposite sign, i.e. equals  $-\Gamma$ . In either case, because of the presumed linearity, the total waveforms at the inlet of the tube are given by the superposition of the composite forward and backward (superscript  $b$ ) travelling waves. [148]

$$\hat{P}_n = \hat{P}_n^f + \hat{P}_n^b, \quad \hat{Q}_n = \hat{Q}_n^f + \hat{Q}_n^b \quad (2.16)$$

Due to the reflections,  $Z_{in}$  no longer equals  $Z_0$ . However, looking at the forward and backward waves separately, they can be interpreted as single waves, travelling undisturbedly through the tube and their relation is therefore again given by

$$\frac{\hat{P}_n^f}{\hat{Q}_n^f} = Z_0(\omega_n) = -\frac{\hat{P}_n^b}{\hat{Q}_n^b}. \quad (2.17)$$

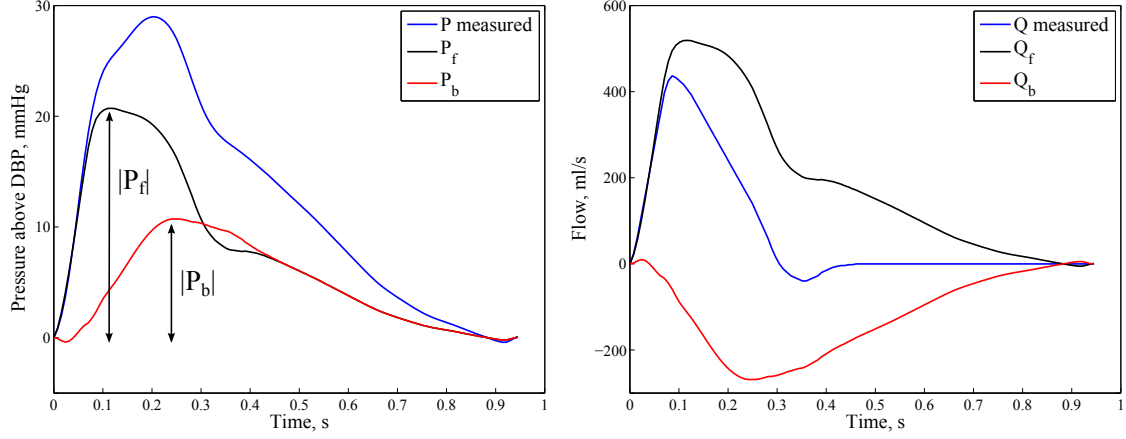


Figure 2.8: Aortic pressure and flow separated in their forward (black) and backward (red) components using wave separation analysis. For illustration,  $P_{f,b}$  and  $Q_{f,b}$  were shifted to start at 0.  $Z_c$  was estimated in the frequency domain using harmonics 4-10.

The negative sign on the right side results from the fact that flow waves are reflected 180 degrees out of phase compared to pressure waves, as already mentioned before.

In the context of the arterial system, the tube represents a short, presumably uniform segment of the ascending aorta and  $Z_L$  the impedance of the branching arterial tree further downstream [148]. Jager and colleagues [43] showed that losses due to friction are very small for large, conduit arteries. Aortic  $Z_0(\omega_n)$  can therefore be regarded a real constant  $Z_c$  [148]. This simplification implies that both the viscosity of the blood as well as the viscoelasticity of the arterial wall are neglected [149].

From equations (2.16) and (2.17), the following expression can be derived for the forward travelling aortic pressure wave  $\hat{P}_n^f$

$$\begin{aligned}\hat{P}_n^f &= \hat{P}_n - \hat{P}_n^b = \hat{P}_n + Z_c \hat{Q}_n^b = \\ &= \hat{P}_n + Z_c (\hat{Q}_n - \hat{Q}_n^f) = \hat{P}_n + Z_c \hat{Q}_n - \hat{P}_n^f,\end{aligned}$$

and hence

$$\hat{P}_n^f = \frac{\hat{P}_n + Z_c \hat{Q}_n}{2}. \quad (2.18)$$

Analogous computations yield

$$\hat{P}_n^b = \frac{\hat{P}_n - Z_c \hat{Q}_n}{2}, \quad \hat{Q}_n^f = \frac{\hat{P}_n + Z_c \hat{Q}_n}{2Z_c}, \quad \hat{Q}_n^b = -\frac{\hat{P}_n - Z_c \hat{Q}_n}{2Z_c}. \quad (2.19)$$

The corresponding temporal waveforms  $P_{f,b}(t)$ ,  $Q_{f,b}(t)$  can be recovered from the Fourier series, see (2.13,2.14). Moreover, since  $Z_c$  is real, the separation can also be performed directly in the



time domain, as exemplarily presented for  $P_f(t)$  below.

$$\begin{aligned} P_f(t) &= \sum_{n=1}^{\infty} \operatorname{Re} \left( \left( \frac{\hat{P}_n + Z_c \hat{Q}_n}{2} \right) e^{i\omega_n t} \right) \\ &= \frac{1}{2} \sum_{n=1}^{\infty} \operatorname{Re} \left( \hat{P}_n e^{i\omega_n t} \right) + \frac{Z_c}{2} \sum_{n=1}^{\infty} \operatorname{Re} \left( \hat{Q}_n e^{i\omega_n t} \right) = \\ &= \frac{(P(t) - \bar{P}) + Z_c (Q(t) - \bar{Q})}{2} \end{aligned}$$

Figure 2.8 shows an exemplary aortic pressure and flow wave and the corresponding forward and backward waves obtained by WSA. To actually quantify the reflections present in the system, the amplitudes of  $P_f$  and  $P_b$  can be computed

$$|P_{f,b}| = \max_{t \in [0, T]} P_{f,b}(t) - \min_{t \in [0, T]} P_{f,b}(t). \quad (2.20)$$

Relative measures can be obtained by determining the reflection magnitude (RM) and the reflection index (RI), which are defined by

$$\text{RM} = \frac{|P_b|}{|P_f|}, \quad (2.21)$$

$$\text{RI} = \frac{|P_b|}{|P_f| + |P_b|}. \quad (2.22)$$

In summary, the total (measured) waveforms of pressure and flow at the aortic root can be separated in their forward and backward components if only aortic characteristic impedance is known. In order to obtain an estimate of  $Z_c$ , different approaches have been suggested, two of which will be introduced in the following section.

### 2.2.3 Estimating aortic characteristic impedance

The first approach is based in the frequency domain and its explanation will follow the one given by Westerhof et al. [144]. Measurements of the reflection coefficients encountered by forward travelling waves at the branching points in larger arteries were found to be "mostly in the order of 0.1 or smaller, approximately real, and only slightly frequency dependent" [144, p.139]. These values increase up to 0.5 in the periphery, meaning that reflections mainly occur in the more peripheral arteries. For backward travelling waves, the reflection coefficients attain much higher values, implying that reflected waves lose much of their amplitude on their way back to the heart.

Furthermore, the way how reflected waves interact with the incident waves depends on the distance to the reflection site relative to the wavelength  $\lambda$ , which is given by the phase velocity divided by the frequency. For low frequencies, i.e. below 3 Hz,  $\lambda$  is long and the waves reach the periphery and return to the heart during one cycle. Therefore, they add in phase amplifying incident pressure. Higher frequency components, in contrast, are reflected at different instances of different cycles. Thus, on the one hand, the large backward reflection coefficients greatly

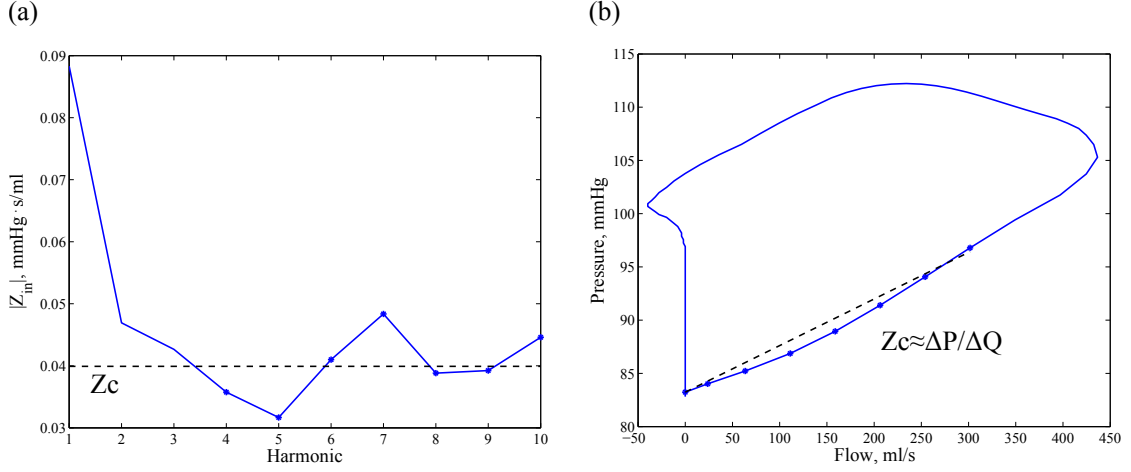


Figure 2.9: Estimation of aortic characteristic impedance. (a) average of the modulus of input impedance for harmonics 4-10 (indicated by stars), (b) slope of the  $PQ$ -loop in early systole assessed from the first 8 data-points  $\approx 55$ ms (indicated by stars).

diminish their magnitude and on the other hand, they tend to cancel out when superimposed on their way back towards the heart. In consequence, almost no reflections of higher frequency waves are present in the ascending aorta and arterial input impedance should therefore approximate aortic characteristic impedance  $Z_c$ .

The characteristic pattern of the modulus of arterial input impedance with frequency observed in humans indeed corresponds well with this concept, see figure 2.9 (a). Starting at its maximum value,  $|Z_{in}|$  rapidly decreases and then oscillates around an approximately constant value, while its phase approaches 0 for increasing frequency [6]. Thus, to obtain an estimate of  $Z_c$ ,  $|Z_{in}|$  is averaged over an appropriate frequency band to eliminate the influence of oscillations [24].

For the second approach, this concept is translated to the time domain. At the beginning of ventricular ejection, both pressure and flow show a rapid upstroke which can be predominantly attributed to the high-frequency components. Their relation should therefore be given by the characteristic impedance [24]. Plotting pressure over flow indeed shows an almost linear relationship during early systole, the slope of which can be used to estimate  $Z_c$ , i.e.  $Z_c \approx \Delta P / \Delta Q$  compare figure 2.9 (b). Values obtained with this estimation procedure were shown to correspond well with their counterparts determined in the frequency domain [24].

Another explanation to use the relation between pressure and flow in early systole is that during this phase reflections have not yet returned and both pressure and flow are therefore composed of forward travelling waves only. The ratio of their slopes should thus approximate  $Z_c$ , i.e.  $Z_c \approx \frac{dP}{dt} / \frac{dQ}{dt}$  [149]. An overview and comparison of different time-domain estimates can be found in a study by Lucas et al. [58].

## 2.3 Windkessel models

Windkessel models belong to the most simple class of cardiovascular models, namely the 0-D models. Thus, in contrast to the wave transmission approach introduced in the previous section, space and therefore also wave travel phenomena are not considered. The properties of the arterial tree are lumped into single parameters and the whole arterial system is modelled as one compartment. Despite their simplicity, they are useful tools to study the dynamic relation between pressure and flow requiring only a few and, what is even more important, physiological meaningful parameters. [145]

Windkessel models owe their name to the so-called Windkessel-effect, which describes the damping and smoothing of pulsatile flow caused by a reservoir coupled in between the pump and the outflow. In the cardiovascular system, the heart represents the pulsatile pump whereas the large elastic arteries and in particular the aorta constitute the reservoir. During left ventricular ejection, their walls expand, thereby storing blood which is released again during diastole when pressure decreases and the walls constrict.

The first mathematical model based on this concept was developed by Otto Frank in 1899 [28] and consisted of only two parameters. Nowadays, various extensions of this initial two-element Windkessel exist and two of them will be introduced in the next sections.

### 2.3.1 Two-element Windkessel

In the original two-element formulation, the arterial system is characterized by the contained blood volume  $V(t)$  and the two parameters peripheral resistance  $R_p$  and arterial compliance  $C_a$ .  $R_p$  represents the resistances to blood flow of all vessels in the system added up to a single value, with the biggest contribution coming from the small peripheral arteries and arterioles.  $C_a$  is a measure of arterial distensibility and therefore mainly characterises the large elastic arteries.

To obtain the model equations, the arterial system is considered a conservative compartment with only one inflow and one outflow. Changes in  $V(t)$  must therefore equal the difference between the blood flow entering the system from the heart  $Q(t)$  and the blood flow out of the system to the periphery  $Q_{out}(t)$ .

$$\frac{dV}{dt}(t) = Q(t) - Q_{out}(t) \quad (2.23)$$

Because the system is distensible, changes in volume are furthermore related to changes in pressure  $P_{RC}(t)$ . Under the assumption of linear-elasticity, this relation can be characterized by the constant factor  $C_a$ ,

$$C_a = \frac{dV}{dP_{RC}}. \quad (2.24)$$

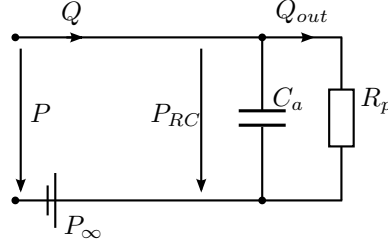


Figure 2.10: Representation of the two-element Windkessel model as an electrical circuit. Pressure  $P$  thereby corresponds to voltage and blood flow  $Q$  to current flow. The two parameters  $R_p$  and  $C_a$  are represented by a resistor and capacitor respectively,  $P_\infty$  by a voltage source.

Together with equation (2.23), this leads to

$$Q - Q_{out} = \frac{dV}{dt} = \frac{dV}{dP_{RC}} \frac{dP_{RC}}{dt} = C_a \frac{dP_{RC}}{dt}. \quad (2.25)$$

According to the hydraulic equivalent of Ohm's law, outflow  $Q_{out}$  can be related to pressure  $P_{RC}$  via the resistance  $R_p$ ,

$$P_{RC} = R_p Q_{out}. \quad (2.26)$$

Combining equations (2.25) and (2.26) yields the following linear ordinary differential equation (ODE) for the pressure  $P_{RC}$ .

$$\frac{dP_{RC}}{dt}(t) + \frac{1}{R_p C_a} P_{RC}(t) = \frac{1}{C_a} Q(t) \quad (2.27)$$

Total aortic pressure  $P(t)$  is then given by  $P(t) = P_{RC}(t) + P_\infty$ , where  $P_\infty$  represents an asymptotic pressure level that is maintained by the vascular system even without excitation from the heart. However, disunity exists about the interpretation of  $P_\infty$  and whether it should be included or not. Its impact on the Windkessel models is discussed in more detail in Appendix A.

Figure 2.10 shows an electrical analogue representation of the two-element Windkessel model and the mathematical definition is given below.

**Windkessel model.** *2-element Windkessel (WK2)*

For  $R_p, C_a > 0$  and  $P_\infty \geq 0$ , the dynamic relation between aortic pressure  $P(t)$  and flow  $Q(t)$  is modelled as

$$P(t) = P_{RC}(t) + P_\infty, \quad (2.28)$$

$$\frac{dP_{RC}}{dt}(t) = \frac{1}{C_a} Q(t) - \frac{1}{R_p C_a} P_{RC}(t). \quad (2.29)$$

If the system is furthermore assumed to be in steady state, the described input impedance as defined in (2.15) can easily be derived from the model equations when bearing in mind that the Fourier transform is linear and that the Fourier coefficients (2.12) of the first derivative equal

$i\omega_n$  times the original ones. Thus, from equation (2.29) it follows that

$$i\omega_n \hat{P}_{RC,n} = \frac{1}{C_a} \hat{Q}_n - \frac{1}{R_p C_a} \hat{P}_{RC,n} \Rightarrow \hat{P}_{RC,n} = \frac{R_p}{1 + i\omega_n R_p C_a} \hat{Q}_n, \quad n \geq 0 \quad (2.30)$$

whereby the zero-frequency component ( $n = 0$ ) denotes the respective mean value, e.g.  $\hat{Q}_0 = \bar{Q}$ .  $P_{RC}$  fully describes the dynamic, oscillatory behaviour of  $P$  whereas  $P_\infty$  affects the steady part only<sup>10</sup>, i.e. in particular  $\hat{P}_n = \hat{P}_{RC,n}$  for  $n \geq 1$  and  $\bar{P} = \bar{P}_{RC} + P_\infty$  for  $n = 0$ , see equation (2.28). Hence, the input impedance can be computed as:

$$Z_{in,WK2}(\omega_n) = \begin{cases} \frac{\bar{P}}{\bar{Q}} = \frac{\bar{P}_{RC} + P_\infty}{\bar{Q}} = \frac{\hat{P}_{RC,0}}{\hat{Q}_0} + \frac{P_\infty}{\bar{Q}} = R_p + \frac{P_\infty}{\bar{Q}}, & n = 0 \\ \frac{\hat{P}_n}{\hat{Q}_n} = \frac{\hat{P}_{RC,n}}{\hat{Q}_n} = \frac{R_p}{1 + i\omega_n R_p C_a}, & n \geq 1 \end{cases} \quad (2.31)$$

### 2.3.2 Three- and four-element Windkessel

Comparison of the input impedance modelled by the WK2 (2.31) with measured data showed a good agreement in the low frequency range. However, as discussed in the last section, the arterial system behaves almost like a uniform, reflectionless tube for higher frequencies with  $|Z_{in}(\omega_n)| \approx Z_c$ , whereas  $\lim_{n \rightarrow \infty} |Z_{in,WK2}(\omega_n)| = 0$ . The two-element Windkessel therefore fails to describe the arterial input impedance over the whole frequency range.

The Windkessel theory, which assumes that all changes in pressure happen instantaneously throughout the arterial system (infinite pulse wave velocity) and the wave transmission models or more precisely the reflectionless tube model (finite pulse wave velocity) have long been considered contradictory. However, Westerhof et al. [144] and later Quick et al. [104] showed that they cover different frequency ranges. While  $Z_{in}(\omega_n) = Z_c$  for  $n \geq 1$  (uniform, infinitely long tube) provides a poor description for lower frequencies, the WK2 reveals its weaknesses in the medium to high frequency range, which become evident as a slow upstroke in the beginning of systole in the time domain, see figure 2.12. Therefore, Westerhof proposed adding aortic characteristic impedance  $Z_c$  as a third element to the WK2, in an attempt to unify these two competing concepts [104].

$Z_c$  enters the model as an additional resistance coupled in series with the  $RC$ -component, as shown in fig. 2.11, whereby the ODE for  $P_{RC}$  remains unaltered. The resulting model equations are given in the following definition.

#### Windkessel model. 3-element Windkessel (WK3)

For  $R_p, C_a > 0$  and  $Z_c, P_\infty \geq 0$  the dynamic relation between aortic pressure  $P(t)$  and flow  $Q(t)$

<sup>10</sup>From  $\frac{dP}{dt} = \frac{dP_{RC}}{dt}$  it follows that  $i\omega_n \hat{P}_n = i\omega_n \hat{P}_{RC,n}$  and therefore  $\hat{P}_n = \hat{P}_{RC,n}$  for  $i\omega_n \neq 0 \Leftrightarrow n \neq 0$ .

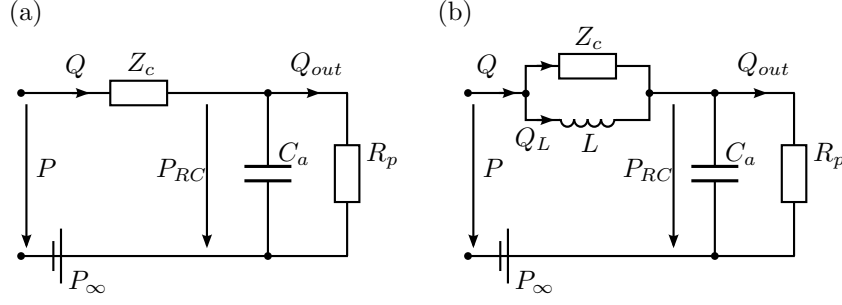


Figure 2.11: Representation of the three- (a) and four-element Windkessel model (b) as electrical circuits. The characteristic impedance  $Z_c$  is modelled as a resistor in series with the RC-component, arterial inertia  $L$  by an inductor in parallel with  $Z_c$ .

is modelled as

$$P(t) = Z_c Q(t) + P_{RC}(t) + P_\infty, \quad (2.32)$$

$$\frac{dP_{RC}}{dt}(t) = \frac{1}{C_a} Q(t) - \frac{1}{R_p C_a} P_{RC}(t). \quad (2.33)$$

From equation (2.32), the steady component of pressure can be computed as  $\bar{P} = Z_c \bar{Q} + \bar{P}_{RC} + P_\infty$ , while the dynamic behaviour is determined by  $Z_c Q + P_{RC}$ . The input impedance modelled by the WK3 is therefore given by:

$$Z_{in,WK3}(\omega_n) = \begin{cases} \frac{\bar{P}}{\bar{Q}} = \frac{Z_c \bar{Q} + \bar{P}_{RC} + P_\infty}{\bar{Q}} = Z_c + R_p + \frac{P_\infty}{\bar{Q}}, & n = 0 \\ \frac{\hat{P}_n}{\hat{Q}_n} = \frac{Z_c \hat{Q}_n + \hat{P}_{RC,n}}{\hat{Q}_n} = Z_c + \frac{R_p}{1 + i\omega_n R_p C_a}, & n \geq 1 \end{cases} \quad (2.34)$$

The inclusion of  $Z_c$  indeed diminishes the high frequency error as  $\lim_{n \rightarrow \infty} |Z_{in,WK3}(\omega_n)| = Z_c$  and the temporal waveforms of modelled pressure show a faster systolic upstroke and a better correspondence to measured data [145], compare figure 2.12. However,  $Z_c$  is technically a wave resistance that describes the relation of the oscillatory components of pressure and flow only. Representing it as a resistor also alters the low and in particular the zeroth frequency component of  $Z_{in}$ , see equation (2.34). As a consequence, the WK3 was found to overestimate  $C_a$  and to underestimate  $Z_c$  in parameter identification studies [115, 145].

Burattini and Gnudi therefore proposed the inclusion of an inductance  $L$  in parallel with  $Z_c$ , as shown in figure 2.11, resulting in the (parallel) four-element Windkessel model WK4p [13]. Initially,  $L$  was considered solely an additional degree of freedom, which improved the accuracy of the fitted parameters but was lacking a direct physical interpretation. However, Stergiopoulos and coworkers were able to demonstrate that  $L$  indeed represents the local arterial inertances added up to a single value and therefore termed it total arterial inertance [119].

By including  $L$ , inertial effects are taken into account, relating pressure to an acceleration or de-

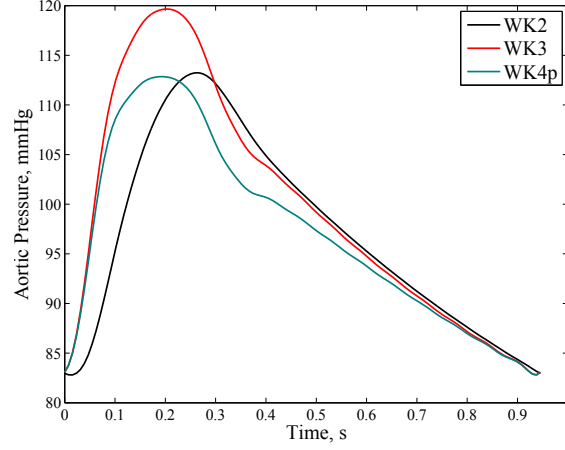


Figure 2.12: Comparison of the aortic pressure waves modelled by the three different Windkessel models. A typical flow curve shown in figure 2.8 was taken as input and the same parameters were used for all three models.

celeration of blood. To derive the model equations of this four-element Windkessel, the auxiliary quantity  $P_{LZ}$  describing the pressure at the LZ-component is introduced. If the flow through  $L$  is denoted by  $Q_L$  the following relations hold according to Kirchoff's circuit laws.

$$P_{LZ} = L \frac{dQ_L}{dt}$$

$$P_{LZ} = Z_c(Q - Q_L)$$

From the first equation, an expression for  $\frac{dQ_L}{dt}$  can be obtained, which, when plugged in the time derivative of the second equation, yields the following ODE for  $P_{LZ}$ .

$$\frac{dP_{LZ}}{dt} = Z_c \frac{dQ}{dt} - \frac{Z_c}{L} P_{LZ} \quad (2.35)$$

The model equations of the WK4p therefore consist of two ODEs, namely one for  $P_{RC}$  (2.27) and one for  $P_{LZ}$  (2.35). Exemplary solutions for both are shown in figure 2.13.

#### Windkessel model. $WK4p$

For  $R_p, C_a, L, Z_c > 0$  and  $P_\infty \geq 0$ , the relation between aortic pressure  $P(t)$  and flow  $Q(t)$  is modelled as

$$P(t) = P_{RC}(t) + P_{LZ}(t) + P_\infty, \quad (2.36)$$

$$\frac{dP_{LZ}}{dt}(t) = Z_c \frac{dQ}{dt}(t) - \frac{Z_c}{L} P_{LZ}(t), \quad (2.37)$$

$$\frac{dP_{RC}}{dt}(t) = \frac{1}{C_a} Q(t) - \frac{1}{R_p C_a} P_{RC}(t). \quad (2.38)$$

From equation (2.37), the following relation between the Fourier coefficients of  $P_{LZ}$  and  $Q$  can

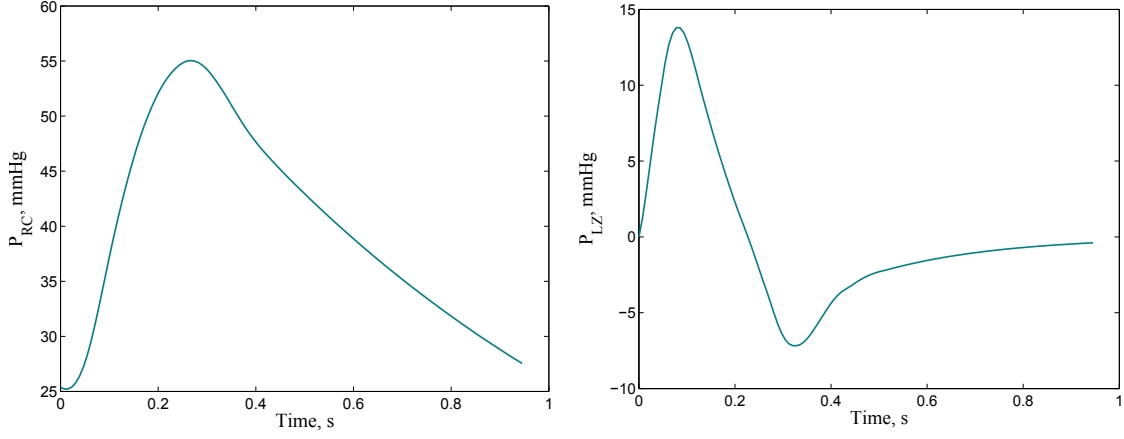


Figure 2.13:  $P_{RC}$  (left) and  $P_{LZ}$  (right) as components of the pressure modelled by the parallel 4-element Windkessel (WK4p) shown in figure 2.12.

be derived:

$$\hat{P}_{LZ,n} = \frac{i\omega_n Z_c L}{i\omega_n L + Z_c} \hat{Q}_n \quad (2.39)$$

The modelled input impedance is thus given by:

$$Z_{in,WK4p}(\omega_n) = \begin{cases} \frac{\bar{P}}{\bar{Q}} = \frac{\hat{P}_{RC,0} + \hat{P}_{LZ,0} + P_\infty}{\bar{Q}} = R_p + \frac{P_\infty}{\bar{Q}}, & n = 0 \\ \frac{\hat{P}_n}{\hat{Q}_n} = \frac{\hat{P}_{RC,n} + \hat{P}_{LZ,n}}{\hat{Q}_n} = \frac{R_p}{1 + i\omega_n R_p C_a} + \frac{i\omega_n Z_c L}{i\omega_n L + Z_c}, & n \geq 1 \end{cases} \quad (2.40)$$

From the above equation it can be seen that  $Z_c$  no longer affects  $Z_{in,WK4p}(0)$  while it is still fulfilled that  $\lim_{n \rightarrow \infty} |Z_{in,WK4p}| = Z_c$ . Thus, the WK4p "switches" between the WK2 in the low-frequency range and the WK3 in the high-frequency range thereby unifying the advantages of both. Moreover, it holds that  $Z_{in,WK4p} \rightarrow Z_{in,WK3}$  for  $L \rightarrow \infty$  and  $Z_{in,WK4p} = Z_{in,WK2}$  for  $L = 0$ . A comparison of the input impedances described by the different Windkessel models is given in figure 2.14.

### 2.3.3 Diastolic decay

During diastole, the aortic valve is closed and therefore  $Q(t) \equiv 0$ . In this phase, the ODEs for both  $P_{RC}$  (2.27) and  $P_{LZ}$  (2.35) become homogeneous, describing an exponential decay with time constants  $R_p C_a$  and  $L/Z_c$  respectively. The resulting diastolic pressure drop modelled by the WK2 and WK3 is given in equation (2.41) and that by WK4p in equation (2.42).

$$P_{dias}(t) = P_{RC}(t_s) \exp\left(\frac{t_s - t}{R_p C_a}\right) + P_\infty \quad (2.41)$$

$$P_{dias}^{WK4p}(t) = P_{dias}(t) + P_{LZ}(t_s) \exp\left(\frac{(t_s - t)Z_c}{L}\right) \quad (2.42)$$



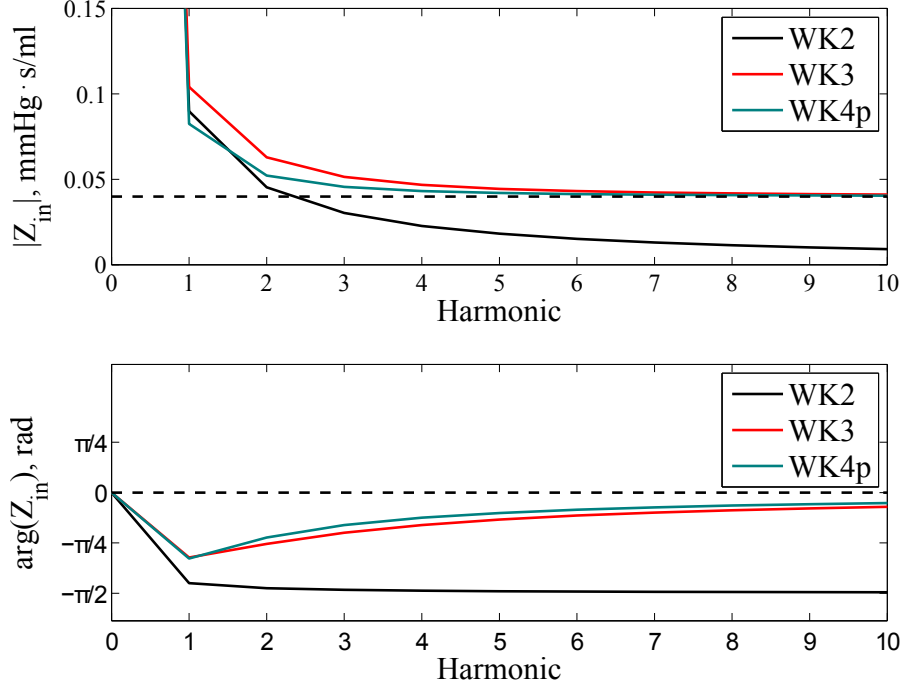


Figure 2.14: Comparison of the modulus (upper panel) and phase (lower panel) of the arterial input impedances described by the three different Windkessel models. The same parameters were used as for the pressure waves obtained in the time-domain shown in figure 2.12.

$t_s$  again denotes the duration of mechanical systole and  $T$  the length of the heartbeat. In both cases, the exponential terms converge to 0 for  $t \rightarrow \infty$ , thus, without further excitation from the heart, the pressure decreases towards  $P_\infty$ , justifying its name asymptotic pressure level.

## 2.4 Wave intensity analysis

Wave intensity analysis (WIA) was proposed by Parker and Jones in 1990 [91] as an alternative to impedance analysis to investigate the wave-phenomena in the arterial system. Impedance analysis, as presented in section 2.2, is based in the frequency-domain and waves are considered sinusoidal wave trains that add up to the measured waveforms when superimposed, assuming a linear system. These periodic waves transmit the energy of cardiac ejection, thereby causing a displacement of blood yet without net mass transport. Wave intensity analysis, in contrast, is a time-domain method where successive wavefronts describing the incremental changes in pressure  $dP$  and velocity  $dU$  are analysed.

Wave intensity analysis is based on the solution of a one-dimensional model of blood flow using the method of characteristics, as will be presented in the following sections.

### 2.4.1 Deriving a 1D model of blood flow and pressure in an elastic vessel

In this section, a one-dimensional description of the haemodynamics in an elastic arterial segment will be derived based on the approach presented by Sherwin et al. [117]. Generally, blood flow velocity  $\vec{u}$  and pressure  $p$  in an artery are functions of space  $\vec{x} = (x, y, z)$  and time  $t$ , i.e.  $\vec{u} = \vec{u}(t, \vec{x})$ ,  $p = p(t, \vec{x})$  with the components of  $\vec{u} = (u, v, w)$  denoting the velocity in  $x$ -,  $y$ - and  $z$ -direction. In order to derive a one-dimensional formulation, several simplifications have to be applied to reduce the spatial dimension. First of all, it is assumed that the vessel is straight and that the  $x$ -direction corresponds to the axial, forward flow direction as shown in figure 2.15. Furthermore, for the purpose of this model, only the velocity in the axial direction  $u(t, \vec{x})$  will be considered.

To eliminate the dependency of velocity and pressure on  $y$  and  $z$ , both state variables are averaged over the cross-sectional area  $A$ . Therefore, it is assumed that the vessel is axisymmetric and deformations apply in radial direction only, meaning that the cross section is always circular and the length of the vessel constant. Hence,  $A$  depends on time and  $x$  only:  $A = A(t, x)$ . The average velocity  $U$  and pressure  $P$  are now defined as

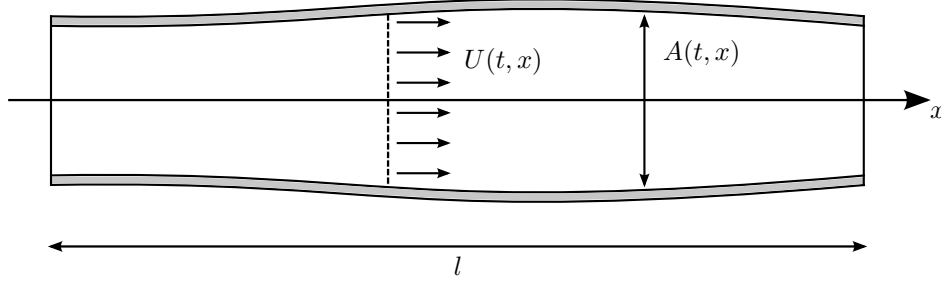
$$U(t, x) := \frac{1}{A(t, x)} \int_{A(t, x)} u(t, \vec{x}) \, dA, \quad (2.43)$$

$$P(t, x) := \frac{1}{A(t, x)} \int_{A(t, x)} p(t, \vec{x}) \, dA. \quad (2.44)$$

In contrast to the previous sections, mean blood flow velocity  $U$  and not volumetric blood flow  $Q$  is used. However, these two state variables are intrinsically linked by  $Q = \int_A u \, dA = AU$ .

A last set of assumptions relates to the properties of blood. In reality, blood is a suspension of particles (e.g. white and red blood cells) in an aqueous solution, the blood plasma. Yet, this property is most relevant at a capillary level, whereas in large arteries, blood can be regarded a homogeneous fluid. Also the non-Newtonian behaviour of blood is negligible in large arteries, where large relates to vessel diameters above  $100\mu\text{m}$  [15]. Therefore, blood will be considered a homogenous, Newtonian fluid. Moreover, it is assumed to be incompressible with constant density, which represents a good approximation for physiological flow rates [15], and viscous effects will not be taken into account.

Overall, the model describes the relation between flow, pressure and cross-sectional area in a straight, axisymmetric, elastic vessel with blood being a homogeneous, inviscid and incompressible fluid, i.e. viscosity is assumed to be zero  $\mu = 0$  and density to be constant  $\rho(t, \vec{x}) = \rho$ . The three state variables  $(A, P, U)$  are thereby assumed to be sufficiently smooth, in particular continuously differentiable in both  $t$  and  $x$ . The governing equations will be derived by applying conservation of mass and balance of momentum to a control volume  $CV(t)$  defined as the arterial segment shown in figure 2.15 with constant, yet arbitrary length  $l$ .

Figure 2.15: A straight arterial segment with length  $l$ , oriented along the  $x$ -axis.

### Conservation of mass

For mass to be conserved, the change in mass within the control volume  $M_{CV}$  with time has to equal the mass flow across the surface. For constant density  $\rho$ ,  $\frac{dM_{CV}}{dt}(t)$  is given by

$$\frac{dM_{CV}}{dt}(t) = \frac{d}{dt} \int_{CV(t)} \rho dV = \rho \frac{d}{dt} \int_0^l A dx = \int_0^l \rho \frac{\partial A}{\partial t} dx.$$

The last equality follows from the assumption that  $A(t, x)$  is continuously differentiable in  $t$  for any  $x$  and thus integration and differentiation can be interchanged.

If it is further assumed that the walls of the vessel are impermeable, mass flow in and out of the control volume is given by

$$\begin{aligned} \int_{A(t,0)} \rho U dA - \int_{A(t,l)} \rho U dA &= \rho(A(t,0)U(t,0) - A(t,l)U(t,l)) \\ &= - \int_0^l \rho \frac{\partial AU}{\partial x} dx. \end{aligned}$$

Conservation of mass can thus be formulated as

$$\int_0^l \rho \frac{\partial A}{\partial t} + \rho \frac{\partial AU}{\partial x} dx = 0.$$

This equality has to hold for any length  $l$  and hence the integrand has to be zero, yielding the equation for conservation of mass in differential form

$$\frac{\partial A}{\partial t} + \frac{\partial AU}{\partial x} = 0. \quad (2.45)$$

### Balance of momentum

According to Newton's second law, the change of momentum with respect to time equals the sum of forces acting on the control volume. As before, the total change in momentum in  $x$ -direction is given by the change within the control volume minus the momentum flux across the surface, taking into account that particles entering or leaving the system take momentum with them. The

change of momentum within the control volume is computed as ("momentum=mass $\times$ velocity")

$$\frac{d}{dt} \int_{CV(t)} \rho U \, dV = \frac{d}{dt} \int_0^l \int_{A(t,x)} \rho U \, dA \, dx = \int_0^l \rho \frac{\partial(AU)}{\partial t} \, dx.$$

The momentum flux across the surface can be calculated as

$$\int_{A(t,0)} (\rho U) U \, dA - \int_{A(t,l)} (\rho U) U \, dA = \rho(A(t,0)U^2(t,0) - A(t,l)U^2(t,l)) \quad (2.46)$$

$$= - \int_0^l \rho \frac{\partial AU^2}{\partial x} \, dx. \quad (2.47)$$

The total force  $\vec{F} = (F_x, F_y, F_z)$  acting on the control volume is comprised of external forces (e.g. gravity) pressure forces and frictional forces. If external forces are neglected, only pressure forces remain since viscosity is not considered, i.e. no friction occurs. Pressure acts on the surface of the volume and the total force is therefore given by

$$\vec{F} = - \int_{\partial CV(t)} P \vec{n} \, dS,$$

with  $\vec{n} = (n_x, n_y, n_z)$  denoting the unit normal vector on the surface pointing in outward direction. For the purpose of this model, again only the  $x$ -component  $F_x$  will be considered.  $n_x$  at the left and right boundary equals  $-1$  and  $1$  respectively. To determine its value along the vessel walls, denote the radius of the vessel as  $r(t, x)$ . In cylindrical coordinates, the vessel wall is given by  $\vec{x}(t, x, \phi) = (x, r(t, x) \cos \phi, r(t, x) \sin \phi)$  for  $0 \leq x \leq l$  and  $0 \leq \phi \leq 2\pi$ . The unit normal can be computed as  $\frac{\partial \vec{x}}{\partial x} \times \frac{\partial \vec{x}}{\partial \phi} / \left\| \frac{\partial \vec{x}}{\partial x} \times \frac{\partial \vec{x}}{\partial \phi} \right\|$  and the  $x$ -component thus equals  $n_x = -\frac{\partial r}{\partial x} r / \left\| \frac{\partial \vec{x}}{\partial x} \times \frac{\partial \vec{x}}{\partial \phi} \right\|$ . Keeping in mind that  $A(t, x) = \pi r^2(t, x)$  and therefore  $\frac{\partial A}{\partial x} = 2\pi r \frac{\partial r}{\partial x}$  yields

$$\begin{aligned} F_x &= - \int_{\partial CV(t)} P n_x \, dS \\ &= - \left( - \int_{A(t,0)} P \, dA + \int_{A(t,l)} P \, dA + \int_0^l \int_0^{2\pi} P n_x \left\| \frac{\partial \vec{x}}{\partial x} \times \frac{\partial \vec{x}}{\partial \phi} \right\| d\phi \, dx \right) \\ &= -(A(t,l)P(t,l) - A(t,0)P(t,0)) + \int_0^l P 2\pi r \frac{\partial r}{\partial x} \, dx \\ &= \int_0^l -\frac{\partial AP}{\partial x} + P \frac{\partial A}{\partial x} \, dx = \int_0^l -A \frac{\partial P}{\partial x} \, dx. \end{aligned}$$

Balance of momentum therefore finally reads in differential form

$$\rho \frac{\partial AU}{\partial t} + \rho \frac{\partial AU^2}{\partial x} + A \frac{\partial P}{\partial x} = 0. \quad (2.48)$$

### The final model

Conservation of mass (2.45) and balance of momentum (2.48) lead to the following set of equations to describe the haemodynamics in terms of the three state variables  $(A, P, U)$ .

$$\frac{\partial A}{\partial t} + \frac{\partial AU}{\partial x} = 0 \quad (2.49)$$

$$\rho \frac{\partial AU}{\partial t} + \rho \frac{\partial AU^2}{\partial x} + A \frac{\partial P}{\partial x} = 0 \quad (2.50)$$

The equation for balance of momentum (2.50) can be further simplified by explicitly computing the derivatives of  $\frac{\partial AU}{\partial t}$  and  $\frac{\partial(AU)U}{\partial x}$  and using conservation of mass (2.49).

$$\begin{aligned} 0 &= \rho U \frac{\partial A}{\partial t} + \rho A \frac{\partial U}{\partial t} + \rho U \frac{\partial AU}{\partial x} + \rho AU \frac{\partial U}{\partial x} + A \frac{\partial P}{\partial x} \\ &= \rho U \underbrace{\left( \frac{\partial A}{\partial t} + \frac{\partial AU}{\partial x} \right)}_{=0} + \rho A \left( \frac{\partial U}{\partial t} + U \frac{\partial U}{\partial x} + \frac{1}{\rho} \frac{\partial P}{\partial x} \right) \\ \Rightarrow 0 &= \frac{\partial U}{\partial t} + U \frac{\partial U}{\partial x} + \frac{1}{\rho} \frac{\partial P}{\partial x} \end{aligned}$$

If it is now assumed that the cross-sectional area is a function of pressure and location and not explicitly time and location<sup>11</sup>,  $A(t, x) = A(P(t, x), x)$ , conservation of mass can be reformulated to become

$$\begin{aligned} 0 &= \frac{\partial A}{\partial P} \frac{\partial P}{\partial t} + U \left( \frac{\partial A}{\partial P} \frac{\partial P}{\partial x} + \frac{\partial A}{\partial x} \right) + A \frac{\partial U}{\partial x} \\ &= \frac{\partial A}{\partial P} \left( \frac{\partial P}{\partial t} + U \frac{\partial P}{\partial x} \right) + U \frac{\partial A}{\partial x} + A \frac{\partial U}{\partial x}. \end{aligned}$$

Defining the quantity  $c$  by

$$c(P(t, x), x)^2 := \left( \frac{A(P(t, x), x)}{\rho \frac{\partial A}{\partial P}(P(t, x), x)} \right), \quad (2.51)$$

the governing one-dimensional equations can finally be formulated as

$$P_t + U P_x + \rho c^2 U_x = - \frac{\rho c^2 U A_x}{A} \quad (2.52)$$

$$U_t + U U_x + \frac{1}{\rho} P_x = 0, \quad (2.53)$$

where sub-indices indicate partial derivatives.  $c$  has the unit of velocity and represents the speed at which the waves travel through the artery, i.e. the pulse wave velocity (PWV). [90] [91]

<sup>11</sup>Strictly speaking, the resulting function should be denoted differently, i.e.  $A(t, x) = \tilde{A}(P(t, x), x)$  and therefore  $\frac{\partial A}{\partial t} = \frac{\partial \tilde{A}}{\partial P} \frac{\partial P}{\partial t}$  and  $\frac{\partial A}{\partial x} = \frac{\partial \tilde{A}}{\partial P} \frac{\partial P}{\partial x} + \frac{\partial \tilde{A}}{\partial x}$ . However, for the sake of ease of notation and readability, they are called the same.

### 2.4.2 Solution using the method of characteristics

The 1D-equations for blood flow and pressure in an artery were originally derived by Euler<sup>12</sup> in 1755. However, only after Riemann<sup>13</sup> introduced the method of characteristics to find a general solution for hyperbolic partial differential equation (PDE) over 100 years later, the theoretical framework was developed to actually solve these equations [89]. In this section the solution using the method of characteristics will be presented following [91] and [90].

The quasilinear, hyperbolic PDEs defined in equations (2.52) and (2.53) can be written in matrix form.

$$\begin{pmatrix} P_t \\ U_t \end{pmatrix} + \begin{pmatrix} U & \rho c^2 \\ \frac{1}{\rho} & U \end{pmatrix} \begin{pmatrix} P_x \\ U_x \end{pmatrix} = \begin{pmatrix} 0 \\ -\frac{\rho c^2 U A_x}{A} \end{pmatrix}$$

The Eigenvalues of the matrix of coefficients for the spatial derivatives are given by

$$(U - \lambda)^2 - c^2 = 0 \Rightarrow \lambda_{1,2} = U \pm c$$

and the characteristic directions are now defined as solutions of

$$\frac{dx_{\pm}}{dt} = U \pm c. \quad (2.54)$$

Hence, the axial location along the tube is parametrised by  $t$ . These paths correspond to a velocity of  $U + c$  (forward,  $x_+$ ) or  $U - c$  (backward,  $x_-$ ) and for every initial value  $x_{\pm}(0) = x_0$  one unique forward and backward solution exists. As stated before,  $c$  represents the velocity of the pulse waves travelling through the vessel. The total velocity of a forward travelling pulse wave is then given by  $c$  plus the velocity of the fluid itself, i.e.  $U + c$ , which equals the velocity along the forward direction. Analogously, for a backward wave travelling with speed  $-c$ , the total velocity is given by  $U - c$ , which equals the velocity along the backward characteristic direction.

Along these directions, the total derivatives of  $P(x_{\pm}(t), t)$  and  $U(x_{\pm}(t), t)$  with respect to time are given by

$$\begin{aligned} \frac{dP}{dt} &= P_x \frac{dx_{\pm}}{dt} + P_t = P_x \cdot (U \pm c) + P_t, \\ \frac{dU}{dt} &= U_x \frac{dx_{\pm}}{dt} + U_t = U_x \cdot (U \pm c) + U_t. \end{aligned}$$

By rearranging the terms, an expression for the partial derivatives  $P_t$  and  $U_t$  can be obtained.

$$\begin{aligned} P_t &= \frac{dP}{dt} - P_x \cdot (U \pm c) \\ U_t &= \frac{dU}{dt} - U_x \cdot (U \pm c) \end{aligned}$$

<sup>12</sup>Leonhard Euler (1707-1783), Swiss mathematician and physicist

<sup>13</sup>Georg Friedrich Bernhard Riemann (1826-1866), German mathematician

These relations can now be plugged in the original system of PDEs (2.52) and (2.53), yielding

$$\begin{aligned}\frac{dP}{dt} \mp cP_x + \rho c^2 U_x &= -\frac{\rho c^2 U A_x}{A}, \\ \frac{dU}{dt} \mp cU_x + \frac{1}{\rho} P_x &= 0.\end{aligned}$$

For the forward direction ( $U + c$ ), the first equation is divided by  $\rho c$  and added to the second one.

$$\left. \begin{array}{l} \text{I} \quad \frac{1}{\rho c} \frac{dP}{dt} - \frac{1}{\rho} P_x + cU_x = -\frac{cU A_x}{A} \\ \text{II} \quad \frac{dU}{dt} + \frac{1}{\rho} P_x - cU_x = 0 \end{array} \right\} \text{I+II: } \frac{dU}{dt} + \frac{1}{\rho c} \frac{dP}{dt} = -\frac{cU A_x}{A} \quad (2.55)$$

Similarly, for the backward direction ( $U - c$ ), the first equation is divided by  $(-\rho c)$  and again added to the second one.

$$\frac{dU}{dt} - \frac{1}{\rho c} \frac{dP}{dt} = \frac{cU A_x}{A} \quad (2.56)$$

Along the characteristic directions, the relation between  $U$  and  $P$  is therefore given by ordinary differential equations. These can be expressed in terms of the so called Riemann variables  $R_{\pm}$ .

$$\frac{dR_{\pm}}{dt}(t) := \frac{dU}{dt}(t, x_{\pm}(t)) \pm \frac{1}{\rho c(P(t, x_{\pm}(t)), x_{\pm}(t))} \frac{dP}{dt}(t, x_{\pm}(t)) \quad (2.57)$$

For small arterial segments without bifurcations or discontinuities, it can be assumed that the vessel is uniform in space, i.e.  $A_x = 0$  [91]. Then, the right hand sides of equations (2.55) and (2.56) become zero, implying that  $R_{\pm}$  is constant along the characteristic directions. In this case,  $R_{\pm}$  are called Riemann invariants. The pulse wave velocity  $c$  is a function of pressure  $P$  and space  $x$ :  $c = c(P, x)$ . Yet for a uniform vessel with  $A(P, x) = A(P)$ ,  $c$  is dependent on pressure only  $c = c(P)$ , see equation (2.51).

Integration of equation (2.57) over time therefore yields

$$R_{\pm} = U \pm \int_{t_0}^t \frac{1}{\rho c} \frac{dP}{dt} dt = U \pm \int_{P_0}^P \frac{1}{\rho c} dP.$$

If it is furthermore assumed that  $c$  is constant, which will be discussed in more detail in appendix B, the expression for  $R_{\pm}$  reduces to

$$R_{\pm} = U(t, x_{\pm}(t)) \pm \frac{1}{\rho c} P(t, x_{\pm}(t)). \quad (2.58)$$

In the following, the Riemann invariants belonging to the characteristic directions  $\hat{x}_{\pm}$  satisfying the initial value condition  $\hat{x}_{\pm}(t_0) = x_0$ , will be denoted by  $R_{\pm}(t_0, x_0)$  or  $R_{\pm}(\hat{x}_{\pm})$ .

From equation (2.58), it follows that for any point  $(t, x)$ , characteristic directions  $\hat{x}_{+}$  and  $\hat{x}_{-}$  with  $\hat{x}_{+}(t) = x = \hat{x}_{-}(t)$  and corresponding Riemann-invariants  $R_{+}(\hat{x}_{+})$  and  $R_{-}(\hat{x}_{-})$ , the flow

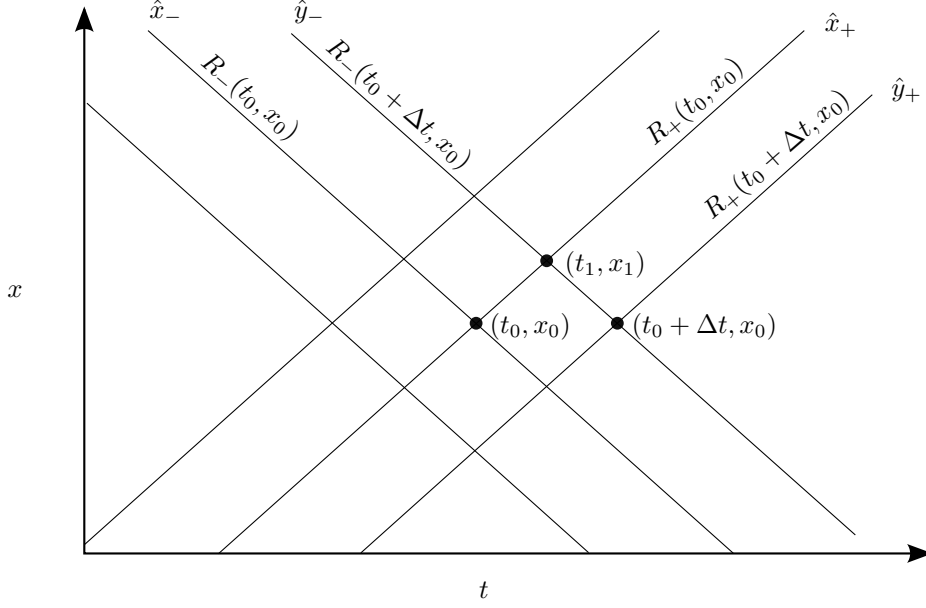


Figure 2.16: Schematic representation of the characteristic directions and the corresponding Riemann invariants. Two points lying on different characteristics ( $\hat{x}_{\pm}, \hat{y}_{\pm}$ ) at different times ( $t_0, t_0 + \Delta t$ ) at the same location  $x_0$  are shown. The corresponding differences can be obtained from the differences between the Riemann invariants  $R_{\pm}(t_0, x_0)$  and  $R_{\pm}(t_0 + \Delta t, x_0)$ .

velocity  $U$  and pressure  $P$  at  $(t, x)$  can be obtained by

$$U(t, x) = \frac{1}{2}(R_+(\hat{x}_+) + R_-(\hat{x}_-)), \quad (2.59)$$

$$P(t, x) = \frac{\rho c}{2}(R_+(\hat{x}_+) - R_-(\hat{x}_-)). \quad (2.60)$$

Hence, to actually solve the system of PDEs defined in equations (2.52) and (2.53) with a zero right-hand side, boundary conditions for  $U$  and  $P$  at both ends of the vessel under consideration have to be prescribed, compare [3] and figure 2.16. From these, the values of the Riemann invariants for any characteristic direction can be obtained according to equation (2.58). Subsequently  $P$  and  $U$  at any point  $(t, x)$  within the vessel can be determined from the Riemann invariants belonging to the characteristic directions intersecting at  $(t, x)$ , see equations (2.59) and (2.60). However, for wave intensity analysis, the focus does not lie on the propagation of flow and pressure, but on the interpretation and analysis of the temporal changes at a specific site  $x_0$ , as will be discussed in the next section.



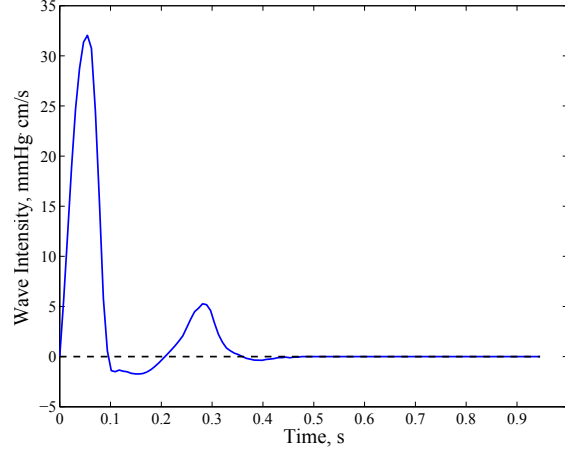


Figure 2.17: Wave intensity obtained from measured pressure and flow velocity.

### 2.4.3 Wave intensity

Equations (2.59) and (2.60) can be used to express the temporal differences of pressure and flow at a specific location  $x_0$  in terms of the Riemann-invariants by

$$dU(t, x_0, \Delta t) := U(t + \Delta t, x_0) - U(t, x_0) \quad (2.61)$$

$$= \frac{1}{2}(R_+(t + \Delta t, x_0) + R_-(t + \Delta t, x_0) - R_+(t, x_0) - R_-(t, x_0)) \quad (2.62)$$

$$= \frac{1}{2}(dR_+(t, x_0, \Delta t) + dR_-(t, x_0, \Delta t)) \quad (2.63)$$

and

$$dP(t, x_0, \Delta t) := P(t + \Delta t, x_0) - P(t, x_0) \quad (2.64)$$

$$= \frac{\rho c}{2}(R_+(t + \Delta t, x_0) - R_-(t + \Delta t, x_0) - R_+(t, x_0) + R_-(t, x_0)) \quad (2.65)$$

$$= \frac{\rho c}{2}(dR_+(t, x_0, \Delta t) - dR_-(t, x_0, \Delta t)). \quad (2.66)$$

Wave intensity is now defined as the product of  $dU$  and  $dP$

$$dI := dU dP = \frac{1}{2}(dR_+ + dR_-) \frac{\rho c}{2}(dR_+ - dR_-) = \quad (2.67)$$

$$= \frac{\rho c}{4}(dR_+^2 - dR_-^2). \quad (2.68)$$

$dI$  has the SI-unit  $\text{kg/s}^3 = \text{W/m}^2$  and corresponds to the rate of energy transfer per unit area associated with the wavefronts  $dU$  and  $dP$  [91]. The property that makes  $dI$  appealing for analysis is that the contribution of forward waves is always positive, whereas backward waves enter with a negative sign, see equation (2.68). The sign of  $dI$  therefore holds information on which waves dominate at an instance  $t$ . Depending on whether pressure is increased ( $dP > 0$ ) or decreased ( $dP < 0$ ), the dominating waves can be further classified as summarised in table 2.1.

Sign of $dI$	Sign of $dP$	Sign of $dU$	Name
$dI > 0$	$dP > 0$	$dU > 0$	forward compression wave
$dI > 0$	$dP < 0$	$dU < 0$	forward expansion wave
$dI < 0$	$dP > 0$	$dU < 0$	backward compression wave
$dI < 0$	$dP < 0$	$dU > 0$	backward expansion wave

Table 2.1: Nomenclature used for the dominating waves according to the sign of  $dI$  and  $dP$ .

To compute the wave intensity  $dI$  from a measured pair of pressure and flow velocity, the differences for each time step determined by the sampling rate are used. Figure 2.17 shows an example of the so-obtained wave intensity. Typically, two positive peaks can be distinguished corresponding to an early-systolic compression wave and a late-systolic expansion wave, which are attributed to the ejection and relaxation dynamics of the left ventricle respectively. The first represents the initial impulse coming from the heart, increasing pressure and accelerating blood flow, whereas the second causes a decrease in pressure and a flow reversal leading to the closure of the aortic valve at the beginning of ventricular relaxation. The negative peak in mid-systole implies that this phase is dominated by reflections of the initial forward wave. [44, 90, 92, 120]

#### 2.4.4 Waterhammer equations and wave separation

For a single wave travelling forward along the characteristic direction  $\hat{x}_+$  in a uniform and lossless vessel, it has to hold that  $U_f(t_0, \hat{x}_+(t_0)) = U_f(t_1, \hat{x}_+(t_1))$ , as no energy is lost and no reflections are present. Expressed in terms of the Riemann invariants, this means that ( $\hat{x}_+(t_0) = x_0$ ,  $\hat{x}_+(t_1) = x_1$ ):

$$\overbrace{\frac{1}{2}(R_+(t_0, x_0) + R_-(t_0, x_0))}^{U_f(t_0, x_0)} = \overbrace{\frac{1}{2}(R_+(t_1, x_1) + R_-(t_1, x_1))}^{U_f(t_1, x_1)} \quad (2.69)$$

$$R_-(t_0, x_0) = R_-(t_1, x_1) \quad (2.70)$$

since  $R_+$  is constant along the forward direction  $\hat{x}_+$ .

Denote the characteristic directions intersecting at  $(t_0, x_0)$  by  $\hat{x}_\pm$  and those intersecting at  $(t_0 + \Delta t, x_0)$  by  $\hat{y}_\pm$ .  $\hat{x}_+$  and  $\hat{y}_-$  intersect at a point  $(t_1, x_1)$  with  $t_1 < t_0 + \Delta t$  and  $x_1 > x_0$ , see figure 2.16. Because of equation (2.70), the Riemann invariants along  $\hat{x}_-$ :  $R_-(t_0, x_0)$ , and along  $\hat{y}_-$ :  $R_-(t_1, x_1) = R_-(t_0 + \Delta t, x_0)$ , have to be equal and therefore it holds that  $R_-(t_0 + \Delta t, x_0) = R_-(t_0, x_0)$ . Thus, for a single, forward travelling wave, (2.62) simplifies to

$$dU_f(t_0, x_0, \Delta t) = \frac{1}{2}(R_+(t_0 + \Delta t, x_0) + R_-(t_0 + \Delta t, x_0) - R_+(t_0, x_0) - R_-(t_0, x_0)) \quad (2.71)$$

$$= \frac{1}{2}(R_+(t_0 + \Delta t, x_0) - R_+(t_0, x_0)). \quad (2.72)$$

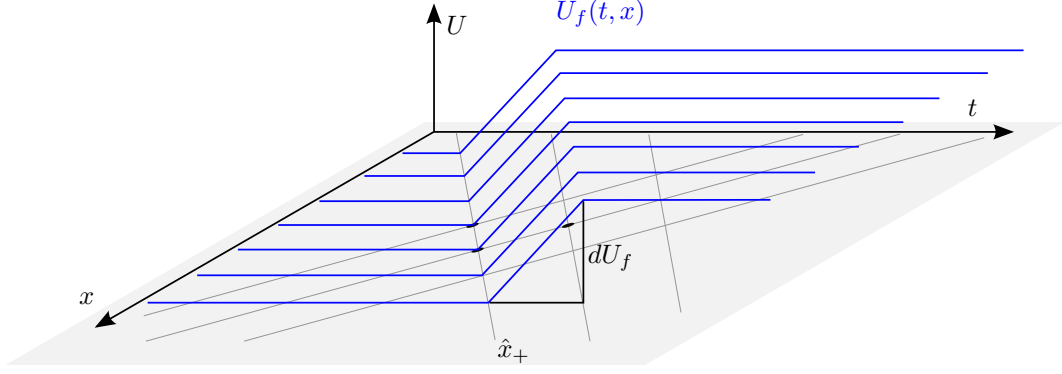


Figure 2.18: A single forward wave travelling in a uniform, lossless vessel along the characteristic direction  $\hat{x}_+$ .

For  $dP_f$  it follows that

$$dP_f(t_0, x_0, \Delta t) = \frac{\rho c}{2} (R_+(t_0 + \Delta t, x_0) - R_-(t_0 + \Delta t, x_0) - R_+(t_0, x_0) + R_-(t_0, x_0)) \quad (2.73)$$

$$= \frac{\rho c}{2} (R_+(t + \Delta t, x_0) - R_+(t, x_0)) \quad (2.74)$$

and therefore

$$dP_f = \rho c dU_f. \quad (2.75)$$

Analogous considerations for a single, backward travelling wave yield

$$dP_b = -\rho c dU_b. \quad (2.76)$$

The relations

$$dP_{f,b} = \pm \rho c dU_{f,b} \quad (2.77)$$

are called the **Waterhammer equations**. Assuming that the interaction between forward and backward travelling waves is linear

$$dP = dP_f + dP_b, \quad dU = dU_f + dU_b, \quad (2.78)$$

the Waterhammer equations (2.77) can be used to separate the wavefronts in their forward and backward travelling components, yielding

$$dP_{f,b} = \frac{dP \pm \rho c dU}{2}, \quad (2.79)$$

$$dU_{f,b} = \frac{\rho c dU \pm dP}{2\rho c}. \quad (2.80)$$

The separated total waveforms  $P_{f,b}$  and  $U_{f,b}$  can be obtained by integration or summation of the successive differences

$$P_{f,b} = \sum dP_{f,b}, \quad U_{f,b} = \sum dU_{f,b}. \quad (2.81)$$

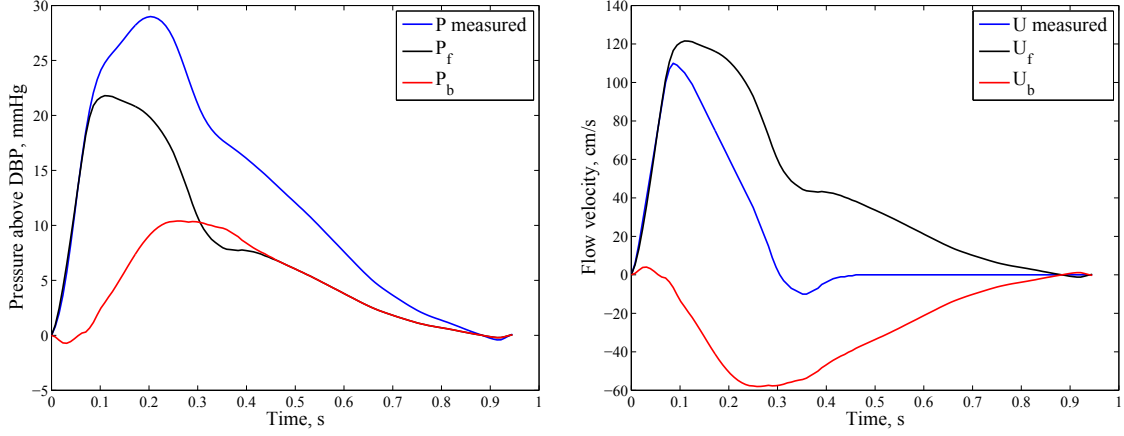


Figure 2.19: Aortic pressure and flow separated in their forward (black) and backward (red) components using wave intensity analysis.  $\rho c$  was estimated in the time domain from the PU-loop using the first 8 data points  $\approx 55$  ms.

These expressions are very similar to the ones obtained in the frequency domain in section 2.2. Indeed, if the characteristic impedance  $Z_c$  is identified with  $\rho c/A$  and the relation  $Q = UA$  is used, both approaches yield formally identical results with differences arising primarily from the chosen approach to estimate  $\rho c$  or  $Z_c$  respectively [41, 147], compare figures 2.19 and 2.8.

With the same argumentation as in section 2.2.3,  $\rho c$  is commonly assessed from the early systolic part of the PU-loop, when reflections are assumed to have not yet returned [90].

From the separated wavefronts, also the forward and backward wave intensity can be computed

$$dI_{f,b} = dP_{f,b}dU_{f,b} = \frac{\pm 1}{4\rho c} (dP \pm \rho c dU)^2, \quad (2.82)$$

the sum of which again yields the net wave intensity  $dI$ .

$$\begin{aligned} dI &= dPdU = (dP_f + dP_b)(dU_f + dU_b) \\ &= dP_f dU_f + dP_b dU_b + dP_f dU_b + dP_b dU_f \\ &= dI_f + dI_b + \rho c dU_f dU_b - \rho c dU_b dU_f \\ &= dI_f + dI_b \end{aligned}$$

For  $dI_f$  and  $dI_b$  the same characteristics as for  $dI$  can be observed, see figure 2.20. The forward intensity shows two peaks denoted as S wave (early systolic) and D wave (late systolic/early diastolic). The backward intensity is most prominent during mid-systole, resulting in a negative R wave representing the reflections in the system. For quantification, usually the amplitudes or the areas under the respective portions are used. The latter has the unit of Joule per square meter ( $\text{mmHg} \cdot \text{cm} \approx 1.3332 \text{ J/m}^2$ ) and represents the "absolute energy carried per unit cross-sectional area by a wave" [19, p. H557]. As a relative index of wave reflection, the ratio of the

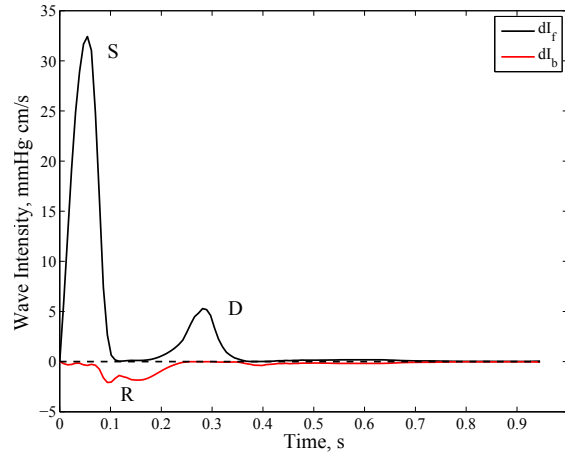


Figure 2.20: Forward (black) and backward (red) wave intensity. Forward intensity shows two peaks  $S$  and  $D$  related to ventricular contraction and relaxation respectively. Reflections represented by backward wave intensity are most prominent in mid-systole resulting in a negative peak  $R$ .

corresponding measures of the  $R$  and the  $S$  wave can be used.

However, it has to be kept in mind that the magnitude of the computed wave intensity strongly depends on the chosen time step  $dt$ , restricting the comparability of the derived parameters between different investigators. Therefore, the use of the time derivative or difference quotient instead of the absolute temporal change was proposed [120].

## Chapter 3

# Models of aortic blood flow based on pressure alone: existing methods and a novel approach

In the last chapter, different concepts to describe and to quantify the mechanisms in the arterial system based on the waveforms of aortic pressure and/or flow were introduced. The derived parameters are intended to help in the assessment of cardiovascular risk and the early detection of cardiovascular disease. To enable a widespread use, the corresponding measurements should therefore be easy to realise and should present no risk for the patient, thus non-invasive methods are desirable. With regards to pressure, validated transfer functions exist to generate aortic pressure waveforms from non-invasive peripheral readings [47] and different commercial devices are available incorporating these algorithms.

Unfortunately, the non-invasive assessment of aortic root flow is more complicated. One of the most widely used techniques is echocardiography, particularly the use of pulsed-wave or continuous wave Doppler ultrasound [105]. However, echocardiographic examination requires dedicated devices and specially trained operators, both limiting its widespread use at a primary care setting. Therefore, different blood flow models based on pressure alone were introduced in literature and three of them will be presented in the following sections. Subsequently, a novel model of blood flow will be proposed which is based on the 4-element parallel Windkessel to compute flow from pressure in the frequency domain.

### 3.1 Triangular flow

Typically, aortic blood flow shows a fast systolic upstroke followed by a, more or less linear, monotone decrease. The overall waveshape might thus be considered triangular. Westerhof and

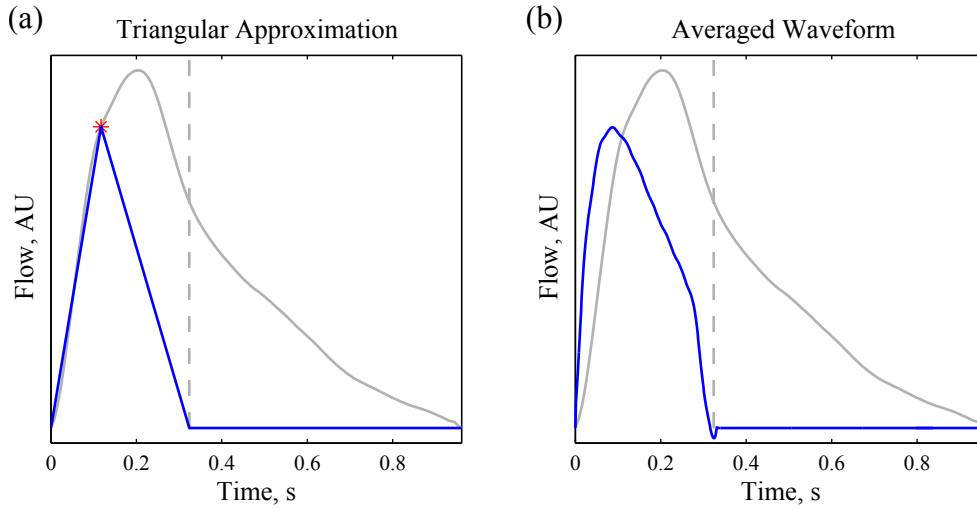


Figure 3.1: Triangular approximation (a) and averaged waveform (b) as estimates of aortic blood flow. In both cases, the ejection duration derived from the pressure wave (indicated in gray) determines the width of the respective waveform. For the triangulation, the timing of peak flow is furthermore set to the timing of the inflection point in the pressure signal.

coworkers [142] therefore proposed the use of a triangular function based on timing information obtained from the pressure wave to estimate the shape of aortic blood flow for the use in wave separation analysis (WSA).

The idea is based on the mechanisms described in section 2.1.2 for the computation of the augmentation index (AIx). The width of the triangle is defined by the ejection duration (ED) and the maximum is aligned with the first shoulder in the pressure signal derived by the fourth derivative [142], see figure 3.1(a).

As a proof of concept, Westerhof et al. applied their flow model on a dataset of 29 simultaneously measured flow and pressure waves of 19 different patients assessed during cardiac catheterisation. They found a good agreement between the WSA-parameters derived from the measured flow wave and the triangular approximation and concluded that it might be suitable also for non-invasive data [142]. In the following, their method which is often referred to as flow triangulation has been used for WSA in a variety of non-invasive studies, e.g. [56, 75, 133].

## 3.2 Averaged flow

Shortly after the introduction of the triangulation method, Kips and coworkers [49] proposed the use of an averaged waveform as an estimate of aortic blood flow to ensure a physiologic shape. Therefore, Doppler flow measurements of 74 healthy subjects (32 female) were collected from the Asklepios population [108], normalised in time and amplitude and finally averaged. The resulting flow waveform is shown in figure 3.1(b). In order to derive a patient-specific estimate,

this waveform is rescaled to match the actual ejection duration.

Kips et al. tested their approximation in the Asklepios population on a dataset comprising non-invasive (carotid) pressure measurements of more than 2300 patients and compared it to Doppler flow as well as the triangular estimate. They found it to be superior to the triangle with regards to the waveshape and the correlation of Doppler and approximated reflection magnitude (RM), yet still showing considerable deviations. [49]

Nevertheless, RM derived from the averaged waveform was shown to be a strong predictor for the onset of congestive heart failure in a subsequent noninvasive study performed by Chirinos et al. [17].

### 3.3 ARCSolver flow

Another class of flow models is based on the arterial Windkessel coupled with an optimality criterion. Generally, the Windkessel models require either one of the two state variables pressure or flow as well as given parameter values to derive the other one. However, if an additional linkage between pressure and flow is included, both state variables can be retrieved at the same time for a given parameter set. This allows for identification of the Windkessel parameters and computation of aortic flow based on a single pressure measurement.

The general procedure for this type of flow model can be summarised in four steps:

1. Formulation of an optimisation problem comprising a Windkessel model, an optimality criterion and suitable boundary conditions as well as constraints.
2. Solving of the optimisation problem in dependency of the Windkessel parameters to obtain an optimal pressure and flow contour.
3. Identification of the Windkessel parameters by minimising the error between the optimal pressure contour from step 2 and the measured one.
4. Computation of the optimal flow time-course using the parameters from step 3.

Since the 1970ies, a variety of models based on this concept was developed with more or less promising results, differing in the Windkessel model used, the optimality criterion demanded as well as the boundary conditions and constraints applied, see e.g. [25, 31, 78, 96, 100, 154]. Starting point for all of them was the assumption of minimal ventricular stroke work or energy dissipation, but also extensions by penalty terms were considered. Moreover, the different presumptions led to different mathematical tools needed for solving, in particular calculus of variation and optimal control theory. A more detailed overview in German can be found in [93].

Also the ARCSolver method for the computation of aortic flow that was developed at the AIT



Austrian Institute of Technology GmbH and is part of the ARCSolver algorithms for pulse wave analysis is based on this principle using a 3-element Windkessel with  $P_\infty = 0$  and a minimal cardiac work criterion [35, 135]. The cardiac work or stroke work  $SW$  is given by the integral of pressure times flow over one heartbeat

$$SW(P, Q) = \int_0^T P(t)Q(t) dt = \int_0^{t_s} P(t)Q(t) dt. \quad (3.1)$$

The second equality follows from the presumption of zero flow during diastole. Using the 3-element Windkessel equations

$$P(t) = Z_c Q(t) + P_{RC}(t), \quad (3.2)$$

$$\frac{dP_{RC}}{dt}(t) = \frac{1}{C_a} Q(t) - \frac{1}{R_p C_a} P_{RC}(t), \quad (3.3)$$

both pressure and flow can be expressed in terms of the peripheral outflow  $Q_{out}(t) = \frac{P_{RC}(t)}{R_p}$  by

$$P(t) = Z_c Q(t) + R_p Q_{out}(t), \quad (3.4)$$

$$Q(t) = C_a R_p \frac{dQ_{out}}{dt}(t) + Q_{out}(t). \quad (3.5)$$

Hence, stroke work  $SW$  can be formulated as a functional of  $Q_{out}$ , i.e.  $SW(P, Q) = SW(Q_{out})$ . Under the additional constraint that a given stroke volume

$$SV = \int_0^T Q(t) dt = \int_0^{t_s} Q(t) dt > 0 \quad (3.6)$$

has to be reached, the optimisation problem can be formulated as follows.

$$\begin{aligned} \underset{x}{\text{minimise}} \quad & SW(x) = \int_0^{t_s} \overbrace{Z_c C_a^2 R_p^2 \dot{x}(t)^2 + C_a R_p (2Z_c + 1) \dot{x}(t)x(t) + (Z_c + R_p)x(t)^2}^{L(x, \dot{x})} dt \\ \text{subject to} \quad & G(x) = \int_0^{t_s} \underbrace{C_a R_p \dot{x}(t) + x(t)}_{K(x, \dot{x})} dt = SV \end{aligned}$$

The constraint has the same form as the functional that is to be minimised and the optimisation problem therefore represents an isoperimetric problem that can be solved using calculus of variation. More specifically, since both Lagrangians  $L$  and  $K$  are polynomials in  $x$  and  $\dot{x}$  and therefore smooth functions, the method of Lagrangian multipliers can be applied. If it is furthermore assumed that  $x = Q_{out}$  is at least two times continuously differentiable, the Euler-Lagrange equations yield the following, necessary condition for a function  $x$  minimising  $SW$ .

$$\frac{\partial}{\partial x}(L + \lambda K) - \frac{d}{dt} \frac{\partial}{\partial \dot{x}}(L + \lambda K) = 0, \quad (3.7)$$

where  $\lambda \in \mathbb{R}$  denotes the Lagrange multiplier. This leads to a linear, inhomogeneous, second

order ordinary differential equation (ODE) for  $x$

$$\ddot{x}(t) - \frac{Z_c + R_p}{Z_c C_a^2 R_p^2} x(t) = \frac{\lambda}{2 Z_c C_a^2 R_p^2}. \quad (3.8)$$

The general solution is given by

$$x(t) = A e^{\mu t} + B e^{-\mu t} + C, \quad (3.9)$$

with  $\mu$  denoting the Eigenvalue of the ODE, i.e.  $\mu = \sqrt{\frac{Z_c + R_p}{Z_c C_a^2 R_p^2}}$ . The three degrees of freedom  $A, B, C$  have to be determined from the boundary conditions and constraints.

For blood flow  $Q$ , a possible choice of boundary values is  $Q(0) = Q(t_s) = 0$ , ensuring flow to be zero during diastole. If the system is in steady state, boundary values for the blood pressure  $P$  can be obtained from the assumption of periodicity, in particular  $P_0 = P(0) = P(T)$ . From the exponential decay predicted by the 3-element Windkessel (WK3) during diastole, this can also be translated to a condition for  $P(t_s)$  by  $P(t_s) = P_0 e^{\frac{t_s - T}{R_p C_a}}$ . Hence, together with the constraint of a fixed stroke volume (SV), 5 possible conditions can be formulated to determine the three constants  $A, B, C$ , leading to an over-determined system of linear equations, which is in general not solvable. Different options exist which conditions to include, resulting in substantially differing behaviour of the obtained optimal pressure and flow contours, which can be qualitatively categorised into three classes depending on the chosen conditions for  $Q$  [33]. Neglecting  $Q(0) = 0$  thereby yields the best results in terms of the pressure waveshape and this also represents the approach that was chosen for all flow models presented in literature so far [25, 100, 154].

In the ARCSolver routine, the conditions  $Q(t_s) = 0$ ,  $P(t_s) = P_0 e^{\frac{t_s - T}{R_p C_a}}$  and  $SV = \frac{\bar{P} \cdot T}{R_p}$  are used. The so obtained optimal pressure contours do indeed resemble measured ones, which allows for identification of the Windkessel parameters, whereby the area under the systolic pressure curve after accounting for wave reflections serves as error measure [64]. However, by neglecting  $Q(0) = 0$ , no physiological flow waveform can be achieved. To overcome this drawback, the simulated flow wave is further modified using a discrete second order delay element to attain  $Q(0) = 0$  [35].

The ARCSolver flow was found to provide accurate estimates compared with Doppler flow measurements in patients with preserved systolic function [35]. Also the derived parameters of WSA as well as wave intensity analysis (WIA) were shown to be in good agreement with the reference values obtained from Doppler flow [35–37].

## 3.4 Windkessel flow

### 3.4.1 Concept

The arterial input impedance  $Z_{in}$  offers a complete description of the arterial system, linking flow to pressure independently of the heart. Knowledge of  $Z_{in}$  therefore provides the means to compute pressure from flow or vice versa according to the relation given in section 2.2.1.

$$Z_{in}(\omega_n) = \frac{\hat{P}_n}{\hat{Q}_n} \Rightarrow \hat{Q}_n = \frac{\hat{P}_n}{Z_{in}(\omega_n)}, \quad n \geq 0 \quad (3.10)$$

However, since  $Z_{in}$  is normally not available it has to be estimated in order to obtain a flow curve based on pressure alone. Therefore, a Windkessel model is used as a parametric approximation of  $Z_{in}$ . The parallel 4-element Windkessel (WK4p) seems to be the best choice for this purpose as it combines the strengths of both the 2-element Windkessel (WK2) regarding the lower frequency range and the WK3 regarding the higher frequencies.

Nevertheless, the WK4p naturally represents a vast simplification of the real impedance and, as stated by Burkhoof and coworkers in 1988 referring to the WK3, "...while the Windkessel model captures many of the gross features of the real impedance, it fails to reproduce many of its details" [14, p. H742]. One of these details is the behaviour of the phase angle of  $Z_{in}$ . From experimental data,  $\arg(Z_{in})$  was found to be negative for low frequencies, cross zero, become positive and either stay positive, oscillate around zero or become zero for higher frequencies [72, 76]. The phase angle of the modelled input impedance, in contrast, remains always negative for all frequencies, approaching zero from below.

To reduce the error introduced by the wrong phase shift, an approach is chosen that is inspired by a work by Quick et al. [104] on the possibilities to determine arterial system geometry and characteristics from measured pressure and flow profiles referred to as the "hemodynamic inverse problem". In their work, Quick and co-workers argue that while the Windkessel behaviour given by the WK2 provides an accurate description for the very low frequencies and the characteristic impedance  $Z_c$  for the high frequencies, the intermediate frequency range depends on arterial topology and wave reflections. To analyse the contribution of each to experimentally determined impedance spectra, they propose to use a hybrid approximation of  $Z_{in}$ , with  $Z_{\text{hybrid}} = Z_{in, \text{WK2}}$  for frequencies lower than a threshold  $f_b$  and  $Z_{\text{hybrid}} = Z_c$  for frequencies above  $f_b$ , where  $f_b$  is individually determined to best fit the data.

Even though their goal is different from the aim of this work, their idea of a hybrid approximation of  $Z_{in}$  with variable threshold is adopted to improve the approximation of  $\arg(Z_{in})$ . More precisely, the model impedance  $Z_{\text{model}}$  is defined such that

$$Z_{\text{model}}(\omega_n) = \begin{cases} Z_{in, \text{WK4p}}(\omega_n) & \text{for } n < \tilde{n} \\ |Z_{in, \text{WK4p}}(\omega_n)| & \text{for } n \geq \tilde{n} \end{cases} \quad (3.11)$$

thereby artificially forcing  $\arg(Z_{\text{model}}(\omega_n)) = 0$  for  $n$  greater than an individual threshold  $\tilde{n}$ .

By the use of the WK4p as an estimate of  $Z_{in}$ , the number of unknowns is greatly reduced. However, the question remains how to identify the 5 parameters needed, namely  $R_c, C_a, Z_c, L$  and  $P_\infty$  and if they can be uniquely determined. For this purpose, different features of the aortic flow wave will be considered. First of all, there should be no ventricular outflow during diastole and thus in particular also at the start of systole which implies

$$Q(t) = 0, \quad t \in [t_s, T] \quad \text{and} \quad Q(0) = 0. \quad (3.12)$$

A second condition can be derived from the argumentation used for the estimation of characteristic impedance presented in section 2.2.3. Namely, at the beginning of ejection, pressure above diastolic level and flow are supposed to be proportional with proportionality factor  $Z_c$ , yielding

$$Q_{\text{early systole}} = \frac{P_{\text{early systole}} - P(0)}{Z_c}. \quad (3.13)$$

These conditions are now combined in a weighted sum to form the cost function used for parameter identification

$$\begin{aligned} \text{error}(\vec{x}) = & w_1 \cdot \tilde{Q}(0)^2 + w_2 \cdot \tilde{Q}(t_s)^2 + w_3 \cdot \sum_{\text{diastole}} \tilde{Q}(t)^2 + \\ & + w_4 \cdot \sum_{\text{early systole}} \left( \frac{P(t) - P(0)}{Z_c} - \tilde{Q}(t) \right)^2, \end{aligned} \quad (3.14)$$

where  $\tilde{Q}$  denotes the estimated flow curve,  $w_i \in \mathbb{R}^+$ ,  $i = 1, \dots, 4$ , the weighting factors and  $\vec{x}$  the parameters considered. Condition (3.12) is split up into three parts in order to allow for different weights being laid on  $Q(0)$  and  $Q(t_s)$ , which are crucial for the overall shape of the flow wave.

In the above conditions, no constraint regarding the flow level, i.e. maximum or mean flow, is considered. However, looking again at equation (3.10), it can be seen that multiplying the impedance with an arbitrary constant  $c > 0$  results in a flow wave with the same shape yet scaled by the factor  $1/c$  for a given pressure contour. From

$$Z_{in, \text{WK4p}}(\omega_n) = \begin{cases} R_p + \frac{P_\infty}{\bar{Q}}, & n = 0 \\ \frac{R_p}{1 + i\omega_n R_p C_a} + \frac{i\omega_n Z_c L}{i\omega_n L + Z_c}, & n \geq 1 \end{cases} \quad (3.15)$$

it furthermore follows that scaling the parameters  $R_p$ ,  $Z_c$  and  $L$  by  $c$  and  $C_a$  as well as mean flow  $\bar{Q}$  by  $1/c$  yields  $c \cdot Z_{in, \text{WK4p}}$ . This means that (1) flow can only be computed qualitatively, in other words only the shape can be obtained as is the case for the triangular as well as the average approximation and (2) the value of at least one parameter has to be fixed in order to allow for identification of the others.

In conclusion, by minimising the cost function (3.14) with respect to the Windkessel parameters assuming a fixed flow level, it should be possible to identify the parameters and at the same time compute a flow profile from a given pressure signal.

### 3.4.2 Methods and implementation

To develop and to test the proposed flow model, a dataset comprising pressure and flow waves of 183 persons was used. Of these 183, 61 were diagnosed as having severely reduced ejection fraction (EF), while the remaining 122 had normal EF. Pressure waveforms were acquired by radial tonometry and central pressure was obtained by a generalised transfer function (SphygmoCor, Atcor Medical, Sydney, Australia). The SphygmoCor system provides one peripheral and one central pressure time-contour, which represent the ensemble average over several heartbeats. These are stored in a proprietary database with a sampling rate of 128 Hz and can be saved as a .txt file with the inbuilt export function for further processing. Aortic blood flow was acquired by Doppler ultrasound and subsequently manually digitised. A more detailed description of the population and the measurements performed can be found in section 4.3 in the next chapter. All computations were realised in Matlab R2011b (The MathWorks Inc, Natick, Massachusetts, United States).

#### Estimation of initial values

In a first step, ED was estimated from the peripheral pressure wave using an algorithm that was developed by the cardiovascular diagnostics research group at the AIT. From the estimate of the time of valve closure  $t_s$ , the diastolic pressure portion was determined. Then, the exponential diastolic decay modelled by the WK4p, compare equation (2.42), was fitted to the experimental data in order to obtain first estimates of the two time constants  $\tau = R_p C_a$  and  $\sigma = L/Z_c$  as well as  $P_\infty$ . To reduce the influence of wave activities, the fitting was not applied to the whole diastolic pressure wave but started with a prespecified offset as proposed in literature [118, 131, 145]. Reported values for this delay range from 10% [145] to 33% [118, 131] of the total diastolic duration when using the monoexponential decay of the 2- or 3-element Windkessel. For this work, the offset was set to 20%. Moreover, the last 5 data points corresponding to the last 39 ms were neglected because the SphygmoCor signals often show a slight upstroke in the end, see figure 3.2.

Fitting of the diastolic decay was performed using the objective function

$$\sum_{j=nn}^{N-5} \left( P_m(t_j) - P_\infty - (\text{DBP} - P_\infty) \exp\left(\frac{T-t_j}{\tau}\right) - P_{LZ}(t_s) \exp\left(\frac{t_s-t_j}{\sigma}\right) \right)^2, \quad (3.16)$$

where  $P_m$  denotes the measured pressure signal,  $N$  the number of datapoints and  $nn$  the index corresponding to the time  $t_{nn} = t_s + 0.2(T - t_s)$ , i.e. the offset. This function was minimised

with respect to  $\tau, \sigma, P_\infty$  and  $P_{LZ}(t_s)$  using Matlab's `lsqnonlin` algorithm. The initial values for optimisation were set to  $[0.5, 0.02, 0.5 \cdot \text{DBP}, -1]$  and lower and upper bounds were defined by

$$0.1 \leq \tau \leq 2, \quad (3.17)$$

$$0.01 \leq \sigma \leq 10, \quad (3.18)$$

$$0 \leq P_\infty \leq 0.9 \cdot \text{DBP}, \quad (3.19)$$

$$-100 \leq P_{LZ}(t_s) \leq 0. \quad (3.20)$$

In the objective function (3.16), the periodicity of the pressure wave was used for the first exponential term in order to reduce the number of parameters to be identified, neglecting the end-diastolic value of  $P_{LZ}$ . Strictly speaking, the multiplicative term before the exponential should read  $(\text{DBP} - P_{LZ}(T) - P_\infty)$  instead of  $(\text{DBP} - P_\infty)$ , since  $P_{RC}(T) = P(T) - P_{LZ}(T) - P_\infty$ . However,  $P_{LZ}(T)$  is presumed to be very small, compare figure 2.13.

From the diastolic decay, initial estimates for  $\tau$ ,  $\sigma$  and  $P_\infty$  were obtained. As discussed above, the flow level has to be fixed to ensure identifiability of the Windkessel parameters. Therefore, the stroke volume SV was set to 70 ml, which is within the normal range for healthy adults at rest [73, p. 211]. Even though this choice is arbitrary, using a physiological flow level ensures that also the other parameters are within the range observed in other studies.

Together with the heartbeat duration  $T$  and the mean pressure  $\bar{P}$  derived from the measured signal, the resistance  $R_p$  was obtained by  $R_p = (\bar{P} - P_\infty)/\bar{Q}$  and subsequently  $C_a$  by  $\tau/R_p$ . The only missing parameter values are therefore  $Z_c$  and  $L$ . Without further information, one of these has to be fixed in order to derive the other one from the estimate of their ratio.  $Z_c$  represent the more widely-used parameter and its value has been investigated more extensively. Therefore,  $Z_c$  was set to 0.07 mmHg·s/ml, based on previously reported values for the WK4p [115, 119].  $L$  was subsequently computed as  $Z_c \cdot \sigma$ . Therewith, initial values for all parameters of the WK4p were available. The estimation procedure is summarised in figure 3.2.

### Computation of flow

The computation of aortic flow was carried out in the frequency domain. Therefore, the Fourier coefficients of the pressure signal were computed by the fast Fourier transform using Matlab's inbuilt `fft` function. For the further computations, the first 15 harmonics were used, compare section 2.2.

For a given parameter set consisting of the 5 Windkessel parameters  $R_p, C_a, Z_c, L$  and  $P_\infty$  as well as the individual threshold  $\tilde{n}$ , the model impedance was computed according to equations (3.15) and (3.11) and the corresponding flow harmonics were obtained by  $\hat{Q}_n = \hat{P}_n/Z_{\text{model}}(\omega_n)$ .

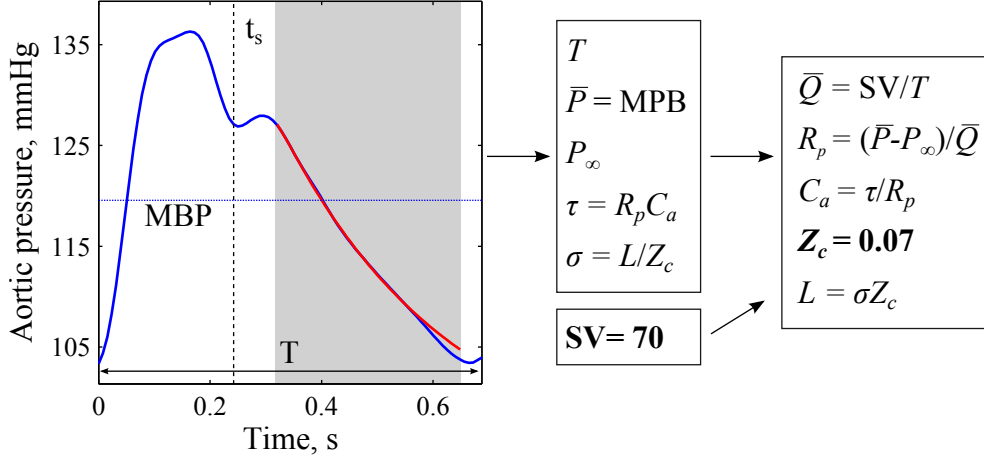


Figure 3.2: Estimation of initial values. From the measured pressure contour (blue), the heart-beat duration  $T$ , time of end of systole  $t_s$  and mean blood pressure  $\text{MBP} = \bar{P}$  are computed. Then the exponential decay of the WK4p (red) is fitted to the measured data during diastole (gray area) yielding estimates of the two time constants  $\tau$  and  $\sigma$  as well as of the asymptotic pressure level  $P_\infty$ . By setting  $\text{SV}$  to 70 ml and  $Z_c$  to 0.07 mmHg·s/ml (indicated by bold letters), initial estimates for all Windkessel parameters can be derived.

The temporal waveform of modelled blood flow was then recovered by

$$\tilde{Q}(t_j) = \bar{Q} + \text{Re} \left( \sum_{n=1}^{14} \hat{Q}_n e^{i\omega_n t_j} \right). \quad (3.21)$$

In order to identify the Windkessel parameters, the cost function defined in equation (3.14) was used. More precisely, the function

$$\begin{aligned} \text{error}(\tau, Z_c, L, P_\infty) = & 4 \cdot \tilde{Q}(0)^2 + 4 \cdot \tilde{Q}(t_s)^2 + \frac{1}{4} \cdot \sum_{j=s+1}^N \tilde{Q}(t_j)^2 + \\ & + \sum_{j=2}^9 \left( \frac{P(t_j) - P(0)}{Z_c} - \tilde{Q}(t_j) \right)^2, \end{aligned} \quad (3.22)$$

which equals  $\|\vec{e}(\tau, Z_c, L, P_\infty)\|_2^2$  for  $\vec{e}$  defined accordingly, was minimised using Matlab's `lsqnonlin` algorithm and the initial values obtained before.  $s$  thereby denotes the index corresponding to the end of systole and  $R_p$  and  $C_a$  were calculated in each step as described above, compare figure 3.2. Lower and upper bounds were moreover specified as

$$\begin{aligned} 0.1 &\leq \tau \leq 10, \\ 0.005 &\leq Z_c \leq 1, \\ 0.000001 &\leq L \leq 0.3, \\ 0 &\leq P_\infty \leq 0.9 \cdot \text{DBP}. \end{aligned}$$

$\tau$  instead of  $C_a$  was included because its value is independent of the absolute scaling of blood flow and boundary conditions are therefore easier to define. The individual threshold  $\tilde{n}$  used for

the definition of  $Z_{\text{model}}$ , compare equation (3.11), was not included in the optimisation procedure because of its discrete values. Instead, parameter identification was performed for each  $\tilde{n}$  varying from 2 to 10 and the result showing the lowest absolute error, i.e.  $\|\tilde{e}\|_1^2$ , was selected.

### 3.4.3 Sensitivity Analysis

#### Model parameters

To analyse the behaviour of the proposed model, as a first step, its sensitivity on changes in the Windkessel parameters as well as in the individual threshold  $\tilde{n}$  was investigated. For this purpose, an exemplary pressure waveform corresponding to a patient with normal EF, as well as one pertaining to a patient with reduced EF were used. From these, the parameters were identified as described in the last section and a flow wave was computed, as shown in figure 3.3. Then, the identified values given in table 3.1 were chosen as baseline and the effect of variations in single parameters was examined as shown in figures 3.4 and 3.5.

Parameter	Description	Unit	normal EF	reduced EF
$R_p$	peripheral resistance	mmHg·s/ml	0.373	0.235
$C_a$	total arterial compliance	ml/mmHg	0.995	2.052
$Z_c$	characteristic impedance	mmHg·s/ml	0.0593	0.0246
$L$	total arterial inductance	mmHg·s <sup>2</sup> /ml	0.0049	0.0018
$P_\infty$	asymptotic pressure level	mmHg	57.6	72.7
$\tilde{n}$	individual threshold, see eqn. (3.11)	-	4	5
SVR	total systemic vascular resistance	mmHg·s/ml	1.25	1.15
HR	heart rate	bpm	56	68
$\bar{P} = \text{MBP}$	mean blood pressure	mmHg	82.0	91.3
ED	ejection duration	ms	336	288
SV	stroke volume	ml	70	70

Table 3.1: Parameter values for the baseline parametrisation.

The baseline parameters differed substantially between the two datasets, resulting in very distinct flow waveforms that bore a strong resemblance to the Doppler flow measurements in both cases, as shown in figure 3.3. It should be kept in mind though that the stroke volume was chosen equally for both patients and the parameters are therefore wrongly scaled. Despite their different appearances and baseline values, the qualitative influence of variations in single parameters on the resulting waveform was very similar for both datasets, and will be discussed for each parameter separately in the following.

**The arterial compliance  $C_a$ .**  $C_a$  was varied over a wide range of values that covers the physiological range reported in literature, see e.g. [115]. In theory, the more compliant the arteries are, the more blood has to be ejected during systole in order to reach a given pressure level. This explains the large increase or decrease observed for peak flow when changing  $C_a$  while keeping all other parameters at their baseline values. Moreover, since SV was fixed, this



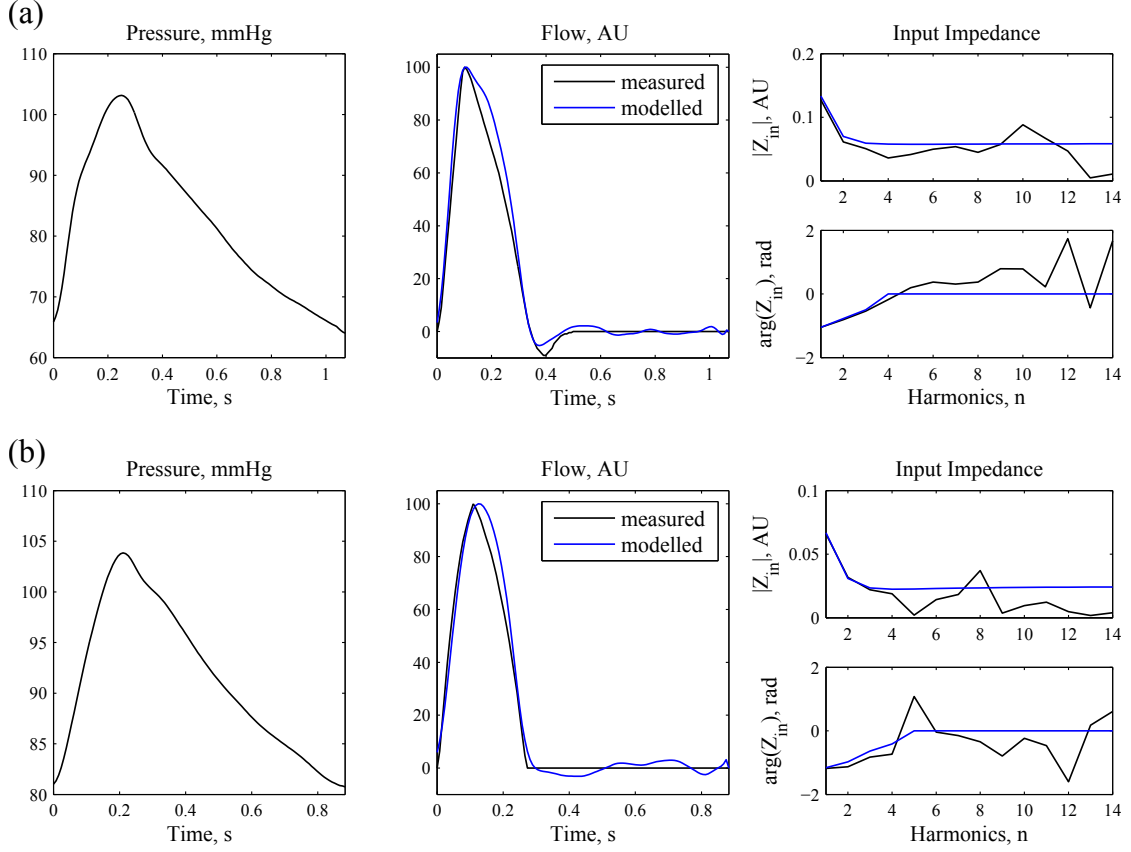


Figure 3.3: Exemplary data of a patient with normal EF (a) and one with reduced EF (b) used for sensitivity analysis. The synthesised aortic pressure (left panels) is used to compute the Windkessel flow (middle panels, blue) with the parameter values given in table 3.1. For comparison, also the Doppler flow waveforms (middle panels, black) as well as the corresponding input impedances (right panels) are shown.

resulted in either a continuation of blood flow or a backflow during diastole if the values were chosen too low or too high respectively. For the patient with reduced EF and high baseline  $C_a$ , it can furthermore be seen that the resulting flow wave resembles the pressure wave for very low values of  $C_a$ , approaching the situation in a rigid tube. The induced changes in the shape of the flow waveform were "monotonic" for both datasets, indicating that the optimal value represents a global minimum of the objective function with respect to  $C_a$ . This is corroborated by the results obtained in the whole study population depicted in figure 3.6(a). For this analysis, the error, more precisely  $\|\tilde{e}\|_2$ , obtained with the baseline value of  $C_a$  was taken as reference and its relative change caused by a change in  $C_a$  of up to 15% relative to its baseline value was computed per patient. For the medians, a parabolic shape can be observed with a symmetric increase in both directions, whereby baseline  $C_a$  represents the vertex.

**The characteristic impedance  $Z_c$ .**  $Z_c$  had a strong impact on the position of peak flow, with a shift to the right for higher values in both datasets, as depicted in figure 3.4. Similar to the behaviour observed for  $C_a$ , a marked increase in the square root of the objective function

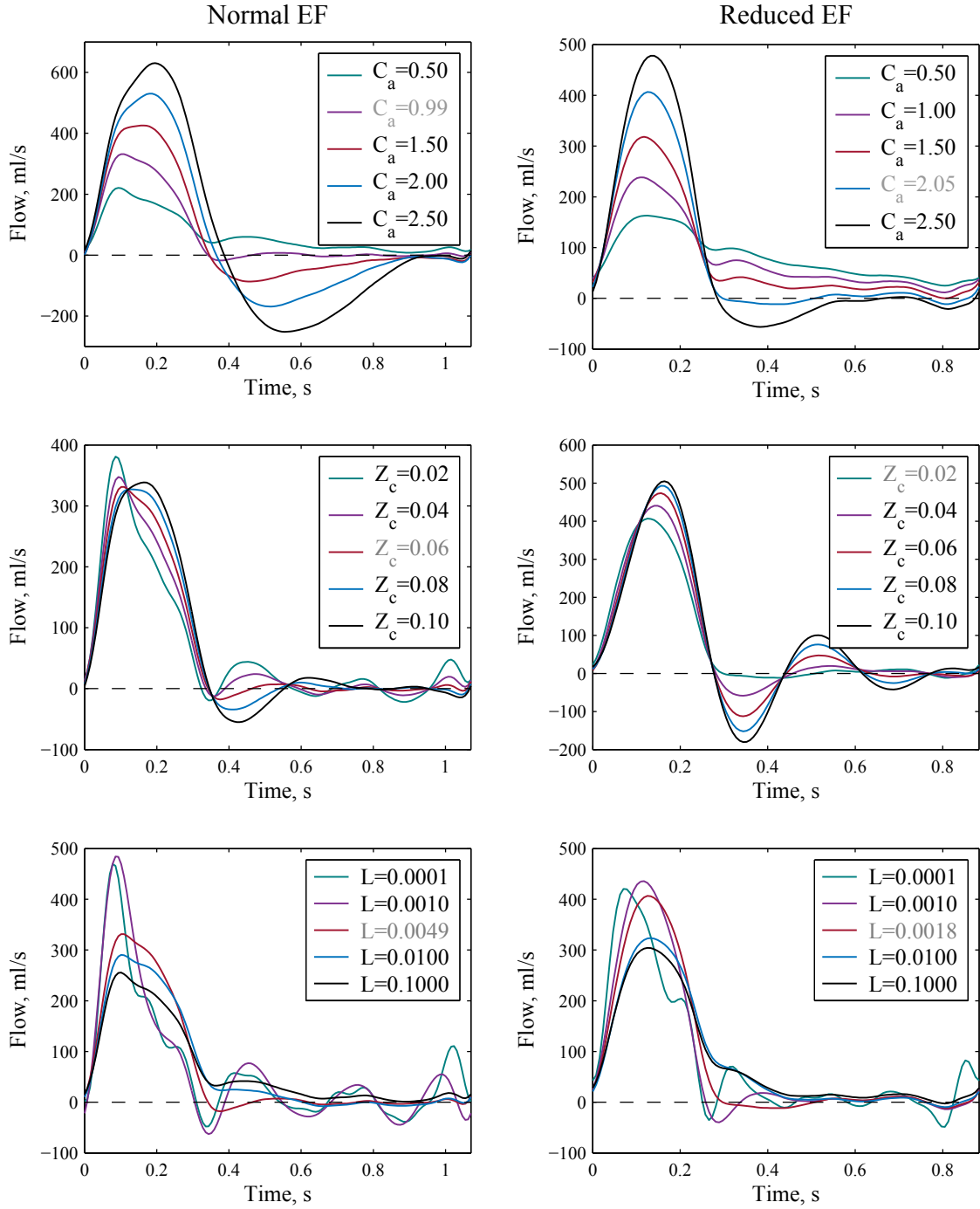


Figure 3.4: Sensitivity analysis showing the effect of changes in the model parameters  $C_a$ ,  $Z_c$  and  $L$  on an exemplary flow waveform of a patient with normal (left) and reduced (right) EF. The respective baseline parameters are indicated in gray.

was found for both an increase as well as a decrease in  $Z_c$  relative to its baseline value, see figure 3.6(b). However, this increase seemed to be less symmetric than for  $C_a$ . Also in the simulation results, a distinct behaviour for values below and above the baseline could be observed, with a more pronounced change in shape in the first case. In contrast to  $C_a$ , which mainly affects the low

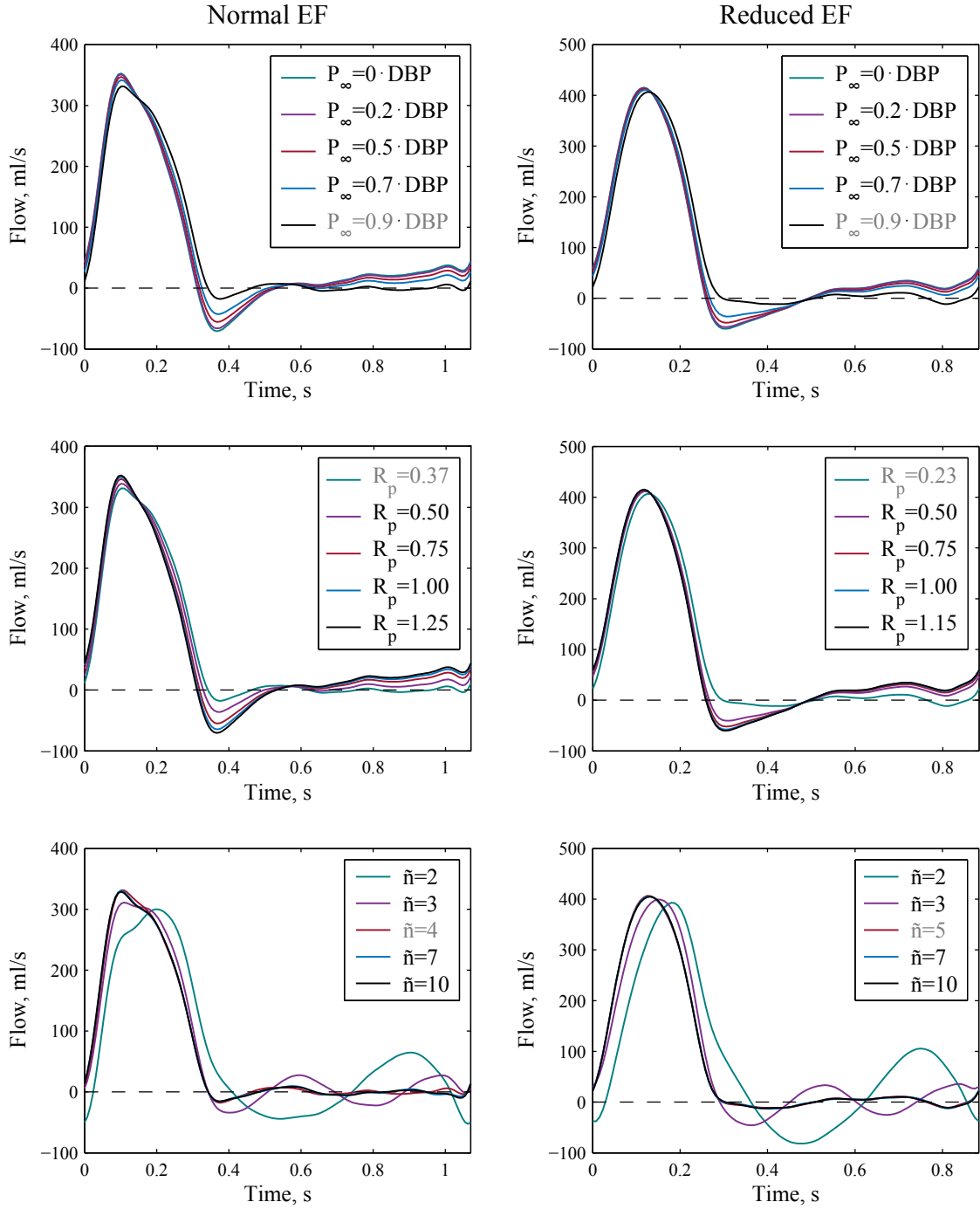


Figure 3.5: Sensitivity analysis showing the effect of changes in the model parameters  $P_\infty$ ,  $R_p$  and  $\tilde{n}$  on an exemplary flow waveform of a patient with normal (left) and reduced (right) EF. The respective baseline parameters are indicated in gray.

frequency range,  $Z_c$  describes the relation of the high frequency components of pressure and flow. Thus, for higher values, the fast pressure oscillations, that are responsible for the fast changes in the waveform like the upstroke, are damped, explaining the slower upstroke and shifted peak in the flow wave. For low values, on the contrary, they are amplified, resulting in a faster upstroke

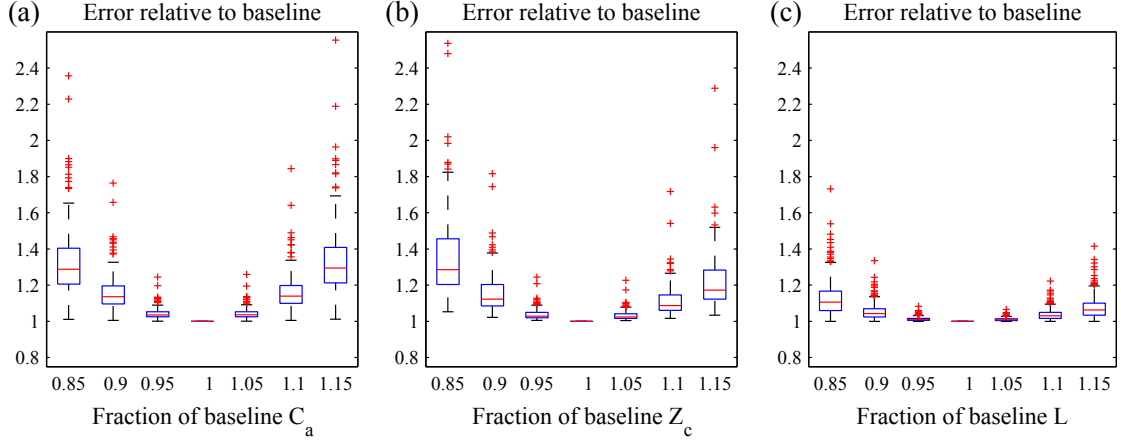


Figure 3.6: Boxplots showing the changes in the objective function relative to its baseline for varying  $C_a$  (a),  $Z_c$  (b) and  $L$  (c) from 85% to 115% of their respective baseline values while keeping all other parameters constant.

and an earlier peak. However, these effects of course depend on the specific pressure wave and the corresponding higher frequency amplitudes. As before for  $C_a$ , the considered range for variation was wide and the induced changes in the waveform moderate in comparison.

**The arterial inertance  $L$ .** The influence of  $L$  was similar to that of  $Z_c$ , showing a more pronounced qualitative change for values below the baseline. For  $L = 0$ , the WK4p equals the WK2, thus, the results obtained for very low values represent the transition from one model to the other. Except for the baseline,  $L$  was increased by a factor 10 per variation step, indicating that the influence of  $L$  on the flow waveform is overall rather small. Nevertheless, figure 3.6(c) shows, that also for  $L$ , the baseline value seems to represent a uniquely defined minimum of the objective function.

**The asymptotic pressure  $P_\infty$  and the peripheral resistance  $R_p$ .**  $P_\infty$  and  $R_p$  show the same effect, because systemic vascular resistance (SVR) as well as its components  $\bar{Q}$  and  $\bar{P}$  were fixed and their values are therefore coupled, see equation (3.15). The two plots are included separately for the sake of completeness only. Even though the values of  $P_\infty$  were varied over the whole range considered in the optimisation, i.e. from 0 to  $0.9 \cdot \text{DBP}$ , the induced changes in the flow waveforms were rather subtle, with a slight shift in maximum and a more pronounced shift in minimum flow. In contrast to the other Windkessel parameters, which all represented inner minima of the marginal error,  $P_\infty$  was optimal at its boundary, i.e.  $P_\infty = 0.9 \cdot \text{DBP}$ , for most of the datasets, including those shown in figure 3.5. This of course challenges the choice of the upper boundary, as will be discussed in the next subsection.

**The threshold  $\tilde{n}$ .**  $\tilde{n}$  appears in the formula for the computation of the model impedance  $Z_{\text{model}}$ , see equation (3.11). It represents the harmonic above which the phase of modelled input impedance is set to zero. Choosing it too low resulted in strong oscillations during diastole for both patients, whereas the influence of choosing it higher than the baseline was rather small,

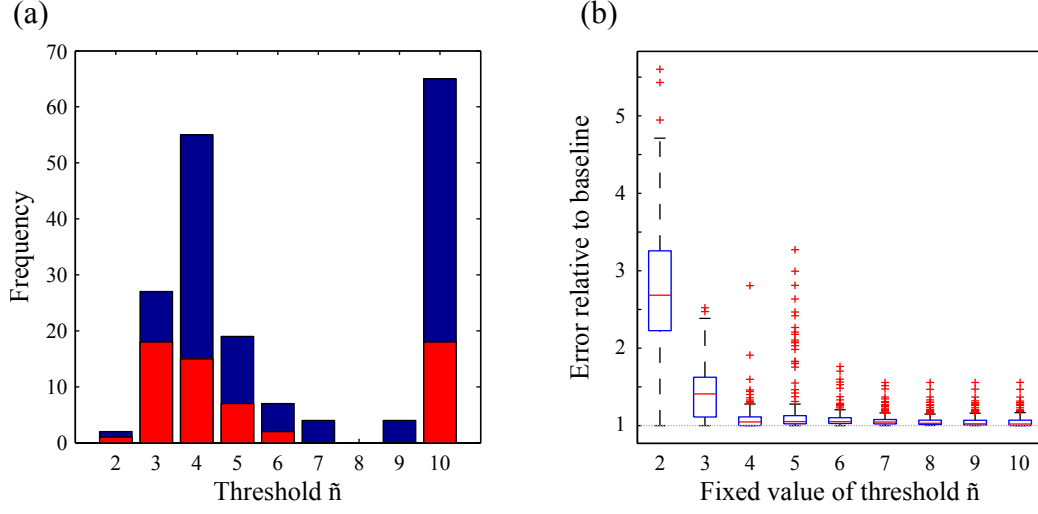


Figure 3.7: Analysis of the effect of the grid-search approach for  $\tilde{n}$ . (a): histogram showing the distribution of the individual threshold  $\tilde{n}$  in patients with reduced EF (red) and controls (blue). (b): boxplots showing the relative error when fixing  $\tilde{n}$  at one value compared to the grid-search approach.

compare figure 3.5. Therefore, the question arises if the computationally expensive grid search approach for  $\tilde{n}$  is expedient at all. Figure 3.7(a) shows a histogram of the distribution of the optimal  $\tilde{n}$  values determined in the whole population of 183 patients. Even though it was equal to its prespecified upper boundary for many, a second peak could be observed around the fourth harmonic, resulting in a higher number of patients with an optimal threshold  $\tilde{n} < 10$  than  $\tilde{n} = 10$ . This finding was furthermore independent of the EF-status. Thus, despite the small changes in the flow waveform observed for the two datasets considered for higher  $\tilde{n}$ , the histogram provides a first indication that allowing for different values of the threshold might be beneficial. To quantify this effect, the absolute error, i.e.  $\|\tilde{e}\|_1^2$ , obtained with the grid search was taken as baseline and its relative changes were analysed when fixing  $\tilde{n}$  between 2 and 10 for all patients. The results are shown in figure 3.7(b). Since the threshold with the lowest error is chosen in the original approach, in other words a second optimisation is performed with respect to  $\tilde{n}$ , naturally no improvement can be achieved when fixing its value implying that all relative errors are  $\geq 1$ , as can be observed in the boxplots. In line with the behaviour found for the two datasets shown in figure 3.5, low values of  $\tilde{n}$  were associated with a considerable increase in error, while for higher values of  $\tilde{n}$  the relative error decreased. However, also for  $\tilde{n} = 10$ , the median error was slightly higher than baseline, and significantly higher for several datasets. Hence, a constant threshold might work well for most patients, but it could still corrupt the results for some, overall justifying the grid search approach.

### Boundary conditions

For the Windkessel parameters  $C_a$ ,  $Z_c$  and  $L$ , the optimal values correspond to inner minima of the objective function for all datasets considered. Therefore, the boundary conditions have no influence on the optimal solution. For  $P_\infty$  on the contrary, its upper boundary value was optimal

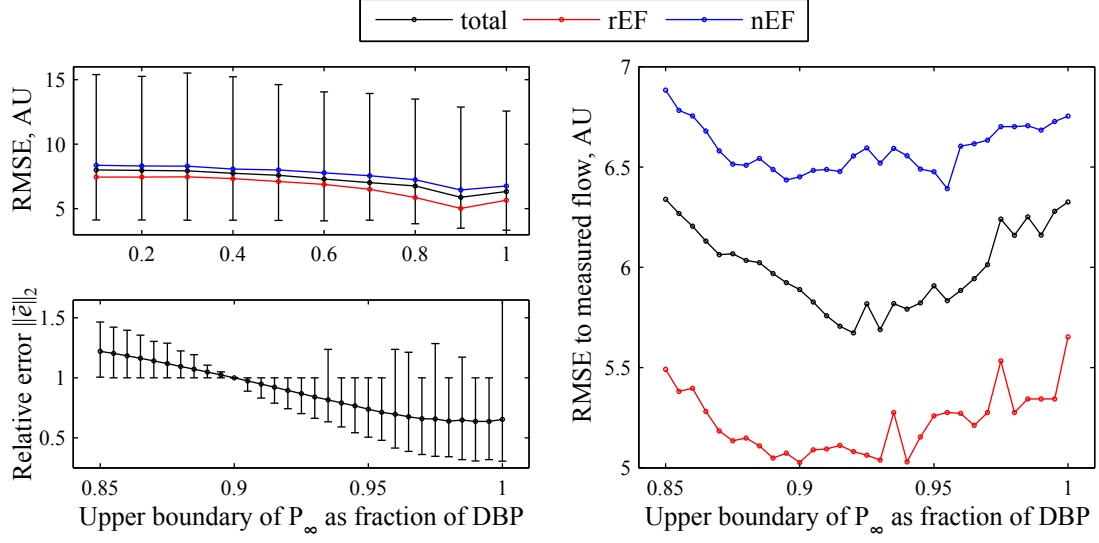


Figure 3.8: Analysis of the effect of the upper boundary of  $P_\infty$  used in the optimisation. The median RMSE between measured and modelled flow waves scaled to 100 AU for the upper boundary varying from 0.1 to 1 times DBP in steps of 0.1 (left, upper panel) as well as from 0.85 to 1 in steps of 0.005 (right, upper panel) is shown for the whole study population (black) as well as for patients with reduced (red) and normal (blue) EF separately. Left, lower panel: error relative to the baseline value of  $0.9 \cdot \text{DBP}$ . Error bars represent the respective 2.5% and 97.5% quantile.

in the great majority of the datasets. In other words, the imposed restrictions have an impact on the modelled flow waveforms in this case.

The choice of  $0.9 \cdot \text{DBP}$  was motivated by several considerations discussed in appendix A. First of all, from a model perspective,  $P_\infty$  is supposed to represent the pressure that is maintained by the vasculature when the heart stops beating and  $P_\infty$  should therefore be  $\leq \text{DBP}$ . From the pressure waves for missing heartbeats presented in appendix A, it can furthermore be seen that even though the pressure drop slows down, pressure continues to decrease without excitation, indicating that  $P_\infty$  should be less than DBP. Moreover, values reported in literature were substantially smaller than DBP. However, higher values seemed to be beneficial for the fitting quality, compare figure A.5. Therefore, the upper boundary of  $0.9 \cdot \text{DBP}$  was chosen as a compromise between the physiological interpretability and a good fitting result.

To investigate how this choice influences the modelled flow waveforms, the upper boundary was varied from 0.1 to 1 and the resulting value of  $\|\bar{e}\|_2$  relative to its baseline value, i.e.  $0.9 \cdot \text{DBP}$ , was computed. Additionally, the root mean square error (RMSE) to the measured flow wave was calculated for each dataset. Therefore, both modelled and measured flow were scaled to the same peak value of 100 arbitrary unit (AU) first. As expected, the objective function was on average decreasing with respect to the upper boundary for  $P_\infty$ , as shown in figure 3.8 for values between 0.85 and 1 times DBP. The number of optimal  $P_\infty$  that were equal to the upper boundary started to decrease rapidly for higher values, dropping from 174 at 0.9 to 17 out of 183 for an upper boundary equal to DBP. The average deviation from measured flow measured

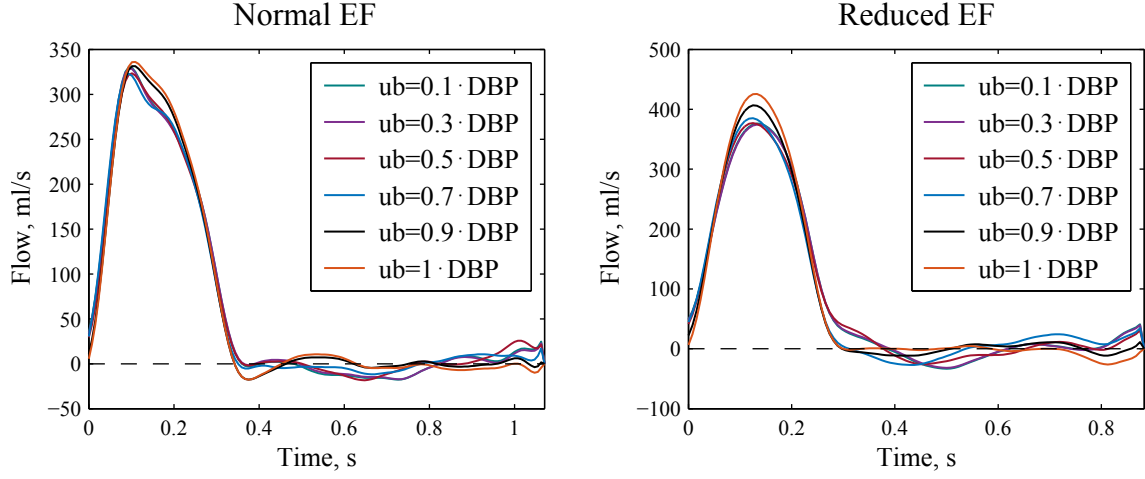


Figure 3.9: Influence of the upper boundary (ub) of  $P_\infty$  on an exemplary pressure wave from a patient with normal (a) and reduced EF (b).

by the RMSE, in contrast, was decreasing at first, but increased again for very high values. This behaviour is depicted in figure 3.8 for the upper boundary ranging from 0.1 to 1 relative to DBP in incremental steps of 0.1, as well as from 0.85 to 1 in steps of 0.005 to allow for a more detailed resolution of the relevant region. Moreover, in addition to the results obtained in the whole population, the RMSE is indicated for the two groups of patients separately. Despite a marked offset, with a substantially smaller error in patients with reduced EF that will be addressed in the next section, the behaviour with respect to the upper boundary of  $P_\infty$  was similar between the groups. Splitting the RMSE into its systolic and diastolic part furthermore showed that the increase for higher values was driven by the systolic part only, whereas the diastolic error resembles the behaviour of  $\|\vec{e}\|_2$ , i.e. it declines until reaching a plateau for very high values. Thus, while both the systolic and the diastolic RMSE decrease at first for increasing values of the upper boundary, this behaviour changes for values above 0.9. However, this qualitative change in the systolic error is not captured by the chosen objective function, which mainly represents the diastolic part, and restricting  $P_\infty$  therefore seems legitimate not only from a model perspective but also from the achieved output.

Overall, in both groups as well for the total median, the choice of 0.9-DBP seems reasonable with regards to the quality of the flow estimate. Furthermore, these results demonstrate that the model is robust against changes in  $P_\infty$ . Figure 3.9 finally shows the influence of variations in the upper boundary of  $P_\infty$  on the two exemplary waveforms used before, again underlining the rather small effect on the derived waveforms.

## Input

Last but not least the sensitivity of the model on changes in the input values, that is to say the pressure waves, will be analysed. For this purpose, the systolic, diastolic and mean pressure were

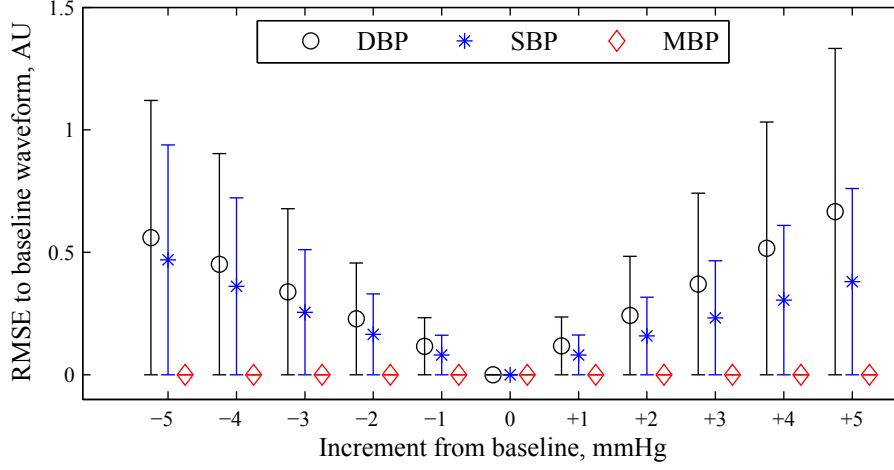


Figure 3.10: Analysis of the influence of changes in DBP, SBP and MBP on the modelled flow waveforms, assessed by the RMSE to the flow contour obtained at baseline. Median values are shown and error bars represent the respective 2.5% and 97.5% quantile.

varied separately according to

$$\begin{aligned}
 P_{\text{DBP}} &= (P - \text{DBP}) \cdot \left(1 - \frac{x}{\text{SBP} - \text{DBP}}\right) + \text{DBP} + x, \\
 P_{\text{SBP}} &= (P - \text{DBP}) \cdot \left(1 + \frac{x}{\text{SBP} - \text{DBP}}\right) + \text{DBP}, \\
 P_{\text{MBP}} &= P \cdot \left(1 + \frac{x}{\text{MBP}}\right),
 \end{aligned}$$

with  $x = -5, -4, \dots, 4, 5$  mmHg.  $\pm 5$  mmHg represents the average accuracy accepted for non-invasive blood pressure measurement devices by the ISO 81060-2. From the equations given above it follows that DBP remains unaltered when changing SBP and vice-versa while MBP of course changes accordingly. Likewise, SBP as well as DBP are affected by changes in MBP. To quantify the effect of the different pressure levels, the flow waveform obtained with the original pressure wave was taken as baseline and the deviation in the modelled waveforms induced by changes in SBP, DBP or MBP was assessed by the RMSE. All flow contours were again normalised to 100 AU to make the values comparable between the patients. The results are shown in figure 3.10 for the whole study population as well as exemplarily for the two datasets in figure 3.11.

The median RMSE as well as its deviation were very small for both DBP and SBP and changes in MBP had no impact at all on the corresponding flow waveforms, indicating that the model is robust against errors in the absolute values of blood pressure. The last result may not be surprising since the same argumentation used for the scaling of blood flow, compare equation 3.15, can of course be used for pressure as well. More precisely, for a fixed level of mean flow  $\bar{Q}$ , the same flow waveform is obtained for MBP and for  $c$ -MPB with an arbitrary positive constant  $c > 0$ , if  $P_\infty$ ,  $R_p$ ,  $Z_c$  and  $L$  are multiplied by  $c$  and  $C_a$  by  $1/c$ . In other words, if a flow contour is optimal for MBP, the same flow contour should be optimal for  $c$ -MBP. The fact



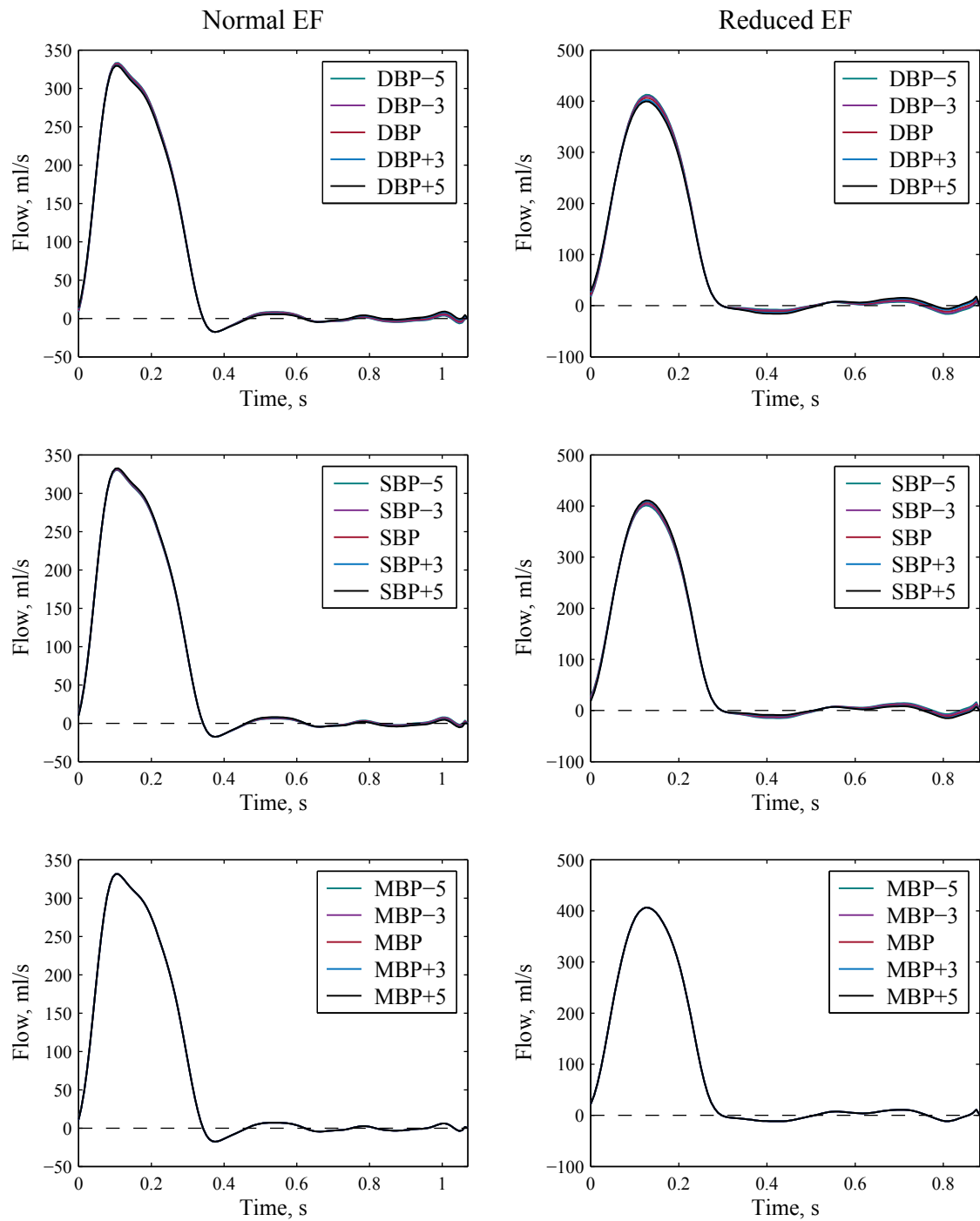


Figure 3.11: Sensitivity analysis showing the effect of changes in the magnitude of  $\pm 5$  mmHg in the input pressure levels DBP, SBP and MBP on an exemplary flow waveform of a patient with normal (left) and reduced (right) EF.

that the parameter identification procedure indeed yielded the same waveforms in both cases demonstrates that not only the model itself but also the numerical realisation is robust.

### 3.4.4 Simulation results

In this section, the capability of the model to reproduce different flow wave shapes and to provide accurate estimates of aortic flow will be investigated based on first simulation results. Therefore, the model was applied to all 183 datasets<sup>1</sup> and the resulting flow waveforms were visually assessed. The identified parameters are summarised in table 3.2 and exemplary waveforms are shown in figures 3.12 and 3.13 for patients with normal and reduced EF respectively. In addition to the modelled flow waves, the corresponding pressure waves computed from measured flow using  $Z_{\text{model}}$  determined from the identified parameters are shown. These can be seen as an indicator for the quality of identified parameters.

	median	IQR	min	max
$C_a$ , ml/mmHg	1.221	0.903 to 1.694	0.356	7.937
$R_p$ , mmHg·s/ml	0.3	0.255 to 0.356	0.111	0.994
$Z_c$ , mmHg·s/ml	0.0527	0.0411 to 0.0670	0.0205	0.117
$L$ , mmHg·s <sup>2</sup> /ml	0.00468	0.00358 to 0.00632	0.00107	0.3
$P_\infty$ , mmHg	71.01	64.43 to 77.28	0	102.38
$\tilde{n}$	5	4 to 10	2	10
SVR, mmHg·s/ml	1.209	1.082 to 1.396	0.597	1.848

Table 3.2: Results of the parameter identification. The median, inter-quartile range as well as total range are given for each parameter.

The results depicted in figures 3.12 and 3.13 were selected to provide a comprehensive impression of the variety of possible (measured) pressure and flow waveforms and of the resulting simulated flow waves. In most cases and in particular in patients with reduced EF, the proposed approach indeed yielded qualitatively correct estimates and the modelled input impedances mostly were in good qualitative agreement with the measured ones. However, the proposed approach and the underlying Windkessel model of course have their limitations, as evidenced by the flow waves shown in figure 3.13(c)-(d), presenting an exaggerated nose or even second peak during the flow decline. This behaviour is related to the upstroke of the pressure wave, more specifically, it is mainly found for waveforms with a pronounced shoulder in early systole. As presented in the last chapter, this shoulder is considered to be caused by the return of the reflected waves and the resulting pressure augmentation. However, the Windkessel models do not incorporate wave phenomena and the only explanation for a bump in the pressure wave is therefore a corresponding one in the flow wave. How pronounced the bump will appear in the flow wave then again depends on the specific parameter values. The fact that the flow model yielded better results for patients with reduced EF is well in line with this observation, since previous results showed a lower AIx for these patients compared to controls [21, 137], as will be discussed in more detail in the next chapters.

<sup>1</sup>The computations took 102s on a personal computer with an Intel®Core™i7-5600 CPU with 2.60GHz and 8GB RAM.

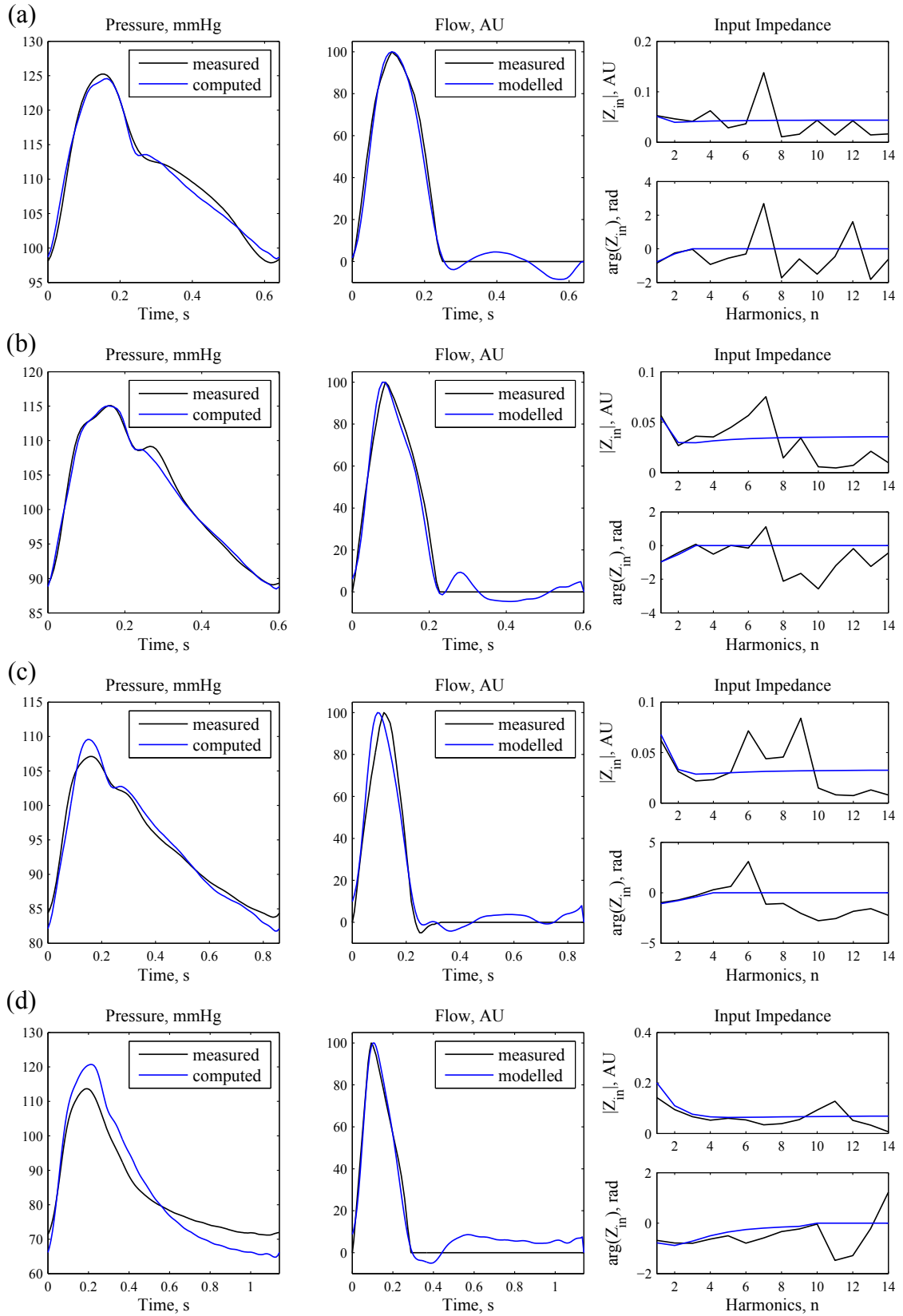


Figure 3.12: Exemplary simulation results for patients with reduced EF. Left panels: measured aortic pressure (black) and pressure computed from the identified parameters and the measured flow wave (blue). Middle panels: measured flow (black) and modelled approximation (blue). Right panels: measured (black) and modelled (blue) input impedance.

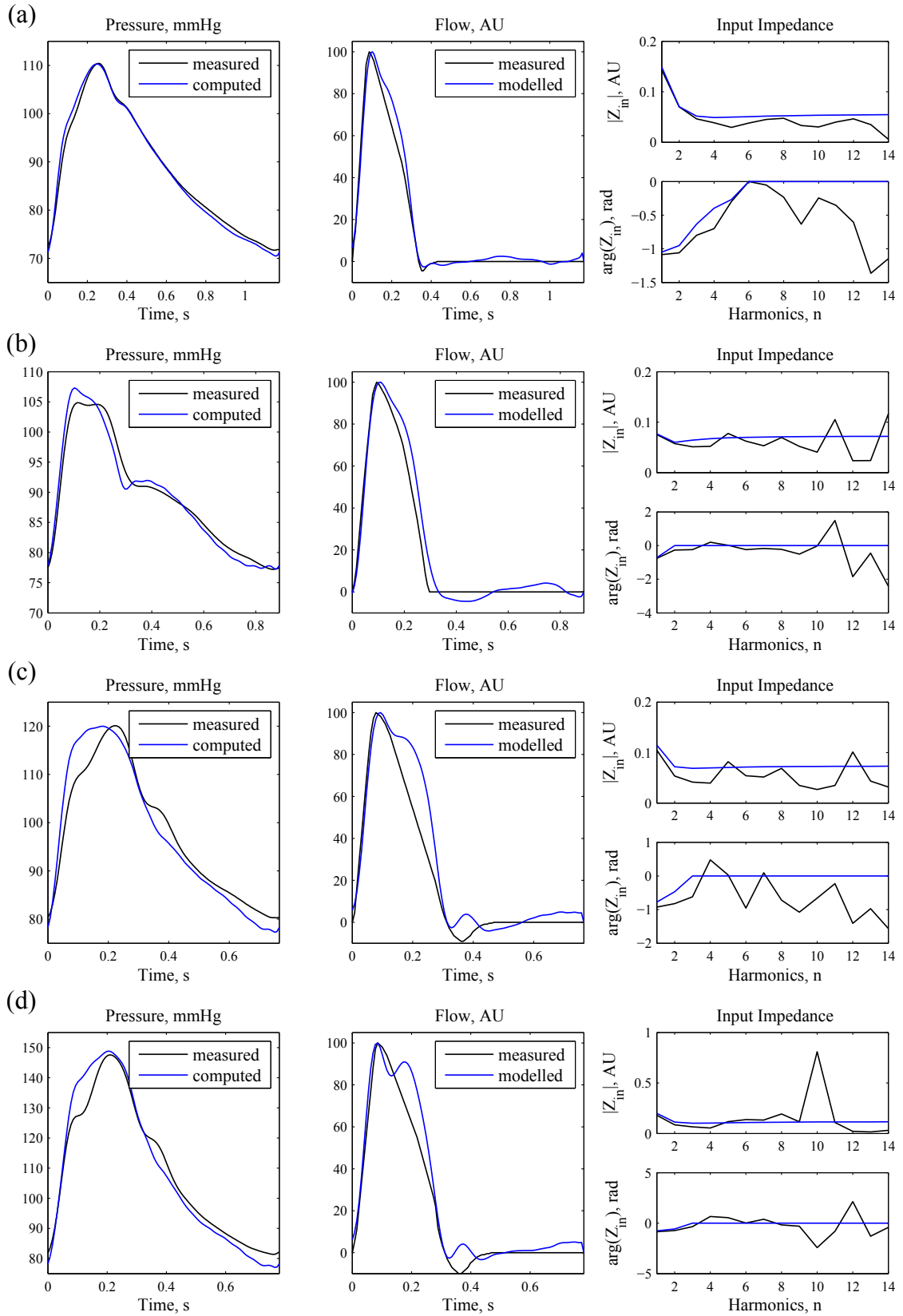


Figure 3.13: Exemplary simulation results for patients with normal EF. Left panels: measured aortic pressure (black) and pressure computed from the identified parameters and the measured flow wave (blue). Middle panels: measured flow (black) and modelled approximation (blue). Right panels: measured (black) and modelled (blue) input impedance.

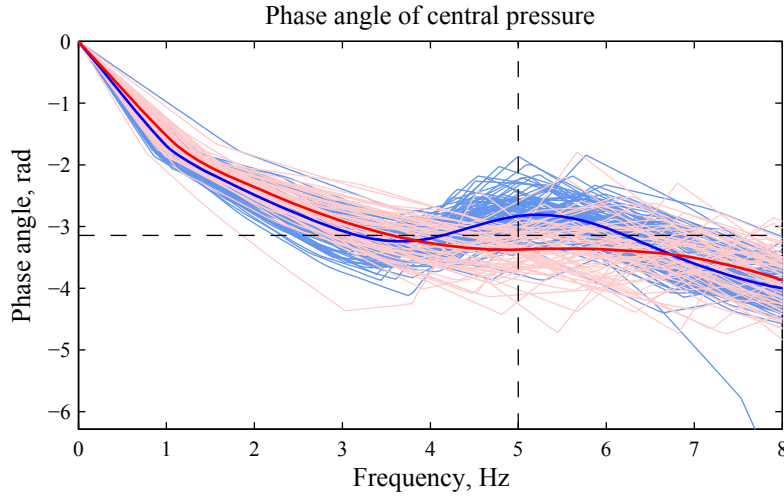


Figure 3.14: Phase angle of central pressure for patients with normal (blue) and reduced (red) EF as well as their corresponding averaged curve (bold line). The dashed lines indicate a phase angle of  $-\pi$  at 5Hz.

### 3.4.5 Combination with ARCSolver flow

The simulation results as well as the sensitivity analysis show that the proposed model is able to reproduce physiological and pathological ejection patterns based on pressure alone and is robust against changes in the model parameters, the input values as well as the boundary conditions applied. The fact that different types of flow contours can be obtained depending on the shape of the input pressure represents one of the main strengths of this approach, since this feature potentially enables its use also for systolic heart failure patients. However, on the downside, because of this flexibility, not all modelled waveforms match the measured ones or at least show the typical characteristics that one would expect from aortic blood flow. In particular, an exaggerated nose or even a second peak in the flow wave were observed in many patients with normal EF, making the waveforms unsuitable for further computations.

In an attempt to identify those pressure waveforms that result in the unwanted behaviour, a Fourier-analysis was performed and differences in the phase angle of pressure at around 5Hz were observed for patients with reduced and normal EF respectively, compare figure 3.14. In particular, for patients with normal EF, the corresponding phase angle tended to be  $> -\pi$ , while for patients with reduced EF it was on average  $< -\pi$ , implying that the first peak of the corresponding harmonic occurs earlier in the control group<sup>2</sup>, which might result in the shoulder in the pressure upstroke. A further analysis indeed indicated an association between high values of the phase angle at 5Hz and the occurrence of a strong bump in the pressure upstroke.

The ARCSolver flow was shown to provide reliable estimates for patients with normal EF [35]. Therefore, a combination of these two approaches might be expedient to obtain suitable estimates

<sup>2</sup>A wave with a frequency of 5Hz and a phase angle equal to  $-\pi$ , i.e. a sine wave, would reach its first peak at 0.1s. An additional phase shift by  $\pm 0.5$  rad would result in a time delay of  $\mp 0.016$ s.

of aortic flow, independent of cardiac function. From the considerations described above,  $-\pi$  was chosen as threshold for the phase angle of pressure at 5Hz to select either the ARCSolver flow (values above the threshold) or the Windkessel flow (values below the threshold). According to this criterion, the ARCSolver flow was chosen in 20 out of 61 patients with reduced EF and in 107 out of 122 patients with normal EF, eliminating all problematic flow waves. As a last finalising step, the modelled flow waveforms obtained with the Windkessel flow were set to 0 at the beginning and end of systole as well as during diastole.

## Chapter 4

# Non-invasive quantification of wave reflections in systolic heart failure: state of the art and data analysis

This chapter is dedicated to the examination of parameters derived by pressure pulse wave analysis (PWA), wave separation analysis (WSA) and wave intensity analysis (WIA) in patients with systolic heart failure. First, a brief summary of the current state of the art is given followed by a data analysis investigating the differences between patients with systolic heart failure and controls.

Most results presented in this chapter were previously published in the article "Determinants and covariates of central pressures and wave reflections in systolic heart failure" in the *International Journal of Cardiology* in 2015 [94].

### 4.1 State of the art

The mechanical factors leading to and resulting from heart failure (HF) as well as the resulting compensation mechanisms have been a main interest of cardiovascular research for many decades. With the development of high fidelity micromanometer catheters and electromagnetic velocity probes mounted at the catheter-tip in the second half of the 20th century, the instantaneous measurement of both aortic blood pressure and flow velocity at sufficient quality became feasible. Their analysis yielded valuable insights in the contractile state of the myocardium and the induced alterations in ventricular haemodynamics in HF. [63]

Various invasive studies were subsequently conducted during the 1970ies and 1980ies, comparing the aortic input impedance of patients with HF with reduced ejection fraction (EF) and controls [51, 52, 66, 99]. In all of these studies, the systemic vascular resistance (SVR), as a measure of the steady part of vascular load, was found to be significantly greater in patients with HF. However, with regards to the aortic characteristic impedance  $Z_c$ , i.e. the pulsatile component of vascular load related to aortic stiffness, findings were less conclusive. While Pepine et al. [99] reported a significant elevation of  $Z_c$  in HF patients, the other investigators found no statistical evidence for a difference between patients with and without HF, although numerical values were consistently higher [51, 52, 66]. Also wave reflections, assessed by the first modulus of the complex aortic reflection coefficient [52] or the reflection magnitude obtained by WSA [51], were (statistically) comparable between the groups. However, the considered study populations were small (10-17 subjects per group) and might have been statistically underpowered.

In contrast to these first, pioneering studies, most modern cross-sectional studies comparing the pulsatile hemodynamics in patients with HF to controls were based on non-invasively acquired data and thus included larger samples of patients [19, 21, 68, 88, 137]. Moreover, while patients were treated primarily with diuretics and digitalis in the earlier studies, recent heart failure patients were also receiving angiotensin-converting enzyme inhibitors or angiotensin receptor blockers and betablockers, in line with the current guidelines [101]. Furthermore, patients included in the more recent studies were generally older (mean age was approximately 60 years versus 40 years in the older studies) and had more comorbidities in comparison to those that were investigated 40 years ago, which might indicate a different aetiology and phenotype of HF in the patients considered [153].

In these contemporary, well treated patients, ejection duration (ED) was markedly shorter (with a mean difference in the range of 30 to 40 ms) in HF patients versus controls in most investigations [21, 68, 137], an observation that was already reported by Weissler and colleagues [141] in 1968. This reduction seems to be related to the severity of left ventricular (LV) systolic dysfunction, since Paglia et al. [88], who studied patients with moderately to severely reduced EF, could not confirm this difference in their data at first. However, when only patients with severe left ventricular systolic dysfunction (LVSD) defined as  $EF \leq 30\%$  were considered, a significant shortening in ED became again apparent. Even Mitchell et al. [68] reported a significant reduction in ED despite pooling patients with heart failure with reduced and preserved EF for analysis. This might have actually led to an underestimation of the real effect since ED was found to be shorter in patients with HF with reduced than with preserved EF [125], a tendency that was also confirmed by Mitchell et al. in subgroup analysis. Indeed, ED was reported to be even prolonged in patients with heart failure with preserved EF compared to subjects without HF [139]. A rather small, yet still significant, reduction in ED was observed by Denardo and colleagues [21] ( $\approx 20\text{ms}$ ), which is possibly due to the intrinsic link between heart rate (HR) and ED and the fact that HR served as a matching criterion for patients with HF and controls in their study. This is again in line with the results presented by Weissler et al. showing an alteration in the association between HR and ED for patients with systolic HF with lower values



of ED for the same HR in HF [141].

Another difference that was repeatedly reported was a significantly lower augmentation index (AIx) in HF patients [21, 68, 137]. In the study by Curtis et al. [19], in contrast, HF was associated with an increased AIx, albeit not significantly. However, compared to the aforementioned works, patients with HF were older than controls in their study and the LV impairment assessed by EF was on average less severe with more female patients included in the HF group which might explain the discrepancy. This is corroborated by the results reported by Paglia and colleagues [88], who found higher values of AIx in patients with moderate than with severe LVSD or controls, which resulted in no difference to controls when looking at the HF patients as a whole.

With regards to the pressure levels, rather contradictory results were obtained. While both peripheral and estimated central systolic blood pressure were either lower [21, 88] or comparable [68, 88, 137] for HF patients versus controls, all three possible cases were reported for the pulse pressure.

Besides the classic pulse wave analysis parameters, Denardo and coworkers [21] as well as Paglia and colleagues [88] additionally reported pressure time integrals and Mitchell and coworkers [68] as well as Curtis et al. [19] included Doppler flow measurements to perform WSA and WIA respectively. It should be noted though that the two last mentioned works both used tonometrically measured carotid pressure waveforms as estimates of central pressure and combined it with either aortic [68] or carotid [19] Doppler flow waveforms.

In keeping with the lower values of AIx, Denardo and coworkers [21] reported a reduction in wasted energy in their HF group, which primarily consisted of patients with severe LVSD. Paglia et al. [88] observed the same behaviour for patients with severe dysfunction but not for their entire group of HF patients. Denardo et al. furthermore found a decrease in systolic pressure time index (SPTI) multiplied by HR, which represents a measure of the LV oxygen requirement per minute (i.e. normalised to HR), and a higher myocardial viability ratio (DPTI/SPTI) in HF, which they speculated to "serve as a compensatory mechanism in severe LVSD to optimize efficiency of the failing LV" [21, p.153].

Mitchell et al. [68] followed the example set by the older invasive studies and examined the characteristic impedance  $Z_c$ , although they used a time domain approach for estimation while prior studies were set in the frequency domain. They observed an elevation of  $Z_c$  in HF and argued that the stiffness of the central conduit arteries might be increased, even though no difference in carotid-femoral pulse wave velocity (PWV) was found. In contrast to the prior studies, SVR was comparable between the groups, as was total arterial compliance. Furthermore, the amplitude of the forward travelling pressure wave  $|P_f|$  was increased, while  $|P_b|$  was similar, resulting in a decreased reflection magnitude (RM) in patients with HF compared to controls.

With respect to the WIA parameters, a totally different behaviour was found by Curtis et al. [19]: the energy of the forward S wave resulting from ventricular ejection was reduced, while the R and D wave energy, related to wave reflections and ventricular relaxation dynamics, were unaltered in patients with systolic HF compared to controls, which led to a significant elevation of relative wave reflections, i.e. the ratio of the R to S wave energy. Also Sugawara et al. [120] reported a significant reduction of the first but not the second peak of wave intensity in patients with dilated cardiomyopathy compared to controls. Unfortunately though, no further information about the study is available, since data was not published.

In summary, studies performed in patients with systolic heart failure yielded rather inconclusive results regarding alterations in arterial stiffness or wave reflections. The common findings of the older studies, i.e. a higher peripheral resistance and a tendency towards higher aortic stiffness in systolic HF patients, could not be confirmed in the more recent ones, which might be due to the differences in medication or even differences in the phenotype and aetiology of HF in the patients considered. The results obtained in the newer studies seem to imply that wave reflections are reduced in patients with HF. However, the composition of the HF groups included was diverging between the non-invasive studies, ranging from a combination of HF with preserved and reduced EF [68], to purely systolic HF patients yet with differing severity levels of LV dysfunction [21, 88, 137]. Furthermore, different matching criteria were applied to select the control group, including age [21, 88, 137], gender [21, 88, 137], anthropometric measures (height, weight, body surface area or body mass index) [21, 137], heart rate [21], brachial pressure levels [88, 137] or none [19, 68], making the results less comparable.

## 4.2 Aim of the study

The number of studies investigating alterations in non-invasively derived parameters of pulsatile haemodynamics in patients with systolic heart failure is very limited, especially with regards to the methods based on pressure and flow, namely WSA and WIA. Moreover, the reported results were inconsistent. Therefore, the aim of this study is threefold: (1) to investigate the differences in PWA, WSA and WIA parameters between patients with systolic HF and controls, (2) to compare the different methods against each other and finally (3) to analyse the relation between measures of cardiac and arterial function.

## 4.3 Methods

### Study population

Patients were collected between 2009 and 2011 from a cohort undergoing diagnostic coronary angiography for suspected coronary artery disease at the university teaching hospital Wels-Grieskirchen in Wels, Austria. All measurements were performed in the hospital Wels-Grieskirchen within the framework of ongoing studies on the role of pulsatile haemodynamics in cardiology,

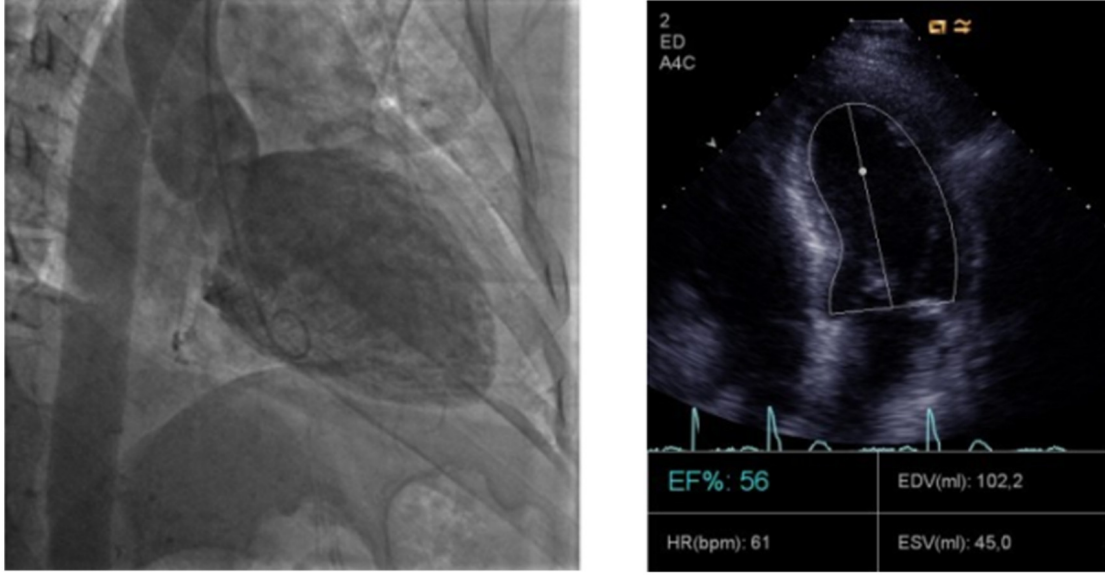


Figure 4.1: Examples of an angiographic and echocardiographic measurement of diastolic LV volume. Left: left ventriculogram during diastole taken from [16], licensed under CC BY-NC 4.0, right: echocardiogram obtained in the apical 4 chamber view during diastole taken from [62], licensed under CC BY 2.0.

which were approved by the local ethics committee. Participants provided written informed consent prior to enrolment. Exclusion criteria included arrhythmias (mainly atrial fibrillation), valvular heart disease exceeding a mild severity level and unstable clinical conditions.

The study population considered throughout this thesis consisted of 61 patients diagnosed with severely reduced EF (rEF) and a control group comprising 122 patients with normal EF (nEF), matched for gender, age, body mass index and brachial blood pressure levels.

### Data acquisition

Pressure waveforms were recorded non-invasively at the radial artery using applanation tonometry (Millar SPT 301, Millar, Inc., Houston, Texas, US) and calibrated with absolute brachial pressure values obtained with an automated oscillometric sphygmomanometer (Omron M5-I, Omron Healthcare, Kyoto, Japan). Aortic pressure was subsequently derived by the SphygmoCor system (AtCor Medical Pty. Ltd, West Ryde, Australia) and its inbuilt generalised transfer function from ensemble averaged peripheral pressure waves. The waveforms of peripheral and central pressure processed by the SphygmoCor system were finally exported and converted to a sampling rate of 83.3 Hz, which represents the sampling rate used in the ARCSolver algorithms, compare figure 4.2. All further computations were carried out in Matlab R2011b.

Besides the pressure reading, coronary angiography, echocardiography as well as a blood exam-

ination were performed in all patients within a maximum of 4 days of each other. 6 French fluid filled pigtail catheters were used for cardiac catheterisation, enabling the invasive measurement of LV and aortic pressure levels before contrast cineangiography. Additional pressure related indices like maximum LV pressure rise, a measure of cardiac contractility, were automatically provided by the coronary angiography system (Siemens Artis Zee with AXIOM Sensis hemodynamic recording system, Siemens healthcare, Erlangen, Germany). From the monoplane cineangiograms in RAO view, cardiac volumes and EF were determined, compare figure 4.1. During catheter pullback, aortic PWV was quantified by the foot-to-foot technique using pressure measured at the ascending aorta and the aortic bifurcation. The corresponding positions were marked with a tape on the catheter to derive the exact distance, compare [138].

Echocardiographic examination comprising a detailed 2-dimensional and Doppler echocardiogram was carried out immediately before or after pressure measurement using a Philips iE33 Ultrasound machine (Philips Medical Systems, Andover, Massachusetts). LV systolic function and geometry were quantified according to the recommendations of the American Society of Echocardiography [50], compare figure 4.1. Blood flow velocity at the LV outflow tract was measured by pulsed wave Doppler ultrasound and the spectral density recordings were manually digitised to obtain aortic blood flow waveforms, whereby the width of the flow was scaled to match the estimated ejection duration provided by the SphygmoCor system. Thereafter, flow and pressure were carefully aligned in time using the respective upstrokes as visual indicators, see figure 4.2. The so-obtained flow velocity  $U$  was normalised to an amplitude of 100 arbitrary units (AU) to be used as a qualitative waveform of volumetric blood flow  $Q$ .

From the blood samples, plasma levels of N-terminal pro-B-type natriuretic peptides (NT-proBNP) were determined with the electrochemiluminescence immunoassay "ECLIA" on the Elecsys 1020 analyser (Roche Diagnostics, Mannheim, Germany). NT-proBNP is produced by the heart "and released into the circulation in response to increased wall tension" [7, p. 150]. An elevation of the NT-proBNP level represents an important indicator of cardiac dysfunction and diagnostic marker for heart failure [101].

### Pulse wave analysis

Pressure levels and timing information, i.e. HR and ED, were automatically derived by the SphygmoCor system. From these estimates, the gender-specific left ventricular ejection time index (LVETI) was computed according to the formulas  $LVETI = 1.7 \cdot HR + ED$  for male and  $LVETI = 1.6 \cdot HR + ED$  for female patients [30], which are based on the work by Weissler et al. [141]. SphygmoCor's inbuilt PWA algorithms furthermore provided the AIx and all associated parameters, compare section 2.1.2.

In addition, the pressure time indices and the wasted energy introduced in section 2.1.3 were computed from the central pressure waveforms using the SphygmoCor parameters to determine the respective portions and Matlab's `trapz` function for integration. These values obviously

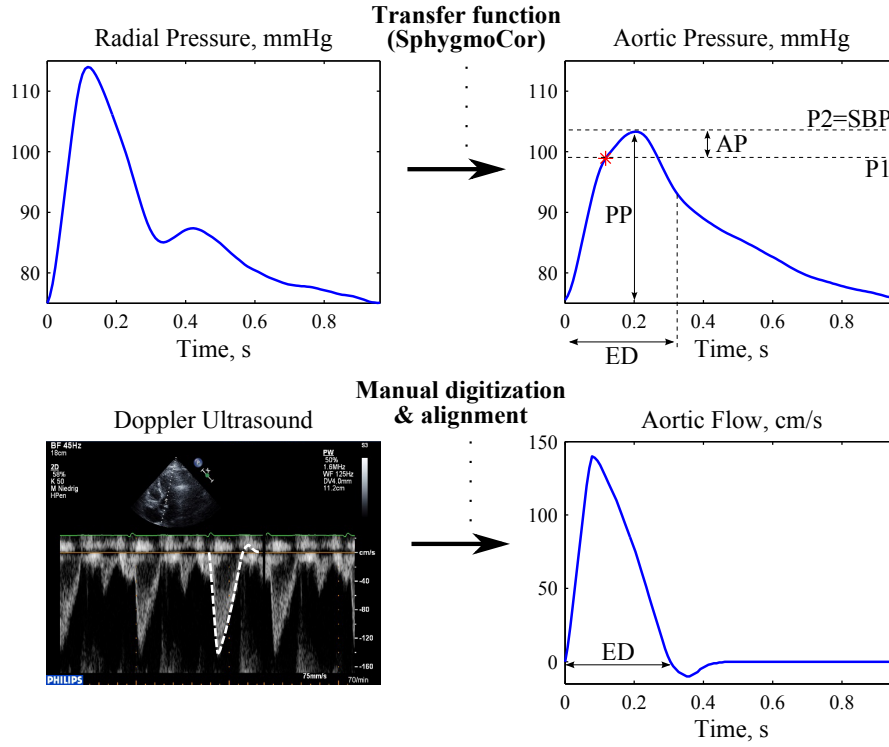


Figure 4.2: Assessment of aortic blood pressure and flow. The tonometrically measured radial pulse waveforms are processed with the SphygmoCor software to obtain aortic pressure as well as the PWA parameters (upper panel). Blood flow velocity is measured by Doppler ultrasound in the LV outflow tract, then manually digitized and aligned with the synthesised aortic pressure waveform (lower panel). Adapted from [95], © Institute of Physics and Engineering in Medicine. Reproduced with permission. All rights reserved.

depend on the integration intervals, i.e. the heart beat duration. To diminish this influence, the pressure time indices per minute were calculated by multiplication with HR, compare [21].

### Wave separation analysis

For wave separation analysis (WSA), central pressure and flow were Fourier transformed using Matlab's `fft` function and  $Z_{in}$  was computed.  $Z_c$  was then estimated as the average of the harmonics  $> 3\text{Hz}$  up to approximately  $10\text{Hz}$ , excluding values bigger than 3 times the median to control for outliers [116]. More precisely, the averaging started at the first harmonic corresponding to a frequency higher than  $3\text{Hz}$  and ended at the harmonic being closest to  $10\text{Hz}$ .

Reported procedures for the estimation of  $Z_c$  most often involve a fixed harmonic range for all patients, e.g. harmonics 4 to 10 [37, 123]. However, the idea behind this estimation procedure is based on the wavelength and therefore the absolute and not the relative frequency with respect to the heart rate, that is to say the harmonic, compare section 2.2.3. Moreover, while the difference in the frequencies considered might be small for similar heart rates, failing of the left ventricle is often reflected in an increase in HR [45]. This implies that, for a fixed harmonic range, different

frequencies might be used for the computation of  $Z_c$  in the two groups of patients included in this work. To ensure comparability, the frequency and not the harmonic range was therefore prescribed in the present analysis, as in the older invasive studies [51, 66, 99], even though this means that the number of harmonics used for estimation could vary between the patients.

From the estimate of  $Z_c$ , forward and backward pressure waves were computed in the time domain, as described in section 2.2, and RM as well as the reflection index (RI) were computed. It should be noted that the normalisation of aortic flow has no impact on the form or magnitude of either  $P_f$  or  $P_b$ , as  $Z_c$  changes inversely proportional with the normalisation factor and the product  $Z_c Q$  therefore remains unchanged.

### Wave intensity analysis

The wavefronts  $dP$  and  $dU$  were computed as the incremental changes in  $P$  and  $U$  per time step  $dt = 0.012$  s resulting from the chosen temporal resolution. For the separation, the wave speed  $c$  times the blood density  $\rho$  was estimated from the slope of the PU-loop during early systole using the first 6 datapoints ( $\approx 60$  ms). From the forward and backward wave intensities, the peaks of and areas under the S, D and R wave were calculated. For the R wave, absolute values were used, i.e. both the peak and energy are reported as positive values.

### Statistics

For the statistical analyses, the statistical software MedCalc version 16.2.1 (MedCalc Software bvba, Ostend, Belgium) as well as Matlab 2011b were used. Continuous data is summarised as mean (standard deviation) if normally distributed and median [inter quartile range] else-wise, depending on the results of a Shapiro-Wilk (platykurtic data) or Shapiro-Francia (leptokurtic data) test for normality<sup>1</sup>. Differences between the groups were assessed using an unpaired t-test (normally or log-normally distributed data with equal variances), Welch-test (normally or log-normally distributed data with unequal variances) or Mann-Whitney-U test (non-normally distributed data), as appropriate. Categorical data is presented as number (percentage) and the chi-squared test was used for group-wise comparison. Multiple regression analysis was performed to correct for confounders (ANCOVA) and associations between different parameters were evaluated with Pearson's correlation coefficient. For all tests, significance was assumed at a 5% level.

## 4.4 Results

The study population consisted of predominantly male patients (92%) and mean age was 60.3 (range 27 to 87) years for patients with reduced EF and 59.5 (range 33 to 80) for controls. The

<sup>1</sup>This test was performed using the `swtest` function by Ahmed Ben Saïda, retrieved from <https://de.mathworks.com/matlabcentral/fileexchange/13964-shapiro-wilk-and-shapiro-francia-normality-tests>, December 2015.

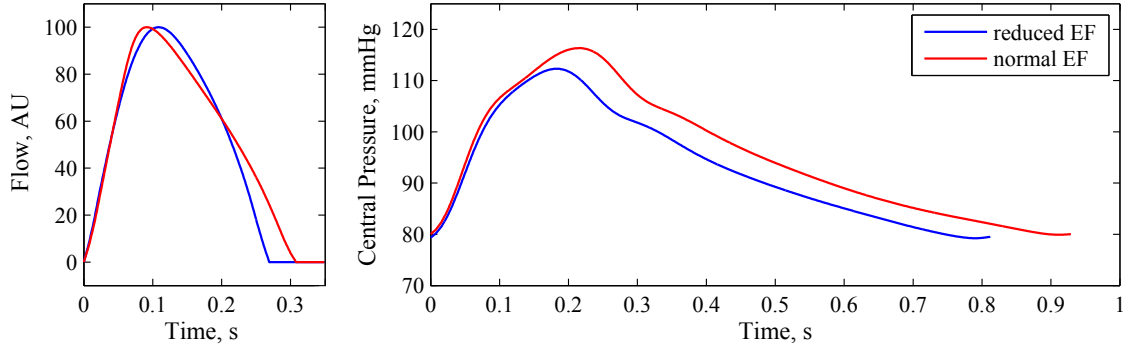


Figure 4.3: Averaged flow and pressure waveform for patients with reduced (blue) and normal (red) EF. Pressure levels, heart rate and ejection duration were set to the respective group means.

	N	reduced EF	normal EF	P value
Patients, n		61	122	
Female gender, n (%)	61/122	5 (8 %)	10 (8 %)	1.00
Age, years	61/122	60.3 (12 SD)	59.5 (10.6 SD)	0.65
Height, cm	61/122	174 [170,178]	174 [170,178]	0.77
Weight, kg	61/122	86 [76.8,97]	85 [76,96]	0.83
Body mass index, kg/m <sup>2</sup>	61/122	28.4 [25.8,31.6]	28.3 [25.1,31.1]	0.68
SBP brachial, mmHg	61/122	125 (20.3 SD)	127 (13.7 SD)	0.53
DBP brachial, mmHg	61/122	78.6 (13.4 SD)	79.1 (9.42 SD)	0.78
Hypertension, n (%)	61/122	40 (66 %)	80 (66 %)	1.00
Diabetes, n (%)	61/122	21 (34 %)	20 (16 %)	0.006
Coronary artery disease, n (%)	61/122	33 (54 %)	50 (41 %)	0.09
Medication				
ACE/ARB, n (%)	61/122	52 (85 %)	47 (39 %)	< 0.0001
Betablocker, n (%)	61/122	51 (84 %)	58 (48 %)	< 0.0001
Calcium channel blocker, n (%)	61/122	6 (10 %)	11 (9 %)	0.86
Diuretics, n (%)	61/122	35 (57 %)	31 (25 %)	< 0.0001
NO donor, n (%)	61/122	9 (15 %)	11 (9 %)	0.24
Acetylsalicylic acid, n (%)	61/122	44 (72 %)	97 (80 %)	0.26
Statin, n (%)	61/122	22 (36 %)	52 (43 %)	0.39

Table 4.1: Baseline characteristics of the study population. ACE, angiotensin converting enzyme inhibitors; ARB, angiotensin receptor blocker. P-values indicate results of a group-wise comparison.

	N	reduced EF	normal EF	P value
Cardiac catheterisation, angiography				
LVEDV, ml	58/113	250 (79.5 SD)	130 (30.9 SD)	< 0.0001
LVESV, ml	57/113	171 [124,242]	33 [25,45]	< 0.0001
SV, ml	57/113	58 [48,79]	93 [75,113]	< 0.0001
EF, %	57/113	27.5 (10.5 SD)	72.6 (9.46 SD)	< 0.0001
LV systolic BP, mmHg	60/119	123 (26.5 SD)	137 (22.3 SD)	0.0005
LV end-diastolic BP, mmHg	60/119	22.9 (8.39 SD)	15.2 (5.22 SD)	< 0.0001
LV dP/dt max, mmHg/s	57/113	1130 [898,1440]	1873 [1627,2148]	< 0.0001
SBP aortic, mmHg	61/120	123 [111,136]	134 [122,147]	0.0006
DBP aortic, mmHg	61/120	70 [59,80.5]	68.5 [61,75.5]	0.71
PP aortic, mmHg	61/120	48 [37,66.8]	65 [53,75]	< 0.0001
PWV, m/s	60/117	8.5 [6.6,9.9]	7.7 [6.6,9.2]	0.24
2-dimensional echocardiography				
LVEDV, ml	61/120	170 [133,246]	81.5 [66.5,95]	< 0.0001
LVESV, ml	61/120	118 [90,175]	25 [17,31]	< 0.0001
SV, ml	61/121	51.9 (21.4 SD)	55.7 (15.6 SD)	0.23
EF, %	61/121	27.9 (8.65 SD)	69.4 (7.55 SD)	< 0.0001
LV mass, g	54/115	257 [206,317]	169 [145,190]	< 0.0001
Laboratory analysis				
NT-proBNP, pg/ml	61/119	1766 [810,5211]	90 [44.8,174]	< 0.0001

Table 4.2: Clinical measurements. LVEDV, LV end-diastolic volume; LVESV, LV end-systolic volume. Echocardiographic LV volumes were assessed by the modified Simpson's rule, compare [50]. P-values indicate results of a group-wise comparison.

two groups were well matched with regards to gender, age, body mass index and brachial systolic and diastolic pressure levels. Coronary artery disease as well as hypertension was as common in rEF patients as in controls, but diabetes was more frequent in rEF. Moreover, the usage of diuretics, betablockers and inhibitors of the renin–angiotensin system was proportionally higher in rEF. Baseline characteristics of the study population are summarised in table 4.1.

Results of the clinical measurements are presented in table 4.2. As expected, all indices of systolic ventricular function were altered in patients with reduced compared to normal EF. More precisely, levels of NT-proBNP were significantly elevated and maximum LV dP/dt was reduced in the low EF group versus controls. Besides the maximum pressure rise, also the maximum (systolic) absolute pressure in the left ventricle was lower while LV enddiastolic pressure was higher in rEF.

Furthermore, differences in LV geometry could be observed. In particular, LV enddiastolic (before ejection) and endsystolic (after ejection) volume as well as LV mass were larger in rEF than in nEF, whereas the resulting stroke volume (i.e. the difference between enddiastolic and endsystolic volume) was lower. Even though the reduction in SV only reached statistical significance for the angiographic and not the echocardiographic value, the corresponding difference in EF



	N	reduced EF	normal EF	P value
HR, bpm	61/122	71 [63,85]	63 [57,69]	< 0.0001
ED, ms	61/122	273 [245,284]	312 [293,321]	< 0.0001
LVETI, ms	61/122	393 (21 SD)	416 (18.6 SD)	< 0.0001
SBP central, mmHg	61/122	112 (18.3 SD)	116 (12.7 SD)	0.13
DBP central, mmHg	61/122	79.2 (13.6 SD)	79.9 (9.45 SD)	0.73
PP brachial, mmHg	61/122	45 [34.8,56]	46 [39,53]	0.30
PP central, mmHg	61/122	32 [23,41]	35.5 [30,42]	0.02
PPamp, -	61/122	1.41 [1.32,1.57]	1.29 [1.21,1.41]	< 0.0001
P <sub>1</sub> height, mmHg	61/122	26 [19,32]	26.5 [22,32]	0.45
AP, mmHg	57/122	5 [3,9.25]	9 [6,12]	< 0.0001
AIx, -	57/122	0.18 [0.12,0.24]	0.26 [0.18,0.31]	< 0.0001
Tr, ms	56/122	139 [132,145]	141 [134,146]	0.23
SPTI, mmHg·s	61/122	27.5 (5.19 SD)	32.5 (4.07 SD)	< 0.0001
DPTI, mmHg·s	61/122	46.3 [38.4,54.5]	54.8 [47.7,63.3]	< 0.0001
$\Delta$ PSA, mmHg·s	61/122	5.77 [3.96,7.08]	6.44 [5.42,7.81]	0.0004
$E_w$ , mmHg·s	61/122	0.401 [0.157,0.882]	1.05 [0.671,1.7]	< 0.0001
SPTI·HR, mmHg/60	61/122	1915 [1647,2275]	2039 [1849,2295]	0.06
DPTI·HR, mmHg/60	61/122	3406 (516 SD)	3481 (418 SD)	0.29
$\Delta$ PSA·HR, mmHg/60	61/122	395 [286,476]	401 [351,496]	0.12
$E_w$ ·HR, mmHg/60	61/122	25.4 [13.4,59.6]	66.2 [42.8,103]	< 0.0001
DPTI/SPTI, -	61/122	1.72 [1.51,1.98]	1.69 [1.51,1.89]	0.53
$E_w/\Delta$ PSA, -	61/122	0.0721 [0.035,0.141]	0.166 [0.089,0.238]	< 0.0001

Table 4.3: PWA parameters derived by the SphygmoCor system and pressure time indices. P-values indicate results of a group-wise comparison.

was very distinct for both measurement techniques. Moreover, the LV ejection pattern showed, on average, a later maximum for patients with impaired ventricular function, compare figure 4.3. Invasively measured aortic systolic blood pressure (SBP) was higher in controls than in the rEF group, while diastolic blood pressure (DBP) was comparable and pulse pressure (PP) therefore increased. For aortic PWV, no statistical significant difference was observed.

PWA parameters obtained with the SphygmoCor system are presented in table 4.3. Temporal characteristics showed significant differences between the groups with a higher HR and a shorter ED as well as LVETI, i.e. ED indexed to HR, in rEF patients vs. controls. Estimated central blood pressures were similar in both groups, with a slightly lower systolic and pulse pressure in patients with rEF, compare also figure 4.3. Both augmented pressure (AP) and AIx were significantly lower in the rEF group, while the height of incident pressure  $P_1$  as well as the round-trip travel time  $T_r$  were very similar.

SPTI, diastolic pressure time index (DPTI),  $\Delta$ PSA and  $E_w$  were all less in the rEF group than in controls, whereas when multiplied by HR to account for the shorter heart beat duration in rEF, only for  $E_w$  a difference remained. Also the ratio of  $E_w$  to  $\Delta$ PSA was significantly lower in rEF, whereas the myocardial viability ratio was comparable, see table 4.3.

	N	reduced EF	normal EF	P value
Wave separation analysis				
$ P_f $ , mmHg	61/122	23.3 [18.4,28.4]	23.8 [19.1,28.6]	0.63
$ P_b $ , mmHg	61/122	13.3 [9.1,17.2]	15 [12.4,17.9]	0.02
RM, -	61/122	0.564 (0.115 SD)	0.625 (0.0984 SD)	0.0002
RI, -	61/122	0.357 [0.323,0.388]	0.386 [0.358,0.413]	0.0002
Wave intensity analysis				
S energy, mmHg·cm	61/122	3.24 [2.25,4.39]	4.58 [3.71,5.76]	< 0.0001
D energy, mmHg·cm	61/122	1 [0.723,1.3]	1.02 [0.783,1.35]	0.28
R energy, mmHg·cm	61/122	0.568 [0.339,0.862]	0.978 [0.699,1.24]	< 0.0001
R/S energy, -	61/122	0.183 [0.134,0.236]	0.201 [0.15,0.262]	0.17
S/D energy, -	61/122	3.2 [2.56,4.31]	4.64 [3.89,5.24]	< 0.0001
S peak, mmHg·cm/s	61/122	49.3 [31.9,71.8]	81 [59.6,113]	< 0.0001
D peak, mmHg·cm/s	61/122	19.3 [13.8,24.7]	16.2 [11.8,21.4]	0.07
R peak, mmHg·cm/s	61/122	6.23 [4.44,8.98]	9.91 [7.22,13.7]	0.0001
R/S peaks, -	61/122	0.137 [0.0938,0.191]	0.118 [0.0864,0.155]	0.03
S/D peaks, -	61/122	2.63 [1.73,3.59]	5.08 [4.11,6.65]	< 0.0001

Table 4.4: WSA and WIA parameters. P-values indicate results of a group-wise comparison.

Table 4.4 finally depicts the results obtained by WSA and WIA. Similar to the behaviour observed for PWA, the forward pressure amplitude  $|P_f|$  was comparable whereas backward amplitude and therefore also RM and RI were lower for patients with reduced EF. The WIA parameters, in contrast, showed a significant reduction not only in the intensity of the backward R but also of the initial forward travelling S wave, both for the wave energy and the peak value. No significant reduction of relative wave reflections assessed by WIA was found for rEF patients. On the contrary, for amplitudes, R/S was even increased. Moreover, the S to D ratio was significantly less in the low EF group than in controls.

To compare the different approaches for the quantification of wave reflections, Pearson's correlation coefficient  $r$  between the corresponding parameters was computed per group, as given in table 4.5. The peaks of forward and backward wave intensities showed the weakest (linear) association to the other methods in both groups, whereas all other parameters were highly correlated with  $r > 0.6$  each. The association of measures describing the backward wave was highest between AP and  $|P_b|$  in both groups (0.88 and 0.82 in rEF and nEF respectively), whereas the correlation of the WIA parameters to the other methodologies was markedly weaker, especially in the control group, with values around 0.8 in rEF and 0.7 in nEF patients for the R wave energy. Regarding the forward wave parameters, the same behaviour could be observed, with  $r > 0.9$  between  $P_1$  and  $|P_f|$  in both groups. For the relative measures of wave reflection, in contrast, the largest  $r$  was found between R/S energy and RM in both groups.

In order to account for the possible confounding effect of the temporal characteristics on the haemodynamic parameters, the different measures of wave reflection were finally adjusted for HR, ED as well as HR in combination with ED, as presented in figure 4.4. HR alone did not

	P <sub>1</sub> height	P <sub>f</sub>	S energy	S peak
P <sub>1</sub> height	-	0.93 [0.90,0.95]	0.71 [0.61,0.79]	0.60 [0.48,0.71]
P <sub>f</sub>	0.92 [0.87,0.95]	-	0.64 [0.52,0.73]	0.53 [0.39,0.64]
S energy	0.85 [0.77,0.91]	0.82 [0.71,0.89]	-	0.96 [0.94,0.97]
S peak	0.75 [0.61,0.84]	0.72 [0.58,0.83]	0.96 [0.93,0.98]	-
	AP	P <sub>b</sub>	R energy	R peak
AP	-	0.82 [0.75,0.87]	0.68 [0.57,0.76]	0.45 [0.30,0.58]
P <sub>b</sub>	0.88 [0.80,0.92]	-	0.72 [0.62,0.80]	0.56 [0.42,0.67]
R energy	0.81 [0.70,0.88]	0.83 [0.73,0.89]	-	0.87 [0.82,0.91]
R peak	0.64 [0.45,0.77]	0.68 [0.52,0.80]	0.92 [0.87,0.95]	-
	AIx	RM	R/S energy	R/S peaks
AIx	-	0.73 [0.63,0.80]	0.73 [0.64,0.80]	0.52 [0.37,0.64]
RM	0.69 [0.52,0.80]	-	0.87 [0.82,0.91]	0.65 [0.54,0.75]
R/S energy	0.69 [0.53,0.81]	0.82 [0.71,0.89]	-	0.87 [0.82,0.91]
R/S peaks	0.38 [0.13,0.58]	0.46 [0.24,0.64]	0.73 [0.59,0.83]	-

Table 4.5: Correlations between PWA, WSA and WIA parameters. The first block represents the respective measures of the initial forward wave, the second those of the reflected backward wave and the third finally the relative indices of wave reflection. Values in the lower triangular matrix pertain to patients with reduced EF whereas those in the upper part (highlighted in gray) pertain to patients with normal EF.

suffice to explain the differences in pulse pressure amplification (PPamp) and AIx, while after adjustment for ED or HR in combination with ED, PPamp, AIx and RM became comparable between the groups. In contrast, the R/S energy, which did initially not differ between the groups, became significantly higher in patients with reduced EF than in controls when adjusted for ED.

The same adjustment was performed for the S to D ratio of both the peak values and the wave energies, see figure 4.5. In contrast to the wave reflection parameters, adjustment for ED or ED in combination with HR had no notable effect on the difference between patients with normal and reduced EF. Accounting for HR alone slightly attenuated the gap between the patients, however, the difference remained highly significant.

The correlations between measures of cardiac function and structure and parameters describing the pulsatile haemodynamics in the arterial system are presented in table 4.6. In the rEF group, ventricular contractility assessed by maximum LV dP/dt was positively associated with all indices describing the forward and backward waves, a relation that could not be found in controls. The association between EF and the temporal characteristics HR and ED was similar in both groups. However, in the low EF group, higher values of EF were moreover related to a lower PPamp and a higher AIx, RM and R wave energy. In both groups, ED was associated to all parameters of wave reflection (with the only exception of peak intensities in controls) but not to aortic PWV. Nevertheless, for the low EF group, correlations were markedly higher than in controls and ED was additionally related to all indices describing the initial forward wave. LV

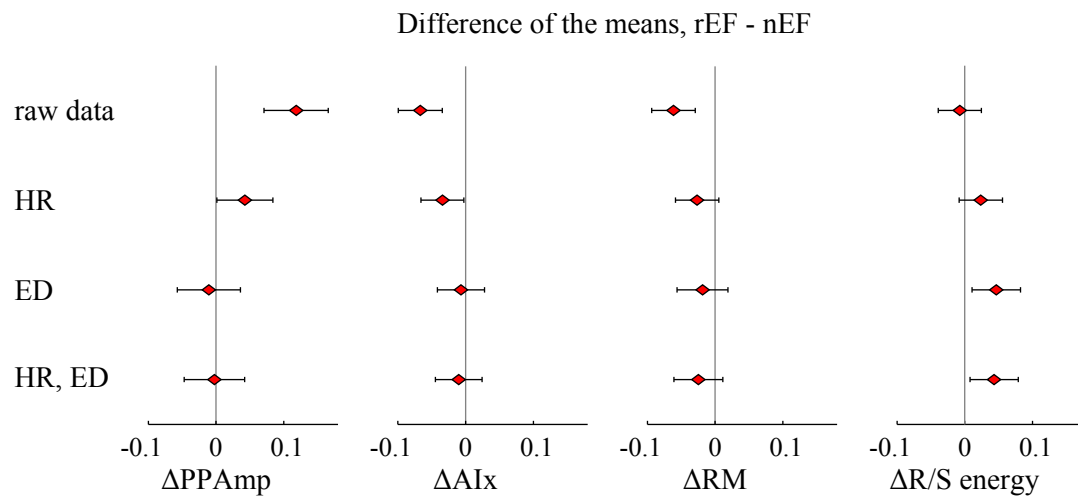


Figure 4.4: Difference of the mean values of wave reflection parameters between patients with reduced and normal EF for the unadjusted data and when adjusted for HR, ED as well as HR in combination with ED. Values represent the regression coefficient of the EF-status in multiple regression analysis and error bars indicate the corresponding 95% confidence interval.

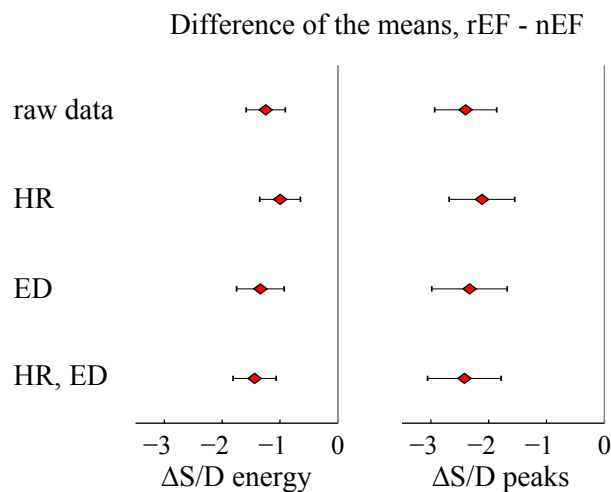


Figure 4.5: Difference of the mean values of the S to D ratio between patients with reduced and normal EF for the unadjusted data and when adjusted for HR, ED as well as HR in combination with ED. Values represent the regression coefficient of the EF-status in multiple regression analysis and error bars indicate the corresponding 95% confidence interval.

volumes were highly negatively correlated with PWV in patients with reduced but not in patients with normal EF. Moreover, although a negative association of LV volumes to most reflection indices could be observed in both groups, only for patients with normal systolic function, this association was also found for stroke volume (SV). In the control group, levels of NT-proBNP were associated with most haemodynamic parameters as well as PWV, whereas in the rEF group, only for the S/D ratio, S peak and PWV a significant association could be found.

## 4.5 Discussion

In this work, differences in clinical and pulse wave characteristics as well as their interrelations were examined in patients with systolic heart failure versus controls. The enlargement of the left ventricle reflected in the increased values of LV mass and filling volumes, and the impaired contractility assessed by LV  $dP/dt$  observed in the rEF group are characteristic for patients with a systolic dysfunction [5]. The elevated enddiastolic LV filling pressure may additionally indicate a decrease in LV compliance and thus an impairment of LV relaxation (diastolic dysfunction). Alternatively, it may be ascribed to the elevated filling volume caused by the impaired emptying [63].

The previously observed reduction of ED in patients with systolic HF [21, 68, 88, 125, 137, 141] could again be confirmed in this work. Furthermore, despite the higher prevalence of betablocker use, patients with rEF had a significantly elevated HR. This elevation is in keeping with the older invasive studies [52, 66], whereas in the more recent works, HR was consistently higher, too, yet mostly without reaching statistical significance [19, 125, 137]. The reduction in LVETI, i.e. ED indexed to HR, moreover implies that ED was reduced beyond the effect of HR alone, in line with earlier results [21, 68]. The alterations in the temporal characteristics might be explained by the inability of the failing ventricle to overcome late systolic load, resulting in a premature stop of ejection (shorter ED) and an increase in HR to compensate the consequently lower stroke volume [146].

To enable a direct comparison of all pressure-dependent parameters, the rEF and nEF patients were matched for brachial blood pressure levels in this study. Nevertheless, estimated central SBP tended to be lower in the rEF group and pulse pressure was significantly reduced, leading to a higher PPamp. For the invasively measured aortic blood pressure levels, this reduction was even more pronounced. Weber et al. [137] previously reported an almost identical behaviour in a very similar study population. Unfortunately, though, no brachial pressure levels were assessed at the time of angiography for a direct comparison. A possible explanation for the differences in estimated central PP can be sought in the elevated HR in rEF patients, since PPamp assessed with the SphygmoCor system has been found to increase linearly with HR [151]. However, Denardo and coworkers [21] observed a higher PPamp in rEF patients despite matching for HR and HR alone could not completely explain the difference in PPamp in multiple regression

	ED	EF	LVEDV	LVESV	SV	LV dP/dt	ln(NT-proBNP)
Reduced EF							
HR	-0.71*	-0.29*	-0.09	0.00	-0.30*	0.01	0.28*
ED	1.00*	0.27*	0.05	-0.04	0.25	0.15	-0.24
LVETI	0.65*	0.10	-0.04	-0.07	0.05	0.25	-0.08
PWV	-0.09	0.08	-0.42*	-0.36*	-0.25	0.29*	0.36*
PP central	0.55*	0.22	-0.25	-0.27*	-0.00	0.46*	-0.08
PPamp	-0.70*	-0.40*	0.19	0.28*	-0.22	-0.24	0.18
P <sub>1</sub> height	0.35*	0.16	-0.23	-0.22	-0.06	0.41*	-0.10
AP	0.63*	0.23	-0.22	-0.25	0.05	0.36*	0.03
Aix	0.62*	0.28*	-0.17	-0.24	0.14	0.25	0.01
P <sub>f</sub>	0.39*	0.03	-0.13	-0.10	-0.12	0.38*	-0.08
P <sub>b</sub>	0.49*	0.22	-0.34*	-0.34*	-0.07	0.49*	-0.02
RM	0.30*	0.32*	-0.38*	-0.42*	0.04	0.30*	0.09
S energy	0.29*	0.18	-0.14	-0.18	0.08	0.42*	-0.06
D energy	0.33*	0.03	0.09	0.08	0.05	0.25	-0.19
R energy	0.50*	0.31*	-0.26*	-0.32*	0.11	0.47*	-0.03
R/S energy	0.48*	0.24	-0.22	-0.25	0.05	0.26*	0.03
S/D energy	0.01	0.19	-0.24	-0.28*	0.07	0.15	0.27*
S peak	0.20	0.15	-0.18	-0.21	0.05	0.40*	0.01
D peak	0.23	0.07	-0.05	-0.04	-0.02	0.26	-0.27*
R peak	0.43*	0.23	-0.19	-0.24	0.11	0.35*	-0.03
R/S peaks	0.35*	0.02	0.01	0.01	0.00	-0.06	0.03
S/D peaks	0.08	0.13	-0.18	-0.21	0.04	0.15	0.28*
Normal EF							
HR	-0.67*	-0.22*	-0.21*	0.07	-0.24*	-0.14	-0.06
ED	1.00*	0.21*	0.08	-0.15	0.12	0.10	0.02
LVETI	0.74*	0.07	-0.07	-0.13	-0.05	0.03	-0.03
PWV	-0.02	0.03	-0.19	-0.16	-0.12	0.16	0.45*
PP central	0.28*	0.03	0.02	-0.03	-0.04	0.13	0.32*
PPamp	-0.51*	-0.07	0.17	0.16	0.14	-0.12	-0.24*
P <sub>1</sub> height	0.14	0.01	0.12	0.04	0.04	0.14	0.26*
AP	0.36*	0.03	-0.14	-0.11	-0.17	0.06	0.29*
Aix	0.34*	0.03	-0.21*	-0.13	-0.19*	0.05	0.21*
P <sub>f</sub>	0.15	0.02	0.11	0.04	0.02	0.08	0.31*
P <sub>b</sub>	0.28*	0.05	-0.04	-0.09	-0.07	0.13	0.30*
RM	0.27*	0.06	-0.25*	-0.21*	-0.16	0.13	0.05
S energy	0.01	0.01	0.11	0.05	0.02	0.12	0.19*
D energy	0.09	0.02	0.08	0.00	-0.01	0.01	0.31*
R energy	0.28*	0.09	-0.18	-0.21*	-0.14	0.17	0.25*
R/S energy	0.27*	0.04	-0.27*	-0.20*	-0.19*	0.07	0.08
S/D energy	-0.10	0.01	0.07	0.04	0.08	0.17	-0.25*
S peak	-0.11	-0.08	0.04	0.09	-0.04	0.13	0.19*
D peak	-0.10	0.01	0.03	0.02	-0.05	-0.03	0.33*
R peak	0.09	0.09	-0.16	-0.20*	-0.12	0.22*	0.18
R/S peaks	0.18	0.09	-0.23*	-0.22*	-0.14	0.11	0.00
S/D peaks	0.00	-0.06	0.05	0.07	0.05	0.18	-0.18*

Table 4.6: Correlations between measures of cardiac function and structure and haemodynamic parameters. Values obtained by angiography were used for EF, LVEDV, LVESV, SV and LV dP/dt. Moderate to high correlations with  $|r| \geq 0.3$  are highlighted in gray, \* indicates Pearson's  $r$  being significantly different from 0 at a 5% level.

analysis in the present work, see figure 4.4. Hence, the difference in central PP is only partially attributable to HR. Adjustment for ED or both ED and HR on the other hand, fully balanced PPamp between the groups.

In line with the lower central pressure amplitude, the absolute parameters quantifying the wave reflections present in the system assessed by PWA and WSA, namely AP and  $|P_b|$ , were reduced in patients with rEF versus controls. In contrast, measures of the incident forward wave did not differ between rEF and nEF patients. The resulting lower values of AIx and RM are consistent with previous studies [21, 51, 68, 137]. Of note, numerical values of RM reported by Laskey and coworkers [51], who worked with a very similar study population regarding age and pressure levels but used invasive measurements of pressure and flow, were almost identical to the values found in this work, namely 0.61 (0.14 SD) and 0.53 (0.14 SD) for normal and reduced EF respectively.

The behaviour of the WIA parameters differed from PWA and WSA in that, besides the reflected wave energy, also the energy of the initial forward compression wave, i.e. the S wave, was lower in rEF. The S wave originates from ventricular ejection and its energy has been found to be positively associated to the contractile state of the left ventricle [27, 44, 120]. The reduction of the S wave energy for patients with impaired systolic ventricular function found in this as well as previous works [19, 120] agrees well with this concept. Also in keeping with literature [19, 120], no difference in the forward decompression wave, the D wave, was observed between the groups.

For WIA, the incremental changes in pressure and flow are used, making the computations susceptible to noise, in particular when using the peak values for quantification. This might explain the rather low correlations of the peak intensities with the other methods, whereas the wave energies, which are more robust because the whole wave and not only a single point is used, showed a stronger association to the PWA and the WSA parameters. PWA and WSA are both based on the absolute values of pressure, which might explain why the respective forward and backward indices were more closely related to each other than to WIA. Nevertheless, for the relative measures of wave reflections, correlation between the R/S energy and RM was higher than between AIx and RM in both groups.

The present results show that the relation between measures of cardiac and arterial function differs between patients with normal and impaired LV systolic function. In the first case, aortic root flow at rest looks very similar between individuals, compare e.g. figure 5.2 in the next chapter, which means that the LV ejection pattern is relatively independent of the opposed afterload. Therefore, differences in the shape of the flow waveform are more or less negligible for the interpretation of the haemodynamic parameters, and characteristics of the pressure waveform can be used to derive information about arterial function only. Changes in the contractile behaviour of the ventricle leading to alterations in the flow waveform, however, directly affect the pressure wave and therefore the derived parameters, compare [46]. This might explain why EF,

as a measure of the severity of LV impairment, as well as the contractility parameter  $LV\ dP/dt$ , showed no association to pulsatile parameters in subjects with normal LV function, whereas a strong correlation was found in patients with LV systolic dysfunction. Thus, while for example a low pulse pressure might be an indicator of healthy, elastic arteries for normal hearts, it rather reflects the inability of the ventricle to pump against the afterload for the failing heart, without revealing much about the status of the arteries. The observed relation between a shortening of the ejection duration, as a manifestation of ventricular failure, and an attenuation of the forward pressure indices in the rEF patients is well in line with this concept too. For nEF, in contrast, no relation of ED to the forward indices was found, in keeping with findings by Namasivayam and coworkers [74]. Westerhof and O'Rourke described this phenomenon in terms of the mechanical pump function of the heart [146]. They argued that the normal heart acts almost like a flow source, being able to eject against the load presented by the arterial system, whereas the failing heart behaves more like a pressure source. Therefore, while wave reflections returning during systole augment pressure but have only little effect on the flow wave in the first case, they diminish flow and thus affect pressure to a lesser extent in the second case. The idea that wave reflections, although equally strong, manifest themselves less in the pressure wave when the ventricle is failing, might explain the lower reflection indices in patients with rEF observed in this study, despite the similar aortic stiffness assessed by PWV between the groups.

Aortic PWV was statistically comparable between the groups in this as well as previous works [68, 137]. Nevertheless, absolute values tended to be higher for patients with low EF. Because of the interplay between elastin and collagen fibers in the arterial media, arteries become stiffer when they dilate [82], meaning in particular that PWV increases with increasing blood pressure [126]. Taking into account that invasively measured aortic blood pressure at the time of PWV measurement was significantly lower in rEF patients, this could indicate that aortic stiffness might even be elevated in rEF patients. However, this notion has to be investigated in future studies.

AIx depends on both the timing and the magnitude of the reflected waves and is known to be strongly influenced by temporal characteristics, which was suggested to be mainly due to alterations in ED [117, 150]. This could explain the differences observed between the rEF and nEF group. Similar to the behaviour of PPamp, adjustment for ED or ED in combination with HR indeed resulted in comparable AIx between the groups. The same held for RM, whereas the R/S energy became even higher in rEF, indicating that wave reflections may at least be equally strong in both groups.

Results regarding the pressure time indices found in previous studies [21, 88] could not all be confirmed in the present work:  $E_w$  and SPTI were indeed lower in rEF versus controls, but the myocardial viability ratio, which was reported to be increased to optimise LV efficiency [21], was very similar between the groups.



Another interesting parameter, not directly related to wave reflections, is the S to D ratio of forward wave intensity, which was first analysed by Hametner et al. [38] as a marker of systolic heart failure in the same population. The S and D wave are supposed to describe the ventricular ejection and relaxation dynamics respectively. Their ratio could thus be seen an index characterising the ventricular dynamics over the whole mechanical systole. For both the energies and the peak values, a significant and very pronounced reduction in this index was found for patients with impaired ventricular function, which might qualify the parameter as a non-invasive indicator of systolic function as proposed in [38]. Even though the reduction was very distinct in patients with low compared to normal EF, no association to EF was found when looking at the groups separately, compare table 4.6. In other words, the S to D ratio seems to depend on whether EF is normal or reduced as a categorical variable, but not on how low or how high the EF really is. Moreover, in contrast to the wave reflection parameters, it seems to be independent of ED, both within the groups as shown in table 4.6 as well as between the groups, since the difference could not be explained by ED, compare figure 4.5. The same holds for the heart rate. Furthermore, the S to D ratio was positively related to NT-proBNP for reduced EF, while the association was negative for controls. However, the mechanisms behind this behaviour still have to be clarified.

The main strength of this study is that patients were matched for brachial blood pressure, thereby enabling the direct comparison of all pressure-dependent parameters. Moreover, a variety of measurements was available including clinical and haemodynamic parameters, which made it possible to analyse the relationships between cardiac and arterial function and the respective differences arising from ventricular impairment. However, also several limitations have to be considered. The number of women included in the study was very low and gender differences could therefore neither be analysed nor accounted for. Previous studies in systolic heart failure showed a similar, unbalanced gender distribution [21, 125] (between 80% and 97% male), which might be due to the unequal prevalence of LVSD in men and women, which was found to be 2.5 times higher in men [70]. Another limitation is that measurements were partly performed on different days, possibly limiting the comparability between the parameters. Moreover, aortic pressure waveforms were synthesised by the means of a generalised transfer function and flow waveforms were manually digitised, an assessment method that is prone to a certain degree of subjectivity.

## Conclusion

In conclusion, the current study showed that haemodynamic parameters are susceptible to cardiac function in patients with ventricular impairment. This has to be kept in mind for interpretation and risk stratification. In particular, parameters of wave reflections might not be suitable indicators of arterial stiffness in patients with severely reduced ejection fraction. However, these intrinsic differences in non-invasively assessed pulsatile haemodynamics might potentially be used as indicator of a systolic dysfunction in the future.

## Chapter 5

# Using flow models based on pressure alone in patients with systolic heart failure: state of the art and data analysis

In this chapter, the use of blood flow models in patients with systolic heart failure is investigated with respect to their applicability in wave separation analysis (WSA) and wave intensity analysis (WIA). While the last chapter dealt with differences in the parameters derived from measured pressure and flow between patients with systolic heart failure and controls, this chapter focuses on the ability of different flow models to provide accurate estimates and, probably even more important, to reproduce these differences. For this purpose, first, again a summary of the relevant literature is given. Then, the same study population as in the previous chapter is used to evaluate and to compare the performance of the four blood flow models presented in chapter 3.

Parts of this chapter are based on the work "Non-invasive wave reflection quantification in patients with reduced ejection fraction" published in "Physiological Measurements" in 2015 [95]. The previously reported results were extended by a comparison with the Windkessel flow introduced in section 3.4.

### 5.1 State of the Art

In 2006, Westerhof and coworkers [142] introduced their triangulation method for flow approximation and compared their estimates with invasive flow measurements collected from previously published works. They found a relatively good agreement of reflection magnitude (RM) and reflection index (RI) derived by their flow model with the ones obtained with measured flow and

concluded that, with their approach, it might be feasible to perform WSA based on non-invasively assessed pressure alone. Thereafter, several investigators applied their method for wave separation in both cross-sectional [56, 74, 75] as well as longitudinal studies [40, 121, 133]: Lieber and colleagues [56], for example, used it to investigate gender-related differences in aortic wave reflections, while Namasivayam and coworkers [75] examined the contribution of the forward and backward wave to the increase in aortic pulse pressure with age. Wang et al. [133] studied the WSA parameters derived with the triangulation method with regards to their prognostic value in a large, community-based population comprising more than 1000 participants. They found the backward wave amplitude  $|P_b|$  to be a strong predictor of 15-year cardiovascular mortality, independent of brachial pressure levels, conventional risk factors and arterial stiffness. Qasem and Avolio [103] moreover proposed a new approach for the one-point estimation of pulse transit time and pulse wave velocity from pressure alone based on wave separation using the triangulation method. Last but not least, AtCor Medical incorporated a WSA algorithm based on the triangulation method in their SphygmoCor software, which has already been used in a variety of studies, e.g. [22, 55].

However, in their original work, Westerhof and coworkers used a very small set of data to proof their concept, consisting of measurements of only 19 different individuals. In 2009, Kips et al. [49] applied the triangulation method to carotid pressure waveforms of 2325 subjects of the Asklepios cohort and compared it to Doppler flow measurements of the aortic root flow. For the construction of the triangle, they used timing information that was directly derived from the measured flow wave to investigate the best possible approximation. Nevertheless, they found only a moderate agreement for  $P_b$ ,  $P_f$  and RM. With their averaged waveform, in contrast, agreement could be markedly improved. Furthermore, RM derived with the averaged waveform was shown to be independently associated to cardiovascular events as well as new onset heart failure in 5960 participants of the MESA study with an average follow up duration of 7.6 years [17].

In 2013, Hametner and coworkers published another comparison of the triangular approximation and the averaged waveform in 148 patients with preserved systolic function [35, 37]. Using Doppler measurements of aortic blood flow as reference, they again found the averaged waveform to be superior to the triangle for wave separation. Additionally, they investigated the performance of the ARCSolver flow for WSA and found a similar agreement to Doppler flow as for the averaged waveform. In a longitudinal study performed by Weber et al. [140],  $|P_b|$  derived using the ARCSolver flow was furthermore shown to be predictive of cardiovascular events, independently of brachial pressure levels, and to be associated to end-organ damage in a high-risk population of 725 patients.

To summarise, for subjects with normal left ventricular (LV) systolic function, the different blood flow models have already been (successfully) used for WSA in a hand-full of studies. However, the question remains if these results can be transferred to patients with systolic heart failure, who often show modified ejection patterns [77]. The only relevant study in this regard might

be the one performed by Sung and colleagues, who used the triangular flow approximation to determine forward and backward amplitude as well as RM in a cohort hospitalised for acute heart failure [122]. They found the value of  $|P_b|$  on admission to be a strong predictor of adverse outcome in both patients with heart failure with preserved (n=48) and reduced ejection fraction (n=72). However, a thorough search of the relevant literature yielded no results with respect to a direct comparison of modelled to measured flow waves or the derived parameters in patients with systolic heart failure.

Regarding the use of blood flow models for WIA, data from literature was restricted to the investigations performed at the Austrian Institute of Technology using the ARCSolver flow [32, 36, 38]. These preliminary results indicated a good agreement between the forward wave energy obtained by Doppler and modelled flow in patients with normal systolic function [36], as well as a similar reduction in the S to D ratio of the respective peak values for patients with systolic heart failure compared to controls [38].

Overall, while the available data on the applicability of the three different blood flow models for wave separation is already limited for patients with normal ventricular function, it is extremely scarce for patients with systolic heart failure. Even though Sung and co-workers were indeed able to demonstrate the prognostic value of a WSA parameter obtained with the triangular flow in heart failure patients, the accuracy of the flow estimate itself as well as of the derived parameters has not yet been investigated in patients with reduced ejection fraction (EF). In their initial study population, Westerhof and colleagues included two patients with heart failure, but this sample is too small to draw any conclusions and results were not reported separately. Also for the other two approaches, an evaluation of their performance in heart failure patients is still missing. For WIA, apparently no data exists about the feasibility of using the triangular or averaged blood flow for computation, regardless of ventricular function. However, first results obtained with the ARCSolver flow imply that it might be feasible to replace the flow measurements also for WIA.

## 5.2 Aim of the study

The aim of this study is to investigate and to compare the performance of the different blood flow models introduced in chapter 3 in patients with systolic heart failure and controls. More specifically, the agreement of the waveforms themselves as well as of the derived WSA and WIA parameters to the corresponding values obtained from Doppler flow measurements will be examined.

### 5.3 Methods

The same study population as in the previous chapter was used and the reader is therefore referred to the corresponding methods section 4.3 for a thorough description of the population as well as of the measurements performed.

The 4 different blood flow models included in this analysis were already presented in detail in chapter 3. Therefore, only a few comments on the numerical realisation will be given in the following. The duration of cardiac ejection  $t_s$  was estimated from the peripheral pressure wave using an algorithm developed by the cardiovascular diagnostics research group at the AIT and was used for all flow models to ensure comparability. The width of the averaged waveform derived by Kips et al. [49] was scaled to  $t_s$  by linear interpolation. For the triangular estimate, the base of the triangle was set to  $t_s$  and its apex to the point in time corresponding to the inflection point in the pressure signal<sup>1</sup> determined by the SphygmoCor system. Moreover, all flow estimates were normalised to 100 arbitrary units (AU). The term "combWK flow" will be used throughout this section to refer to the combination of the Windkessel flow model and the ARCSolver flow, as presented in section 3.4.5.

To evaluate the performance of the different blood flow models, the digitised Doppler flow measurements scaled to 100 AU (compare again section 4.3) served as reference. All parameters were summarised as median [95% central range], independently of their actual distribution, to facilitate the comparison between the models. Moreover, the Mann-Whitney-U test (non-parametric) was used to statistically assess between-group differences for all parameters. The root mean square error (RMSE) between measured and estimated flow during systole was computed to compare the shape of the waveforms, whereas the derived parameters were assessed quantitatively by calculating the median (accuracy) and 95% central range (precision) of the difference to the reference values, as well as Pearson's correlation coefficient. Results obtained with the ARCSolver and combWK flow were furthermore compared graphically to the reference method by Bland-Altman plots using mean and standard deviation of the differences to determine the limits of agreement.

In contrast to the previous chapter, also for WIA the flow waveform was normalised to 100 AU. Therefore, all absolute parameters, i.e. the peaks and time-integrals of wave intensity, are wrongly scaled. This has to be kept in mind for quantitative comparisons. Relative measures like ratios are of course unaffected by the scaling of blood flow.

<sup>1</sup>This point was identified from the augmentation index (AIx).

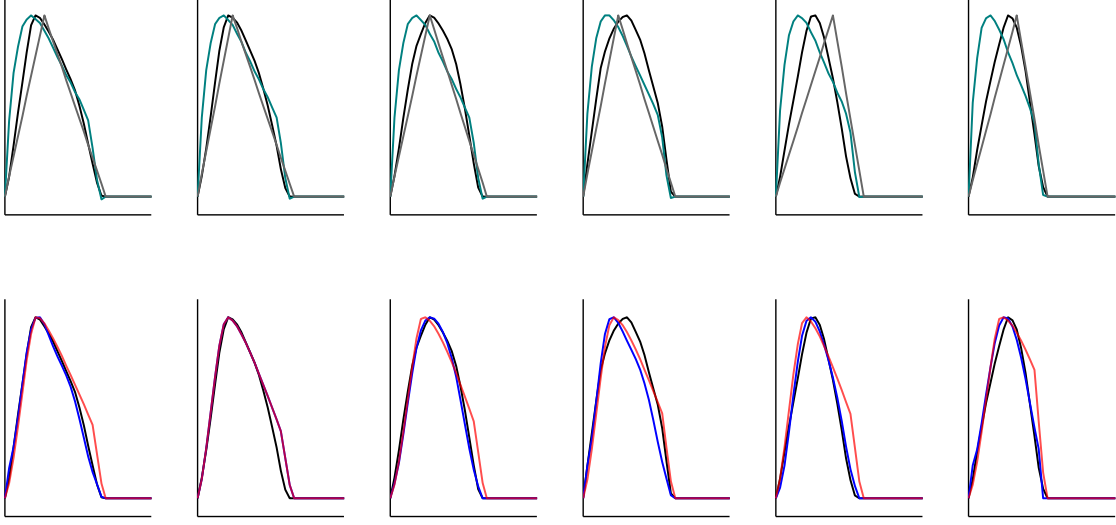


Figure 5.1: Examples of Doppler flow waves (black solid line) and the corresponding triangular (gray) and averaged (teal) estimates (upper panel) as well as the ARCSolver (red) and combWK (blue) flow (lower panel) for patients with reduced EF. The flow waves are arranged according to the timing of maximum flow relative to the respective ejection duration. All flow waves were scaled to the same peak value and the x-axis depicts 0.4 seconds.

## 5.4 Results

### Flow waveform

Examples of the flow wave estimates obtained by the different models and the corresponding Doppler-based flow waves are shown in figure 5.1 for patients with reduced EF (rEF) and in figure 5.2 for patients with normal EF (nEF). Also cases where combWK and ARCSolver flow coincide are shown, which occurred in 20 patients (33%) with reduced and 107 (88%) patients with normal EF. In the rEF group, a much greater variation in shape can be observed for the measured flow waves as compared to controls, in particular with respect to the timing of peak flow. On average, maximum flow is reached significantly later relative to the ejection duration for patients with ventricular impairment, as presented in table 5.1. The same behaviour could be observed for the triangular, ARCSolver and combWK flow, but not for the averaged waveform, which, by definition, does not vary in shape. In both groups, the highest correlation between the position of modelled and measured maximum flow was found for the ARCSolver, closely followed by the combWK flow. The latter method furthermore reached the lowest median RMSE between Doppler and modelled waveform for both normal and reduced EF, which was almost identical in both groups.

### Wave separation analysis

Table 5.1 summarises the results obtained by WSA with the different flow estimates in comparison to the reference method. For the amplitude of the forward travelling pressure wave  $|P_f|$ , correlation was high with  $r \geq 0.9$  for all flow models and all but the triangular estimate even

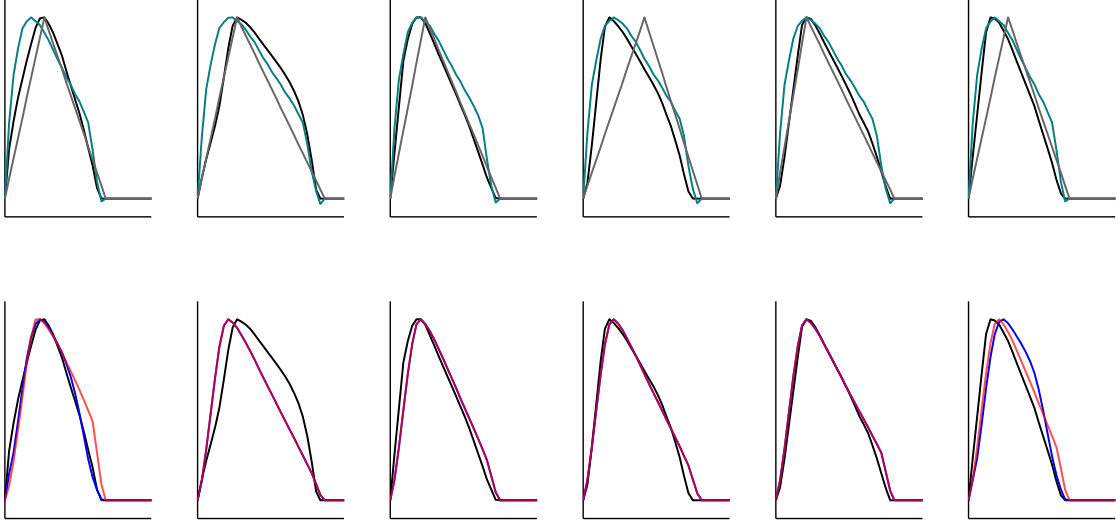


Figure 5.2: Examples of Doppler flow waves (black solid line) and the corresponding triangular (gray) and averaged (teal) estimates (upper panel) as well as the ARCSolver (red) and combWK (blue) flow (lower panel) for controls. For most of the controls, the combWK flow coincides with the ARCSolver flow. All flow waves were scaled to the same peak value and the x-axis depicts 0.4 seconds.

attained  $r \geq 0.95$ . However, both the triangle and the averaged waveform yielded significantly lower values of  $|P_f|$  for patients with reduced EF versus controls, while the reference values were comparable. For the backward amplitude, correlations were even higher than for the forward amplitude for the averaged, ARCSolver and combWK flow in both groups. Moreover, all models were able to reproduce the reduction in  $|P_b|$  for rEF compared to controls, although it did not reach statistical significance for the averaged flow. With regards to RM, correlation was highest for the combWK flow independent of the EF-status. Even though RM obtained with the ARCSolver estimate and averaged waveform yielded very similar correlations with the reference method, using the averaged flow for computation resulted in no difference in RM between patients with rEF and nEF, in contrast to the behaviour of the Doppler measurements and the other flow models.

For both the forward and backward amplitudes, the widest scatter in the deviation from the reference values was found for the triangular approximation in patients with reduced as well as normal ejection fraction, whereby estimates were even less precise in the latter group. The averaged waveform provided the most precise and most accurate estimate of  $|P_f|$  for patients with normal EF. In the rEF group, accuracy was highest for the combWK flow, while precision was similar for the combWK and ARCSolver method, with slightly better results obtained by the latter as also shown in figure 5.3. Looking at the whole study population, precision was very similar for both methods, but accuracy was again better for the combWK flow. With regards to  $|P_b|$ , precision was highest for the combWK flow in both groups, followed by the ARCSolver flow. A direct comparison of these two methods for patients with rEF as well as for the whole study population is shown in figure 5.4. In line with the ordering implied by the correlation coefficients,

the combWK method yielded the most accurate and most precise values of RM, closely followed by the ARCSolver flow, see figure 5.5. Also for the whole study population, a closer agreement could be observed for the combWK than for the ARCSolver flow, as shown again in figure 5.5. Furthermore, the Bland-Altman plots revealed no systematic trends for neither the ARCSolver nor the combWK method for any WSA parameter.

### Wave intensity analysis

The WIA parameters derived with the different flow estimates are depicted in tables 5.2 and 5.3 for the wave energies and peak intensities respectively. Again it should be noted that all absolute values are wrongly scaled because of the normalisation of blood flow velocity. Similar to the findings for  $|P_f|$ , correlation of the S wave energy obtained with the different flow models to the reference value was very high in both groups, i.e.  $r \geq 0.94$ . Peak values showed a lower, but still high correlation with  $r \geq 0.83$  for all flow models and  $r \geq 0.90$  for ARCSolver and combWK flow. However, the reduction in S wave energy observed for patients with impaired ventricular function when using the Doppler flow measurements was not captured well by the models. For the peak values on the other hand, the combWK flow was able to imitate this behaviour. Nevertheless, the deviation from the reference value differed significantly between the groups, with an almost three times higher median deviation for rEF compared to nEF patients for all but the triangular flow. A comparison of the S wave energy obtained by ARCSolver and combWK method to Doppler flow is shown in figure 5.6.

The R wave energy was consistently lower in the rEF than in the nEF group when using the Doppler, triangular, ARCSolver or combWK flow. This reduction was significant for all but the ARCSolver method. Using the averaged waveform, however, resulted in the opposite behaviour. Correlations between modelled and measured R wave energy were generally higher for patients with reduced than with normal EF, with the strongest association found for the combWK flow in the rEF group, while the correlation was comparable for averaged, ARCSolver and combWK flow in controls. Also the 95% central interval of the difference to the reference was by far narrowest for the combWK flow in the rEF group, and almost identical to the corresponding 95% central interval found in controls. In comparison, the range was almost twice as large in rEF for the other methods, yet similar to the combWK for the averaged and ARCSolver flow in the nEF group, compare figure 5.7.

Regarding the peak values of the R wave, no statistical evidence for a difference between patients with normal and reduced EF could be found for Doppler, triangular or combWK flow, whereas both the ARCSolver and averaged waveform resulted in significantly greater values for controls. Accuracy was worst for the averaged waveform, while precision was best for the combWK flow in both groups. Correlations were throughout lower than for the wave energies.

The relative magnitude of wave reflections assessed by the R/S energy was similar between the groups for the ARCSolver and combWK method, in line with the results obtained by Doppler



flow. The median error found for the combWK method was furthermore identical between the groups, as was the observed scatter. Compared to the ARCSolver method, accuracy and precision could therefore be slightly improved for both the rEF group alone as well as for the whole study population, see figure 5.8. Also the correlation was highest for the combWK method in both groups. The lowest correlation and largest deviation from the reference in terms of both accuracy and precision was found for the triangle, with  $r = 0.66$  in the reduced EF and  $r = 0.20$  in the normal EF group. For the peak values, correlations were again lower.

The increase of the energy of the second forward wave, i.e. the D wave, in the rEF group found using Doppler measurements<sup>2</sup> could also be observed for the triangular, ARCSolver and combWK flow but not for the averaged waveform, despite showing the highest correlation and highest precision to the reference method in both groups. The same held true for the peak intensities. Bland-Altman plots for the ARCSolver and combWK flow are depicted in figure 5.9.

For the ratio of the S to D energy, finally, correlations were markedly lower than for the other WIA parameters, with values in the range of 0.2 for the triangle, 0.5-0.7 for the ARCSolver and combWK flow and 0.7 for the averaged waveform. The averaged waveform tended to overestimate the ratio for rEF and underestimate it for nEF, resulting in virtually equal values in both groups, contrary to the reduction in rEF observed for the Doppler, triangular, ARCSolver and combWK flow. However, even though the triangulation method could reproduce this difference with respect to the median, the obtained values scattered excessively around the reference. In the low EF group, using the combWK flow could improve the precision compared to the ARCSolver flow, which resulted in a slight improvement over the whole study population, see figure 5.10. Looking at the peak values, correlations were doubled for the triangle but further attenuated for all other methods with  $r \approx 0.4$  for the averaged waveform and  $r \approx 0.3$  for the ARCSolver flow in both groups. The combWK flow resulted in the highest correlation ( $r = 0.57$ ) and highest precision for patients with reduced EF. However, by overestimating the S to D ratio for rEF and underestimating it for nEF, the very distinct difference between the groups found for the reference values was strongly diminished. This effect could be observed for all flow models, although in varying degrees.

Overall, for most of the WIA parameters, estimates of the peak values obtained with the different flow models were markedly less precise than estimates of the wave energies.

## 5.5 Discussion

With the increasing popularity of wave separation and wave intensity analysis, blood flow models are more and more finding their way into clinical research, facilitating the quantification of wave reflections from pressure alone [17, 133, 140]. Different commercially available pulse wave

<sup>2</sup>The discrepancy to the previous chapter, where no difference in D wave energy or peak intensity was observed between patients with rEF and nEF, is due to the fact that flow was scaled to 100 AU in the present analysis.

	Doppler	Triangular	Averaged	ARCSolver	combWK
<b>Reduced EF</b>					
RMSE flow, AU	-	11.9 [7.51,24.1]*	16.7 [9.67,26.2]*	9.69 [4.32,20.5]	7.06 [3.74,15.3]
tmax/ED, -	0.387 [0.259,0.533]*	0.42 [0.306,0.632]*	0.274 [0.247,0.301]	0.343 [0.274,0.434]*	0.368 [0.274,0.474]*
	$\Delta$	0.0465 [-0.0985,0.215]	-0.112 [-0.253,0]*	-0.046 [-0.168,0.0634]*	0 [-0.147,0.0928]
	$r$	0.48 [0.27,0.66]	-0.07 [-0.32,0.19]	0.63 [0.45,0.76]	0.60 [0.40,0.74]
$ P_f $ , mmHg	23.3 [12.3,45.5]	26.1 [13.7,45.8]*	20.6 [10.9,40.6]*	22.1 [11.5,41.9]	22.8 [12.1,41.3]
	$\Delta$	1.15 [-4.33,8.64]*	-2.24 [-7.43,1.59]*	-1.32 [-5.68,2.32]*	-0.377 [-5.67,2.69]*
	$r$	0.93 [0.89,0.96]	0.96 [0.94,0.98]	0.96 [0.94,0.98]	0.96 [0.94,0.98]
$ P_b $ , mmHg	13.3 [5.89,25.7]*	12.6 [5.33,31.1]*	15 [7.54,29.7]	11.7 [5.27,24.5]*	12.2 [5.59,25.1]*
	$\Delta$	-0.506 [-2.87,5.55]*	2.3 [-0.0165,5.08]	-1.02 [-3.42,1.5]	-0.568 [-3.1,2.8]
	$r$	0.95 [0.92,0.97]	0.98 [0.96,0.99]	0.98 [0.97,0.99]	0.99 [0.98,0.99]
RM, -	0.555 [0.356,0.815]*	0.499 [0.337,0.711]*	0.731 [0.597,0.855]	0.535 [0.324,0.711]*	0.545 [0.301,0.788]*
	$\Delta$	-0.0403 [-0.171,0.0616]*	0.172 [-0.0323,0.284]*	-0.0216 [-0.111,0.0725]	-0.0176 [-0.0984,0.0856]
	$r$	0.76 [0.63,0.85]	0.82 [0.71,0.89]	0.83 [0.74,0.90]	0.91 [0.85,0.94]
<b>Normal EF</b>					
RMSE flow, AU	-	11 [6,27.8]*	14.2 [9.87,19.1]*	7.1 [2.98,15.9]	7.03 [2.98,15.9]
tmax/ED	0.272 [0.216,0.368]*	0.344 [0.298,0.589]*	0.273 [0.258,0.296]	0.289 [0.247,0.347]*	0.29 [0.247,0.37]*
	$\Delta$	0.0752 [0.0,0.316]	0 [-0.0926,0.0698]*	0 [-0.0549,0.0722]*	0 [-0.0463,0.0858]
	$r$	0.25 [0.08,0.41]	0.00 [-0.17,0.18]	0.48 [0.33,0.61]	0.45 [0.30,0.58]
$ P_f $ , mmHg	23.8 [13.8,39.2]	28.4 [16.4,52.1]*	23.5 [13.6,39]*	23.2 [14.1,38.5]	23.5 [14.1,38.5]
	$\Delta$	4.85 [-1.13,14.8]*	-0.0922 [-4.7,2.12]*	0.215 [-5.02,3.02]*	0.392 [-4.59,3.7]*
	$r$	0.90 [0.86,0.93]	0.97 [0.96,0.98]	0.96 [0.94,0.97]	0.96 [0.94,0.97]
$ P_b $ , mmHg	15 [7.69,25.2]*	15.9 [7.57,27.5]*	17.2 [9.41,27.8]	14.1 [7.2,25.6]*	14.1 [7.2,25.6]*
	$\Delta$	0.164 [-2.21,7.69]*	1.85 [-0.0485,5.99]	-0.708 [-2.94,2.02]	-0.661 [-2.8,1.54]
	$r$	0.85 [0.79,0.89]	0.95 [0.93,0.97]	0.97 [0.95,0.98]	0.97 [0.96,0.98]
RM, -	0.628 [0.448,0.799]*	0.548 [0.38,0.736]*	0.728 [0.58,0.833]	0.596 [0.401,0.767]*	0.593 [0.401,0.767]*
	$\Delta$	-0.0813 [-0.238,0.0589]*	0.102 [-0.0226,0.221]*	-0.0404 [-0.148,0.124]	-0.0401 [-0.148,0.111]
	$r$	0.66 [0.55,0.75]	0.73 [0.64,0.81]	0.75 [0.65,0.82]	0.78 [0.69,0.84]

Table 5.1: Comparison of the flow shape and the WSA parameters obtained by the different blood flow models. Values are given as median [95% central range] and correlations as Pearson's correlation coefficient and 95% confidence interval (CI).  $\Delta$  indicates the difference and  $r$  the correlation to the Doppler derived values. \* indicate a significant difference of a group-wise comparison rEF vs nEF.

		Doppler	Triangular	Averaged	ARCSolver	combWK
Reduced EF						
S energy, AU	$\Delta$	3.76 [2.03,6.87]*	3.49 [1.77,6.09]	4.43 [2.42,7.54]	4.21 [2.29,7.42]	4.04 [2.18,7.3]
	$r$	-	-0.425 [-1.33,0.127]*	0.364 [0.0214,1.07]*	0.225 [-0.0732,0.864]*	0.131 [-0.205,0.914]*
D energy, AU	$r$	-	0.97 [0.95,0.98]	0.98 [0.97,0.99]	0.99 [0.98,0.99]	0.98 [0.97,0.99]
	$\Delta$	1.16 [0.416,2.19]*	0.988 [0.209,2.67]*	1.09 [0.429,2.17]	1.14 [0.545,2.1]*	1.09 [0.482,2.27]*
R energy, AU	$r$	-	-0.224 [-1.02,1.3]*	-0.0892 [-0.48,0.3]*	-0.0494 [-0.64,0.778]	-0.0404 [-0.638,0.301]*
	$r$	-	0.52 [0.31,0.68]	0.90 [0.84,0.94]	0.73 [0.59,0.83]	0.89 [0.82,0.93]
R/S energy, -	$\Delta$	0.619 [0.25,1.98]*	0.665 [0.0585,1.66]*	1.46 [0.68,3.17]*	0.651 [0.327,1.73]	0.558 [0.177,1.67]*
	$r$	-	0.0041 [-1.18,0.41]	0.675 [0.155,1.44]*	0.00529 [-1.2,0.338]*	-0.0974 [-0.557,0.223]
S/D energy, -	$r$	-	0.83 [0.72,0.89]	0.89 [0.82,0.93]	0.92 [0.87,0.95]	0.96 [0.94,0.98]
	$\Delta$	0.183 [0.0756,0.44]	0.196 [0.0209,0.427]*	0.346 [0.174,0.614]*	0.17 [0.0917,0.335]	0.156 [0.0635,0.337]
S/D energy, -	$r$	-	0.0184 [-0.238,0.289]	0.137 [0.0249,0.346]*	-0.0113 [-0.236,0.0542]*	-0.0319 [-0.12,0.0325]
	$r$	-	0.66 [0.49,0.78]	0.82 [0.71,0.89]	0.90 [0.83,0.94]	0.95 [0.92,0.97]
S/D energy, -	$\Delta$	3.2 [1.87,6.04]*	3.65 [1.01,17.3]*	3.9 [2.59,6.15]	3.44 [2.06,5.4]*	3.91 [1.87,5.67]*
	$r$	-	0.503 [-2.13,14.9]*	0.647 [-1.19,2.47]*	0.382 [-2.56,2.07]*	0.264 [-1.18,2.53]*
S/D energy, -	$r$	-	0.26 [0.01,0.48]	0.68 [0.52,0.80]	0.52 [0.31,0.68]	0.69 [0.53,0.80]
	$r$	-				
Normal EF						
S energy, AU	$\Delta$	4.17 [2.57,7.8]*	3.55 [2.09,6.39]	4.4 [2.78,7.7]	4.28 [2.7,7.33]	4.25 [2.7,7.33]
	$r$	-	-0.585 [-1.92,-0.13]*	0.133 [-0.34,0.687]*	0.0415 [-0.536,0.528]*	0.0315 [-0.536,0.528]*
D energy, AU	$r$	-	0.94 [0.92,0.96]	0.98 [0.98,0.99]	0.98 [0.98,0.99]	0.98 [0.98,0.99]
	$\Delta$	0.946 [0.499,1.89]*	0.805 [0.452,2.38]*	1.14 [0.658,2.15]	0.953 [0.547,1.71]*	0.953 [0.547,1.72]*
R energy, AU	$r$	-	-0.109 [-0.75,1.23]*	0.231 [-0.111,0.493]*	0.00559 [-0.594,0.283]	0.0119 [-0.594,0.345]*
	$r$	-	0.56 [0.42,0.67]	0.91 [0.88,0.94]	0.85 [0.79,0.89]	0.84 [0.77,0.88]
R/S energy, -	$\Delta$	0.924 [0.294,1.88]*	0.849 [0.367,1.52]*	1.29 [0.641,2.17]*	0.79 [0.298,1.72]	0.766 [0.272,1.72]*
	$r$	-	-0.0219 [-0.657,0.884]	0.374 [-0.0772,0.882]*	-0.0969 [-0.54,0.283]*	-0.124 [-0.54,0.269]
S/D energy, -	$r$	-	0.54 [0.40,0.65]	0.81 [0.74,0.86]	0.81 [0.74,0.87]	0.81 [0.74,0.86]
	$\Delta$	0.201 [0.0844,0.433]	0.235 [0.133,0.507]*	0.276 [0.16,0.486]*	0.174 [0.0756,0.366]	0.172 [0.0756,0.366]
S/D energy, -	$r$	-	0.0233 [-0.109,0.414]	0.078 [-0.014,0.188]*	-0.025 [-0.107,0.0358]*	-0.03 [-0.118,0.0334]
	$r$	-	0.20 [0.02,0.37]	0.84 [0.78,0.89]	0.85 [0.79,0.89]	0.85 [0.79,0.89]
S/D energy, -	$\Delta$	4.64 [2.97,7.09]*	4.53 [0.987,6.84]*	3.86 [2.92,5.25]	4.53 [3.3,6.57]*	4.5 [3.01,6.57]*
	$r$	-	-0.0862 [-2.5,2.1]*	-0.738 [-2.32,0.743]*	0.00895 [-1.75,1.59]*	-0.00719 [-1.97,1.59]*
S/D energy, -	$r$	-	0.23 [0.06,0.39]	0.73 [0.64,0.81]	0.58 [0.45,0.69]	0.58 [0.44,0.68]
	$r$	-				

Table 5.2: Comparison of the WIA energies obtained by the different blood flow models. Values are given as median [95% central range] and correlations as Pearson's correlation coefficient and 95% CI.  $\Delta$  indicates the difference and  $r$  the correlation to the Doppler derived values. \* indicates a significant difference of a group-wise comparison rEF vs. nEF.

		Doppler	Triangular	Averaged	ARCSolver	combWK
Reduced EF						
S peak, AU		67.6 [23.5,115]*	44.6 [19.4,102]*	101 [40.8,182]	74.7 [34.3,151]	69.9 [31.6,155]*
	$\Delta$	-	-15.8 [-43.5,-0.18]*	38.9 [-6.05,79.9]*	12.2 [-12.1,40.6]*	9.48 [-9.58,41.5]*
D peak, AU	$r$	-	0.89 [0.82,0.93]	0.83 [0.73,0.89]	0.92 [0.86,0.95]	0.91 [0.85,0.95]
		23.1 [8.91,48.4]*	13 [4.81,29.1]*	30.8 [12.8,54.6]	28.8 [13.4,55.2]*	21.8 [8.64,41.1]*
R peak, AU	$\Delta$	-	-10.5 [-36.6,6.02]*	7.81 [-17,20.9]*	4.47 [-21.1,34]	-2.34 [-25.9,13.8]*
	$r$	-	0.52 [0.31,0.68]	0.70 [0.54,0.81]	0.28 [0.03,0.50]	0.50 [0.28,0.67]
R/S peaks, -		7.79 [2.8,25.4]	9.57 [1.34,21]	19.2 [10.4,38.8]*	8.96 [3.74,29.7]*	6.59 [1.73,18.8]
	$\Delta$	-	1.56 [-13.4,8.72]*	10.3 [-3.59,24.5]*	0.841 [-17,11.4]*	-2.04 [-11.5,8.36]
S/D peaks, -	$r$	-	0.64 [0.47,0.77]	0.49 [0.27,0.66]	0.51 [0.29,0.67]	0.75 [0.62,0.85]
		0.137 [0.0557,0.562]	0.218 [0.0441,0.566]*	0.197 [0.108,0.4]*	0.113 [0.0564,0.406]*	0.0897 [0.0319,0.403]*
Normal EF	$\Delta$	-	0.0785 [-0.186,0.262]*	0.0638 [-0.177,0.176]	-0.00797 [-0.194,0.202]*	-0.0504 [-0.194,0.102]*
	$r$	-	0.46 [0.24,0.64]	0.54 [0.34,0.70]	0.45 [0.22,0.63]	0.56 [0.36,0.71]
S/D peaks, -		2.63 [1.25,8.04]*	3.61 [1.26,7.01]*	3.29 [1.88,4.48]*	2.62 [1.22,6.18]*	3.6 [1.23,7.01]*
	$\Delta$	-	0.957 [-2.97,3.41]*	0.609 [-4.11,2.7]*	0.211 [-5.14,3.11]*	0.664 [-1.69,3.54]*
Normal EF	$r$	-	0.53 [0.33,0.69]	0.42 [0.18,0.60]	0.30 [0.05,0.51]	0.57 [0.37,0.72]
Normal EF						
S peak, AU		76.2 [41.4,178]*	47.1 [25.2,104]*	90.8 [52,185]	80.7 [46.5,157]	80.5 [46.5,157]*
	$\Delta$	-	-24.9 [-94,-5.85]*	12.6 [-24.6,51.9]*	4.25 [-35.9,29.1]*	3.87 [-35.9,29.1]*
D peak, AU	$r$	-	0.85 [0.79,0.89]	0.87 [0.82,0.91]	0.90 [0.86,0.93]	0.90 [0.86,0.93]
		15.1 [7.27,45.1]*	10.6 [6.3,23.2]*	30 [18.4,55.7]	18.4 [8.37,38.7]*	18 [8.37,37]*
R peak, AU	$\Delta$	-	-3.47 [-29.3,2.02]*	14.9 [1.09,27.5]*	2.81 [-21.2,16.5]	2.4 [-21.2,15.5]*
	$r$	-	0.59 [0.47,0.70]	0.75 [0.66,0.82]	0.48 [0.33,0.61]	0.51 [0.36,0.63]
R/S peaks, -		9.43 [3.44,20.8]	8.75 [3.75,16.6]	15.9 [10.26,1]*	7.69 [3.33,15.5]*	7.04 [2.74,15.5]
	$\Delta$	-	-0.137 [-11.3,8.04]*	6.4 [-1.51,14.6]*	-1.28 [-10.1,3.97]*	-1.42 [-10.2,2.85]
S/D peaks, -	$r$	-	0.53 [0.38,0.64]	0.43 [0.28,0.57]	0.62 [0.50,0.72]	0.59 [0.46,0.69]
		0.118 [0.0472,0.3]	0.169 [0.0942,0.392]*	0.174 [0.107,0.295]*	0.0912 [0.0413,0.212]*	0.0856 [0.0413,0.212]*
S/D peaks, -	$\Delta$	-	0.0524 [-0.0639,0.254]*	0.0563 [-0.0702,0.156]	-0.0232 [-0.117,0.0345]*	-0.0271 [-0.137,0.0222]*
	$r$	-	0.34 [0.18,0.49]	0.53 [0.38,0.64]	0.77 [0.68,0.83]	0.75 [0.66,0.82]
S/D peaks, -		5.08 [2.47,8.93]*	4.71 [1.29,8.33]*	2.99 [2.05,4.5]*	4.41 [2.25,9.29]*	4.32 [2.56,9.29]*
	$\Delta$	-	-0.477 [-4.19,3.35]*	-2.29 [-5.69,0.808]*	-0.677 [-3.99,4.37]*	-0.572 [-3.99,4.37]*
Normal EF	$r$	-	0.44 [0.29,0.58]	0.40 [0.24,0.54]	0.30 [0.13,0.45]	0.30 [0.13,0.45]

Table 5.3: Comparison of the WIA peaks obtained by the different blood flow models. Values are given as median [95% central range] and correlations as Pearson's correlation coefficient and 95% CI.  $\Delta$  indicates the difference and  $r$  the correlation to the Doppler derived values. \* indicates a significant difference of a group-wise comparison rEF vs nEF.

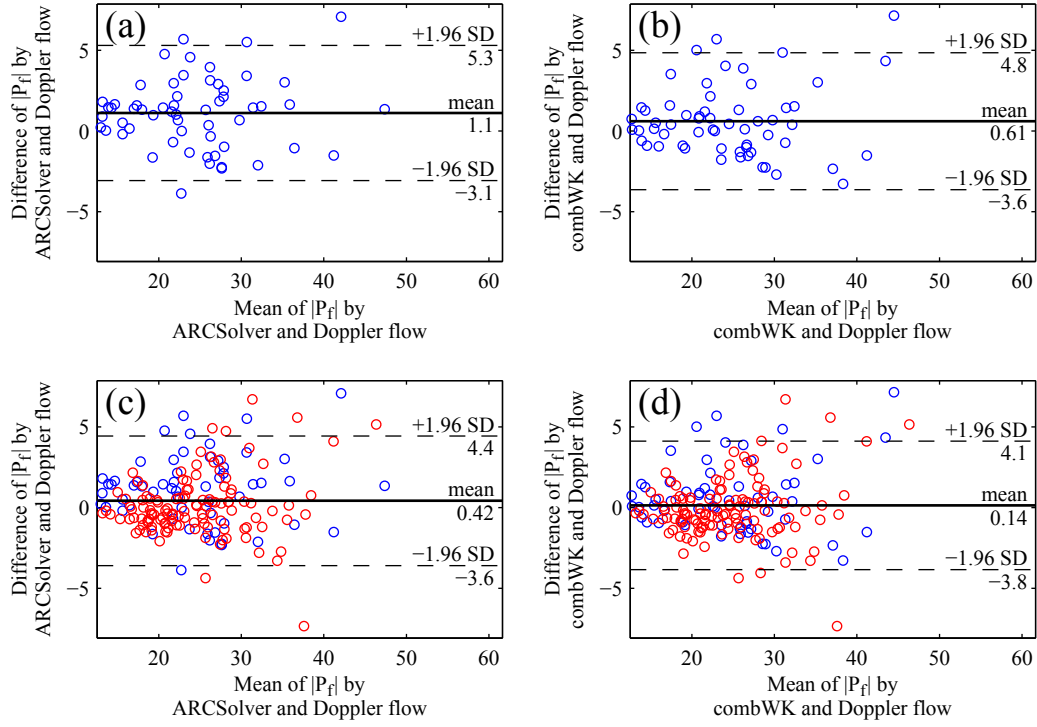


Figure 5.3: Bland-Altman plots comparing  $|P_f|$  derived by Doppler and ARCSolver flow (a,c) and by Doppler and combWK flow (b,d) for patients with reduced EF (a,b) and the whole study population (rEF blue, nEF red) (c,d).

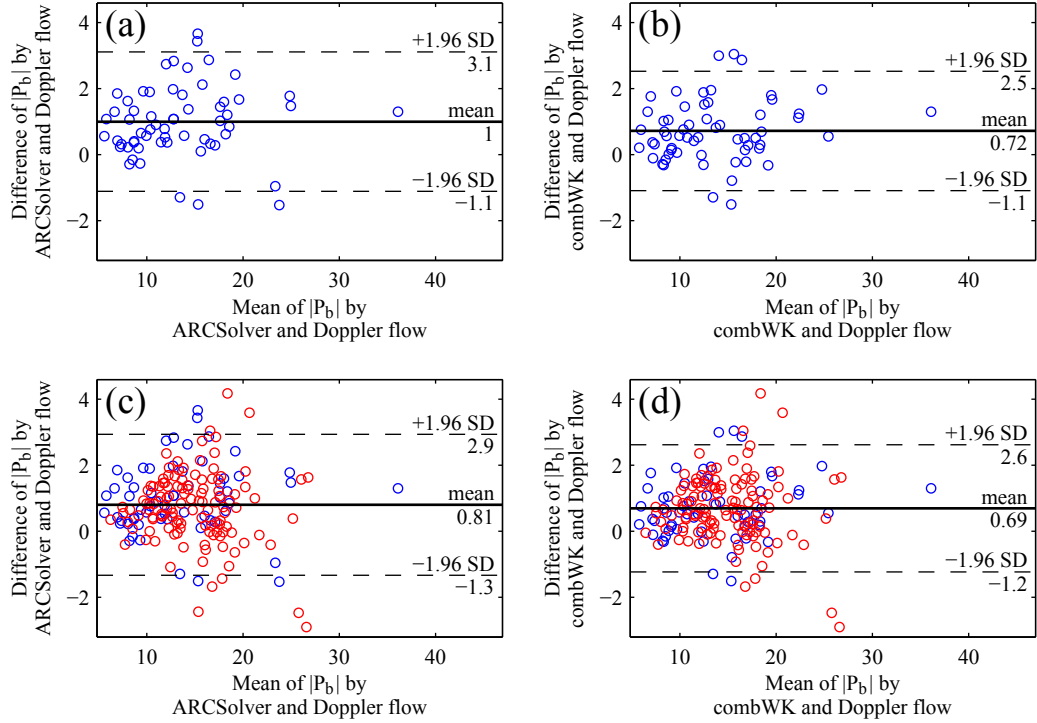


Figure 5.4: Bland-Altman plots comparing  $|P_b|$  derived by Doppler and ARCSolver flow (a,c) and by Doppler and combWK flow (b,d) for patients with reduced EF (a,b) and the whole study population (rEF blue, nEF red) (c,d).

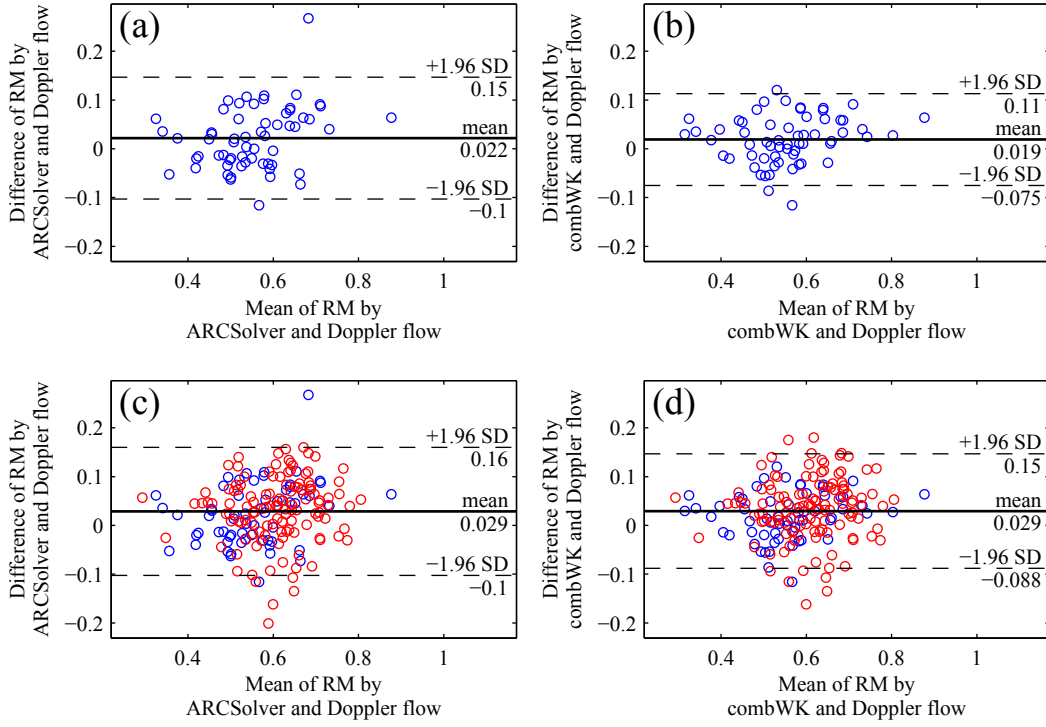


Figure 5.5: Bland-Altman plots comparing RM derived by Doppler and ARCSolver flow (a,c) and by Doppler and combWK flow (b,d) for patients with reduced EF (a,b) and the whole study population (rEF blue, nEF red) (c,d).

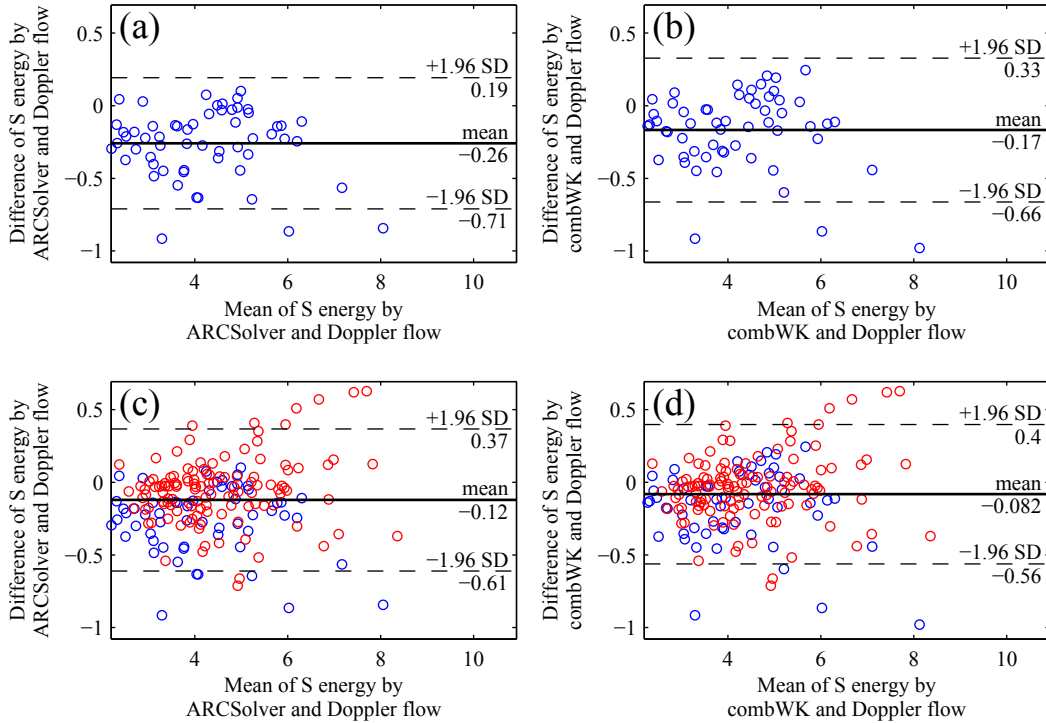


Figure 5.6: Bland-Altman plots comparing the S wave energy derived by Doppler and ARCSolver flow (a,c) and by Doppler and combWK flow (b,d) for patients with reduced EF (a,b) and the whole study population (rEF blue, nEF red) (c,d).

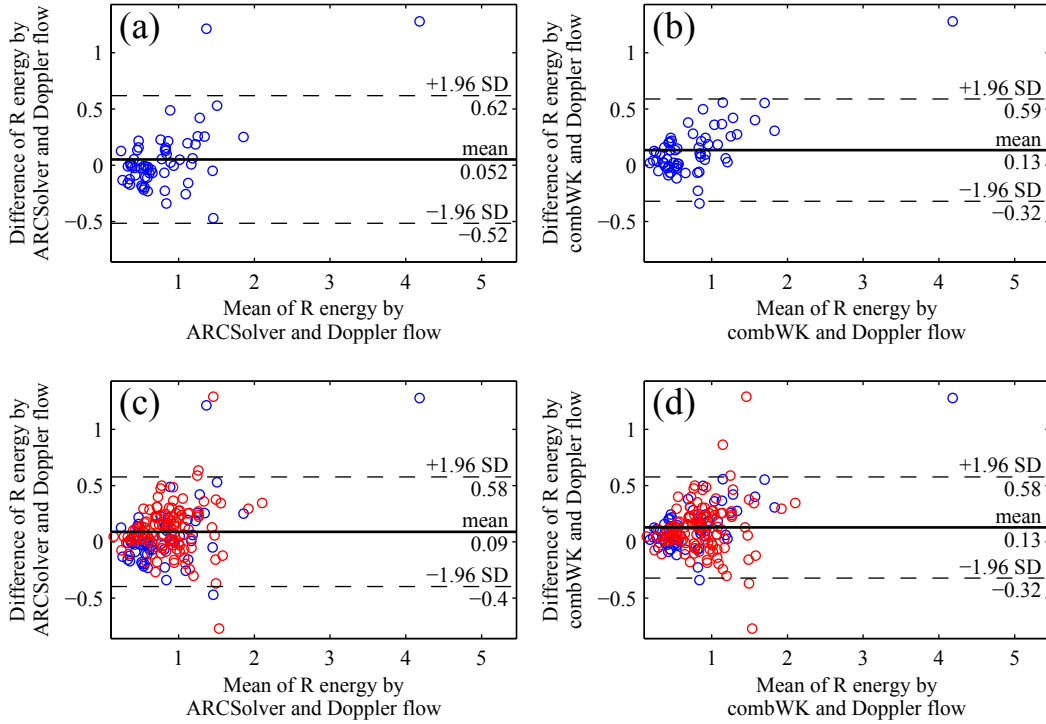


Figure 5.7: Bland-Altman plots comparing the R wave energy derived by Doppler and ARCSolver flow (a,c) and by Doppler and combWK flow (b,d) for patients with reduced EF (a,b) and the whole study population (rEF blue, nEF red) (c,d).

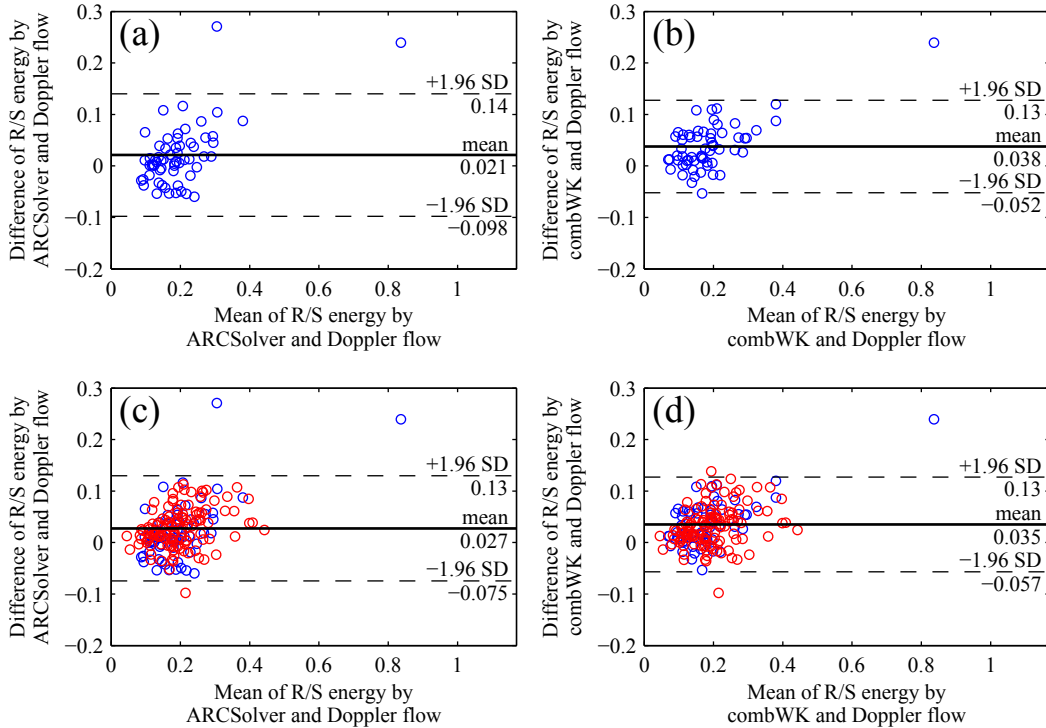


Figure 5.8: Bland-Altman plots comparing the ratio of the R to S wave energy derived by Doppler and ARCSolver flow (a,c) and by Doppler and combWK flow (b,d) for patients with reduced EF (a,b) and the whole study population (rEF blue, nEF red) (c,d).

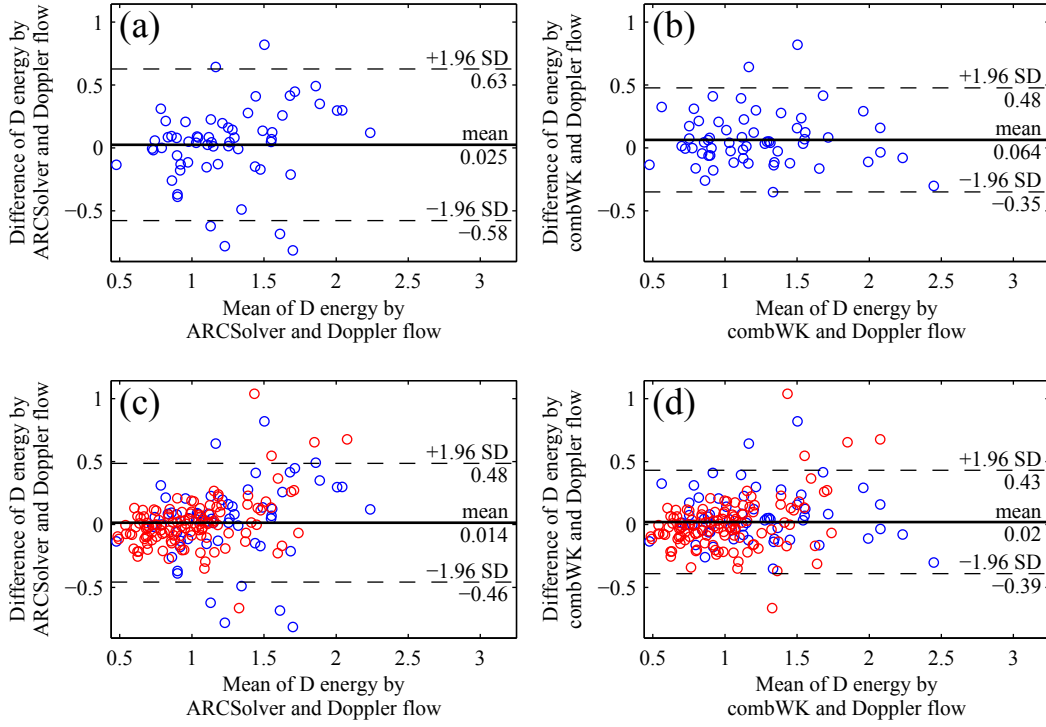


Figure 5.9: Bland-Altman plots comparing the D wave energy derived by Doppler and ARCSolver flow (a,c) and by Doppler and combWK flow (b,d) for patients with reduced EF (a,b) and the whole study population (rEF blue, nEF red) (c,d).

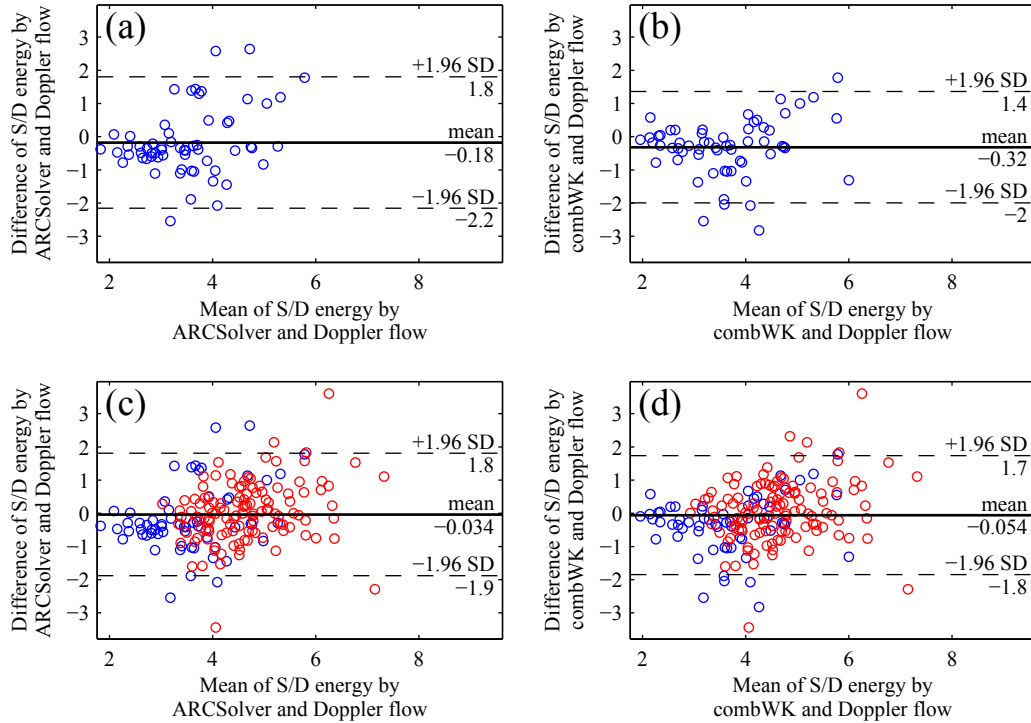


Figure 5.10: Bland-Altman plots comparing the ratio of the S to D wave energy derived by Doppler and ARCSolver flow (a,c) and by Doppler and combWK flow (b,d) for patients with reduced EF (a,b) and the whole study population (rEF blue, nEF red) (c,d).



analysis (PWA) devices already incorporate flow estimation procedures and also for heart failure patients, first studies have been performed based on modelled blood flow [122]. Nonetheless, in fact little is known about the applicability of these methods for WSA and WIA in patients with systolic heart failure so far. This was the starting point of the present work with the aim of providing first data regarding the performance of four different approaches for the estimation of aortic blood flow from pressure alone in patients with impaired systolic LV function. For this purpose, derived parameters were compared against the reference values obtained with Doppler flow measurements on the one hand, and between patients with reduced and normal EF on the other hand.

In their initial study, Westerhof and coworkers [142] observed that the triangular approximation tended to overestimate  $|P_f|$  and slightly underestimate  $|P_b|$  compared to the amplitudes obtained with measured flow. This is in accordance with the present findings in the rEF group. Subsequent studies [35, 49] then again reported an overestimation of both the backward and, even more pronounced, the forward amplitude when using the triangle, which is in line with the results obtained in patients with normal EF in this work. A possible reason for this discrepancy between the groups might be sought in the fact that Westerhof and coworkers [142] used a sample comprising different pathologies including heart failure, while both Kips and coworkers [49] and Hametner et al. [35] investigated patients with normal systolic function only. Correlations between the WSA parameters obtained with the triangular flow and the measured waveform were almost identical to those found by Hametner and coworkers in the control group [35], overall less than those reported by Westerhof [142], but greater than those found by Kips when using timing information derived from the pressure wave as in the present work [49].

By using the inflection point of the pressure wave to determine the position of the apex, the triangular flow was able to reproduce also belated flow peaks in the rEF group, compare figure 5.1. The estimated timing of maximum flow even showed a closer agreement to the measured one in patients with reduced EF than in controls. This might explain why the triangulation method provided better estimates of the WSA parameters for patients with reduced than for patients with normal EF, despite a higher median RMSE from the measured flow waveform for low EF. However, in both groups, modelled maximum flow tended to occur later than measured one. This might be due to the temporal difference between the first shoulder in the pressure wave, which was found to coincide well with peak flow [48], and the inflection point, which always occurs afterwards. Also Westerhof and coworkers [142] reported a slight overestimation as well as a wider scatter when using the inflection point to estimate the time of peak flow compared to measured values.

For the averaged waveform, correlations of  $|P_f|$  and  $|P_b|$  for estimated and measured flow in the control group were very similar to the earlier reported values [35, 49]. Furthermore, this approach performed better in patients with normal than with reduced EF, which might not be surprising considering that the waveform was derived from healthy subjects with normal systolic function. In these patients, the relative position of peak flow was well described by the averaged flow. Also

in line with previous findings [35, 49], the averaged waveform was superior to the triangle for wave separation in terms of both precision and correlation. Interestingly though, this held true for both patients with normal as well as reduced EF, despite the considerable variations in flow wave morphology introduced by the impairment of LV systolic function, as depicted in figure 5.1. Actually, one might expect that a flow model that is capable to adapt in shape would provide a more accurate approximation of aortic blood flow in patients with systolic heart failure. The averaged waveform, which does not allow for any changes in shape beyond a scaling in width, indeed resulted in the highest RMSE of all flow models in the rEF group. Nonetheless, the derived WSA parameters showed a smaller deviation from the reference values than those obtained with the triangulation method when looking at patients with reduced and normal EF separately. However, when considering both groups, the deficiency of the averaged waveform became apparent, namely its inability to reproduce the reduction in reflection magnitude associated with ventricular impairment found with the Doppler flow. This indicates that a constant waveform is in fact too simplistic to capture all group characteristics. Moreover, it underlines the importance of the flow wave morphology for the computation of the WSA parameters, and in particular the dependency on the position of maximum flow.

The ARCSolver as well as the Windkessel flow are based on Windkessel models to describe the dynamic relation between pressure and flow. Therefore, in contrast to both the triangular and the averaged waveform, the whole pressure pulse is taken into account to construct the corresponding flow contour. As a consequence, both methods were indeed able to mimic the ejection patterns found for normal and failing hearts, compare figures 5.1 and 5.2. Moreover, both approaches yield physiological flow waveforms, thereby eluding the drawbacks of the triangular approximation (no physiological shape) as well as of the averaged waveform (no adoption in shape). For the ARCSolver routine, some additional postprocessing steps are applied to obtain the final waveform [35], which is why its shape is more restricted than the Windkessel flow. Additionally, the ARCSolver flow is computed using a 3-element Windkessel model while the Windkessel flow is based on a 4-element model extended by  $P_\infty$ , resulting in two additional degrees of freedom, which again allow for a greater variation in shape. However, this higher degree of flexibility comes with the price of a loss in robustness compared to the ARCSolver flow, see section 3.4. In an attempt to unify the strengths of both, these two approaches were therefore combined in the combWK flow used in this chapter. In fact, the combWK flow provided the most accurate estimate of aortic flow assessed by the RMSE in both groups, and even more importantly, was the only method that resulted in the same RMSE for patients with reduced and normal EF. In other words, the quality of the estimate did not depend on the EF status, while the error became larger in patients with reduced EF for all other models. This is also reflected in the position of peak flow, which was most accurately estimated by the combWK model in both groups of patients.

The correlations found for  $|P_f|$  and  $|P_b|$  in controls when using the ARCSolver flow are well in line with the values reported by Hametner et al. [35] and are very similar to those obtained with the combWK flow as well as with the averaged waveform. Also in terms of accuracy and

precision, the three approaches showed a comparable behaviour for patients with normal systolic function, whereby the averaged waveform performed slightly better than the other two models with regards to  $|P_f|$ , while the ARCSolver and combWK flow yielded better results for  $|P_b|$ . In patients with reduced EF, on the other hand, both the ARCSolver and combWK flow were favourable to the averaged waveform and, with the combWK flow, estimates of  $|P_b|$  and RM could be further improved compared to the ARCSolver flow, as shown in figures 5.4 and 5.5.

In the control group, the combWK flow equals the ARCSolver flow in 88% of the cases. Therefore, the parameters derived with the two flow models are very similar for patients with normal EF, which is why the nEF group is not depicted separately in Bland-Altman plots. Instead, a comparison for the whole study population was included. With the aim of developing a flow model that is applicable in the general population, the quality and behaviour of the estimates should ideally be independent of the EF-status. Even though some differences in performance of course persisted between the groups, the limits of agreement could be noticeable tightened for  $|P_b|$  and RM when using the combWK flow compared to the ARCSolver flow, not only for the rEF group but also for the whole study population.

As already discussed in the previous chapter, WIA can be considered less robust than WSA because the computations are based on the product of the incremental changes in pressure and flow and not the absolute values. While robustness referred to the effect of measurement noise or errors in the last chapter, with respect to the flow models it means that also small deviations from the measured flow wave might have a large effect on the derived parameters. These effects can be expected to be particularly pronounced when using peak intensities, while the wave energies should be less affected. Moreover, different portions of the flow wave affect different parameters: those associated to the S wave depend mostly on the early systolic upstroke up to the flow peak, those describing the D wave on the late systolic decline and for the R wave, the mid-systolic part is most relevant. However, of course the shape of the pressure waveform, i.e. its raising and falling, also has an impact on which specific aspects or portions of the flow wave are most emphasised.

For the triangular flow, both upstroke and decline are always linear resulting in a poor correspondence to the measured waveforms in this regard. This is also reflected in the derived wave energies, since accuracy and precision were, of all methods included, by far worst for the triangular approximation independent of ventricular function. The median difference to the reference value was up to a factor 10 greater than for the best estimate and the limits of agreement were partly more than twice as wide. Because of its non-physiological shape, the triangular flow wave therefore represents no suitable approximation of blood flow for WIA, neither for patients with normal nor with reduced ejection fraction.

The averaged waveform, in contrast, was computed from measured flow waves and therefore displays all the typical features of a physiological ejection pattern. However, from figure 5.2 it

can be seen that, also for controls, the upstroke tends to be more concave than in the Doppler flow waves used in this work, resulting in a larger maximum slope. This might explain the overestimation of peak forward wave intensity and wave energy during early systole. For patients with reduced EF and belated maximum, peak flow is moreover reached too early, the upstroke is therefore too steep and the duration of the forward compression wave, i.e. the time to peak flow, is consequently shorter than for the measured waves. The first two arguments justify the excessive overestimation of the S peak found for the averaged waveform. This effect is less pronounced for the wave energy, probably because of the shorter duration of the forward compression wave compared to the reference method. For the decline, similar observations can be made. In particular, in patients with impaired ventricular function, the premature flow peak causes a prolongation of the backward compression wave, possibly explaining the enormous overestimation of the R wave energy. The beginning of the forward decompression wave, in contrast, depends on the pressure contour only, which might explain why estimates of the D wave energy were more precise in both groups of patients. However, by assuming flow to be qualitatively constant in all patients, differences between the groups observed for the Doppler flow could not be reproduced. Thus, in line with the results obtained for WSA, not all characteristics were captured. The present data therefore suggests that, even though the averaged waveform might represent an acceptable approximation for patients with normal systolic function only, it might not be the best choice for the use in the general population, where subjects with different degrees of ventricular impairment might be included.

WIA estimates obtained with the ARCSolver and combWK flow were more accurate than those derived using the averaged or triangular waveform, indicating that the respective modelled flow waves showed less systematic deviation from the measured one. Furthermore, both methods were overall superior to the triangle in the present dataset and, in contrast to the averaged waveform, differences in wave energies and their ratios between the groups observed for the Doppler flow were well captured, with the only exception of the reduction in S wave energy. However, the combWK showed a tendency towards lower values in the rEF group, yet without reaching statistical significance. Comparison of the ARCSolver and combWK flow showed an improvement for all but the S wave energy, both at a group and a population level when using the combWK flow. Nevertheless, it should be stressed again that the limits of agreement were relatively large for all WIA parameters and in particular for the peak values.

To summarise, for WSA, it seems feasible to replace aortic blood flow by modelled waveforms also for patients with systolic heart failure. For this purpose, the model should be able to adopt in shape and at the same time provide a physiological waveform in order to attain high precision as well as the correct qualitative behaviour, as observed for the combWK flow in this work. The triangulation method has already been used for WSA in a longitudinal study in patients with systolic heart failure and a prognostic value of  $|P_b|$  for the occurrence of cardiovascular events has been found [122]. The results obtained in this work show that estimates of  $|P_b|$  can be markedly improved when applying a more sophisticated flow model. Therefore, also its association to adverse events and its value for risk prediction might potentially be enhanced by the use of a more

appropriate flow estimation.

As expected, WIA was more sensitive than WSA and the considered flow estimates resulted in rather large deviations from the reference values. In order to improve the performance, measurements with higher sampling rates might be beneficial. Alternatively, a postprocessing, e.g. smoothing or averaging, of the data could help to make the parameters more reliable. However, peak values might generally be too sensitive on the particular waveform to be used with flow models and wave energies therefore seem to be preferable. Nonetheless, despite these drawbacks, some of the main features observed for the WIA parameters derived with Doppler measurements could again be reproduced using the ARCSolver or combWK flow.

With regards to the combWK flow, it has to be emphasised that this work represents a proof of concept only. The same study population was used to develop and to test the method, which might of course introduce considerable bias. Also the criterion when to use the ARCSolver and when to use the Windkessel flow was derived from this population, even if it was not optimised to avoid a possible overfitting. Moreover, it should be kept in mind that the criterion might not work in different data sets, especially when using central pressure waves assessed by a different device. The age of the study population represents another limitation. Ideally, the combWK flow should be tested in a larger sample, including also younger subjects. In particular because it has been suggested that with age and the associated increase in wavelength, the arterial system "degenerates" into a Windkessel [69]. Thus it is possible that the model fits middle-aged to elderly subjects with increased stiffness better than the young and healthy ones. For patients with systolic heart failure, on the other hand, the considered population seems to be representative for this cohort, at least when compared to other data found in literature, e.g. [21, 88, 137]. However, also in this regard, the behaviour of the model for different severity levels of ventricular impairment should be examined.

## Conclusion

In conclusion, with the proposed novel approach first promising results could be obtained. As discussed in the last chapter, the change in flow wave morphology associated with ventricular impairment had a considerable impact on the derived WSA and WIA parameters, which could not be reproduced by all flow models considered. This should be kept in mind when applying a flow model, not only in patients with systolic heart failure but also in the general population, where subjects with differing LV systolic performance might be included. Nevertheless, for WSA it seems feasible to replace flow measurements with modelled flow waves derived from non-invasively recorded pressure alone also in patients with systolic heart failure. This would greatly facilitate the assessment of WSA parameters and would therefore enable its use in large population studies or, in a next step, its inclusion in regular patient check-ups or screening strategies based on a single non-invasive pressure measurement. WIA parameters were found to be extremely sensitive on the flow waveforms, unfortunately resulting in a rather poor quality of the estimated parameters.

## Chapter 6

# Summary and conclusions

The haemodynamics in the arterial system result from a complex interaction of the ejecting heart and the vasculature, i.e. the ventriculo-arterial coupling. For healthy hearts, the ventricular component is more or less negligible because the way how the heart ejects is (qualitatively) very similar across individuals as well as for different loading conditions. In systolic heart failure (SHF), however, the interaction becomes much more relevant, making these patients especially interesting but at the same time challenging from a haemodynamic point of view.

One of the aims of this thesis was to analyse the role of cardiac function for the parameters of pulsatile haemodynamics derived by PWA, WSA and WIA. The obtained results indicate that the derived parameters can indeed be used to characterise the properties of the arteries only in subjects with normal systolic function. For patients with SHF, on the contrary, cardiac performance was associated to most haemodynamic measures, including indices of wave reflections, which complicates their interpretability. The apparent reduction in wave reflections in SHF patients compared to controls could be explained by a shortening of the ejection duration as a manifestation of the impaired coupling between the ventricle and the arterial system. Hence, the magnitude of wave reflections might not be a suitable indicator of arterial stiffness when the heart is failing. These observations underscore the importance of considering cardiac function for risk stratification. This applies in particular for patients with SHF and more widely for the general population, where asymptomatic subjects with varying degrees of systolic impairment might be included.

SHF is very heterogeneous in its appearance, including in the resulting ejection patterns. Therefore, a new model of blood flow (combWK) was developed in the course of this work, with a special focus on its ability to reproduce also pathological flow waveforms. This method was compared to already existing models of blood flow, namely the triangular, averaged and ARCSolver flow and their performance in patients with SHF and controls was investigated using measured flow as reference. The triangular flow represented a rather poor description in both groups with respect to the precision of the derived estimates of WSA and WIA compared to the reference. This was

most probably caused by the unphysiological shape of the flow wave, which became especially noticeable for the WIA parameters. The averaged waveform achieved a better precision, but it was too simplistic to capture the qualitative differences between the groups. The ARCSolver and the combWK flow are both based on mathematical models to describe the dynamic relation between pressure and flow and provide a physiological waveform as well as a certain flexibility in shape. Nonetheless, the good performance of the ARCSolver flow observed for patients with normal systolic function could not be fully transferred to patients with SHF. This drawback could be eliminated with the proposed combined model, for which the accuracy of the estimated flow waves and of the derived parameters was almost independent of cardiac function. However, these results present a proof of concept only, because the same study population was used to develop and to test the model. Further research is needed to evaluate the performance of the model on different datasets. Moreover, there is still room for improvement regarding the parameter identification procedure and in particular the definition of the objective function used for optimisation.

Overall, replacing the flow measurement by an approximation derived from non-invasively assessed central pressure seems feasible for WSA in both patients with SHF and controls. WIA is very sensitive on the flow waveforms and the parameter estimates were less accurate than for WSA, especially when using peak intensities for quantification. The use of wave energies might therefore be preferable. Nonetheless, also for WIA, distinct differences between SHF and controls found with measured flow could be reproduced with modelled flow waveforms. These differences might potentially be used as indicators for a systolic dysfunction in the future, enabling the detection of SHF from non-invasively measured pressure alone as well as an improvement of risk stratification in patients with impaired systolic function.

## Appendix A

# Asymptotic pressure as an additional parameter in the Windkessel models

The Windkessel models surely belong to the most extensively investigated models of the cardiovascular system. Nevertheless, disunity exists whether aortic pressure should be modelled as resulting from ventricular ejection only or if an asymptotic pressure level  $P_\infty$  should be included.  $P_\infty$  thereby represents a pressure that is sustained by the vasculature even without further excitation from the heart.

The aim of this chapter is therefore twofold. First, the influence of an additional model parameter  $P_\infty$  on the overall behaviour of the three Windkessel models presented in section 2.3 is examined. For this purpose, simulated pressure contours with and without  $P_\infty$  are compared in the time as well as in the frequency domain based on a talk given at the MATHMOD 2015 and published in [97].

Second, the question whether pressure should be modelled as dropping to zero or as approaching an asymptotic level  $P_\infty$  when the heart stops beating is investigated. Therefore, invasively acquired pressure contours of patients presenting with missing heart beats and thus prolonged diastolic pressure drops are examined. More precisely, the fitting performance of the (mono-) exponential decay described by the Windkessel models is analysed with respect to  $P_\infty$ . This part is based on a poster presented at the ARTERY conference 2014 [98].



Model	$Z_{in}(0) = SVR$	$Z_{in}(\omega_n), n > 0$
WK2, 2-element Windkessel	$R_p + \frac{P_\infty}{Q}$	$\frac{R_p}{1 + i\omega_n R_p C_a}$
WK3, 3-element Windkessel	$R_p + Z_c + \frac{P_\infty}{Q}$	$Z_c + \frac{R_p}{1 + i\omega_n R_p C_a}$
WK4p, parallel 4-element Windkessel	$R_p + \frac{P_\infty}{Q}$	$\frac{i\omega_n Z_c L}{i\omega_n L + Z_c} + \frac{R_p}{1 + i\omega_n R_p C_a}$

Table A.1: The input impedances  $Z_{in}$  described by the three different Windkessel models.

## A.1 Methods

### A.1.1 Simulation runs

In order to investigate the influence of  $P_\infty$ , first of all it is important to understand its effect on the other model parameters.  $P_\infty$  directly affects the steady part of pressure only and therefore the zero frequency component of the arterial input impedance  $Z_{in}$ , which is usually identified with the systemic vascular resistance (SVR). Strictly speaking, the pressure drop between mean aortic  $\bar{P}$  and right atrial pressure  $\bar{P}_{ra}$  should be used for the computation of SVR, but, since  $\bar{P}_{ra} \ll \bar{P}$ , right atrial pressure is usually neglected [77].

$$SVR = \frac{\bar{P} - \bar{P}_{ra}}{Q} \approx \frac{\bar{P}}{Q} = Z_{in}(0) \quad (\text{A.1})$$

Originally, the model parameter  $R_p$  was supposed to represent SVR. However, even without including  $P_\infty$ , the identity  $R_p = SVR$  only holds for the 2-element (WK2) and parallel 4-element Windkessel (WK4p), but not for the 3-element Windkessel (WK3), where SVR equals  $R_p + Z_c$ , see table A.1. Thus, for the further investigation, SVR and  $R_p$  were considered two distinct parameters, which are connected via the following relations in dependency of  $P_\infty$ .

$$\text{WK2, WK4p: } R_p = \frac{\bar{P} - P_\infty}{Q} = SVR - \frac{P_\infty}{Q} \quad (\text{A.2})$$

$$\text{WK3: } R_p = \frac{\bar{P} - P_\infty}{Q} - Z_c = SVR - \frac{P_\infty}{Q} - Z_c \quad (\text{A.3})$$

If both pressure and flow of a specific person are known, SVR as well as  $Z_c$  can be estimated, compare equation (A.1) and section 2.2.3. Considering these parameters to be given, the above equations thus imply that only  $R_p$  is directly affected by  $P_\infty$ , whereby higher values of  $P_\infty$  result in lower values of  $R_p$ . This means that even though  $P_\infty$  explicitly appears in the formula for  $Z_{in}(0)$  only, its effect on  $Z_{in}$  will be observable over the whole frequency range due to its quantitative influence on  $R_p$ . However, the term including  $R_p$  equals  $\frac{R_p}{1 + i\omega_n R_p C_a}$  in all three models, compare table A.1, which converges to 0 for  $n \rightarrow \infty$ . It is therefore expected that differences in  $Z_{in}$  will be most noticeable in the lower frequency range.

To enable a direct comparison of the simulated pressure waves with and without  $P_\infty$ , the pa-

Parameter	Description	Used for	Value	Unit
SVR	systemic vascular resistance	WK2,WK3,WK4p	1.4	mmHg · s/ml
$C_a$	total arterial compliance	WK2,WK3,WK4p	1.6	ml/mmHg
$Z_c$	characteristic impedance	WK3,WK4p	0.04	mmHg · s/ml
$L$	total arterial inductance	WK4p	0.014	mmHg · s <sup>2</sup> /ml
$\bar{Q}$	mean flow	WK2,WK3,WK4p	73.6	ml/s
DBP	diastolic blood pressure	WK2,WK3,WK4p	90.1	mmHg

Table A.2: Parameter values for the standard parametrisation.

rameters  $C_a$ ,  $Z_c$ ,  $L$  and SVR were fixed and  $R_p$  was varied according to the above relations for  $P_\infty \in \{0, 25, 50, 75\}$  mmHg. A typical flow curve depicted in figure A.2 was taken as input to the models and the parameters were chosen based on values reported in literature for a healthy, adult population [115] as given in table A.2.

### A.1.2 Fitting performance

Aortic blood pressure waveforms were assessed invasively using high-fidelity pressure-tip catheters (5F Millar SPC-454D) at the university teaching hospital Wels-Grieskirchen in Wels, Austria. The recordings of 5 different patients presenting with missing heartbeats were used for analysis, resulting in a total of 35 data sets of irregular heartbeats. The regular heartbeat duration  $T$  was determined from the preceding beat and diastolic blood pressure (DBP) was set to  $P(0)$ . An exemplary pressure reading is depicted in figure A.1.

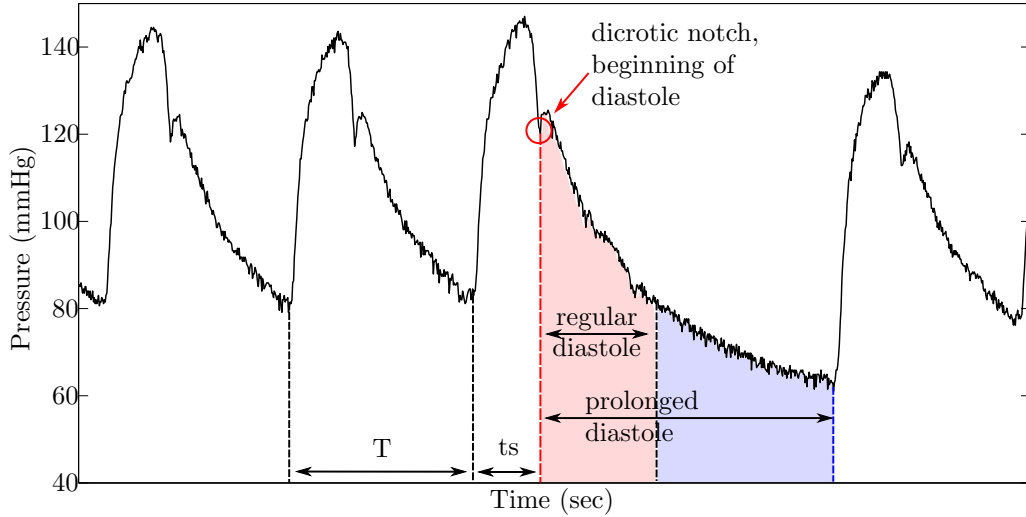


Figure A.1: Exemplary aortic pressure signal including a missing heart beat. The duration of a regular cardiac cycle  $T$  is determined from the preceding beat.

The decrease of aortic pressure has been found to be approximately exponential during diastole, a feature that is well caught by the Windkessel models, compare section 2.3.3. Therefore, the

monoexponential pressure drop modelled by the 2- and 3-element Windkessel

$$P_{\text{dias}}(t) = P_{\infty} + P_{RC}(t_s) \exp\left(\frac{t_s - t}{R_p C_a}\right)$$

with time constant  $\tau = R_p C_a$  was used to describe the diastolic pressure. In order to investigate how  $P_{\infty}$  influences the fitting performance, the exponential decline in its equivalent formulation (assuming periodicity)

$$P_{\infty} + (P_{\infty} - \text{DBP}) \cdot \exp\left(\frac{T - t}{R_p C_a}\right)$$

was fitted to both the regular and the prolonged diastole of the experimental data for  $P_{\infty}$  increasing from 0 to 100% of DBP in steps of 5 percentage points. The fitting was performed in Matlab R2011b (The MathWorks Inc, Natick, Massachusetts, United States) by minimising the squared error with respect to  $\tau$  using the inbuilt `fminsearch` function with initial estimate  $\tau = 1.5$  s. To compare the results for different values of  $P_{\infty}$ , the root mean square error (RMSE) between fitted and measured pressure over both the regular and the prolonged diastole was computed. Results were finally averaged first per patient and subsequently over the group to account for the different number of individual measurements.

## A.2 Results

### A.2.1 Simulation runs

The results of the simulation runs for the three different Windkessel models and  $P_{\infty}$  varying from 0 to 75 mmHg are depicted in figure A.2. In all three cases, the effect is most prominent during diastole with a steeper decline for higher values of  $P_{\infty}$ . The systolic upstroke, in contrast, remains almost unchanged with the largest changes observed for the WK4p.

The differences between the modelled input impedances for  $P_{\infty} = 0$  and  $P_{\infty} = 75$  mmHg are presented in figure A.3. As expected, the differences are largest for low frequencies and decline for increasing  $n$ .

### A.2.2 Fitting performance

The prolonged heart beats were on average 1.81 (range 1.49 to 2.02) times longer than the preceding regular beats and the mean duration of diastole was more than doubled. More precisely, regular diastole endured on average 0.52 s (range 0.39 to 0.69 s), while the mean duration of a prolonged diastole was 1.22 s (range 0.86 to 1.66 s), resulting in a 2.3-fold increase (range 1.81 to 2.62) in diastolic duration. Mean diastolic blood pressure was 77 mmHg (7.2 SD) and mean systolic blood pressure 137 mmHg (11.6 SD).

Figure A.4 shows a representative example of the results obtained with the two different fitting

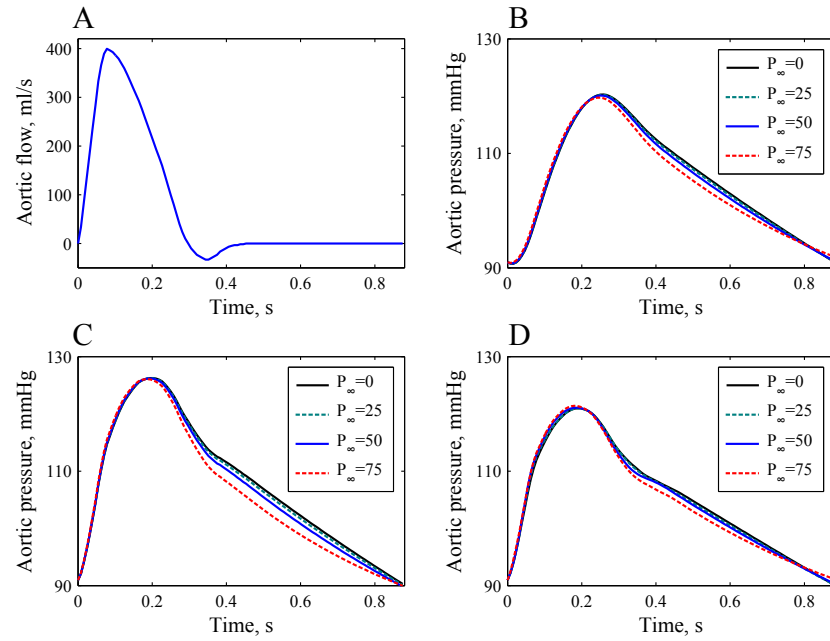


Figure A.2: A: typical flow curve used as input to the models. B-D: simulated pressure waves for  $P_\infty$  ranging from 0 to 75 mmHg obtained with the WK2 (B), WK3 (C) and the WK4p (D).

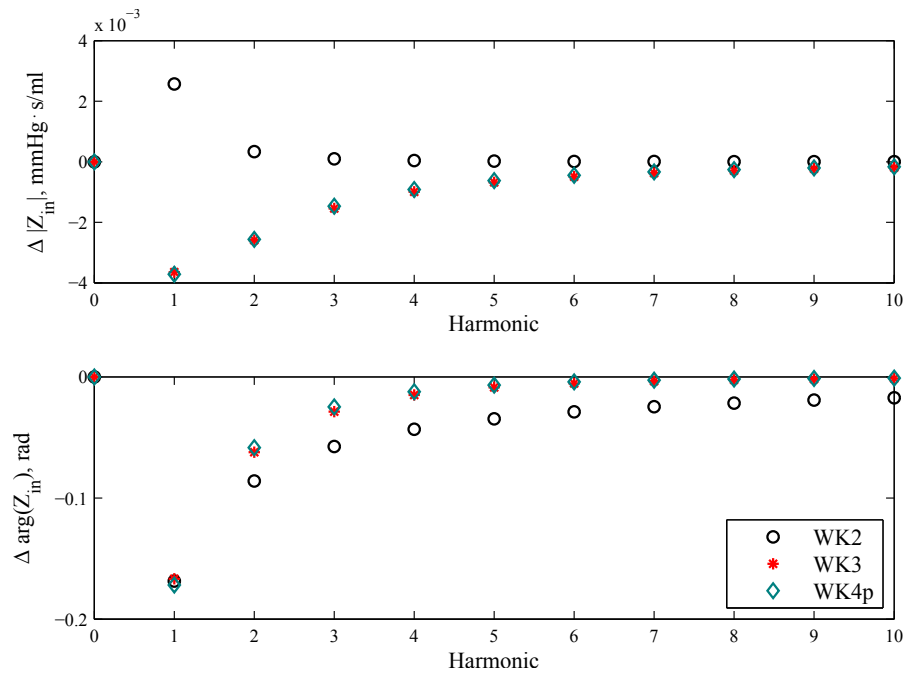


Figure A.3: Difference between modulus (top) and phase (bottom) of modelled input impedance for  $P_\infty = 0$  and  $P_\infty = 75$  mmHg for the three different Windkessel models. Relative to the respective  $Z_{in}$  for  $P_\infty = 0$  as reference, the maximum deviation equals 5% for the modulus and 15% for the phase angle, compare also figure 2.14.

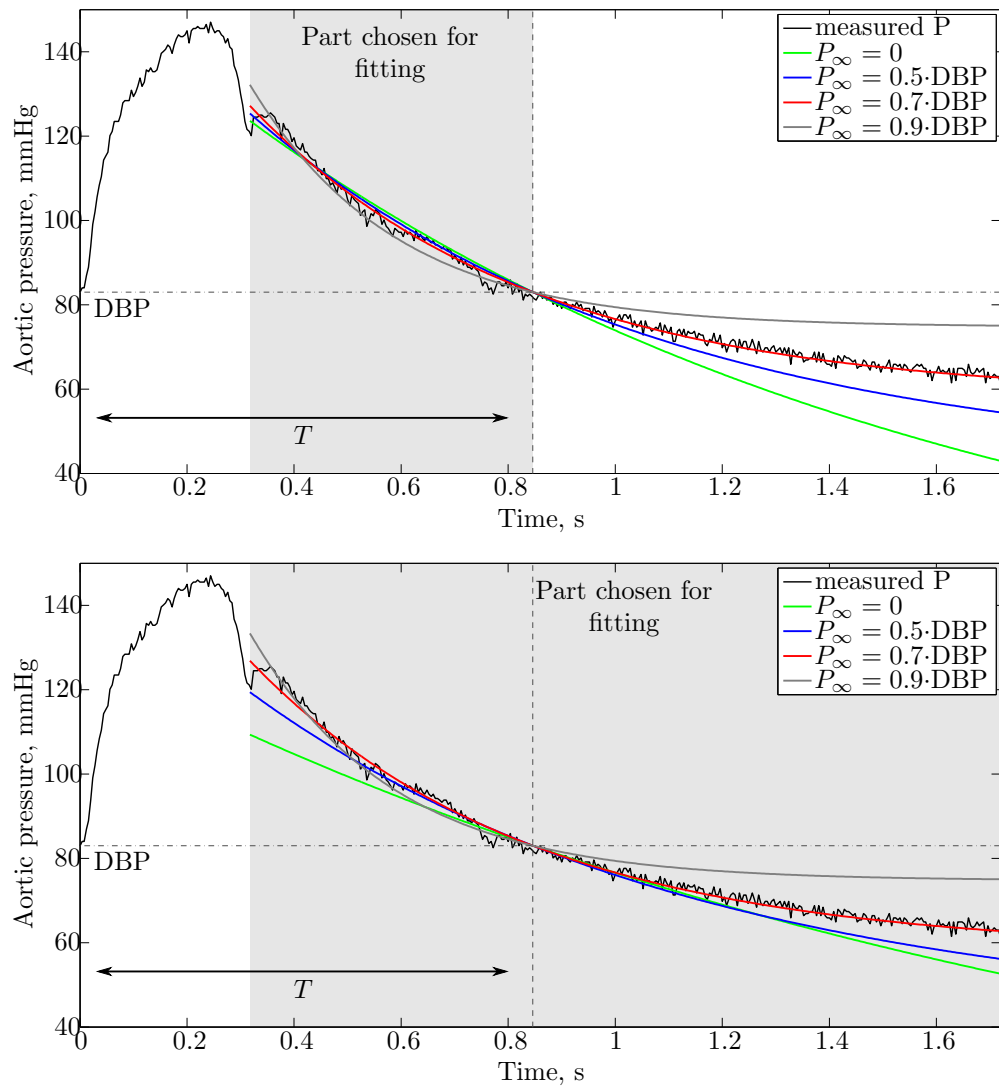


Figure A.4: Exemplary result of fitting. Top: fitted over the duration of the regular diastole, bottom: fitted over prolonged diastole.

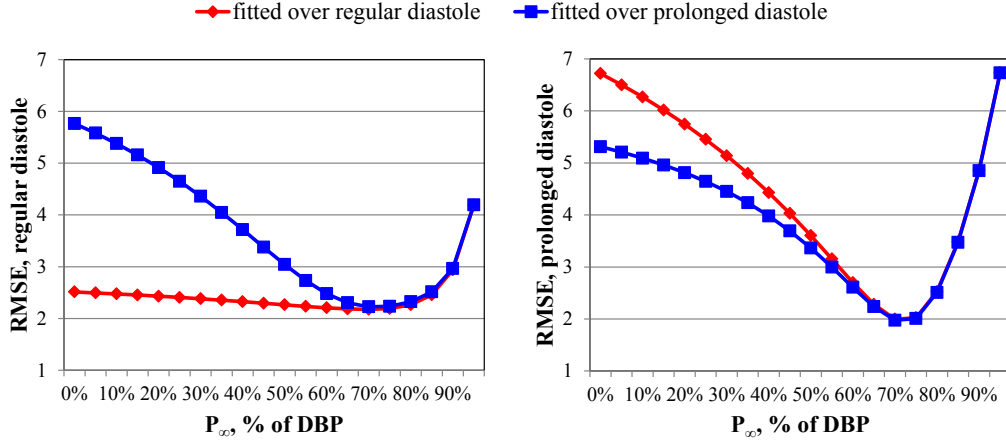


Figure A.5: Mean RMSE between analytical function and regular (left) and prolonged (right) diastole when fitted to the regular (red) and prolonged (blue) part respectively.

procedures. Independently of the part chosen for fitting, mean RMSE was lowest for  $P_\infty = 0.7 \cdot \text{DBP}$ , compare figure A.5. When  $P_\infty$  was not included, the RMSE between modelled pressure drop and prolonged diastole was more than twice as high as for  $P_\infty = 0.7 \cdot \text{DBP} \approx 54 \text{ mmHg}$  (5.1 SD), regardless of the part chosen for fitting.

### A.3 Discussion

The simulation runs show that the temporal waveforms of modelled pressure are only moderately affected by  $P_\infty$  if SVR is fixed and  $R_p$  varied accordingly. Because of the stronger impact of  $P_\infty$  on the lower frequency range of the modelled input impedance, the biggest changes could thereby be observed during diastole, with a steeper decline for higher values of  $P_\infty$ . The fast systolic upstroke, in contrast, remained nearly unaltered, reflecting the negligible influence of  $P_\infty$  on  $Z_{in}$  for higher frequencies.

Because SVR and  $C_a$  were fixed, higher values of  $P_\infty$  resulted in lower values of  $R_p$  and therefore smaller time constants  $\tau$ . The corresponding pressure waveforms thus showed a faster diastolic drop towards a higher asymptotic value, which explains the greater curvature observed in figure A.2. The results obtained with the fitting experiments suggest that this effect might indeed improve the accuracy of an exponential decline as a model of the diastolic pressure decay. The deviation from measured data could be markedly reduced when pressure was not assumed to drop to zero, compare figure A.4. This reduction was particularly notable with regards to the prolonged diastole, where the RMSE could be more than halved by including  $P_\infty$ . However, even when only the regular diastole was considered, an improvement in the RMSE could be achieved.

The physiological meaning and magnitude of  $P_\infty$  has been investigated before [2, 129, 131]. From the definition of SVR in equation (A.1), it follows that choosing  $P_\infty$  equal to mean right atrial pressure  $\bar{P}_{ra} \approx 5 \text{ mmHg}$  would agree with the classical physiological interpretation of  $R_p$  as total

vascular resistance SVR. This approach was adopted by Aguado-Sierra et al. [2] in a simulation study investigating wave reflections in the arterial system. However, Wang et al. [130] observed that  $P_\infty$  is influenced by the vasoactive state of the arteries and suggested that  $P_\infty$  is thus "a function of the local biochemical, humoral, and mechanical milieu" [130, p.H162], i.e. a varying parameter that does not coincide with venous or right atrial pressure. Moreover, when  $P_\infty$  was estimated together with  $\tau$  from the diastolic decay in experimental data, indeed values greater than  $\bar{P}_{ra}$  were obtained. In a study in mongrel dogs, values between 30-40 mmHg were found for a mean aortic pressure of 83 mmHg [131]. Schipke et al. [112] analysed human aortic pressure waves during periods of up to 20s of controlled cardiac arrest and reported values in the range of 25 mmHg for the constant term in the exponential decay when fitted to the measured diastolic pressure drop. Also the fitting results obtained in this work show that a value of  $P_\infty$  above right atrial pressure might be preferable. However  $P_\infty = 0.7 \cdot \text{DBP}$ , which corresponds to a minimum RMSE in this work, is markedly higher than the values previously proposed.

As mentioned before, the equality  $R_p = \text{SVR}$  is lost for  $P_\infty \neq \bar{P}_{ra}$ . However, it should be noted that  $R_p$  and SVR were considered two distinct parameters in this work and the value of SVR, as an important characteristic of the arterial system, stays completely unaffected by  $P_\infty$ . For a clear distinction between the two parameters,  $R_p$  has previously been termed "effective resistance of the peripheral systemic circulation" [2, 131]. Although the physiological meaning and anatomic counterpart of  $R_p$  are not yet entirely clear, it was suggested to represent the resistance of the small arteries with a diameter  $> 60\mu\text{m}$  [129].

Overall, the results suggest that the fitting performance might be improved by including  $P_\infty$  and that this inclusion does not affect the modelled characteristics of the arterial system, like resistance SVR and compliance  $C_a$ . The so-called decay time method is a common technique for the estimation of arterial compliance [145]. Since the time constant  $\tau$  of the exponential pressure drop described by the Windkessel models equals  $R_p$  times  $C_a$ ,  $\tau$  is supposed to hold information on both peripheral resistance and arterial compliance. Thus, to obtain an estimate of  $C_a$ , the decay time  $\tau$  is identified by fitting the analytic function to the measured diastolic pressure. If  $R_p$  is known,  $C_a$  can subsequently be derived. Even though  $P_\infty$  is not considered in the classic decay time method [118], the results of this work demonstrate that, by determining both  $\tau$  and  $P_\infty$  from a measured diastolic pressure drop, the estimate of  $\tau$  might become more accurate. From this estimate, as with the classic decay time method without  $P_\infty$ ,  $C_a$  can then be computed from the knowledge of SVR using the relation given in equation (A.2) to derive  $R_p$ .

In conclusion,  $P_\infty$  influences the model parameter  $R_p$  only and mainly affects the diastolic part of the pressure described by the three different Windkessel models. Thereby,  $P_\infty$  might actually improve the model accuracy during diastole, while leaving the general qualitative behaviour unchanged, which could be beneficial for any kind of parameter identification. However, the physiological meaning as well as the appropriate size of  $P_\infty$  still need to be determined in future studies.

## Appendix B

# Remarks on the pulse wave velocity

In order to solve the 1D model of blood flow introduced in section 2.4.1, it was assumed that the pulse wave velocity  $c$  defined in equation 2.51 is constant. This assumption will be investigated in more in detail in this chapter. Therefore, first, an equation for pulse wave velocity introduced by Bramwell and Hill in 1922 [9] will be derived from the Moens-Korteweg pulse wave velocity (PWV) given in equation (2.4). Then it will be shown that, for small increases in area,  $c$  is approximately equal to the Bramwell-Hill PWV if it is assumed to be constant.

### B.1 Moens-Korteweg and Bramwell-Hill

For an inviscid fluid, the Moens-Korteweg equation introduced in equation (2.4) states that the pulse wave velocity can be computed as

$$\text{PWV}_{MK} = \sqrt{\frac{Eh}{2\rho r_0}},$$

with  $E$  denoting the incremental (angular) elastic modulus,  $\rho$  the blood density,  $h$  the stationary wall thickness and  $r_0$  the stationary inner radius of the artery. The incremental elastic modulus  $E$  is defined as the slope of the (presumably linear) stress-strain relation

$$E = \frac{\sigma_\theta}{\epsilon_\theta},$$

where  $\sigma_\theta$  denotes the stress and  $\epsilon_\theta$  the strain, i.e. the deformation, in angular direction. For a thin-walled cylinder (thickness of the wall is at least one tenth of the radius) the circumferential or hoop stress created by an inner change in uniform pressure  $\Delta P$  is given by

$$\sigma_\theta = \frac{\Delta P r_0}{h}, \tag{B.1}$$



compare [11]. The deformation caused by the stress equals the change in circumference divided by the stationary circumference.

$$\epsilon_\theta = \frac{2\pi(r_0 + \Delta r) - 2\pi r_0}{2\pi r_0} = \frac{\Delta r}{r_0}$$

$E$  is therefore given by

$$E = \frac{\sigma_\theta}{\epsilon_\theta} = \frac{\frac{\Delta P r_0}{h}}{\frac{\Delta r}{r_0}} = \frac{\Delta P r_0^2}{h \Delta r}.$$

From the above equation, an expression for  $\Delta r$  can be derived.

$$\Delta r = \frac{\Delta P r_0^2}{E h} \quad (\text{B.2})$$

Hence, because of the assumed linear elasticity,  $r$  is increasing linearly with  $P$ . For the cross-sectional area of the vessel it holds that

$$A = r^2 \pi = (r_0 + \Delta r)^2 \pi = r_0^2 \pi \left( 1 + \frac{2\Delta r}{r_0} + \left( \frac{\Delta r}{r_0} \right)^2 \right).$$

For rather small relative changes in radius  $\frac{\Delta r}{r_0}$ , the last quadratic term can be neglected, which equals a linearisation of  $A$  with respect to  $r$ , i.e.  $A$  is increasing linearly instead of quadratically with  $r$  and therefore  $P$ . Using equation (B.2) leads to

$$A \approx A_0 \left( 1 + \frac{2\Delta r}{r_0} \right) = A_0 \left( 1 + \Delta P \frac{2r_0}{E h} \right)$$

and hence

$$\frac{\partial A}{\partial P} \approx A_0 \left( \frac{2r_0}{E h} \right) \Rightarrow \frac{A_0}{\frac{\partial A}{\partial P}} \approx \frac{E h}{2r_0},$$

which finally yields the Bramwell-Hill equation for pulse wave velocity

$$\text{PWV}_{MK} = \sqrt{\frac{E h}{2\rho r_0}} \approx \sqrt{\frac{A_0}{\rho \frac{\partial A}{\partial P}}} = \text{PWV}_{BH}. \quad (\text{B.3})$$

## B.2 Investigating the assumption of constant pulse wave velocity

Recalling the definition of  $c$  given in equation (2.51),

$$c^2 = \frac{A}{\rho \frac{\partial A}{\partial P}},$$

a constant  $c$  implies that  $\frac{\partial A}{\partial P} \frac{1}{A}$  is constant. This term describes the relative change in area caused by a change in pressure, in other words the distensibility of the artery [90]. Constant  $c$  thus implies constant distensibility.

The rearranged equation  $\frac{\partial A}{\partial P} = \frac{1}{\rho c^2} A$  describes an exponential increase of  $A$  with pressure

$$A(P) = A_0 e^{\frac{P-P_0}{\rho c^2}},$$

for  $A(P_0) = A_0$ . Examples for the resulting distension of the cross sectional area for different values of  $c$  are shown in figure B.1.

Linearisation of the above equation at the stationary pressure  $P_0$ , i.e. approximating the exponential term by  $\exp(\frac{P-P_0}{\rho c^2}) \sim 1 + \frac{P-P_0}{\rho c^2}$ , yields the Bramwell-Hill PWV

$$A(P) = A_0 e^{\frac{P-P_0}{\rho c^2}} \sim A_0 \left( 1 + \frac{\Delta P}{\rho c^2} \right) \Rightarrow \frac{\partial A}{\partial P} \sim A_0 \frac{1}{\rho c^2} \Rightarrow c^2 \sim \frac{A_0}{\rho \frac{\partial A}{\partial P}} = \text{PWV}_{BH}^2. \quad (\text{B.4})$$

The error introduced by linearisation depends on the magnitude of the factor  $\Delta P/\rho c^2$  and consequently on the resulting relative dilation of the artery  $A/A_0$ , compare figure B.1. Hence, for small (relative) changes in cross-sectional area  $A$ , it holds that

$$c \approx \text{PWV}_{BH}.$$

In the previous section, a very similar condition was needed to derive the Bramwell-Hill PWV from the Moens-Korteweg PWV, namely a small relative change in radius  $r$ . Hence, taken together, it follows that

$$c \approx \text{PWV}_{BH} \approx \text{PWV}_{MK},$$

for small relative changes in the cross-sectional area. The pulse wave velocity obtained by applying the method of characteristics to the 1D-model of blood flow derived in section 2.4.1 is thus, in a first approximation, equal to the pulse wave velocities derived by Bramwell and Hill or Moens and Korteweg.

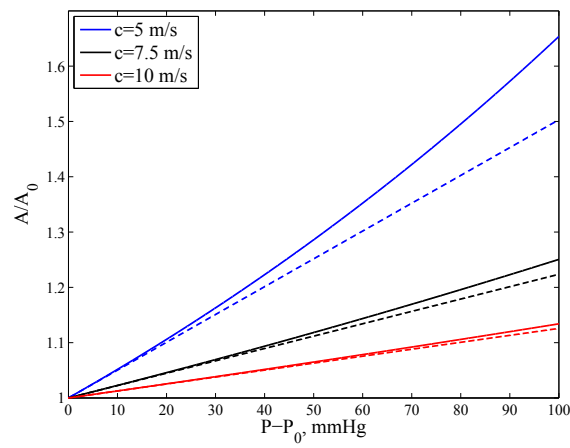


Figure B.1: Distension of the cross-sectional area for a constant pulse wave velocity as a function of pressure.  $\rho$  was set to  $1060 \text{ kg/m}^3$ . For a stiffer artery ( $c = 10 \text{ m/s}$ , red line), an increase in pressure by 100 mmHg leads to a distension of 1.13 times the original area, whereas in the more elastic case ( $c = 5 \text{ m/s}$ , blue line), the area increases by a factor of 1.67. The dashed lines represent the linearised equations.

# Bibliography

- [1] E. Agabiti-Rosei, G. Mancia, M. F. O'Rourke, M. J. Roman, M. E. Safar, H. Smulyan, J.-G. Wang, I. B. Wilkinson, B. Williams, and C. Vlachopoulos. Central blood pressure measurements and antihypertensive therapy. *Hypertension*, 50(1):154–160, 2007.
- [2] J. Aguado-Sierra, J. Alastruey, J. Wang, N. Hadjiloizou, J. Davies, and K. Parker. Separation of the reservoir and wave pressure and velocity from measurements at an arbitrary location in arteries. *Proceedings of the Institution of Mechanical Engineers, Part H: Journal of Engineering in Medicine*, 222(4):403–416, 2008.
- [3] J. Alastruey, K. H. Parker, J. Peiró, and S. J. Sherwin. Lumped parameter outflow models for 1-D blood flow simulations: effect on pulse waves and parameter estimation. *Communications in Computational Physics*, 4(2):317–336, 2008.
- [4] D. Aronson and A. J. Burger. Relation between pulse pressure and survival in patients with decompensated heart failure. *The American Journal of Cardiology*, 93(6):785–788, 2004.
- [5] Authors/Task Force Members, J. J. McMurray, S. Adamopoulos, S. D. Anker, A. Auricchio, M. Böhm, K. Dickstein, V. Falk, G. Filippatos, C. Fonseca, M. A. Gomez-Sanchez, T. Jaarsma, L. Køber, G. Y. Lip, A. P. Maggioni, A. Parkhomenko, B. M. Pieske, B. A. Popescu, P. K. Rønnevik, F. H. Rutten, J. Schwitter, P. Seferovic, J. Stepinska, P. T. Trindade, A. A. Voors, F. Zannad, and A. Zeiher. ESC Guidelines for the diagnosis and treatment of acute and chronic heart failure 2012. *European Journal of Heart Failure*, 14(8):803–869, 2012.
- [6] A. Avolio. Input impedance of distributed arterial structures as used in investigations of underlying concepts in arterial haemodynamics. *Medical & Biological Engineering & Computing*, 47(2):143–151, 2009.
- [7] M. Bay, V. Kirk, J. Parner, C. Hassager, H. Nielsen, K. Krogsgaard, J. Trawinski, S. Boesgaard, and J. Aldershvile. NT-proBNP: a new diagnostic screening tool to differentiate between patients with normal and reduced left ventricular systolic function. *Heart*, 89(2):150–154, 2002.
- [8] G. S. Bleumink, A. M. Knetsch, M. C. Sturkenboom, S. M. Straus, A. Hofman, J. W. Deckers, J. C. Witteman, and B. H. Stricker. Quantifying the heart failure epidemic:

- prevalence, incidence rate, lifetime risk and prognosis of heart failure. *European Heart Journal*, 25(18):1614–1619, 2004.
- [9] J. C. Bramwell and A. V. Hill. The velocity of the pulse wave in man. *Proceedings of the Royal Society of London B: Biological Sciences*, 93(652):298–306, 1922.
- [10] E. Braunwald. Cardiovascular medicine at the turn of the millennium: Triumphs, concerns, and opportunities. *New England Journal of Medicine*, 337(19):1360–1369, 1997.
- [11] B. H. Brown, R. H. Smallwood, D. C. Barber, P. V. Lawford, and D. R. Hose. *Medical Physics and Biomedical Engineering*. IOP Publishing, London, 1999.
- [12] G. D. Buckberg, D. E. Fixler, J. P. Archie, and J. I. Hoffman. Experimental subendocardial ischemia in dogs with normal coronary arteries. *Circulation Research*, 30(1):67–81, 1972.
- [13] R. Burattini and G. Gnudi. Computer identification of models for the arterial tree input impedance: Comparison between two new simple models and first experimental results. *Medical & Biological Engineering & Computing*, 20(2):134–144, 1982.
- [14] D. Burkhoff, J. Alexander, and J. Schipke. Assessment of Windkessel as a model of aortic input impedance. *American Journal of Physiology - Heart and Circulatory Physiology*, 255(4):H742–H753, 1988.
- [15] C. G. Caro, T. J. Pedley, R. C. Schroter, and W. A. Seed. *The Mechanics of the Circulation*. Cambridge University Press, second edition, 2011.
- [16] S. Chandraprakasam, S. Kanuri, and C. Hunter. Mid-ventricular variant of dobutamine-induced stress cardiomyopathy. *Research in Cardiovascular Medicine*, 4(2):e25223, 2015.
- [17] J. A. Chirinos, J. G. Kips, D. R. Jacobs, L. Brumback, D. A. Duprez, R. Kronmal, D. A. Bluemke, R. R. Townsend, S. Vermeersch, and P. Segers. Arterial Wave Reflections and Incident Cardiovascular Events and Heart Failure, MESA (Multiethnic Study of Atherosclerosis). *Journal of the American College of Cardiology*, 60(21):2170–2177, 2012.
- [18] M. R. Cowie, S. D. Anker, J. G. F. Cleland, G. M. Felker, G. Filippatos, T. Jaarsma, P. Jourdain, E. Knight, B. Massie, P. Ponikowski, and J. López-Sendón. Improving care for patients with acute heart failure: before, during and after hospitalization. *ESC Heart Failure*, 1(2):110–145, 2014.
- [19] S. L. Curtis, A. Zambanini, J. Mayet, S. A. M. Thom, R. Foale, K. H. Parker, and A. D. Hughes. Reduced systolic wave generation and increased peripheral wave reflection in chronic heart failure. *American Journal of Physiology - Heart and Circulatory Physiology*, 293(1):H557–H562, 2007.
- [20] M. De Melis, U. Morbiducci, E. Rietzschel, M. De Buyzere, A. Qasem, L. Van Bortel, T. Claessens, F. Montecvecchi, A. Avolio, and P. Segers. Blood pressure waveform analysis by means of wavelet transform. *Medical & Biological Engineering & Computing*, 47(2):165–173, 2009.

- [21] S. J. Denardo, R. Nandyala, G. L. Freeman, G. L. Pierce, and W. W. Nichols. Pulse wave analysis of the aortic pressure waveform in severe left ventricular systolic dysfunction. *Circulation: Heart Failure*, 3(1):149–156, 2010.
- [22] A. T. Djami-Tchatchou, G. R. Norton, A. Raymond, H. L. Booyesen, B. Hodson, E. Libhaber, P. Sareli, and A. J. Woodiwiss. Intrafamilial aggregation and heritability of aortic reflected (backward) waves derived from wave separation analysis. *American Journal of Hypertension*, 28(12):1427–1433, 2015.
- [23] G. M. Drzewiecki, J. Melbin, and A. Noordergraaf. Arterial tonometry: Review and analysis. *Journal of Biomechanics*, 16(2):141–152, 1983.
- [24] J.-P. L. Dujardin and D. N. Stone. Characteristic impedance of the proximal aorta determined in the time and frequency domain: a comparison. *Medical & Biological Engineering & Computing*, 19(5):565–568, 1981.
- [25] W. Estelberger. Eine neue nichtinvasive Pulskontur- Schlagvolumenbestimmungsmethode aufgrund eines Optimierungsmodells der Herzarbeit. *Biomedizinische Technik*, 22(9):211–217, 1977.
- [26] R. H. Fagard, K. Pardaens, and J. Vanhaecke. Is the predictive power of a low-pulse pressure independent of peak oxygen uptake in advanced chronic heart failure? *Journal of Human Hypertension*, 22(1):57–59, 2007.
- [27] H. Fok, A. Guilcher, Y. Li, S. Brett, A. Shah, B. Clapp, and P. Chowienczyk. Augmentation pressure is influenced by ventricular contractility/relaxation dynamics: Novel mechanism of reduction of pulse pressure by nitrates. *Hypertension*, 63(5):1050–1055, 2014.
- [28] O. Frank. Die Grundform des Arteriellen Pulses: Mathematische Analyse. *Zeitschrift für Biologie*, 37:483–526, 1899.
- [29] D. D. Gutterman and A. W. Cowley. Relating cardiac performance with oxygen consumption: historical observations continue to spawn scientific discovery. *American Journal of Physiology - Heart and Circulatory Physiology*, 291(6):H2555–H2556, 2006.
- [30] A. Haiden, B. Eber, and T. Weber. U-shaped relationship of left ventricular ejection time index and all-cause mortality. *American Journal of Hypertension*, 27(5):702–709, 2014.
- [31] J. Hämäläinen and R. Hämäläinen. Energy cost minimization in left ventricular ejection: an optimal control model. *Journal of Applied Physiology*, 61(5):1972–1979, 1986.
- [32] B. Hametner, C. Mayer, M. Bachler, T. Weber, S. Parragh, and S. Wassertheurer. Pulse wave intensity and ECG: A multisensor approach for the risk assessment in systolic heart failure. In *Sensors Applications Symposium (SAS), 2015 IEEE*, pages 1–5, April 2015.
- [33] B. Hametner, S. Parragh, C. Mayer, J. Kropf, and S. Wassertheurer. Optimizing ventricular work: a matter of constraints. In *The 24th European Modeling and Simulation Symposium*, pages 322–327, 2012.

- [34] B. Hametner, S. Wassertheurer, J. Kropf, C. Mayer, B. Eber, and T. Weber. Oscillometric estimation of aortic pulse wave velocity: comparison with intra-aortic catheter measurements. *Blood Pressure Monitoring*, 18(3):173–176, 2013.
- [35] B. Hametner, S. Wassertheurer, J. Kropf, C. Mayer, A. Holzinger, B. Eber, and T. Weber. Wave reflection quantification based on pressure waveforms alone - Methods, comparison, and clinical covariates. *Computer Methods and Programs in Biomedicine*, 109(3):250–259, 2013.
- [36] B. Hametner, S. Wassertheurer, T. Weber, and F. Breiteneker. Non-invasive determination of pulse wave intensity using a dynamic blood flow model. In *Abstract Booklet Einsteins in the City 2011*, 2011.
- [37] B. Hametner, T. Weber, C. Mayer, J. Kropf, and S. Wassertheurer. Calculation of arterial characteristic impedance: a comparison using different blood flow models. *Mathematical and Computer Modelling of Dynamical Systems*, 19(4):319–330, 2013.
- [38] B. Hametner, T. Weber, S. Parragh, B. Eber, and S. Wassertheurer. Impaired systolic function is associated with altered forward wave intensity. *Artery Research*, 8(4):136, 2014.
- [39] J. Hashimoto, W. W. Nichols, M. F. O’Rourke, and Y. Imai. Association between wasted pressure effort and left ventricular hypertrophy in hypertension: Influence of arterial wave reflection. *American Journal of Hypertension*, 21(3):329–333, 2008.
- [40] J. Hashimoto, B. Westerhof, N. Westerhof, Y. Imai, and M. O’Rourke. Different role of wave reflection magnitude and timing on left ventricular mass reduction during antihypertensive treatment. *Journal of Hypertension*, 26(5):1017–1024, 2008.
- [41] A. D. Hughes and K. H. Parker. Forward and backward waves in the arterial system: impedance or wave intensity analysis? *Medical & Biological Engineering & Computing*, 47(2):207–210, 2009.
- [42] C. E. Jackson, D. Castagno, A. P. Maggioni, L. Køber, I. B. Squire, K. Swedberg, B. Andersson, A. M. Richards, A. Bayes-Genis, C. Tribouilloy, J. Dobson, C. A. Ariti, K. K. Poppe, N. Earle, G. Whalley, S. J. Pocock, R. N. Doughty, and J. J. McMurray. Differing prognostic value of pulse pressure in patients with heart failure with reduced or preserved ejection fraction: results from the MAGGIC individual patient meta-analysis. *European Heart Journal*, 36(18):1106–1114, 2015.
- [43] G. N. Jager, N. Westerhof, and A. Noordergraaf. Oscillatory Flow Impedance in Electrical Analog of Arterial System: Representation of Sleeve Effect and Non-Newtonian Properties of Blood. *Circulation Research*, 16(2):121–133, 1965.
- [44] C. J. H. Jones and M. Sugawara. “Wavefronts” in the aorta – implications for the mechanisms of left ventricular ejection and aortic valve closure. *Cardiovascular Research*, 27(11):1902–1905, 1993.
- [45] W. B. Kannel and A. J. Belanger. Epidemiology of heart failure. *American Heart Journal*, 121(3):951–957, 1991.

- [46] M. Karamanoglu and M. P. Feneley. Late systolic pressure augmentation: role of left ventricular outflow patterns. *American Journal of Physiology - Heart and Circulatory Physiology*, 277(2):H481–H487, 1999.
- [47] M. Karamanoglu, M. F. O'Rourke, A. P. Avolio, and R. P. Kelly. An analysis of the relationship between central aortic and peripheral upper limb pressure waves in man. *European Heart Journal*, 14(2):160–167, 1993.
- [48] R. Kelly, C. Hayward, A. Avolio, and M. O'Rourke. Noninvasive determination of age-related changes in the human arterial pulse. *Circulation*, 80(6):1652–1659, 1989.
- [49] J. G. Kips, E. R. Rietzschel, M. L. De Buyzere, B. E. Westerhof, T. C. Gillebert, L. M. Van Bortel, and P. Segers. Evaluation of noninvasive methods to assess wave reflection and pulse transit time from the pressure waveform alone. *Hypertension*, 53(2):142–149, 2009.
- [50] R. Lang, M. Bierig, R. Devereux, F. Flachskampf, E. Foster, P. Pellikka, M. Picard, M. Roman, J. Seward, J. Shanewise, S. Solomon, K. Spencer, M. Sutton, and W. Stewart. Recommendations for chamber quantification: a report from the American Society of Echocardiography's Guidelines and Standards Committee and the Chamber Quantification Writing Group, developed in conjunction with the European Association of Echocardiography, a branch of the European Society of Cardiology. *Journal of the American Society of Echocardiography*, 18(12):1440–1463, 2005.
- [51] W. K. Laskey and W. G. Kussmaul. Arterial wave reflection in heart failure. *Circulation*, 75(4):711–722, 1987.
- [52] W. K. Laskey, W. G. Kussmaul, J. L. Martin, J. P. Kleaveland, J. W. Hirshfeld, and S. Shroff. Characteristics of vascular hydraulic load in patients with heart failure. *Circulation*, 72(1):61–71, 1985.
- [53] W. K. Laskey, J. Wu, P. J. Schulte, A. F. Hernandez, C. W. Yancy, P. A. Heidenreich, D. L. Bhatt, and G. C. Fonarow. Association of arterial pulse pressure with long-term clinical outcomes in patients with heart failure. *Journal of the American College of Cardiology: Heart Failure*, 4(1):42–49, 2016.
- [54] S. Laurent, J. Cockcroft, L. Van Bortel, P. Boutouyrie, C. Giannattasio, D. Hayoz, B. Pannier, C. Vlachopoulos, I. Wilkinson, and H. Struijker-Boudier. Expert consensus document on arterial stiffness: methodological issues and clinical applications. *European Heart Journal*, 27(21):2588–2605, 2006.
- [55] E. Libhaber, A. J. Woodiwiss, A. Raymond, M. Gomes, M. J. Maseko, P. Sareli, and G. R. Norton. Independent associations of circulating galectin-3 concentrations with aortic pulse wave velocity and wave reflection in a community sample: novelty and significance. *Hypertension*, 65(6):1356–1364, 2015.
- [56] A. Lieber, S. Millasseau, L. Bourhis, J. Blacher, A. Protogerou, B. I. Levy, and M. E. Safar. Aortic wave reflection in women and men. *American Journal of Physiology - Heart and Circulatory Physiology*, 299(1):H236–H242, 2010.



- [57] T. F. Lüscher. Heart failure: the cardiovascular epidemic of the 21st century. *European Heart Journal*, 36(7):395–397, 2015.
- [58] C. L. Lucas, B. R. Wilcox, B. Ha, and G. W. Henry. Comparison of time domain algorithms for estimating aortic characteristic impedance in humans. *IEEE Transactions on Biomedical Engineering*, 35(1):62–68, 1988.
- [59] M. Ruiz Villarreal, alias LadyofHats. Circulatory system no tags. Wikimedia Commons, released into the public domain. [https://commons.wikimedia.org/wiki/File:Circulatory\\_System\\_no\\_tags.svg](https://commons.wikimedia.org/wiki/File:Circulatory_System_no_tags.svg) [last retrieved: 16 September 2016].
- [60] F. A. Mahomed. The physiology and clinical use of the sphygmograph. *The Medical Times and Gazette*, 1:62–64, 1872.
- [61] G. Mancia, R. Fagard, K. Narkiewicz, J. Redón, A. Zanchetti, M. Böhm, T. Christiaens, R. Cifkova, G. De Backer, A. Dominiczak, et al. Task Force Members. 2013 ESH/ESC Guidelines for the management of arterial hypertension: the Task Force for the management of arterial hypertension of the European Society of Hypertension (ESH) and of the European Society of Cardiology (ESC). *Journal of Hypertension*, 31(7):1281–357, 2013.
- [62] E. Maret, L. Brudin, L. Lindstrom, E. Nylander, J. L. Ohlsson, and J. E. Engvall. Computer-assisted determination of left ventricular endocardial borders reduces variability in the echocardiographic assessment of ejection fraction. *Cardiovascular Ultrasound*, 6(1):1–14, 2008.
- [63] D. T. Mason, J. F. Spann Jr., R. Zelis, and E. A. Amsterdam. Alterations of hemodynamics and myocardial mechanics in patients with congestive heart failure: Pathophysiologic mechanisms and assessment of cardiac function and ventricular contractility. *Progress in Cardiovascular Diseases*, 12(6):507–557, 1970.
- [64] C. Mayer. *Pulse contour analysis model for non-invasive determination of hemodynamical parameters*. PhD thesis, Technische Universität Wien, 2007.
- [65] C. M. McEniery, J. R. Cockcroft, M. J. Roman, S. S. Franklin, and I. B. Wilkinson. Central blood pressure: current evidence and clinical importance. *European Heart Journal*, 35(26):1719–1725, 2014.
- [66] J. Merillon, G. Fontenier, J. Lerallut, M. Jaffrin, J. Chastre, P. Assayag, G. Motte, and R. Gourgon. Aortic input impedance in heart failure: comparison with normal subjects and its changes during vasodilator therapy. *European Heart Journal*, 5(6):447–455, 1984.
- [67] G. F. Mitchell, L. A. Moyé, E. Braunwald, J.-L. Rouleau, V. Bernstein, E. M. Geltman, G. C. Flaker, M. A. Pfeffer, and for the SAVE Investigators. Sphygmomanometrically determined pulse pressure is a powerful independent predictor of recurrent events after myocardial infarction in patients with impaired left ventricular function. *Circulation*, 96(12):4254–4260, 1997.

- [68] G. F. Mitchell, J.-C. Tardif, J. M. O. Arnold, G. Marchiori, T. X. O'Brien, M. E. Dunlap, and M. A. Pfeffer. Pulsatile hemodynamics in congestive heart failure. *Hypertension*, 38(6):1433–1439, 2001.
- [69] M. W. Mohiuddin, G. A. Laine, and C. M. Quick. Increase in pulse wavelength causes the systemic arterial tree to degenerate into a classical windkessel. *American Journal of Physiology - Heart and Circulatory Physiology*, 293(2):H1164–H1171, 2007.
- [70] A. Mosterd, A. Hoes, M. de Bruyne, J. Deckers, D. Linker, A. Hofman, and D. Grobbee. Prevalence of heart failure and left ventricular dysfunction in the general population; The Rotterdam Study. *European Heart Journal*, 20(6):447–455, 1999.
- [71] D. Mozaffarian, E. J. Benjamin, A. S. Go, D. K. Arnett, M. J. Blaha, M. Cushman, S. R. Das, S. de Ferranti, J.-P. Després, H. J. Fullerton, V. J. Howard, M. D. Huffman, C. R. Isasi, M. C. Jiménez, S. E. Judd, B. M. Kissela, J. H. Lichtman, L. D. Lisabeth, S. Liu, R. H. Mackey, D. J. Magid, D. K. McGuire, E. R. Mohler, C. S. Moy, P. Muntner, M. E. Mussolino, K. Nasir, R. W. Neumar, G. Nichol, L. Palaniappan, D. K. Pandey, M. J. Reeves, C. J. Rodriguez, W. Rosamond, P. D. Sorlie, J. Stein, A. Towfighi, T. N. Turan, S. S. Virani, D. Woo, R. W. Yeh, and M. B. Turner. Heart disease and stroke statistics—2016 update. *Circulation*, 2015.
- [72] J. P. Murgo, N. Westerhof, J. P. Giolma, and S. A. Altobelli. Aortic input impedance in normal man: relationship to pressure wave forms. *Circulation*, 62(1):105–116, 1980.
- [73] E. Mutschler, G. Thews, P. Vaupel, and H.-G. Schaible. *Anatomie, Physiologie, Pathophysiologie des Menschen*. Wissenschaftliche Verlagsgesellschaft Stuttgart, 2007.
- [74] M. Namasivayam, A. Adji, and M. F. O'Rourke. Influence of aortic pressure wave components determined noninvasively on myocardial oxygen demand in men and women. *Hypertension*, 57(2):193–200, 2011.
- [75] M. Namasivayam, A. Adji, and M. F. O'Rourke. Evaluating the hemodynamic basis of age-related central blood pressure change using aortic flow triangulation. *American Journal of Hypertension*, 29(2):178–184, 2016.
- [76] W. W. Nichols, C. R. Conti, W. E. Walker, and W. R. Milnor. Input impedance of the systemic circulation in man. *Circulation Research*, 40(5):451–458, 1977.
- [77] W. W. Nichols, M. F. O'Rourke, and C. Vlachopoulos. *McDonald's Blood Flow in Arteries: Theoretical, Experimental and Clinical Principles*. Hodder Arnold, London, sixth edition, 2011.
- [78] E. Noldus. Optimal control aspects of left ventricular ejection dynamics. *Journal of Theoretical Biology*, 63(2):275–309, 1976.
- [79] E. O'Brien and D. Fitzgerald. The history of blood pressure measurement. *Journal of Human Hypertension*, 8(2):73–84, 1994.

- [80] G. Ogedegbe and T. Pickering. Principles and techniques of blood pressure measurement. *Cardiology Clinics*, 28(4):571–586, 2010.
- [81] M. S. Olufsen. *Applied Mathematical Models in Human Physiology*, chapter 5 - Modeling Flow and Pressure in the Systemic Arteries, pages 77–111. SIAM, 2003.
- [82] M. F. O’Rourke. Arterial stiffness, systolic blood pressure, and logical treatment of arterial hypertension. *Hypertension*, 15(4):339–47, 1990.
- [83] M. F. O’Rourke. Time domain analysis of the arterial pulse in clinical medicine. *Medical & Biological Engineering & Computing*, 47(2):119–129, 2009.
- [84] M. F. O’Rourke and D. E. Gallagher. Pulse wave analysis. *Journal of Hypertension*, 14:S147–S158, 1996.
- [85] M. F. O’Rourke and J. Hashimoto. Mechanical factors in arterial aging: A clinical perspective. *Journal of the American College of Cardiology*, 50(1):1–13, 2007.
- [86] M. F. O’Rourke, A. Pauca, and X.-J. Jiang. Pulse wave analysis. *British Journal of Clinical Pharmacology*, 51(6):507–522, 2001.
- [87] M. F. O’Rourke and M. G. Taylor. Donald Arthur McDonald. *Clinical Cardiology*, 16(11):842–843, 1993.
- [88] A. Paglia, L. Sasso, F. Pirozzi, A. Iannuzzi, A. Carlomagno, P. Abete, M. Petretta, and D. Bonaduce. Arterial wave reflections and ventricular-vascular interaction in patients with left ventricular systolic dysfunction. *International Heart Journal*, 55(6):526–532, 2014.
- [89] K. H. Parker. A brief history of arterial wave mechanics. *Medical & Biological Engineering & Computing*, 47(2):111–118, 2009.
- [90] K. H. Parker. An introduction to wave intensity analysis. *Medical & Biological Engineering & Computing*, 47(2):175–188, 2009.
- [91] K. H. Parker and C. J. H. Jones. Forward and backward running waves in the arteries: analysis using the method of characteristics. *Journal of Biomechanical Engineering*, 112(3):322–326, 1990.
- [92] K. H. Parker, C. J. H. Jones, J. R. Dawson, and D. G. Gibson. What stops the flow of blood from the heart? *Heart and Vessels*, 4(4):241–245, 1988.
- [93] S. Parragh. Modelle zur Bestimmung des aortalen Blutflusses basierend auf Optimalitätsbedingungen. Master’s thesis, Technische Universität Wien, 2013.
- [94] S. Parragh, B. Hametner, M. Bachler, J. Kellermair, B. Eber, S. Wassertheurer, and T. Weber. Determinants and covariates of central pressures and wave reflections in systolic heart failure. *International Journal of Cardiology*, 190(0):308–314, 2015.
- [95] S. Parragh, B. Hametner, M. Bachler, T. Weber, B. Eber, and S. Wassertheurer. Non-invasive wave reflection quantification in patients with reduced ejection fraction. *Physiological Measurement*, 36(2):179–190, 2015.

- [96] S. Parragh, B. Hametner, and S. Wassertheurer. Simulating aortic blood flow and pressure by an optimal control model. *SNE Simulation Notes Europe*, 23(2):101–106, 2013.
- [97] S. Parragh, B. Hametner, and S. Wassertheurer. Influence of an Asymptotic Pressure Level on the Windkessel Models of the Arterial System. *IFAC-PapersOnLine*, 48(1):17–22, 2015.
- [98] S. Parragh, B. Hametner, T. Weber, B. Eber, and S. Wassertheurer. The decay of aortic blood pressure during diastole: Influence of an asymptotic pressure level on the exponential fit. *Artery Research*, 8(4):162, 2014.
- [99] C. J. Pepine, W. W. Nichols, and C. R. Conti. Aortic input impedance in heart failure. *Circulation*, 58(3):460–465, 1978.
- [100] K. Pfeiffer and T. Kenner. Minimization of the external work of the left ventricle and optimization of flow and pressure pulses. In R. Bauer and R. Busse, editors, *The arterial system*, pages 216–223. Springer, 1978.
- [101] P. Ponikowski, A. A. Voors, S. D. Anker, H. Bueno, J. G. F. Cleland, A. J. S. Coats, V. Falk, J. R. González-Juanatey, V.-P. Harjola, E. A. Jankowska, M. Jessup, C. Linde, P. Nihoyannopoulos, J. T. Parissis, B. Pieske, J. P. Riley, G. M. C. Rosano, L. M. Ruilope, F. Ruschitzka, F. H. Rutten, and P. van der Meer. 2016 ESC Guidelines for the diagnosis and treatment of acute and chronic heart failure. *European Heart Journal*, 37(27):2129–2200, 2016.
- [102] Prospective Studies Collaboration. Age-specific relevance of usual blood pressure to vascular mortality: a meta-analysis of individual data for one million adults in 61 prospective studies. *The Lancet*, 360(9349):1903–1913, 2002.
- [103] A. Qasem and A. Avolio. Determination of aortic pulse wave velocity from waveform decomposition of the central aortic pressure pulse. *Hypertension*, 51(2):188–195, 2008.
- [104] C. M. Quick, D. S. Berger, R. H. Stewart, G. A. Laine, C. J. Hartley, and A. Noordergraaf. Resolving the hemodynamic inverse problem. *Biomedical Engineering, IEEE Transactions on*, 53(3):361–368, 2006.
- [105] M. A. Quiñones, C. M. Otto, M. Stoddard, A. Waggoner, and W. A. Zoghbi. Recommendations for quantification of Doppler echocardiography: a report from the Doppler Quantification Task Force of the Nomenclature and Standards Committee of the American Society of Echocardiography. *Journal of the American Society of Echocardiography*, 15:167–184, 2002.
- [106] C. E. Raphael, Z. I. Whinnett, J. E. Davies, M. Fontana, E. A. Ferenczi, C. H. Manisty, J. Mayet, and D. P. Francis. Quantifying the paradoxical effect of higher systolic blood pressure on mortality in chronic heart failure. *Heart*, 95(1):56–62, 2009.
- [107] V. Regnault, J. Lagrange, A. Pizard, M. E. Safar, R. Fay, B. Pitt, P. Challande, P. Rossignol, F. Zannad, and P. Lacolley. Opposite Predictive Value of Pulse Pressure and Aortic Pulse Wave Velocity on Heart Failure With Reduced Left Ventricular Ejection Fraction:

- Insights From an Eplerenone Post-Acute Myocardial Infarction Heart Failure Efficacy and Survival Study (EPHESUS) Substudy. *Hypertension*, 63(1):105–111, 2014.
- [108] E.-R. Rietzschel, M. L. De Buyzere, S. Bekaert, P. Segers, D. De Bacquer, L. Cooman, P. Van Damme, P. Cassiman, M. Langlois, P. van Oostveldt, P. Verdonck, G. De Backer, and T.C. Gillebert, on behalf of the Asklepios investigators. Rationale, design, methods and baseline characteristics of the Asklepios Study. *European Journal of Cardiovascular Prevention & Rehabilitation*, 14(2):179–191, 2007.
- [109] V. L. Roger. Epidemiology of heart failure. *Circulation Research*, 113(6):646–659, 2013.
- [110] M. J. Roman, R. B. Devereux, J. R. Kizer, E. T. Lee, J. M. Galloway, T. Ali, J. G. Umans, and B. V. Howard. Central pressure more strongly relates to vascular disease and outcome than does brachial pressure. *Hypertension*, 50(1):197–203, 2007.
- [111] S. Sakuragi and W. P. Abhayaratna. Arterial stiffness: Methods of measurement, physiologic determinants and prediction of cardiovascular outcomes. *International Journal of Cardiology*, 138(2):112–118, 2010.
- [112] J. D. Schipke, G. Heusch, A. P. Sanii, E. Gams, and J. Winter. Static filling pressure in patients during induced ventricular fibrillation. *American Journal of Physiology - Heart and Circulatory Physiology*, 285(6):H2510–H2515, 2003.
- [113] R. Schmitt. 8 - Transmission Lines. In R. Schmitt, editor, *Electromagnetics Explained*, EDN Series for Design Engineers, pages 153–179. Newnes, Burlington, 2002.
- [114] P. Segers, E. R. Rietzschel, M. L. De Buyzere, D. De Bacquer, L. M. Van Bortel, G. De Backer, T. C. Gillebert, and P. R. Verdonck. Assessment of pressure wave reflection: getting the timing right! *Physiological Measurement*, 28(9):1045–1056, 2007.
- [115] P. Segers, E. R. Rietzschel, M. L. De Buyzere, N. Stergiopulos, N. Westerhof, L. M. Van Bortel, T. Gillebert, and P. R. Verdonck. Three-and four-element Windkessel models: assessment of their fitting performance in a large cohort of healthy middle-aged individuals. *Proceedings of the Institution of Mechanical Engineers, Part H: Journal of Engineering in Medicine*, 222(4):417–428, 2008.
- [116] P. Segers, E. R. Rietzschel, M. L. De Buyzere, S. J. Vermeersch, D. De Bacquer, L. M. Van Bortel, G. De Backer, T. C. Gillebert, P. R. Verdonck, et al. Noninvasive (input) impedance, pulse wave velocity, and wave reflection in healthy middle-aged men and women. *Hypertension*, 49(6):1248–1255, 2007.
- [117] S. Sherwin, V. Franke, J. Peiró, and K. Parker. One-dimensional modelling of a vascular network in space-time variables. *Journal of Engineering Mathematics*, 47(3-4):217–250, 2003.
- [118] N. Stergiopulos, J. J. Meister, and N. Westerhof. Evaluation of methods for estimation of total arterial compliance. *American Journal of Physiology - Heart and Circulatory Physiology*, 268(4):H1540–H1548, 1995.

- [119] N. Stergiopulos, B. E. Westerhof, and N. Westerhof. Total arterial inertance as the fourth element of the windkessel model. *American Journal of Physiology - Heart and Circulatory Physiology*, 276(1):H81–H88, 1999.
- [120] M. Sugawara, K. Niki, N. Ohte, T. Okada, and A. Harada. Clinical usefulness of wave intensity analysis. *Medical & Biological Engineering & Computing*, 47(2):197–206, 2009.
- [121] S.-H. Sung, H.-M. Cheng, K.-L. Wang, W.-C. Yu, S.-Y. Chuang, C.-T. Ting, E. G. Lakatta, F. C. Yin, P. Chou, and C.-H. Chen. White coat hypertension is more risky than prehypertension: Important role of arterial wave reflections. *Hypertension*, 61(6):1346–1353, 2013.
- [122] S.-H. Sung, W.-C. Yu, H.-M. Cheng, C.-W. Lee, M.-M. Lin, S.-Y. Chuang, and C.-H. Chen. Excessive wave reflections on admission predict post-discharge events in patients hospitalized due to acute heart failure. *European Journal of Heart Failure*, 14(12):1348–1355, 2012.
- [123] A. Swillens and P. Segers. Assessment of arterial pressure wave reflection: Methodological considerations. *Artery Research*, 2(4):122–131, 2008.
- [124] K. Takazawa, N. Tanaka, K. Takeda, F. Kurosu, and C. Ibukiyama. Underestimation of vasodilator effects of nitroglycerin by upper limb blood pressure. *Hypertension*, 26(3):520–523, 1995.
- [125] J.-M. Tartiere, D. Logeart, M. Safar, and A. Cohen-Solal. Interaction between pulse wave velocity, augmentation index, pulse pressure and left ventricular function in chronic heart failure. *Journal of Human Hypertension*, 20(3):213–219, 2006.
- [126] The Reference Values for Arterial Stiffness’ Collaboration. Determinants of pulse wave velocity in healthy people and in the presence of cardiovascular risk factors: establishing normal and reference values. *European Heart Journal*, 31(19):2338–2350, 2010.
- [127] G. Tocci, S. Sciarretta, and M. Volpe. Development of heart failure in recent hypertension trials. *Journal of hypertension*, 26(7):1477–1486, 2008.
- [128] C. W. Tsao, A. Lyass, M. G. Larson, D. Levy, N. M. Hamburg, J. A. Vita, E. J. Benjamin, G. F. Mitchell, and R. S. Vasan. Relation of central arterial stiffness to incident heart failure in the community. *Journal of the American Heart Association*, 4(11), 2015.
- [129] J. V. Tyberg, N. G. Shrive, J. C. Bouwmeester, K. H. Parker, and J. Wang Jr. The reservoir-wave paradigm: potential implications for hypertension. *Current Hypertension Reviews*, 4(3):203–213, 2008.
- [130] J.-J. Wang, J. A. Flewitt, N. G. Shrive, K. H. Parker, and J. V. Tyberg. Systemic venous circulation. waves propagating on a windkessel: relation of arterial and venous windkessels to systemic vascular resistance. *American Journal of Physiology - Heart and Circulatory Physiology*, 290(1):H154–H162, 2005.

- [131] J.-J. Wang, A. B. O'Brien, N. G. Shrive, K. H. Parker, and J. V. Tyberg. Time-domain representation of ventricular-arterial coupling as a windkessel and wave system. *American Journal of Physiology-Heart and Circulatory Physiology*, 284(4):H1358–H1368, 2003.
- [132] J.-J. Wang and K. H. Parker. Wave propagation in a model of the arterial circulation. *Journal of Biomechanics*, 37(4):457–470, 2004.
- [133] K.-L. Wang, H.-M. Cheng, S.-H. Sung, S.-Y. Chuang, C.-H. Li, H. A. Spurgeon, C.-T. Ting, S. S. Najjar, E. G. Lakatta, F. C. Yin, P. Chou, and C.-H. Chen. Wave reflection and arterial stiffness in the prediction of 15-year all-cause and cardiovascular mortalities: A community-based study. *Hypertension*, 55(3):799–805, 2010.
- [134] S. Wassertheurer, J. Kropf, T. Weber, M. van der Giet, J. Baulmann, M. Ammer, B. Hametner, C. Mayer, B. Eber, and D. Magometschnigg. A new oscillometric method for pulse wave analysis: comparison with a common tonometric method. *Journal of Human Hypertension*, 24:498–504, 2010.
- [135] S. Wassertheurer, C. Mayer, and F. Breiteneker. Modeling arterial and left ventricular coupling for non-invasive measurements. *Simulation Modelling Practice and Theory*, 16(8):988–997, 2008.
- [136] T. Weber, M. Ammer, M. Rammer, A. Adji, M. O'Rourke, S. Wassertheurer, S. Rosenkranz, and B. Eber. Noninvasive determination of carotid-femoral pulse wave velocity depends critically on assessment of travel distance: a comparison with invasive measurement. *Journal of Hypertension*, 27(8):1624–1630, 2009.
- [137] T. Weber, J. Auer, G. Lamm, M. F. O'Rourke, and B. Eber. Arterial stiffness, central blood pressures, and wave reflections in cardiomyopathy-implications for risk stratification. *Journal of Cardiac Failure*, 13(5):353–359, 2007.
- [138] T. Weber, S. Wassertheurer, B. Hametner, S. Parragh, and B. Eber. Noninvasive methods to assess pulse wave velocity: comparison with the invasive gold standard and relationship with organ damage. *Journal of Hypertension*, 33(5):1023–1031, 2015.
- [139] T. Weber, S. Wassertheurer, M. F. O'Rourke, A. Haiden, R. Zweiker, M. Rammer, B. Hametner, and B. Eber. Pulsatile hemodynamics in patients with exertional dyspnea: Potentially of value in the diagnostic evaluation of suspected heart failure with preserved ejection fraction. *Journal of the American College of Cardiology*, 61(18):1874–1883, 2013.
- [140] T. Weber, S. Wassertheurer, M. Rammer, A. Haiden, B. Hametner, and B. Eber. Wave reflections, assessed with a novel method for pulse wave separation, are associated with end-organ damage and clinical outcomes. *Hypertension*, 60(2):534–541, 2012.
- [141] A. M. Weissler, W. S. Harris, and C. D. Schoenfeld. Systolic time intervals in heart failure in man. *Circulation*, 37(2):149–159, 1968.
- [142] B. E. Westerhof, I. Guelen, N. Westerhof, J. M. Karemaker, and A. Avolio. Quantification of Wave Reflection in the Human Aorta From Pressure Alone: A Proof of Principle. *Hypertension*, 48(4):595–601, 2006.

- [143] B. E. Westerhof and N. Westerhof. Magnitude and return time of the reflected wave: the effects of large artery stiffness and aortic geometry. *Journal of Hypertension*, 30(5):932–939, 2012.
- [144] N. Westerhof, F. Bosman, C. J. De Vries, and A. Noordergraaf. Analog studies of the human systemic arterial tree. *Journal of Biomechanics*, 2(2):121–143, 1969.
- [145] N. Westerhof, J. W. Lankhaar, and B. E. Westerhof. The arterial Windkessel. *Medical & Biological Engineering & Computing*, 47(2):131–141, 2009.
- [146] N. Westerhof and M. F. O’Rourke. Haemodynamic basis for the development of left ventricular failure in systolic hypertension and for its logical therapy. *Journal of Hypertension*, 13(9):943–952, 1995.
- [147] N. Westerhof, P. Segers, and B. E. Westerhof. Wave separation, wave intensity, the reservoir-wave concept, and the instantaneous wave-free ratio: Presumptions and principles. *Hypertension*, 66(1):93–98, 2015.
- [148] N. Westerhof, P. Sipkema, G. Van Den Bos, and G. Elzinga. Forward and backward waves in the arterial system. *Cardiovascular Research*, 6(6):648–656, 1972.
- [149] N. Westerhof, N. Stergiopulos, and M. I. M. Noble. *Snapshots of Hemodynamics, An Aid for Clinical Research and Graduate Education*, volume 18 of *Basic Science for the Cardiologist*. Springer US, 2005.
- [150] I. B. Wilkinson, H. MacCallum, L. Flint, J. R. Cockcroft, D. E. Newby, and D. J. Webb. The influence of heart rate on augmentation index and central arterial pressure in humans. *The Journal of Physiology*, 525(1):263–270, 2000.
- [151] I. B. Wilkinson, N. H. Mohammad, S. Tyrrell, I. R. Hall, D. J. Webb, V. E. Paul, T. Levy, and J. R. Cockcroft. Heart rate dependency of pulse pressure amplification and arterial stiffness. *American Journal of Hypertension*, 15(1):24–30, 2002.
- [152] J. R. Womersley. *An elastic tube theory of pulse transmission and oscillatory flow in mammalian arteries*. Wright Air Development Center, 1957.
- [153] C. M. Wong, N. M. Hawkins, P. S. Jhund, M. R. MacDonald, S. D. Solomon, C. B. Granger, S. Yusuf, M. A. Pfeffer, K. Swedberg, M. C. Petrie, and J. J. McMurray. Clinical Characteristics and Outcomes of Young and Very Young Adults With Heart Failure: The CHARM Programme (Candesartan in Heart Failure Assessment of Reduction in Mortality and Morbidity). *Journal of the American College of Cardiology*, 62(20):1845–1854, 2013.
- [154] S. Yamashiro, J. Daubenspeck, F. Bennett, S. Edelman, and F. Grodins. Optimal control analysis of left ventricular ejection. *Cardiovascular System Dynamics*, pages 427–437, 1978.
- [155] C. W. Yancy, M. Jessup, B. Bozkurt, J. Butler, D. E. Casey, M. H. Drazner, G. C. Fonarow, S. A. Geraci, T. Horwich, J. L. Januzzi, M. R. Johnson, E. K. Kasper, W. C. Levy, F. A. Masoudi, P. E. McBride, J. J. McMurray, J. E. Mitchell, P. N. Peterson, B. Riegel, F. Sam, L. W. Stevenson, W. W. Tang, E. J. Tsai, and B. L. Wilkoff. 2013 ACCF/AHA Guideline



- for the Management of Heart Failure: A Report of the American College of Cardiology Foundation/American Heart Association Task Force on Practice Guidelines. *Circulation*, 128(16):e240–e327, 2013.
- [156] M. Zamir. *The Physics of Pulsatile Flow*. Biological and Medical Physics, Biomedical Engineering. Springer-Verlag New York, first edition, 2000.
- [157] L. Zhao, Y. Song, P. Dong, Z. Li, X. Yang, and S. Wang. Brachial pulse pressure and cardiovascular or all-cause mortality in the general population: A meta-analysis of prospective observational studies. *The Journal of Clinical Hypertension*, 16(9):678–685, 2014.

# Abbreviations

<b>AIx</b> Augmentation Index	<b>PP</b> Pulse Pressure
<b>AP</b> Augmented Pressure	<b>PPAmp</b> Pulse Pressure Amplification
<b>AU</b> Arbitrary Unit	<b>PSA</b> Pressure Systolic Area
<b>CI</b> Confidence Interval	<b>PWA</b> Pulse Wave Analysis
<b>DBP</b> Diastolic Blood Pressure	<b>PWV</b> Pulse Wave Velocity
<b>DPTI</b> Diastolic Pressure Time Index	<b>rEF</b> Reduced Ejection Fraction
<b>ED</b> Ejection Duration	<b>RI</b> Reflection Index
<b>EF</b> Ejection Fraction	<b>RM</b> Reflection Magnitude
<b>ESC</b> European Society of Cardiology	<b>RMSE</b> Root Mean Square Error
<b>HF</b> Heart Failure	<b>SBP</b> Systolic Blood Pressure
<b>HR</b> Heart Rate	<b>SHF</b> Systolic Heart Failure
<b>LV</b> Left Ventricle; Left Ventricular	<b>SPTI</b> Systolic Pressure Time Index
<b>LVETI</b> Left Ventricular Ejection Time Index	<b>SV</b> Stroke Volume
<b>LVSD</b> Left Ventricular Systolic Dysfunction	<b>SVR</b> Systemic Vascular Resistance
<b>MBP</b> Mean Blood Pressure	<b>WIA</b> Wave Intensity Analysis
<b>nEF</b> Normal Ejection Fraction	<b>WK2</b> 2-element Windkessel
<b>NT-proBNP</b> N-terminal pro-B-type natri- uretic peptides	<b>WK3</b> 3-element Windkessel
<b>ODE</b> Ordinary Differential Equation	<b>WK4p</b> parallel 4-element Windkessel
<b>PDE</b> Partial Differential Equation	<b>WSA</b> Wave Separation Analysis

# Nomenclature

Term	Description	Unit	Page
$A$	cross-sectional area of an artery	$\text{cm}^2$	29
AIx	augmentation index	-	10
AP	augmented pressure	mmHg	10
$c$	wave speed	cm/s	32
$C_a$	total arterial compliance	ml/mmHg	22
D wave	late systolic/early diastolic peak in forward intensity	mmHg·cm/s	39
DBP	diastolic blood pressure	mmHg	1
$dI$	wave intensity	mmHg·cm/s	36
$dI_{f,b}$	forward and backward wave intensity	mmHg·cm/s	39
DPTI	diastolic pressure time index	mmHg·s	14
$E$	Young's modulus, elastic modulus	mmHg	11
$\vec{e}$	error vector used in the objective function of the parameter identification procedure		50
$E_w$	wasted effort	s·mmHg	14
ED	ejection duration	ms	9
EF	ejection fraction	%	2
$h$	wall thickness	cm	11
HR	heart rate	bpm	9
$L$	total arterial inductance	mmHg·s <sup>2</sup> /ml	109
LVETI	left ventricular ejection time index	ms	71
MBP	mean blood pressure	mmHg	9
$\tilde{n}$	individual threshold used for the definition of $Z_{\text{model}}$		47
$\omega_n$	n-th harmonic angular frequency	rad/s	15
$P$	arterial blood pressure	mmHg	9
$P_\infty$	asymptotic pressure level	mmHg	23
$P_{LZ}$	auxiliary variable used in the 4-element Windkessel model to describe the pressure across the LZ-component	mmHg	26
$P_{RC}$	auxiliary variable used in the Windkessel models to describe the pressure across the RC-component	mmHg	22
$\hat{P}_n$	n-th complex Fourier coefficient (phasor) of pressure $P$		16
$\bar{P}$	$= \hat{P}_0$ , mean blood pressure	mmHg	15

Term	Description	Unit	Page
$P_1$	first shoulder in the pressure wave	mmHg	10
$P_2$	second shoulder in the pressure wave	mmHg	10
$P_{f,b}$	forward, backward travelling pressure wave	mmHg	19
$ P_{f,b} $	amplitude of $P_{f,b}$	mmHg	20
PP	pulse pressure	mmHg	9
PPAmp	pulse pressure amplification	-	13
$\Delta PSA$	pressure systolic area related to ventricular ejection	mmHg·s	14
PSA	pressure systolic area	mmHg·s	14
PWV	pulse wave velocity	m/s	11
$Q$	volumetric blood flow	ml/s	15
$\hat{Q}_n$	n-th complex Fourier coefficient (phasor) of blood flow $Q$		16
$\bar{Q}$	$= \hat{Q}_0$ , mean blood flow	ml/s	15
$\tilde{Q}$	modelled blood flow	ml/s	47
R wave	mid-systolic peak in backward intensity	mmHg·cm/s	39
$r$	radius	cm	11
$R_p$	peripheral resistance	s·mmHg/ml	22
$\rho$	blood density	g/ml	11
RI	reflection index	-	20
RM	reflection magnitude	-	20
S wave	early systolic peak in forward intensity	mmHg·cm/s	39
SBP	systolic blood pressure	mmHg	1
$\sigma$	$= L/Z_c$ , time constant of the exponential decay of $P_{LZ}$ during diastole	s	48
$\Delta SPTI$	pressure systolic area below DBP	mmHg·s	14
SPTI	systolic pressure time index	mmHg·s	13
SV	stroke volume	ml	45
SVR	systemic vascular resistance	mmHg·s/ml	17
$T$	heartbeat duration	s	9
$T_r$	round trip travel time	ms	11
$t_s$	time of end of systole	s	14
$\tau$	$= R_p C_a$ , time constant of the exponential decay of $P_{RC}$ during diastole	s	48
$U$	arterial blood flow velocity	cm/s	29
$Z_0$	complex characteristic impedance, frequency-dependent		18
$Z_c$	real characteristic impedance, frequency-independent	mmHg·s/ml	18
$Z_{in}$	complex input impedance, frequency-dependent		17
$Z_{model}$	complex model impedance, frequency-dependent		46

# List of Publications

## Journal articles

- [1] S. Parragh, B. Hametner, M. Bachler, J. Kellermair, B. Eber, S. Wassertheurer, and T. Weber. Determinants and covariates of central pressures and wave reflections in systolic heart failure. *International Journal of Cardiology*, 190(0):308–314, 2015.
- [2] S. Parragh, B. Hametner, M. Bachler, T. Weber, B. Eber, and S. Wassertheurer. Non-invasive wave reflection quantification in patients with reduced ejection fraction. *Physiological Measurement*, 36(2):179–190, 2015.
- [3] S. Parragh, B. Hametner, and S. Wassertheurer. Influence of an Asymptotic Pressure Level on the Windkessel Models of the Arterial System. *IFAC-PapersOnLine*, 48(1):17–22, 2015.
- [4] S. Parragh, B. Hametner, and S. Wassertheurer. Simulating aortic blood flow and pressure by an optimal control model. *SNE Simulation Notes Europe*, 23(2):101–106, 2013.
- [5] M. Hillebrand, G. Nouri, B. Hametner, S. Parragh, J. Köster, K. Mortensen, A. Schwarz, Y. von Kodolitsch, and S. Wassertheurer. Ambulatory (24 h) blood pressure and arterial stiffness measurement in marfan syndrome patients: a case control feasibility and pilot study. *BMC Cardiovascular Disorders*, 16:81, 2016.
- [6] B. Hametner, S. Parragh, C. Mayer, T. Weber, L. Van Bortel, M. De Buyzere, P. Segers, E. Rietzschel, and S. Wassertheurer. Assessment of model based (input) impedance, pulse wave velocity, and wave reflection in the asklepios cohort. *PLoS ONE*, 10(10):e0141656, 10 2015.
- [7] T. Weber, S. Wassertheurer, B. Hametner, S. Parragh, and B. Eber. Noninvasive methods to assess pulse wave velocity: comparison with the invasive gold standard and relationship with organ damage. *Journal of Hypertension*, 33(5):1023–1031, 2015.
- [8] T. Weber, S. Parragh and S. Wassertheurer. Is blood-pressure independent arterial de-stiffening possible? *American Journal of Hypertension*, Invited commentary, submitted for publication.

**Talks and poster presentations (first author only)**

- [1] S. Parragh, B. Hametner, C. C. Mayer, S. Wassertheurer, and T. Weber. Nichtlinearer Zusammenhang zwischen aortalem Reservoirdruck und kardiovaskulären Ereignissen in Patienten mit systolischer Herzinsuffizienz. Poster presentation at the *ÖGH Jahrestagung 2016*, Vienna, Austria, 2016-11-18 – 2016-11-19.
- [2] S. Parragh, B. Hametner, C. C. Mayer, S. Wassertheurer, and T. Weber. U-shaped relationship of reservoir pressure to cardiovascular events in patients with heart failure with reduced ejection fraction. In *Artery Research*, 16:55, 2016. Talk at the *Artery 16*, Copenhagen, Denmark, 2016-10-13 – 2016-10-15.
- [3] S. Parragh, B. Hametner, M. Bachler, T. Weber, B. Eber, and S. Wassertheurer. Non-invasive wave reflection quantification in patients with reduced ejection fraction. Invited talk at the *MPEC, Medical Physics and Engineering Conference 16*, Manchester, UK, 2016-09-12 – 2016-09-14.
- [4] S. Parragh, B. Hametner, and S. Wassertheurer. Influence of an Asymptotic Pressure Level on the Windkessel Models of the Arterial System. In *IFAC-PapersOnLine*, 48(1):17–22, 2015. Talk at the *MATHMOD 2015 - 8th Vienna International Conference on Mathematical Modelling*, Vienna, Austria, 2015-02-08 – 2015-02-20.
- [5] S. Parragh, B. Hametner, T. Weber, B. Eber, and S. Wassertheurer. The decay of aortic blood pressure during diastole: Influence of an asymptotic pressure level on the exponential fit. In *Artery Research*, 8(4):162, 2014. Poster presentation at the *Artery 14*, Maastricht, Netherlands, 2014-10-09 – 2014-10-11.

# Curriculum Vitæ

## Personal Information

---

Name	Stephanie Parragh
Address	Währinger Gürtel 166/2/4, 1090 Wien, Austria
Date of Birth	September 1, 1986
Citizenship	Austria
Email	stephanie.parragh@gmx.at

## Education

---

Since 2013	TU WIEN <i>Doctoral programme in Engineering Sciences - Technical Mathematics</i>
2005 – 2013	TU WIEN <i>Diploma programme Technical Mathematics</i> <i>Diploma thesis "Modelle zur Bestimmung des aortalen Blutflusses basierend auf Optimalitätsbedingungen"</i> <i>Graduated as Diplom-Ingenieurin</i>
2012 – 2013	TU WIEN <i>Applied Modelling and Simulation and Decision Making (AMSDM) Masterschool</i>
2010	TECHNICAL UNIVERSITY OF DENMARK <i>Erasmus Programme</i>
2004 – 2005	EF SPANISH LANGUAGE SCHOOL BARCELONA <i>EF Academic Year Abroad</i>
1996 – 2004	AKADEMISCHES GYMNASIUM SALZBURG <i>Humanistic secondary school</i> <i>School pilot project with a main focus on languages</i> <i>Graduated with honours</i>

---

**Work Experience**

- 
- Since 2014    TU WIEN  
*Lecturer at the Institute for Analysis and Scientific Computing*  
*Courses: “Modelling and Simulation of the Heart Circulation” and*  
*“Preparatory Course Mathematics”*
- Since 2013    AIT AUSTRIAN INSTITUTE OF TECHNOLOGY GMBH  
*Health & Environment Department, Biomedical Systems*  
*Research Fellow*
- 2012 – 2013    AIT AUSTRIAN INSTITUTE OF TECHNOLOGY GMBH  
*Health & Environment Department, Biomedical Systems*  
*Internship (FEMtech scholarship)*
- 2011 – 2013    TU WIEN  
*Teaching Assistant at the Institute for Analysis and Scientific Computing*  
*Courses: “Mathematics for Electrical Engineers” (1 and 2) and*  
*“Preparatory Course Mathematics”*

---

**Memberships and Awards**

- 
- Since 2015    ARTERY SOCIETY  
*Student member of the Association for Research into Arterial Structure and Physiology.*
- 2016    MARTIN BLACK PRIZE  
*for the best paper published in Physiological Measurements in 2015, awarded by IOP Publishing in association with IPEM (Institute of Physics and Engineering in Medicine).*

---

**Research Skills**

---

Mathematical modelling & simulation

Medical statistics

Programming/software skills for mathematical applications: Matlab, Maple, Mathematica, AnyLogic, R

---

**Language Skills**

---

German (native language), English (fluent), Spanish (advanced), French (basic)